# Radiation Magnetohydrodynamic Simulations of Star Formation Processes

Kengo Tomida

DOCTOR OF
PHILOSOPHY

Department of Astronomical Science
School of Physical Sciences
The Graduate University for Advanced Studies

2011

# Acknowledgement

First of all, I heartily thank my supervisor, Prof. Kohji Tomisaka. During my five-year PhD course, he gave me a lot of thoughtful advice and always kindly supported me even when he was very busy. I would like to express my gratitude to my collaborators, Prof. Ryohei Kawabe, Prof. Tomoaki Matsumoto, Prof. Masahiro N. Machida, Dr. Kazuya Saigo, Dr. Yasunori Hori, Dr. Satoshi Okuzumi, Dr. Masako Yamada and Dr. Ken Ohsuga. I could not achieve my works without their help. Prof. Nobuo Arimoto, Prof. Shu-ichiro Inutsuka, Prof. Tomoyuki Hanawa, Prof. Junichiro Makino, Prof. Toshikazu Onishi, Prof. Fumitaka Nakamura, Prof. Kazuyuki Omukai, Prof. Eiichiro Kokubo, Dr. Takahiro Kudoh, Dr. Takashi Hosokawa, Dr. Naoki Seto, Dr. Hiroyuki Takahashi, Dr. Shigenobu Hirose, Dr. Tsuyoshi Inoue, Dr. Ko Nakamura, Dr. Dai Yamazaki and Dr. Masaomi Tanaka also warmly supported me. I especially express my gratitude to Dr. Yuichiro Sekiguchi for his kind help. I'm also grateful to Dr. Masahiro Ikoma for providing his notes on EOS and Dr. Takahiro Miyoshi for providing information about the HLLD and HLLD$-$ solvers. I thank my friends in National Astronomical Observatory of Japan, especially Mr. Yousuke Utsumi, Mr. Kazuhiro Hada and Ms. Nagisa Oi, and my deepest appreciation goes to Ms. Shioko Izumi who always supported my life in NAOJ for five years.

I am heartily grateful to my friends, Prof. Matthew R. Bate, Prof. Gilles Chabrier, Prof. Isabelle Baraffe, Prof. Shantanu Basu and Dr. Patrick Hennebelle who highly appreciated my works, and I express my deep gratitude to Dr. Benoît Commerçon, who is my best rival. Discussions and competition with them surely drove my works in this field. I also thank Prof. Tim Harries for providing his code TORUS.

And finally, I really appreciate my family's understanding and cooperation. I owe what I am today to their explicit and implicit assistance.

Numerical computations presented in this thesis were partly performed on NEC SX-9 at Center for Computational Astrophysics of National Astronomical Observatory of Japan, at Japan Aerospace Exploration Agency and at Osaka University. I also acknowledge the Research Fellowship from the Japan Society for the Promotion of Science (JSPS) for Young Scientists.

# Abstract

This thesis is devoted to theoretical studies of star formation processes using computational simulations. We develop a three-dimensional nested-grid radiation magnetohydrodynamic (RMHD) simulation code and investigate collapse from a molecular cloud core to a protostellar core. We also predict the observational properties of star forming clouds, particularly of first cores, directly from the RMHD simulations. Our RMHD simulations include necessary physical processes in star formation processes, and will significantly contribute our understanding in this field.

Stars are most fundamental elements in our universe, and understanding their formation is one of the most highlighted topics in astrophysics. Therefore star formation processes have been extensively studied so far. Because star formation is quite a complicated and highly non-linear process involving many physical processes, and because the immediate sites of star formation are difficult to observe, numerical simulations have played crucial roles in expanding our knowledge on star formation. Despite the long history of the studies, computational simulations of star formation including complicated physical processes are still being developed, and multi-dimensional RMHD simulations are surely most important topic in this field. Because the Atacama Large Millimeter/submillimeter Array (ALMA) recently started its early-science operations, such realistic simulations are highly demanded.

During star formation, the energetics of the system is dominated by the release of gravitational energy in the very central region around the formed protostar. Both magnetic and radiation feedback are of major importance in this region, but there has been no work resolving this small scale ($< 1\,\mathrm{AU}$) including required physics. To tackle this problem, we develop a new high-resolution simulation code including required physical processes such as magnetohydrodynamics, self-gravity, chemical reactions and radiation transfer.

In this thesis, we present our works in five parts. In the first part, we describe the development of the three dimensional nested-grid RMHD simulation code including many physical processes in detail. For radiation transfer, we adopt flux limited diffusion approximation and implicit time-integration which significantly reduce the computational load and enable stable simulations. We also implement additional physics

required in star formation simulations such as non-ideal MHD effects and realistic equation-of-state.

The other chapters are devoted to the results and applications of the RMHD code. First, we show the evolution in the early phase of protostellar collapse, especially focusing on the formation and properties of so-called first hydrostatic cores. In comparison with previous simulations without proper treatment of radiation transfer, radiation transfer does not seem to drastically change the global scenario of low-mass star formation. However, quantitatively there is non-negligible difference; for example, the temperature distribution is significantly changed by introducing radiation transfer. Realistic treatment of gas thermodynamics alters some properties and structure of the core quantitatively. The mass and size of the first core at a certain central density become larger because of higher entropy, and the lifetime becomes slightly longer. We also find two components of bipolar outflow are driven from the first core via respectively different mechanisms.

Next, we show observational properties predicted directly from the results of RMHD simulations using post-processing radiation transfer calculations. We calculate Spectral Energy Distributions and Visibility Amplitude Distributions in thermal dust continuum emissions. We propose a strategy to identify first cores distinguishing from young stellar objects and starless molecular cloud cores. We also perform non-LTE molecular line transfer simulations and predict future observations with ALMA such as channel maps and position-velocity diagrams. Our results can be directly compared to observations and are useful for planning and interpreting observations.

We describe our novel theoretical model of first cores in the next chapter; the Exposed Long-lived First-core. We find that first cores formed in very low mass cloud cores can be significantly long-lived. Their evolution is strongly affected by radiation cooling and is qualitatively different from ordinary first cores. We also calculate the observational properties of such first cores and show that they can be observed with current instruments such as ALMA and *Herschel*. Our results suggest that such first cores can be observed more frequently than those in molecular cloud cores of ordinary masses.

Finally, we report the results of the RMHD simulations of the formation of protostellar cores with and without Ohmic dissipation. In the ideal MHD models, the evolution of the protostellar cores are very similar to that in spherically symmetric non-rotating models due to efficient angular momentum transport. However, if the resistivity presents, rotationally-supported circumstellar disks are rapidly built up in the vicinity of the protostellar cores. Magnetic fields are amplified by rotation and fast outflows are launched from the protostellar cores via magnetic pressure gradient force. These are the first 3D RMHD simulations resolving the protostellar cores in the world.

# Contents

# List of Figures

# Chapter 1

# Introduction

Stars are the most fundamental elements constructing clusters, galaxies and the whole (visible) universe. They affect the evolution of the Universe by generating energy and producing heavy elements. Furthermore, stars and circumstellar disks are the sites of planet formation which are directly connected to the origin of life and ourselves. Therefore, formation and evolution of stars have attracted much interest and have been extensively studied from both theoretical and observational viewpoints.

In this thesis, we investigate formation processes of low mass stars ($M \lesssim 8 M_\odot$), particularly collapse of molecular cloud cores in the present-day environment, with computational simulations involving many physical processes. Sophisticated theoretical models are highly demanded these days because it is being expected that observational studies of star formation will progress greatly with the Atacama Large Millimeter/submillimeter Array (ALMA), which started its operation in 2011. One of the goals of this work is to provide good theoretical models to cater to such demand. Here we review our current understanding and precedent studies related to this work.

## 1.1 Environment of Star Formation

It is a well-accepted concept that stars are formed as a group in molecular clouds (for review, refer to Shu et al. (1987) and McKee & Ostriker (2007)). Such molecular clouds and young stellar objects (YSO) have been systematically well studied with radio, infrared and optical telescopes and we have quite good statistics on molecular cloud cores and YSOs (Mizuno et al. (1995); Onishi et al. (1996, 1998, 2002); Luhman et al. (2000); Luhman (2004); Ridge et al. (2006); Narayanan et al. (2008); Dunham et al. (2008); Evans et al. (2003, 2009) and references therein) (e.g., Figure 1.1).

Each star is formed in dense and cold condensations of molecular gas. Such a condensation, or a molecular cloud core, is formed in the turbulent molecular clouds. Typically, the scale of a molecular cloud core is $\sim 0.1\,\mathrm{pc}$, and its gas density and tem-

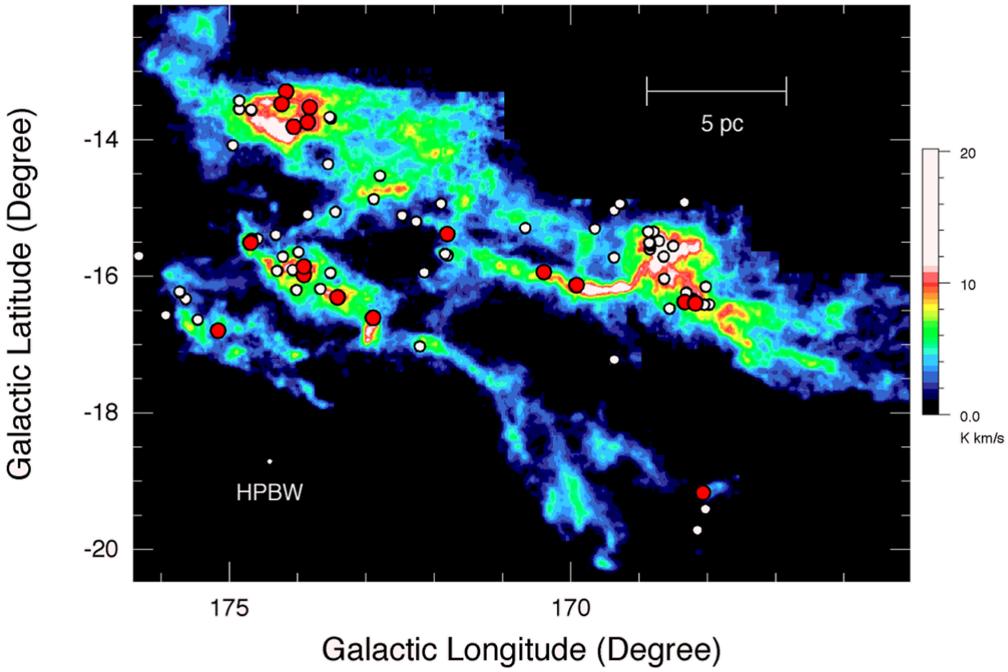

Figure 1.1: $^{13}$CO (J=1-0) total intensity map of the Taurus Molecular Cloud observed with 4m radio telescope at Nagoya University. Red circles are candidates of protostars identified with IRAS and white circles are T Tauri stars. Taken from Mizuno et al. (1995).

perature are $n \gtrsim 10^4\,\mathrm{cm}^{-3}$ and $T \sim 10\,\mathrm{K}$. Such molecular cores can be initially stable supported by gas pressure, internal turbulence or magnetic fields, but some of them become gravitationally unstable for some reason, such as sufficient gas accumulation, external pressure, dissipation of internal turbulence or loss of magnetic flux via the ambipolar diffusion. When a molecular cloud core gets gravitationally unstable, it starts to collapse and eventually form a star (or a binary or multiple system). Therefore, roughly speaking, a molecular cloud core is regarded as the initial condition of the formation of a star. The properties of a molecular cloud core must be linked to the global states of the molecular clouds as the initial and boundary conditions.

### 1.1.1 Interstellar Turbulence

One of the notable features observed in star forming regions is the presence of supersonic turbulence. Larson (1981) found a tight power-law relation between the spatial scale and the internal velocity dispersion in molecular clouds. This famous Larson's law seems to be universal in star forming regions (Heyer & Brunt, 2004) and related to the nature of turbulence.

Because the supersonic turbulence must dissipate very quickly via shocks in the sound-crossing timescale (Stone et al., 1998; Mac Low et al., 1998), the common presence of the supersonic turbulence indicates the existence of mechanisms driving the turbulence. Thermal instability (Field, 1965; Hennebelle & Pérault, 1999, 2000; Koyama & Inutsuka, 2000) in shock-compressed interstellar media is thought to be one of the most promising driving mechanisms (Koyama & Inutsuka, 2002; Hennebelle & Audit, 2007; Hennebelle et al., 2007; Inoue & Inutsuka, 2008, 2009). Actually, the molecular cloud is thought to experience such a shock from supernova explosions frequently, about once in several Myrs. The outflow feedbacks from formed protostars also input sufficient energy to maintain the turbulence (Li & Nakamura, 2006; Nakamura & Li, 2007; Wang et al., 2010).

Some properties of molecular cloud cores are linked to the properties of the turbulence. The mass distribution of cloud cores (core mass function, CMF) can be explained from the nature of interstellar turbulence (Padoan & Nordlund, 2002; Hennebelle & Chabrier, 2008, 2009; McKee et al., 2010). Recently, global simulations of star formation in such turbulent clouds have been extensively performed and their statistical properties were investigated (Bate et al., 2003; Bate, 2009a,b, 2011b; Offner et al., 2009; Krumholz et al., 2011; Vázquez-Semadeni et al., 2011). Also, the rotation (or more generally, the internal motion) of molecular cloud cores is originated from the large scale turbulence (Ohashi et al., 1997; Matsumoto & Hanawa, 2011).

### 1.1.2 Magnetic Fields

Magnetic fields in molecular clouds are another important factor in star formation processes. As we describe below, magnetic fields have significant impact on star formations. Observations of magnetic fields are very challenging, but some observations in star forming regions involving polarimetry and measurement of Zeeman effects in different scales have been performed (Heiles & Crutcher, 2005; Girart et al., 2006, 2009; Troland & Crutcher, 2008; Falgarone et al., 2008; Crutcher et al., 2009; Sugitani et al., 2011). Theoretically, a strongly magnetized cloud cannot collapse gravitationally when the ratio between its mass and threading magnetic flux (or column density to magnetic flux density) is below a critical value; this critical value is called the critical mass to flux ratio (Mouschovias & Spitzer, 1976; Nakano & Nakamura, 1978). From Figure 1.2, we can see that the observed magnetic fields are scattered around this critical value. These results imply the importance of magnetic fields in star formation, although there are large scattering and observational uncertainties.

Beside the gravitational instability, magnetic fields have significant impact on the evolution of collapsing molecular cloud cores. In particular, magnetic fields efficiently extract the angular momentum in the rotating cloud and enable the rotationally-

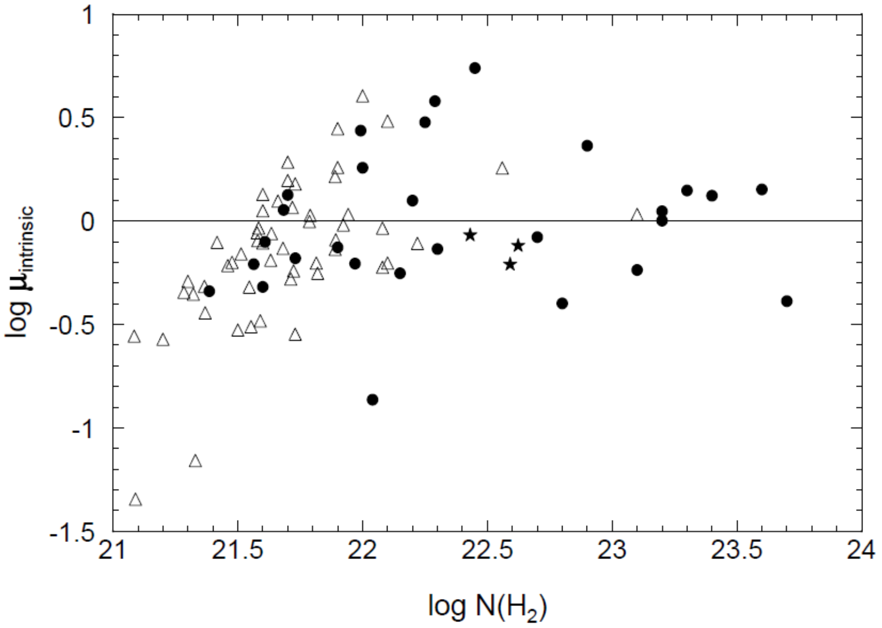

Figure 1.2: The observed mass-to-flux ratio of molecular cloud cores as a function of the column density. $\mu = 1$ is the critical value for gravitational instability. Taken from Heiles & Crutcher (2005).

supported cloud to collapse. As a result of interaction between rotation and magnetic fields, outflows are launched (for review, see Arce et al. (2007) and references therein). There are mainly two types of outflows associated with YSOs: slow outflow with wide opening angle, and fast, well-collimated jet. Recent magnetohydrodynamic (MHD) simulations naturally explain the driving mechanism of such multi-component outflows (see Section 1.3.2). Typically the former is observed in molecular lines (Bontemps et al., 1996; Lee et al., 2000; Phan-Bao et al., 2008; Launhardt et al., 2009; Arce et al., 2010; Nakamura et al., 2011b,a) and the latter is observed in both molecular lines (Takami et al., 2006; Tafalla et al., 2010; Hirano et al., 2010) and optical/infrared emissions (Reipurth et al., 1999; Burrows et al., 1996; Pyo et al., 2002; Velusamy et al., 2007). The fast jet often forms Herbig-Haro objects when it interacts with interstellar media. Interestingly, rotational motions in outflows are detected in some cases (Launhardt et al., 2009; Zapata et al., 2010), which may be signature of the angular momentum transport. Such outflows and jets are fairly common phenomena associated with YSOs, therefore considered as strong evidence showing the importance of magnetic activities in star formation processes.

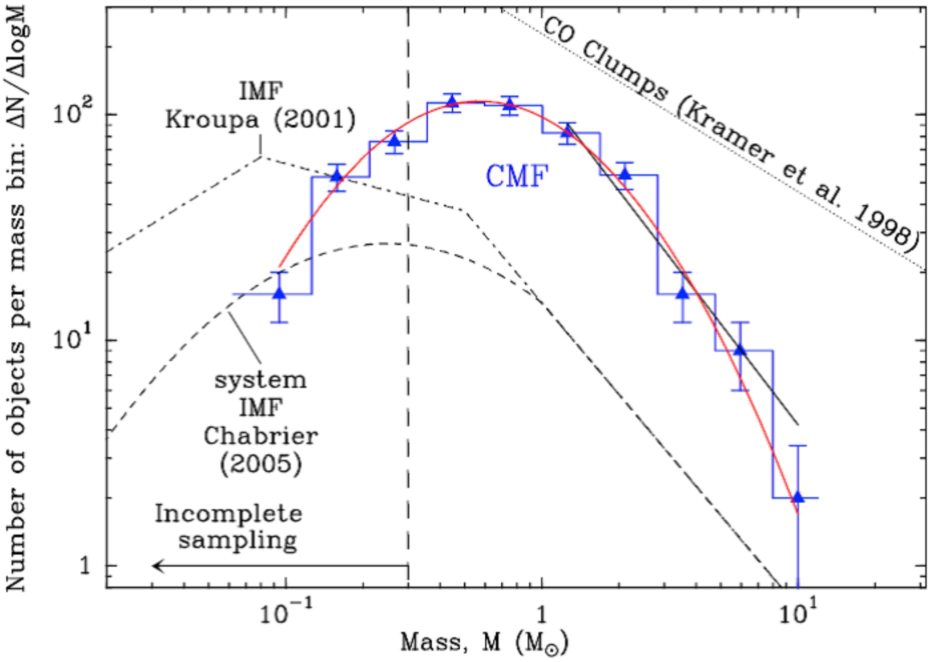

Figure 1.3: Core Mass Function in the Aquila rift observed with *Herschel*. Stellar IMFs are also plotted. Taken from André et al. (2010).

## 1.2 IMF and CMF

It is well known that the initial mass function (IMF) of stars seems to be almost universal among star forming regions (at least in normal Galactic environments), and there is very good resemblance between the CMF and IMF (Salpeter, 1955; Scalo, 1986; Motte et al., 1998; Kroupa, 2001; Chabrier, 2003, 2005; Enoch et al., 2007; Rathborne et al., 2009; André et al., 2010; Ikeda & Kitamura, 2009, 2011) (Figure 1.3). Although the high mass ends of the two mass functions are uncertain statistically and the low mass ends are difficult to determine observationally, the global shapes of mass functions can be well represented by power-law or log-normal functions. The shapes of the mass functions are similar but dense cores tend to be more massive by a factor of several. Naively speaking, this similarity may imply that the origin of the IMF is already implemented in the CMF, and dense cores are converted into stars at certain efficiency (this is called star formation efficiency, or SFE). In other words, molecular cloud cores without infrared sources can be direct progenitors of protostars.

Since the massive stars affect the evolution of galaxies and the whole Universe through the energy feedback and nucleosynthesis, determining the mass distribution of stars are of critical importance among all the astrophysical problems. Therefore, the origin of the IMF is regarded as one of the ultimate goals of star formation studies. To clarify the relation between CMF and IMF, we have to investigate the formation process of each star from a dense molecular cloud core, i.e., protostellar collapse. To be more specific, we need to understand the physical mechanisms controlling SFE, or the final mass of a protostar.

## 1.3 Collapse of a Molecular Cloud Core

Once a molecular cloud core becomes gravitationally unstable, it starts to collapse dynamically. There are many precedent studies investigating the physics in collapsing molecular cloud cores. In early days, the isothermal collapse of spherical clouds is intensively studied based on self-similar solutions (Larson, 1969; Penston, 1969; Shu, 1977; Hunter, 1977; Whitworth & Summers, 1985). These analytic works are very important to reveal the theoretical aspects of gravitational collapse. However, the collapse of a molecular cloud core is in reality a complicated and highly non-linear process involving many physics. Therefore computational simulations have been extensively utilized in this field and contributed our understanding significantly. Theoretical studies of protostellar collapse have progressed by introducing additional physical processes and extending simulations step by step.

### 1.3.1 Early 1D Simulations

Larson (1969) first showed the global picture of protostellar collapse using one dimensional spherically-symmetric calculations including radiation transfer with diffusion approximation. He found that the collapse initially goes almost isothermally because dust thermal emission is very efficient in this phase. The gas temperature starts to rise when the central region gets very thick and radiation cooling becomes inefficient, then the collapse almost stops and a quasi-hydrostatic object forms. This object, so-called Larson's first hydrostatic core (or simply, first core), evolves under the gas accretion from the envelope. When the central temperature reaches about 2,000 K where hydrogen molecules start to dissociate, the core becomes unstable and collapses again because $H_2$ dissociation is strongly endothermic and gas pressure fails to balance with gravity. This second collapse ends when molecular hydrogen dissociates completely and there forms a quasi-static object again. This is the second core or the protostellar core, and it acquires its mass via accretion in dynamical timescale of the natal cloud core. Then the formed protostar will evolve into a main-sequence star via Kelvin-Helmholtz contraction. He also derived analytic solutions describing isothermal collapse (see also Penston (1969)). This story is later confirmed by more sophisticated simulations with increased resolution and better treatment of radiation transfer (Winkler & Newman, 1980a,b). Masunaga & Inutsuka (2000) performed 1D radiation hydrodynamic sim-

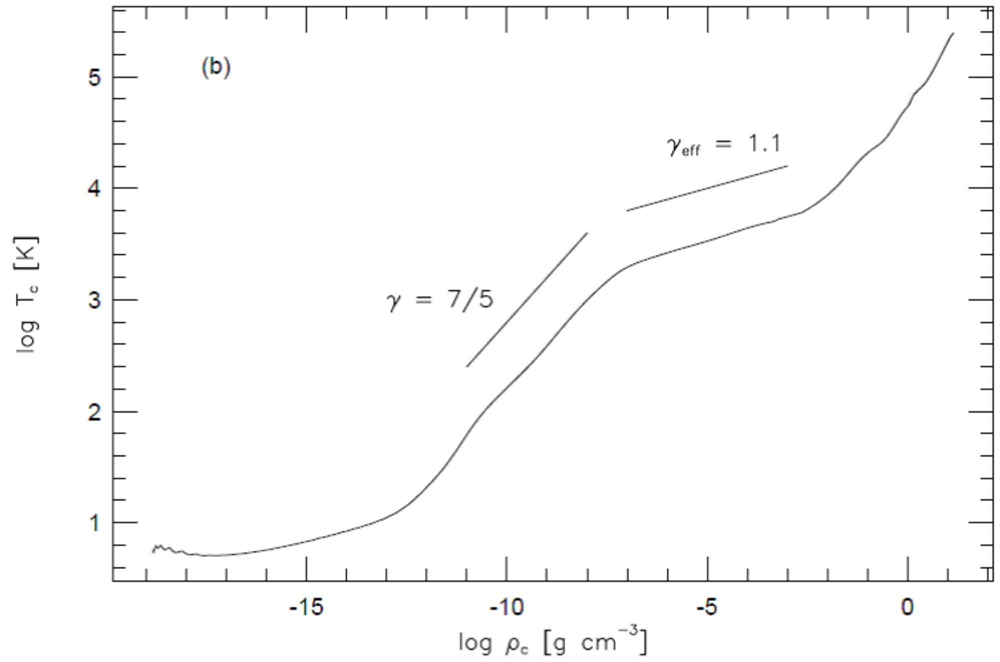

Figure 1.4: Typical thermal evolution of the central gas element in a spherically symmetric simulation of protostellar collapse. Taken from Masunaga & Inutsuka (2000).

ulations considering full non-gray radiation transfer with ray-tracing technique and conclusively clarified the whole story of protostellar collapse (Figure 1.4).

## 1.3.2 Multidimensional and Multi-Physics Simulations

### Angular Momentum Problem and Magnetic Activities

Although those 1D simulations revealed the essential story of protostellar collapse, in reality there present non-negligible rotation, turbulence and magnetic fields in the molecular clouds, so obviously 1D spherically symmetric calculations are not sufficient to understand realistic star formation processes. Larson (1972) first performed 2D axisymmetric calculations including rotation. Black & Bodenheimer (1975, 1976) and Tscharnuter (1975) also performed similar simulations. They showed that centrifugal force significantly affects the evolution of the cloud preventing the collapse. Typical angular momenta in initial molecular cloud cores are far larger than those in resulting protostars, which means that there must be efficient mechanisms for angular momentum transport during the protostellar collapse. However, no physical process except for viscosity can transport angular momentum in axisymmetric circumstances without magnetic fields, but physical viscosity is clearly ineffective. This problem is called the angular momentum problem in star formation.

There are two major solutions for the angular momentum problem. Bate (1998) performed first 3D hydrodynamic simulations using Smoothed Particle Hydrodynamics

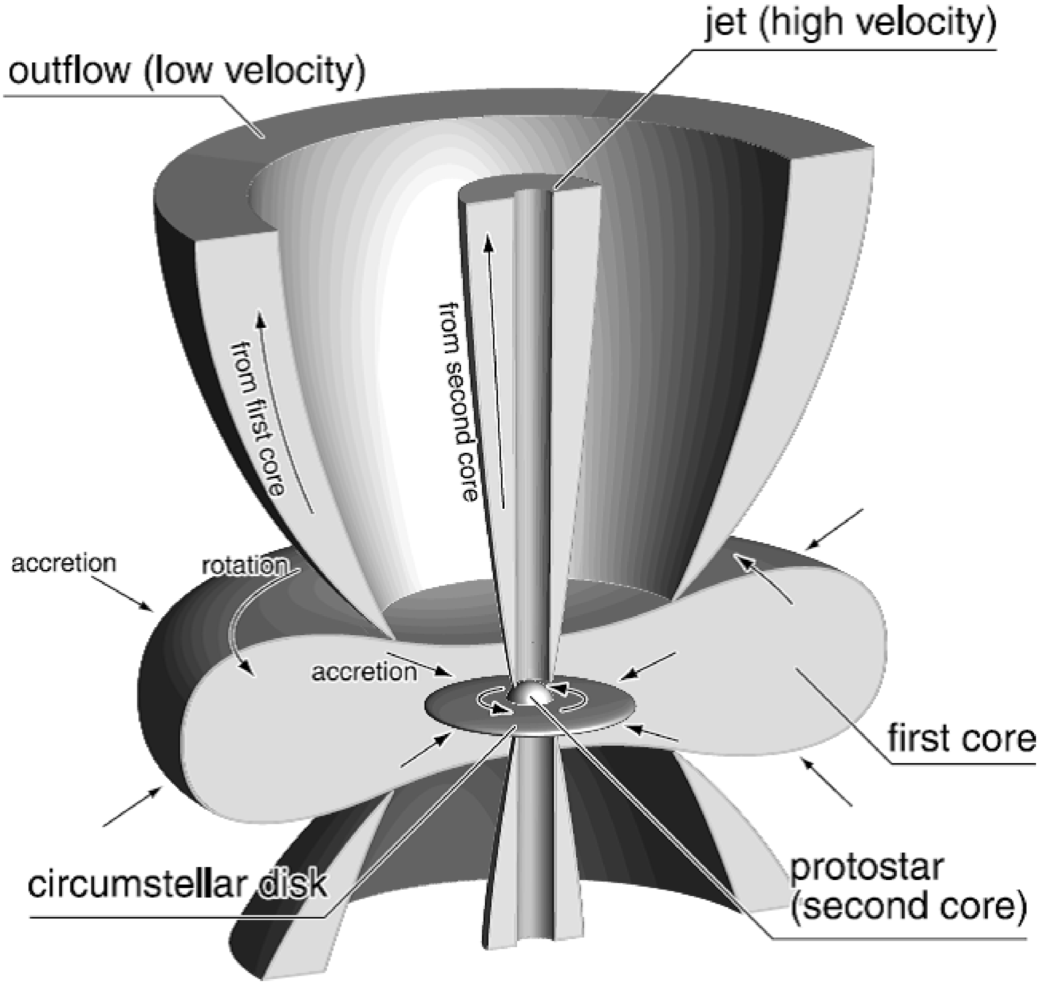

Figure 1.5: Schematic picture of the multi-component outflow launched from the first and second cores. Taken from Machida et al. (2008a).

(SPH) from a molecular cloud core to the formation of a protostellar core. He showed gravitational torque via non-axisymmetric structures like spiral arms spontaneously formed through gravitational instability in massive disks can efficiently transport the angular momentum. Matsumoto & Hanawa (2003b) and Saigo et al. (2008) carried out a number of numerical experiments for various initial rotations using nested-grid hydrodynamic simulations and showed the detailed evolution scenario, modes and criteria of fragmentation.

The other essential mechanism of angular momentum transport is interaction between gas and magnetic fields. The outflows and jets driven from YSOs are thought to be evidence of such magnetic activities. Historically, the origin of the slow outflows are explained by the so-called entrainment mechanism (e.g., Raga et al. (1993); Raga & Cabrit (1993); see also Arce et al. (2007) and references therein); the fast jet driven from the protostar by magnetic activities is the primary component and the slow outflow is secondarily driven being dragged by the jet. Some of the fast molecular outflows can be explained by this mechanism, but it is difficult to reproduce the wide opening-angle of the slow outflows and also it does not account for the angular momentum problem.

Recently, more consistent and natural solutions to the origin of the outflows and the angular momentum problem are proposed based on MHD simulations of protostellar collapse (note that the entrainment mechanism itself can work, but we suppose that the MHD models give better explanation in the context of protostellar collapse). Tomisaka (1998, 2000, 2002) performed 2D axisymmetric MHD simulations of the collapse of magnetized rotating molecular clouds using nested-grids. He showed that the outflow driven via interaction of magnetic fields and rotation carries the angular momentum very efficiently. Torsional Alfvén waves also take the angular momentum away from the contracting gas (this is so-called magnetic braking, Mouschovias & Paleologou (1979, 1980)). The outflow is mainly driven by magneto-centrifugal force (Blandford & Payne (1982), see also Kudoh et al. (1998)) when magnetic fields are relatively strong (U-type in Tomisaka (2002)). When magnetic fields are weak, then magnetic pressure of toroidal magnetic fields amplified by rotation drives the outflow (I-type in Tomisaka (2002)). Machida et al. (2004) first reported 3D nested-grid MHD simulations of similar problems (see also Matsumoto & Tomisaka (2004); Matsumoto et al. (2006); Price & Bate (2007); Hennebelle & Fromang (2008); Hennebelle & Teyssier (2008); Duffin & Pudritz (2009); Hennebelle & Chabrier (2009); Hennebelle & Ciardi (2009); Seifried et al. (2011a,b); Bürzle et al. (2011)). Machida et al. (2005b,a, 2008b) studied the formation mechanism of binaries in magnetized clouds and derived general criteria of fragmentation in magnetized rotating cores by a very large parameter survey (see also Hosking & Whitworth (2004)). Machida et al. (2006) (see also Banerjee & Pudritz (2006); Machida et al. (2008a)) simulated the collapse from molecular cloud core to the protostellar core and showed that two different outflows are launched from different scales; slow, loosely-collimated outflow from the first core and fast well-collimated outflow from the second core (Figure 1.5). Similar multi-component outflows are observed in some objects (Lee et al., 2000; Santiago-García et al., 2009) (Figure 1.6).

### Magnetic Flux Problem and Magnetic Braking Catastrophe

In ideal MHD approximation, the magnetic flux in the formed protostar must be equal to that of the initial molecular cloud core. However, the observed magnetic flux in main-sequence stars is considerably smaller than that in molecular cloud cores. This magnetic flux problem is another important topic in the studies of protostellar collapse. Moreover, assuming typical initial rotation and magnetic fields, the angular momentum transport due to the magnetic fields actually seems too strong in ideal MHD cases.

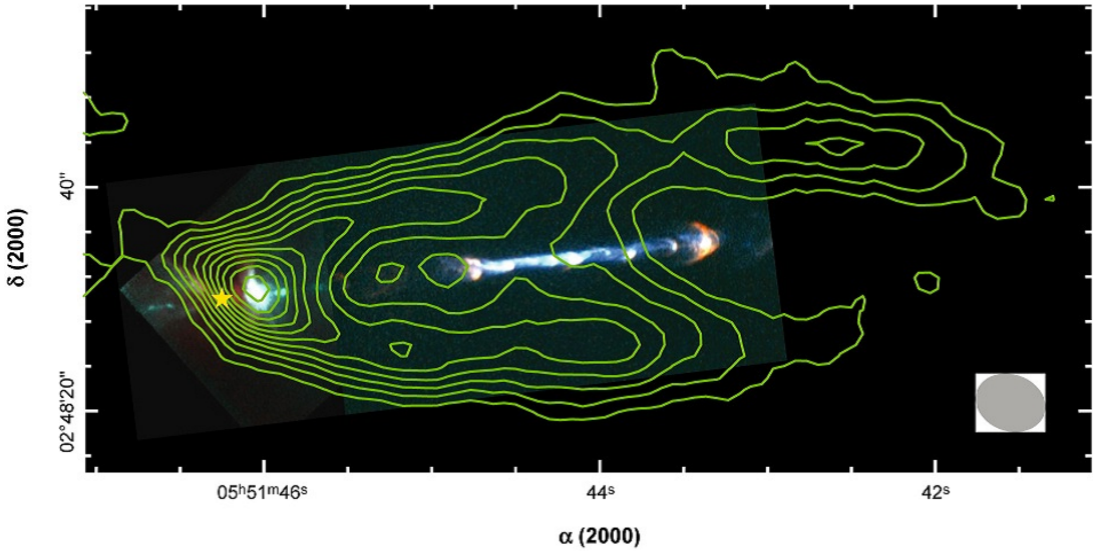

Figure 1.6: The HH111 system where the optical jet and molecular outflow coincide. Taken from McKee & Ostriker (2007) (originally from Reipurth et al. (1999) and Lee et al. (2000)).

Many works on MHD protostellar collapse reported that large-scale rotationally supported circumstellar disks are difficult to form (e.g., Mellon & Li, 2008; Hennebelle & Ciardi, 2009). If the angular momentum transport is too efficient, insufficient rotation means that the gravitational instability and resulting fragmentation rarely realize. In reality, however, there is a lot of observational evidence of large rotationally-supported circumstellar disks. The probabilities of binaries and multiples are also very high, suggesting that sufficiently large angular momentum remains in the circumstellar disk. This discrepancy is called "magnetic braking catastrophe" (Li et al., 2011). There are some models proposed to solve these problems, and non-ideal MHD effects, such as the Ohmic dissipation, the ambipolar diffusion, and the Hall diffusion, are one of promising scenarios to solve them. The non-ideal MHD effects can work during the collapse due to the low ionization degree and may remedy the situation by reducing the magnetic field strength (Machida et al., 2006, 2008a, 2011a). However, this problem is still under debate (Mellon & Li, 2009; Dapp & Basu, 2010).

### Radiation (Magneto)Hydrodynamic Simulations

In most multidimensional simulations so far, the effects of radiation transfer were treated with rough approximation because of computational difficulties. But recently, thanks to the development of supercomputers, some groups are working on radiation (magneto-)hydrodynamic simulations of star formation. Flux limited diffusion approximation (hereafter FLD; Levermore & Pomraning (1981), Minerbo (1978)) is often adopted to reduce the computational costs. Although FLD is still crude approximation of radiation transfer, it is useful to grasp the thermal evolution via radiation with reasonable costs. The early work on 2D nested-grid FLD RHD simulations was done by Yorke & Kaisig (1995). Whitehouse & Bate (2004) and Whitehouse et al. (2005) developed a new method to implement FLD into SPH and they performed first 3D SPH radiation hydrodynamic simulations of protostellar core formation (Whitehouse & Bate, 2006; Bate, 2010, 2011a). Schönke & Tscharnuter (2011) also investigated protostellar collapse using 2D axisymmetric FLD RHD simulations. Krumholz et al. (2007, 2009) performed 3D FLD RHD simulations with their adaptive mesh refinement (AMR) RHD code Orion in the context of high-mass star formation. Very recently Commerçon et al. (2010) and we (Tomida et al., 2010b) independently reported RMHD simulations of protostellar collapse.

## 1.4 Early Evolution of Protostars and Disks

### 1.4.1 Circumstellar Disks

As a consequence of the angular momentum in molecular cloud cores, the circumstellar disks are formed as natural by-products of star formation processes (although the debate on the magnetic braking catastrophe is still on-going, see 1.3.2). In classical theory of star formation, circumstellar disks were supposed to be formed in the main accretion phase after the formation of central protostars (Shu et al., 1987). However, recent 3D simulations revealed that circumstellar disks are formed in the early phase of protostellar collapse; rotating first cores continuously evolve into circumstellar disks (Bate, 1998, 2010, 2011a; Machida & Matsumoto, 2011), even under the presence of magnetic fields (Machida et al., 2011a). Observationally, Jørgensen et al. (2009) reported that Class-0 sources (young, embedded) are associated with more massive disks than Class-I sources, which implies the early formation of circumstellar disks.

The structure and evolution of circumstellar disks are important topics not only in star formation but also in the context of planet formation. The number of reported exoplanets is increasing very rapidly, and more than 700 extra-solar planets are already identified so far. The existence of many exoplanet systems unlike our solar system suggests that a variety of formation mechanisms can be realized. Gravitational instability and subsequent fragmentation in protoplanetary disks will be one of the promising formation mechanisms for some observed system, especially for ones having giant planets in outer region (Boss, 1997, 2008, 2011; Mayer et al., 2007; Stamatellos & Whitworth, 2008; Boley & Durisen, 2008; Boley, 2009; Boley et al., 2011; Meru & Bate, 2010). However, it is still controversial whether the gravitational instability scenario

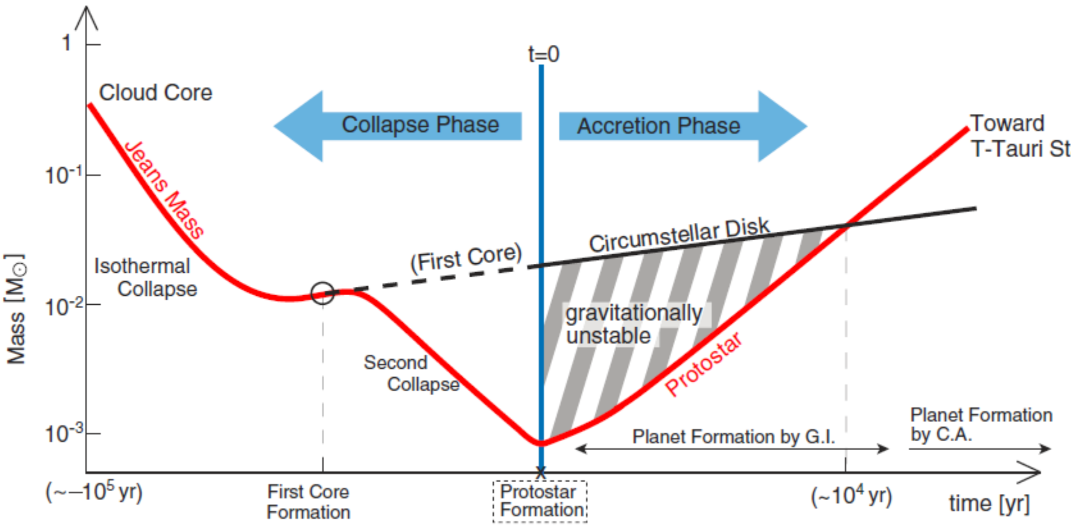

Figure 1.7: Schematic diagram representing relation of the mass between a protostar and its circumstellar disk. At the formation epoch of the protostar, the circumstellar disk, which is originated from the first core, is naturally much heavier than the protostar and therefore susceptible to gravitational instability. Taken from Inutsuka et al. (2010).

can occur in realistic situations. It seems that the most serious matter in the current studies on the gravitational instability scenario is the initial and boundary conditions, such as the initial disk profile (e.g., the minimum mass solar nebula model (Hayashi, 1981)) and accretion from the envelope. In principle, since the disks are by-products of protostellar collapse, we should derive those conditions from star formation simulations. Inutsuka et al. (2010) and Machida et al. (2011b) showed that a massive, gravitationally-unstable circumstellar disk is naturally formed in the early phase of star formation and planets can be formed (Figure 1.7) (see also Tsukamoto & Machida (2011)). Both magnetic fields and radiation transfer are essential in such simulations, because they play crucial roles in the evolution and structure of the disks.

### 1.4.2 Luminosity Problem and Episodic Accretion

One of the most serious discrepancies between observations and theories of YSOs is the luminosity problem, that is, most observed accreting (embedded, optically invisible) YSOs are fainter than the theoretical predictions for typical accretion rate. This problem is first addressed by Kenyon et al. (1990) and later investigated more systematically (Evans et al., 2003, 2009). This discrepancy can be solved if the accretion is non-steady; protostars are mostly in the quiescent accretion phase and sometimes experience a burst-like accretion of short duration. The episodic accretion can also affect the nature of resulting protostars and may explain the observed scattering from the (non-accreting) isochrone in the Hertzsprung-Russell (HR) diagram of (optically visible) YSOs in star forming regions. It is of critical importance whether this scattering in the HR diagram reflects the accretion histories or real age distribution because it is directly linked to the timescale of star formation in molecular clouds, which is a long argued problem in the star formation field (Zuckerman & Evans, 1974; Ballesteros-Paredes et al., 1999; Elmegreen, 2000; Hartmann, 2001; Tassis & Mouschovias, 2004; Krumholz & Tan, 2007; Hartmann et al., 2011).

A lot of mechanisms which trigger the episodic accretion are proposed: gravitational instability in the massive circumstellar disk (Vorobyov, 2009; Vorobyov & Basu, 2010), magneto-rotational instability (MRI) (Zhu et al., 2009), large-scale turbulence (Offner et al., 2009), and so on. The effects of such episodic accretion on protostellar evolution are studied, but there are ambiguities from the initial condition of stellar evolution (e.g., the structure of the zero-age protostar) and outer boundary condition of the accreting protostar (Baraffe et al., 2009; Hosokawa et al., 2011a). Such conditions should be given from the global time-dependent simulation of protostellar collapse, and we expect that our RMHD simulations resolving protostellar cores will be useful for future discussions.

### 1.4.3 End of the Main Accretion Phase

After the formation of the protostellar core, it acquires the mass through the accretion and evolves into a main-sequence star (this phase is called the main accretion phase). The most crucial problem unresolved in this phase is the mechanism to cease the gas accretion. Nakano et al. (1995) and Machida et al. (2009a) suggested that mass ejection by the magnetically driven outflow can halt the accretion, especially in the low mass cases. On the other hand, radiation feedback is thought to be significant in high mass cases (Wolfire & Cassinelli, 1987; Yorke & Sonnhalter, 2002; Krumholz et al., 2009; Peters et al., 2010; Kuiper et al., 2010, 2011b; Hosokawa et al., 2011b). Both radiation and magnetic feedbacks are important in the small scale (i.e., around the protostar), and will be significantly affected by the structure of the accretion flow. However, precedent simulations have utilized the sink cell/particle technique (Bate et al., 1995; Krumholz et al., 2004; Federrath et al., 2010) with low resolution; when a gas element satisfies certain thresholds (e.g., the gas density exceeds a threshold value, the gas is contracting, etc.), it is replaced with a collisionless accreting particle, assuming a star is formed. The sink particle interacts with gas and other particles only via gravity and radiation feedback calculated from a subgrid stellar model. The radiative feedback from the formed protostar, for example, can be highly anisotropic ("flash light effect") due to the small-scale optically-thick disk in the vicinity of the protostar (Yorke & Bodenheimer, 1999; Vaidya et al., 2009; Tanaka & Nakamoto, 2011), but such fine structures are not well resolved in the current simulations. So it seems that there is still no conclusive work to answer this problem including all the required physics and resolving small scale structures around the protostar so far, and we require farther efforts to understand the physics in the main accretion phase.

## 1.5 This Work

As we discussed above, we have to clarify the formation processes of protostars from molecular cloud cores in order to understand the origin of stellar masses. We also need to understand protostellar collapse because the properties and structures of formed protostars and accretion flow are directly linked to stellar evolution, circumstellar disk formation and subsequent planet formation. For this purpose, we require sophisticated numerical simulations including necessary physical processes consistently. To be more specific, magnetic fields and non-ideal MHD effects are of critical importance in the angular momentum transport, and radiation transfer plays a crucial role in thermal evolution in star formation processes. However, there has been no work performed yet studying the whole collapse from a molecular cloud core to a protostellar core including both magnetic fields and radiation transfer. Moreover, as we are now expecting that new observational instruments such as ALMA and *Herschel* will open a new frontier in this field, we need precise theoretical models which can be compared directly with observations. To approach these problems, we develop a new high-resolution RMHD simulation code and investigate star formation processes from molecular cloud cores to protostellar cores. Our ultimate goal is constructing realistic and reliable theoretical models of protostellar collapse based on RMHD simulations with required physics.

In this thesis, we study the formation processes of low mass stars using 3D nested-grid RMHD simulations. This thesis is organized as follows; first, we describe the numerical methods of our RMHD simulations (Chapter 2). In Chapter 3, we show the results of the RMHD simulation of the formation and evolution of the first core in a rotating magnetized molecular cloud core. We discuss the structure and properties of the first core and outflows, mainly focusing on the effects of radiation transfer on thermodynamics. Next, we derive the observational properties of the first cores directly from our simulations (Chapter 4). Chapter 5 is devoted to explain a new model of first cores based on RHD simulations. We show that first cores formed in very low mass molecular cloud cores can be considerably long-lived compared to those in ordinary mass cloud cores. In Chapter 6, we report our results of RMHD simulations of the second collapse and formation of protostellar cores including non-ideal MHD effects. Finally, we summarize this thesis and give some future perspectives in Chapter 7.

# Chapter 2

# Nested-Grid RMHD Simulation

## 2.1 Introduction

There are a variety of studies focusing on different stages and scales of star formation processes. There are a number of works investigating formation of dense molecular cloud cores in large-scale turbulent interstellar media. Some studies are focusing on large scale and long-term evolution covering the scale of whole molecular clouds or clusters. Such studies are important to understand the global evolution of star forming regions, but formation and evolution of each star are hardly resolved due to the limitation of computational resources. Here we investigate the formation process of each protostar, i.e., protostellar collapse, starting from a molecular cloud core to one or several protostars.

The very early phase (or large scale structure) and the very late phase of star formation are well understood by observations. Stars form in molecular clouds, and there are a number of dense molecular cloud cores in star forming regions which correspond to “the initial conditions” of star formation. The properties of molecular cloud cores such as rotation, turbulence, energy balance, chemical composition and mass distribution are extensively studied by radio observations. On the other hand, young protostars (and more evolved pre-main-sequence stars), “the final states” of star formation, are also well understood by infrared and optical observations. However, the immediate stage of star formation in which a forming protostar acquires its mass occurs in very dense envelope of large column density, and the timescale of star formation is relatively short compared to the timescale of the evolution of YSOs. Such a part of star formation processes is quite hard to observe directly with present observational instruments, therefore, theoretical studies have played crucial roles to understand the formation of stars. Particularly, computational simulations are extensively utilized because star formation is quite a complicated non-linear process involving many physical processes such as multi-dimensionality, hydrodynamics, self-gravity, magnetic fields, chemical reactions, radiation transfer, and so on. There are a lot of precedent studies in this field (see Chapter 1). Many groups including us are recently working on multidimensional radiation (magneto)hydrodynamic simulations (Whitehouse & Bate, 2006; Krumholz et al., 2007, 2009; Offner et al., 2009; Bate, 2010, 2011a; Commerçon et al., 2010, 2011b; Tomida et al., 2010b,a). Such simulations had been rarely performed due to their computational difficulties and costs, but the advance of computing technologies and development of new techniques enable us to push the frontiers. Here we present new computational simulations involving more physical processes than any other previous works. For the review of the precedent studies, see the previous Chapter.

## 2.2 Basic Equations

As described in the previous section, we require highly sophisticated simulations to study star formation processes, but there has been no conclusive work including all the required physical processes. In order to achieve realistic protostellar collapse simulations, we have to simulate many physics properly. In current version of our simulation code, “ngr$^3$mhd” (abbreviation for nested-grid, radiation transfer, realistic EOS and resistive MHD), solves the basic equations described in this section on the nested-grid hierarchy.

Here we describe the physics and numerical methods adopted in our RMHD simulation code. We mainly focus on radiation transfer and newly developed parts because other parts are almost standard and similar to previous works.

### 2.2.1 MHD equations with additional terms

We start from standard resistive magnetohydrodynamic equations in the Eulerian coordinate with additional terms related to self-gravity and radiation.

$$\frac{\partial \rho}{\partial t} + \nabla \cdot (\rho \mathbf{v}) = 0, \tag{2.1}$$

$$\frac{\partial \rho \mathbf{v}}{\partial t} + \nabla \cdot \left[\rho \mathbf{v} \otimes \mathbf{v} + \left(p + \frac{1}{2}|\mathbf{B}|^2\right)\mathbb{I} - \mathbf{B} \otimes \mathbf{B}\right] = \mathbf{S}_{f,grav} + \mathbf{S}_{f,rad}, \tag{2.2}$$

$$\frac{\partial \mathbf{B}}{\partial t} - \nabla \times (\mathbf{v} \times \mathbf{B} - \eta \nabla \times \mathbf{B}) = 0, \tag{2.3}$$

$$\nabla \cdot \mathbf{B} = 0, \tag{2.4}$$

$$\frac{\partial e}{\partial t} + \nabla \cdot \left[\left(e + p + \frac{1}{2}|\mathbf{B}|^2\right)\mathbf{v} - \mathbf{B}(\mathbf{v} \cdot \mathbf{B}) - \eta \mathbf{B} \times (\nabla \times \mathbf{B})\right] = S_{e,grav} + S_{e,rad}. \tag{2.5}$$

Here $\rho$ denotes the gas density, $\mathbf{v}$ the fluid velocity, $\mathbf{B}$ the magnetic flux density, $p$ the gas pressure, $e = e_g + \frac{1}{2}\rho v^2 + \frac{1}{2}|\mathbf{B}|^2$ the total gas energy density ($e_g$ is the internal energy of the gas), $\eta$ the resistivity, respectively. These equations are the equation of mass conservation, the equation of motion, the induction equation, the solenoidal constraint for the magnetic flux density and the energy equation from top to bottom. Basically we use the Gaussian cgs units but we rescale the magnetic flux density to eliminate the constant coefficients, i.e., $\mathbf{B} = \mathbf{B}_0/\sqrt{4\pi}$ where $\mathbf{B}_0$ is given in Gauss. $\mathbf{S}_{f,grav}$ and $\mathbf{S}_{f,rad}$ are the force per volume due to gravity and radiation, $S_{e,grav}$ and $S_{e,rad}$ are the energy source terms per volume due to gravity and radiation, respectively. Additionally, we require the equation-of-state (EOS) which gives the relations between thermodynamic variables $\rho, p, T$ and $e_g$ to close the system.

### 2.2.2 Self-Gravity

The source terms related to self-gravity are given by the gravitational potential $\Phi$ as follows:

$$\mathbf{S_{f,grav}} = -\rho\nabla\Phi, \tag{2.6}$$

$$S_{e,grav} = -\rho\mathbf{v}\cdot\nabla\Phi. \tag{2.7}$$

The gravitational potential $\Phi$ is the solution of the Poisson's equation:

$$\nabla^2\Phi = 4\pi G\rho. \tag{2.8}$$

### 2.2.3 Radiation

#### Radiation Transfer Equation

In this section we show the derivation of the radiation transfer part. For simplicity, here we omit the terms come from the motion of fluid. The terms related to radiation are calculated from the frequency dependent radiation transfer equation:

$$\frac{1}{c}\frac{\partial I_\nu}{\partial t} + \mathbf{n}\cdot\nabla I_\nu = j_\nu - (\sigma_a^\nu + \sigma_s^\nu)I_\nu + \sigma_s^\nu J_\nu, \tag{2.9}$$

$I_\nu = I_\nu(\mathbf{r}, t, \mathbf{n})$ is the specific intensity in the direction specified by the unit vector $\mathbf{n}$. $j_\nu, \sigma_a^\nu$ and $\sigma_s^\nu$ are the emissivity, absorption and scattering coefficients, respectively, and related to the absorption (scattering) opacity $\kappa_a^\nu$ ($\kappa_s^\nu$); $j_\nu = \rho\kappa_a^\nu B_\nu(T)$, $\sigma_a^\nu = \rho\kappa_a^\nu$ and $\sigma_s^\nu = \rho\kappa_s^\nu$. Here we assume that the matter is in local thermodynamic equilibrium and its emission is the black-body radiation of temperature $T$, and also the scattering is isotropic (i.e., $\sigma_s^\nu$ does not depend on the direction). $B_\nu(T)$ is the Planck function:

$$B_\nu(T) = \frac{2h\nu^3}{c^2}\frac{1}{e^{\frac{h\nu}{kT}} - 1}, \tag{2.10}$$

The zeroth, first and second moments of the specific intensity are defined as follows:

$$J_\nu = \frac{1}{4\pi}\int I_\nu d\Omega, \tag{2.11}$$

$$\mathbf{H}_\nu = \frac{1}{4\pi}\int_{4\pi} \mathbf{n} I_\nu d\Omega, \tag{2.12}$$

$$\mathbb{K}_\nu = \frac{1}{4\pi}\int_{4\pi} \mathbf{nn} I_\nu d\Omega. \tag{2.13}$$

These moments are related to the radiation energy density, radiation flux and radiation pressure tensor, through the following relations:

$$E_r^\nu = \frac{1}{c}\int_{4\pi} I_\nu d\Omega = \frac{4\pi}{c} J_\nu, \tag{2.14}$$

$$\mathbf{F}_r^\nu = \int_{4\pi} \mathbf{n} I_\nu d\Omega = 4\pi \mathbf{H}_\nu, \tag{2.15}$$

$$\mathbb{P}_r^\nu = \frac{1}{c}\int_{4\pi} \mathbf{nn} I_\nu d\Omega = \frac{4\pi}{c}\mathbb{K}_\nu. \tag{2.16}$$

In principle, by solving Eq. (2.9) we can obtain the specific intensity and related quantities. In multi-dimensional and long-term problems like ours, however, such computations are unreasonably difficult and time-consuming because Eq. (2.9) is a seven-dimensional problem: three in positions, two in directions, one in frequency and one in time. If we solve this system directly, then the computational load per step will be proportional to $\mathcal{O}(N^6)$ at least, which is far more expensive than that of magnetohydrodynamic part, $\mathcal{O}(N^3)$ where $N$ represents the number of cells in one dimension.

### Moment Equations and Gray Approximation

To overcome this computational difficulty, we adopt two large approximations in this work: the flux limited diffusion approximation (FLD) and gray approximation. First, we take the zeroth and first moments of the radiation transfer equation (2.9) by integrating it over $4\pi$ solid angle:

$$\frac{\partial E_r^\nu}{\partial t} + \nabla \cdot \mathbf{F}_r^\nu = 4\pi\sigma_a^\nu B_\nu(T) - c\sigma_a^\nu E_r^\nu, \tag{2.17}$$

$$\frac{\partial \mathbf{F}_r^\nu}{\partial t} + c^2 \nabla \cdot \mathbb{P}_r^\nu = -c(\sigma_a^\nu + \sigma_s^\nu)\mathbf{F}_r^\nu. \tag{2.18}$$

These are the moment equations of radiation transfer. Then we average the equations over frequency:

$$\frac{\partial E_r}{\partial t} + \nabla \cdot \mathbf{F}_r = 4\pi \int_0^\infty \sigma_a^\nu B_\nu(T) d\nu - c \int_0^\infty \sigma_a^\nu E_r^\nu d\nu, \tag{2.19}$$

$$\frac{\partial \mathbf{F}_r}{\partial t} + c^2 \nabla \cdot \mathbb{P}_r = -c \int_0^\infty (\sigma_a^\nu + \sigma_s^\nu) \mathbf{F}_r^\nu d\nu, \tag{2.20}$$

where

$$E_r = \int_0^\infty E_r^\nu d\nu, \tag{2.21}$$

$$\mathbf{F}_r = \int_0^\infty \mathbf{F}_r^\nu d\nu, \tag{2.22}$$

$$\mathbb{P}_r = \int_0^\infty \mathbb{P}_r^\nu d\nu, \tag{2.23}$$

are frequency-averaged radiation quantities. We replace the terms in the RHS by properly averaged opacities.

$$\kappa_P = \frac{\int_0^\infty \kappa_a^\nu B_\nu(T) d\nu}{\int_0^\infty B_\nu(T) d\nu}, \tag{2.24}$$

$$\kappa_E = \frac{\int_0^\infty \kappa_a^\nu E_r^\nu(T) d\nu}{\int_0^\infty E_r^\nu(T) d\nu}, \tag{2.25}$$

$$\kappa_F = \frac{\int_0^\infty (\kappa_a^\nu + \kappa_s^\nu) F_r^\nu(T) d\nu}{\int_0^\infty F_r^\nu(T) d\nu}, \tag{2.26}$$

Then we get the following equations:

$$\frac{\partial E_r}{\partial t} + \nabla \cdot \mathbf{F}_r = c(\sigma_P a_r T^4 - \sigma_E E_r), \tag{2.27}$$

$$\frac{\partial \mathbf{F}_r}{\partial t} + c^2 \nabla \cdot \mathbb{P}_r = -c\sigma_F \mathbf{F}_r, \tag{2.28}$$

where $\sigma_P = \rho\kappa_P$, $\sigma_E = \rho\kappa_E$, and $\sigma_F = \rho\kappa_F$, respectively. These mean opacities are called the Planck mean opacity, the energy mean opacity and the flux mean opacity. Here we use the Stefan-Boltzmann law:

$$4\pi \int_0^\infty B_\nu(T) d\nu = 4\sigma T^4 = a_r c T^4, \tag{2.29}$$

where $\sigma = 5.6704 \times 10^{-5} \mathrm{erg\,cm^{-2}\,K^{-4}}$ is the Stefan-Boltzmann constant and $a_r = 4\sigma/c = 7.5657 \times 10^{-15} \mathrm{erg\,cm^{-3}\,K^{-4}}$ is the radiation (density) constant.

### Flux Limited Diffusion Approximation

We have derived the gray radiation moment equations in the previous section, but the moment equations (2.19) and (2.20) are not closed yet. To close the system, we require a closure relation to relate higher order moments to lower order ones.

In this work we adopt flux limited diffusion approximation (FLD) proposed by Levermore & Pomraning (1981). In the limit of large optical depth, the radiation flux can be expressed by the gradient of radiation energy. In sufficiently optically thick media, radiation is well thermalized; the radiation field is almost isotropic and its spectrum is the black body. Then the radiation pressure tensor will be isotropic, i.e.,

$$\mathbb{P}_r^\nu = \frac{1}{3} E_r^\nu \mathbb{I}, \tag{2.30}$$

and we can neglect the time variation of the radiation flux in Eq. (2.18). Then the radiation flux can be written in simple Fick's law:

$$\mathbf{F}_r^\nu = \frac{c}{3(\sigma_a^\nu + \sigma_s^\nu)} \nabla B_\nu(T). \tag{2.31}$$

This equation can be rewritten as follows:

$$\mathbf{F}_r^\nu = \frac{c}{3(\sigma_a^\nu + \sigma_s^\nu)} \frac{dB_\nu(T)}{dT} \nabla T. \tag{2.32}$$

By averaging this relation over frequency and replacing the opacities with proper mean opacities, we obtain the closure relation in the gray diffusion approximation:

$$\mathbf{F}_r = \frac{c}{3\sigma_R} \nabla E_r, \tag{2.33}$$

$$\kappa_R^{-1} = \frac{\int_0^\infty (\kappa_a^\nu + \kappa_s^\nu)^{-1} \frac{dB_\nu(T)}{dT} d\nu}{\int_0^\infty \frac{dB_\nu(T)}{dT} d\nu}. \tag{2.34}$$

Here $\kappa_R$ is called the Rosseland mean opacity, and $\sigma_R = \rho \kappa_R$.

By assuming the black body spectrum, we can replace $\sigma_E$ with $\sigma_P$. We also replace $\sigma_F$ with $\sigma_R$, which is valid approximation in the optically thick region. In the early phase of star formation, the coupling between gas and radiation is so strong that the gas and radiation have similar temperature close to equilibrium, i.e., $T_g \sim T_r$. Since this is valid in almost all the region and time in our simulations, we calculate the opacities using local gas temperature for simplicity. Thus we can replace all the opacities in the basic equations with the Planck and Rosseland mean opacities calculated with local gas temperature. Note that, however, these assumptions may cause the loss of accuracy in the optically thin region. We adopt these simplifications because optically thick region (e.g., the central first and second cores) dominates the global dynamics in our cases.

Fick's law (2.33) is valid only in optically thick regions, but in FLD we apply this relation to optically thin regions with a correction. In optically thin regions, the radiation flux (2.33) can be large unlimitedly ($\mathbf{F}_r \to \infty$ when $\sigma_R \to 0$). But in reality, the radiation flux must be limited by causality, i.e., $|\mathbf{F}_r| \to cE_r$. To satisfy the causality and smoothly connect the optically thick and thin limits, we introduce a correction factor, or flux limiter, $\lambda$:

$$\mathbf{F}_r = \frac{c\lambda}{\sigma_R}\nabla E_r. \tag{2.35}$$

Some forms of flux limiters are proposed but here we use the flux limiter of Levermore & Pomraning (1981), which is based on Chapman-Enskog approach.

$$\lambda(R) = \frac{1}{R}\Big(\coth R - \frac{1}{R}\Big), \tag{2.36}$$

$$R = \frac{|\nabla E_r|}{\sigma_R E_r}. \tag{2.37}$$

$R$ is a variable reflecting the degree of anisotropy or optical depth. In our simulations we adopt a simple fitting formula of (2.36):

$$\lambda(R) = \frac{2+R}{6+2R+R^2}. \tag{2.38}$$

This flux limiter behaves like

$$\lambda(R) \to \begin{cases} \frac{1}{3} & (R \to 0 \quad \text{or} \quad \tau \gg 1), \\ \frac{1}{R} & (R \to \infty \quad \text{or} \quad \tau \ll 1), \end{cases} \tag{2.39}$$

and the resulting radiation flux has proper asymptotic limits:

$$\mathbf{F_r}(R) \to \begin{cases} \frac{c}{3\sigma_R}\nabla E_r & (R \to 0 \quad \text{or} \quad \tau \gg 1), \\ cE_r\mathbf{n} & (R \to \infty \quad \text{or} \quad \tau \ll 1), \end{cases} \tag{2.40}$$

where $\mathbf{n}$ is the normal direction of the radiation energy gradient:

$$\mathbf{n} = \frac{\nabla E_r}{|\nabla E_r|}. \tag{2.41}$$

Minerbo (1978) proposed another form of flux limiter, but the difference between the flux limiters is not supposed to be important.

Now we have the closed system of Eqs. (2.35), (2.36) and the zeroth moment equation (2.19), and we can calculate the time evolution of the radiation system.

The radiation pressure tensor doesn't appear in the zeroth moment equation (2.19) neglecting the fluid motion, but we need it when we proceed to radiation hydrodynamics. In FLD, the Eddington tensor $\mathbb{D}_r$ which gives the relation between radiation pressure tensor and other lower order moments is given by the following formulae (Levermore, 1984)

$$\mathbb{P}_r = \mathbb{D}_r E_r, \tag{2.42}$$

$$\mathbb{D}_r = \frac{1-\chi}{2}\mathbb{I} + \frac{3\chi - 1}{2}\mathbf{n}\otimes\mathbf{n}, \tag{2.43}$$

$$\chi = \lambda + \lambda^2 R^2 \tag{2.44}$$

### Limitation of FLD and Higher Order Moment Method

We have to note that FLD is just a crude approximation of radiation transfer. There are two major drawbacks in FLD. FLD is constructed on the basis of the diffusion approximation which is valid in highly optically thick and almost isotropic situations. Therefore FLD cannot handle the anisotropies correctly; the radiation fields can propagate only in the direction of the radiation energy gradient. As a result, the radiation fields tend to be isotropic (or spherical), and no shadow will form for example. Another deficit of FLD is that the hyperbolic nature of the underlying radiation transfer equation is not preserved. The propagation of radiation fields are quite unphysical in optically thin media, for instance, it cannot handle the propagation of a radiation pulse. The greatest benefit of FLD is its low computational cost, and we should use a better method if possible. But in star formation processes, most of radiation energy is produced in the centrally condensed optically thick region, and the system is relatively close to spherically symmetric, at least in the early phase. Therefore we regard FLD as a reasonable choice as the first step for radiation hydrodynamic simulations of star formation processes.

To improve the treatment of radiation fields, we need to solve higher order moment equations. In variable tensor Eddington factor (VTEF) method (Stone et al., 1992; Hayes & Norman, 2003), the zeroth and first moment equations (2.19, 2.20) are solved and the Eddington tensor as a closure relation is calculated from ray-tracing using the stationary radiation transfer equation. This is the most rigorous treatment but it requires enormous computational costs, so we need some numerical techniques to reduce the costs (or extremely high performance and efficient supercomputers). In $M_1$ closure scheme (Dubroca & Feugeas, 1999; González et al., 2007), on the other hand, the zeroth and first moment equations are solved and the system is closed with Eq. (2.43). The assumption used here is that the radiation field can be expressed by a Lorentz transform of an isotropic field in a certain inertial frame (or equivalently, the radiation entropy is maximized). This scheme enables us to handle strongly anisotropic situations such as shadows and beams, if there is only one direction of anisotropy. If there are two or more directions (e.g., multiple point sources), the scheme will fail to reproduce realistic radiation transfer. But it is at least better than FLD because it gives proper behaviors both in optically thick and thin media. Another strong advantage of $M_1$ closure scheme is that it is Lorentz covariant (Chan, 2011), which is beneficial in relativistic systems. In this work, we adopt FLD due to the limitation of the computational resources, but we will extend our simulations using these higher-moment methods in the future.

### Radiation Hydrodynamics in Comoving Frame

Next, we combine the FLD radiation transfer equations with magnetohydrodynamic equations. First, we have to fix a frame in which we describe the physical quantities related to radiation. There are three major choices: the comoving frame (Castor, 2004; Lowrie et al., 2001), the mixed frame (Krumholz et al., 2007) and the laboratory frame (Mihalas & Auer, 2001). In the laboratory frame equations, all the radiation quantities are defined in the same inertial frame of an observer, and therefore the coupling terms between matter and radiation are complicated. It is convenient to define the quantities related to radiation-matter interaction in the comoving frame of the matter. In the mixed frame equations, the radiation quantities are defined in the laboratory frame and the matter quantities such as opacities are written in the comoving frame. In principle it is good scheme because the total energy is conserved exactly, but it is still complicated due to the frame conversion. In this work, we adopt the comoving frame radiation hydrodynamic equations because of simplicity. However, we should note that the comoving fame equations have some deficits: they are accurate only to $\mathcal{O}(v/c)$, they are not conservative and additional non-conservative terms appear in the system, rays do not travel straightly. For non-relativistic problems like star formation where $v \ll c$, the difference will be small.

The comoving frame FLD radiation transfer equations are given as follows (Castor, 2004):

$$\frac{\partial E_r}{\partial t} + \nabla \cdot (\mathbf{v} E_r) + \nabla \cdot \mathbf{F}_r + \mathbb{P}_r : \nabla \mathbf{v} = c(\sigma_P a_r T_g^4 - \sigma_E E_r). \tag{2.45}$$

Here all the radiation quantities and opacities are defined in the comoving frame. The second term in the LHS is advective flux due to the fluid motion. The last term in the LHS is non-conservative term due to the choice of the comoving frame.

The source terms in the equations of matter (2.2) and (2.5) can be described in two parts: the radiation-matter coupling and radiation force.

$$S_{e,rad} = -c(\sigma_P a_r T^4 - \sigma_E E_r) + \frac{\sigma_F}{c}\mathbf{F}_r \cdot \mathbf{v}, \tag{2.46}$$

$$\mathbf{S}_{f,rad} = \frac{\sigma_F}{c}\mathbf{F}_r. \tag{2.47}$$

The first term of the RHS in Eq. (2.46) is the radiation-matter coupling term, and other terms are related to the work done by the radiation force.

### Radiation Timescales

Before closing this section, we discuss the timescales in the radiation hydrodynamics of star formation processes. We should consider the following processes related to thermal evolution:

- Dynamics: adiabatic compression and expansion
- Gas-dust interaction
- Dust-radiation interaction
- Gas-radiation interaction
- Radiation transfer

Here we discuss the relations between these processes. The dynamical timescale will be on the order of the free fall time. We estimate the gas-dust interaction timescale based on Leung (1975) (see also Saigo & Tomisaka (2011)), and it is far shorter than other timescales in almost all the region of our interest. Therefore we can assume the gas and dust are in equilibrium, $T_{\rm gas} = T_{\rm dust}$ (the basic equations described above use this condition). The timescales of both dust-radiation and gas-radiation interactions are derived from the RHS of (2.45); dust is the main opacity source in low temperature, and gas becomes dominant above the dust evaporation temperature ($T \gtrsim 1500\,{\rm K}$). Finally, we can estimate the radiation transfer timescale from the radiation flux. We estimate these timescales of the central gas element in spherically symmetric collapse of a molecular cloud. Here we assume simple thermal evolution; the gas temperature is 10K while radiation cooling is efficient and the gas behave adiabatic ($\gamma = 7/5$) when radiation cooling is inefficient (This corresponds to so-called barotropic approximation). We also adopt simple fitting formulae for opacities, mimicking the opacities of Semenov et al. (2003). We show these timescales as functions of the gas density in Figure 2.1. Here we assume the Jeans length as the typical spatial scale.

From this Figure, we can see the scenario of the protostellar collapse. Initially the timescales of gas-radiation interaction and radiation transfer are far shorter than the dynamical one, therefore the cloud evolves isothermally. When the gas density gets sufficiently high, the gas-radiation coupling timescale exceeds the dynamical timescale

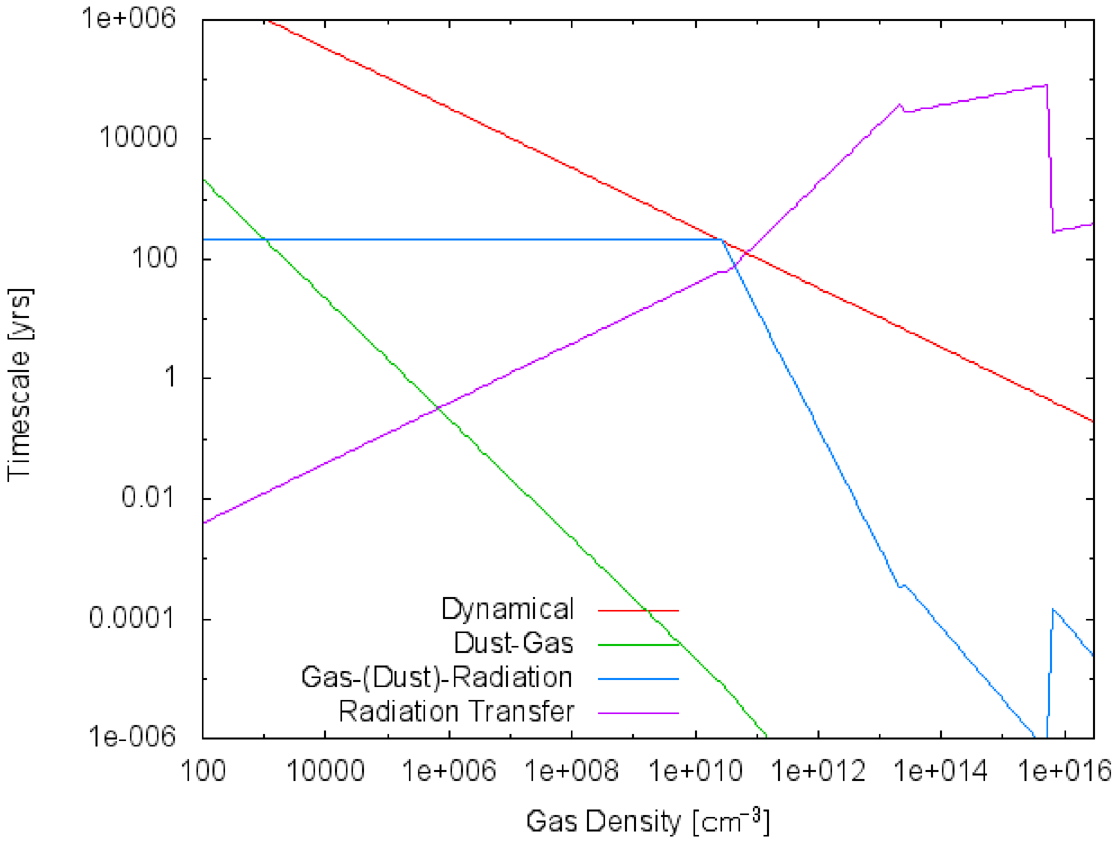

Figure 2.1: The timescales of important processes related to radiation and hydrodynamics in protostellar collapse as functions of density, calculated assuming typical thermal evolution track and simplified opacities.

and the temperature starts to rise. Soon after the break of isothermality, the first core forms (Masunaga & Inutsuka, 1999). As the gas density increases, the gas becomes optically thick and radiation transfer becomes inefficient. Thus the first core evolves quasi-adiabatically.

We have to consistently take these physics of different timescales into account at the same time in RHD simulations. It is computationally difficult to involve the phenomena of very short timescales. We require an implicit time-integration scheme to calculate these radiation processes robustly with reasonable computational costs.

### 2.2.4 Summary of Basic Equations

By summarizing the descriptions above, the basic equations we use in our simulations can be written as follows:

$$\frac{\partial \rho}{\partial t} + \nabla \cdot (\rho \mathbf{v}) = 0, \tag{2.48}$$

$$\frac{\partial \rho \mathbf{v}}{\partial t} + \nabla \cdot \left[ \rho \mathbf{v} \otimes \mathbf{v} + \left( p + \frac{1}{2}|\mathbf{B}|^2 \right) \mathbb{I} - \mathbf{B} \otimes \mathbf{B} \right] = -\rho \nabla \Phi + \frac{\sigma_R}{c} \mathbf{F}_r, \tag{2.49}$$

$$\frac{\partial \mathbf{B}}{\partial t} - \nabla \times (\mathbf{v} \times \mathbf{B} - \eta \nabla \times \mathbf{B}) = 0, \tag{2.50}$$

$$\nabla \cdot \mathbf{B} = 0, \tag{2.51}$$

$$\begin{aligned} \frac{\partial e}{\partial t} + \nabla \cdot \left[ \left( e + p + \frac{1}{2}|\mathbf{B}|^2 \right) \mathbf{v} - \mathbf{B}(\mathbf{v} \cdot \mathbf{B}) - \eta \mathbf{B} \times (\nabla \times \mathbf{B}) \right] &= \\ -\rho \mathbf{v} \cdot \nabla \Phi - c\sigma_P (a_r T^4 - E_r) + \frac{\sigma_R}{c} \mathbf{F}_r \cdot \mathbf{v}&, \end{aligned} \tag{2.52}$$

$$\nabla^2 \Phi = 4\pi G \rho, \tag{2.53}$$

$$\frac{\partial E_r}{\partial t} + \nabla \cdot (\mathbf{v} E_r) + \nabla \cdot \mathbf{F}_r + \mathbb{P}_r : \nabla \mathbf{v} = c\sigma_P (a_r T_g^4 - E_r), \tag{2.54}$$

$$\mathbf{F}_r = \frac{c\lambda}{\sigma_R} \nabla E_r, \quad \lambda(R) = \frac{2 + R}{6 + 2R + R^2}, \quad R = \frac{|\nabla E_r|}{\sigma_R E_r}, \tag{2.55}$$

$$\mathbb{P}_r = \mathbb{D}_r E_r, \quad \mathbb{D}_r = \frac{1 - \chi}{2} \mathbb{I} + \frac{3\chi - 1}{2} \mathbf{n} \otimes \mathbf{n}, \quad \chi = \lambda + \lambda^2 R^2, \quad \mathbf{n} = \frac{\nabla E_r}{|\nabla E_r|}. \tag{2.56}$$

From top to bottom, they represent conservation of mass, the equation of motion, the induction equation with resistivity, the solenoidal constraint, the Poisson's equation of gravity, and the FLD radiation transfer equations.

## 2.3 Code Description

We extend the nested-grid MHD simulation code originally developed by Matsumoto & Hanawa (2003b) and extended in Machida et al. (2004). This code has been extensively used in star formation studies (Matsumoto & Tomisaka, 2004; Machida et al., 2005b,a, 2006, 2008a,b; Saigo et al., 2008; Machida et al., 2009a,b, 2010; Machida & Matsumoto, 2011; Machida et al., 2011b,a). The original code solves self-gravitational ideal magnetohydrodynamics of polytropic gas. In this work, we introduce gray radiation transfer based on FLD, realistic EOS and resistive MHD.

### 2.3.1 Operator-Splitting

In order to solve the complex system (2.48 – 2.56), we divide the system into five parts and solve them separately. We update our system in the following strategy:

**Step 1. Ideal MHD part:**

$$\frac{\partial \rho}{\partial t} + \nabla \cdot (\rho \mathbf{v}) = 0, \tag{2.57}$$

$$\frac{\partial \rho \mathbf{v}}{\partial t} + \nabla \cdot \left[\rho \mathbf{v} \otimes \mathbf{v} + \left(p + \frac{1}{2}|\mathbf{B}|^2\right)\mathbb{I} - \mathbf{B} \otimes \mathbf{B}\right] = 0, \tag{2.58}$$

$$\frac{\partial \mathbf{B}}{\partial t} - \nabla \times (\mathbf{v} \times \mathbf{B}) = 0, \tag{2.59}$$

$$\nabla \cdot \mathbf{B} = 0, \tag{2.60}$$

$$\frac{\partial e}{\partial t} + \nabla \cdot \left[\left(e + p + \frac{1}{2}|\mathbf{B}|^2\right)\mathbf{v} - \mathbf{B}(\mathbf{v} \cdot \mathbf{B})\right] = 0, \tag{2.61}$$

$$\frac{\partial E_r}{\partial t} + \nabla \cdot (\mathbf{v} E_r) = 0. \tag{2.62}$$

**Step 2. Self-Gravity part:**

$$\nabla^2 \Phi = 4\pi G \rho, \tag{2.63}$$

$$\frac{\partial \rho \mathbf{v}}{\partial t} = -\rho \nabla \Phi, \tag{2.64}$$

$$\frac{\partial e}{\partial t} = -\rho \mathbf{v} \cdot \nabla \Phi, \tag{2.65}$$

**Step 3. Resistivity part:**

$$\frac{\partial \mathbf{B}}{\partial t} + \nabla \times (\eta \nabla \times \mathbf{B}) = 0, \tag{2.66}$$

$$\frac{\partial e}{\partial t} - \nabla \cdot [\eta \mathbf{B} \times (\nabla \times \mathbf{B})] = 0. \tag{2.67}$$

**Step 4. Radiation part:**

$$\frac{\partial e_g}{\partial t} = -c(\sigma_P a T_g^4 - \sigma_E E_r), \tag{2.68}$$

$$\frac{\partial E_r}{\partial t} + \nabla \cdot \mathbf{F}_r + \mathbb{P}_r : \nabla \mathbf{v} = c(\sigma_P a_r T_g^4 - \sigma_E E_r), \tag{2.69}$$

$$\mathbf{F}_r = \frac{c\lambda}{\sigma_R} \nabla E_r, \quad \lambda(R) = \frac{2 + R}{6 + 2R + R^2}, \quad R = \frac{|\nabla E_r|}{\sigma_R E_r}, \tag{2.70}$$

$$\mathbb{P}_r = \mathbb{D}_r E_r, \quad \mathbb{D}_r = \frac{1 - \chi}{2}\mathbb{I} + \frac{3\chi - 1}{2}\mathbf{n} \otimes \mathbf{n}, \quad \chi = \lambda + \lambda^2 R^2, \quad \mathbf{n} = \frac{\nabla E_r}{|\nabla E_r|}. \tag{2.71}$$

**Step 5. Radiation Force part:**

$$\frac{\partial \rho \mathbf{v}}{\partial t} = \frac{\sigma_F}{c} \mathbf{F}_r, \tag{2.72}$$

$$\frac{\partial e}{\partial t} = \frac{\sigma_F}{c} \mathbf{F}_r \cdot \mathbf{v}. \tag{2.73}$$

Introducing such an operator-splitting technique causes loss of time-accuracy. The overall accuracy of our time-integration is first order, theoretically.

### 2.3.2 Magnetohydrodynamics

Here we explain how to update the Step 1. equations. The MHD system (2.57 – 2.61) in one-dimension can be written in the form of the conservation law:

$$\frac{\partial \mathbf{U}}{\partial t} + \nabla \cdot \mathbf{F} = 0, \tag{2.74}$$

$$\mathbf{U} = \begin{pmatrix} \rho \\ \rho\mathbf{v} \\ \mathbf{B} \\ e \end{pmatrix}, \qquad \mathbf{F} = \begin{pmatrix} \rho\mathbf{v} \\ \rho\mathbf{v}\mathbf{v} + \left(p + \frac{1}{2}|\mathbf{B}|^2\right)\mathbb{I} - \mathbf{B}\mathbf{B} \\ \mathbf{v}\mathbf{B} - \mathbf{B}\mathbf{v} \\ \left(e + p + \frac{1}{2}|\mathbf{B}|^2\right)\mathbf{v} - \mathbf{B}(\mathbf{v}\cdot\mathbf{B}) \end{pmatrix}. \tag{2.75}$$

We solve this system using the HLLD approximate Riemann solver (Miyoshi & Kusano, 2005). To achieve second-order accuracy in space and time, we adopt standard MUSCL (Monotone Upstream-centered Scheme for Conservation Laws) approach and the directionally-unsplit two-step predictor-corrector scheme (e.g., Hirsch, 1990). We store ($\rho$, $\mathbf{v}$, $\mathbf{B}$, $e_g$, $\psi$, $E_r$) as primitive variables and interpolate them for spatial reconstruction with the minmod slope limiter for robustness ($\psi$ is a variable related to the solenoidal constraint, see below). We use the gas internal energy $e_g$ as a primitive variable instead of the gas pressure $p$ which is the textbook notation in order to minimize the numerical error when we use tabulated EOS. That is, the discretization error of the EOS table will be directly reflected in the result if we perform mutual conversion between $p$ and $e_g$ (i.e., $p \to e_g \to p$), but we can avoid this error if we use one-way conversion ($e_g \to p$) only; the discretization error only affects the flux and its effect is kept small.

#### Riemann Solver

Because the flow appears in astrophysical problems are highly supersonic and compressible, accurate shock capturing schemes are often necessary in hydrodynamic calculations. Riemann solvers, a class of shock capturing scheme solving the Riemann problem between contacting cells, have been extensively explored in preceding studies.

In the older version of our code, we adopted MHD version of Roe's linearized Riemann solver (Fukuda & Hanawa, 1999) which is quite accurate. However, it is complicated to implement general EOS onto Roe's solver because it requires derivatives of thermodynamic variables to calculate eigenvalues and eigenvectors of the system. Such a scheme is proposed (Mikami et al., 2008), but here we adopt the HLLD (Harten-Lax-van Leer, Discontinuities) solver recently proposed by Miyoshi & Kusano (2005). This scheme does not require the detailed knowledge about the EOS in calculations. It is simple, robust, highly efficient, almost as accurate as Roe's Riemann solver and therefore commonly used in astrophysical simulations these days.

In the HLLD scheme, we approximate the Riemann fan with four intermediate states separated by five characteristic waves: oppositely directed two fast sonic waves, oppositely directed two Alfvén waves and one entropy wave. In Figure 2.2, $S_L$ and $S_R$ represent the left- and right-going fast waves, $S_L^*$ and $S_R^*$ the Alfvén waves, and $S_M$ the entropy wave. The left, right and four intermediate states $U_L, U_R, U_L^*, U_R^*, U_L^{**}, U_R^{**}$ are connected through the physical jump conditions across these waves.

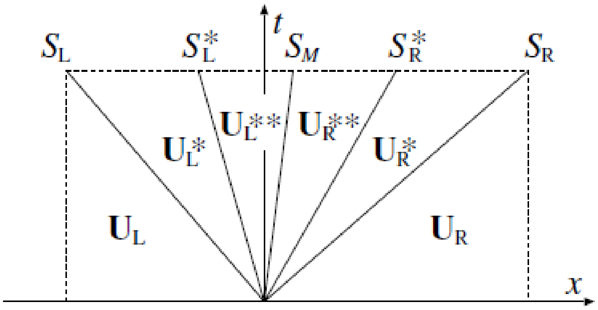

Figure 2.2: The structure of the waves and intermediate states in HLLD. Adapted from Miyoshi & Kusano (2005).

In the HLLD scheme, the slow sonic waves are neglected. Therefore, compared to Roe's solver, additional numerical dissipation occurs in the isolated slow wave, but its effective resolution is still acceptable (Stone et al., 2008). Generally, the HLLD solver gives a numerical solution as accurate as Roe's solver. One of the significant merits of the HLLD solver is its robustness, especially it is proved to be positively conservative in one-dimensional problems, i.e., no negative density nor pressure appears in the solution calculated with the HLLD flux. Therefore, it is quite robust even in a strong rarefaction wave such that Roe's solver may fail to solve. Also, it does not require the entropy fix required in Roe's Riemann solver (Harten & Hyman, 1983; Toro, 2009).

We update the advective flux of radiation energy (2.62) separately using Roe's upwind method. When the radiation energy dominates the gas energy, the radiation pressure affects the sonic speed of the gas and the characteristics are modified, but we neglect this effect. In our star formation simulations (at least in low mass cases), we expect that we encounter such a radiation dominant region only in the deep interior of the protostellar core in the late phase of protostellar collapse, and we do not expect this effect will be significant.

### Solenoidal Constraint

Physically, the solenoidal constraint, or the divergence-free condition for the magnetic flux density **B** (2.51) is always satisfied automatically while the magnetic fields are updated using the induction equation (2.50). However, it is not trivial in multi-dimensional numerical simulations because of inevitable numerical errors due to discretization. We have to take care of this solenoidal constraint because there may appear unphysical force when non-zero $\nabla \cdot \mathbf{B}$ is generated numerically.

There are three classes of methods to care this constraint: projection, constrained transport (CT), and generalized Lagrangian multiplier (GLM). In this work, we adopt the mixed correction based on the GLM approach proposed by Dedner et al. (2002). They investigated a series of GLM schemes and showed that the mixed correction gives the best results. In this scheme, we introduce additional variable $\psi$ related to (numerical) $\nabla \cdot \mathbf{B}$, and solve its evolution. We solve the MHD equations modified as follows:

$$\frac{\partial \rho}{\partial t} + \nabla \cdot (\rho \mathbf{v}) = 0, \tag{2.76}$$

$$\frac{\partial \rho \mathbf{v}}{\partial t} + \nabla \cdot \left[\rho \mathbf{v} \otimes \mathbf{v} + \left(p + \frac{1}{2}|\mathbf{B}|^2\right)\mathbb{I} - \mathbf{B} \otimes \mathbf{B}\right] = -(\nabla \cdot \mathbf{B})\mathbf{B}, \tag{2.77}$$

$$\frac{\partial \mathbf{B}}{\partial t} - \nabla \times (\mathbf{v} \times \mathbf{B}) + \nabla \psi = -(\nabla \cdot \mathbf{B})\mathbf{v}, \tag{2.78}$$

$$\frac{\partial e}{\partial t} + \nabla \cdot \left[\left(e + p + \frac{1}{2}|\mathbf{B}|^2\right)\mathbf{v} - \mathbf{B}(\mathbf{v} \cdot \mathbf{B})\right] = -(\nabla \cdot \mathbf{B})\mathbf{v} \cdot \mathbf{B} - \mathbf{B} \cdot (\nabla \psi), \tag{2.79}$$

$$\frac{\partial \psi}{\partial t} + c_h^2 \nabla \cdot \mathbf{B} = -\mathbf{v} \cdot (\nabla \psi) - \frac{c_h^2}{c_p^2}\psi. \tag{2.80}$$

We solve an additional equation including both hyperbolic and parabolic terms (thus it is called mixed correction) as well as the evolution of the normal component of the magnetic fields $B_x$. We take the hyperbolic propagation speed $c_h$ as large as possible not to violate the CFL condition and take $c_p^2 = 0.18 c_h$ as proposed in Dedner et al. (2002). In this scheme, $\nabla \cdot \mathbf{B}$ generated due to the numerical error is kept small by being dumped and transferred. Note that additional source terms proportional to $\nabla \cdot \mathbf{B}$ are introduced in the RHS of the MHD equations. Physically these source terms should be zero and do not appear in MHD equations, but introducing these terms improve the nature of the MHD equations and results in better robustness (Dedner et al., 2002).

Basically CT is a good scheme for ideal MHD that exactly preserve $\nabla \cdot \mathbf{B}$, but practically it requires a lot of memory. It is not trivial to implement non-ideal MHD effects onto CT scheme because respective components of magnetic fields ($B_x, B_y$ and $B_z$) are defined at different surfaces of the cell. On the other hand, GLM is quite fast, memory efficient, easy to implement and gives good results. It is easy to implement additional physics because all the physical variables are defined at the cell center.

#### Carbuncle Phenomenon and Cure for it

Some high resolution (magneto-) hydrodynamic solvers show strange behaviors at strong shocks which are aligned to the grid structure. This problem called Carbuncle phenomenon is obviously unphysical. Diffusive schemes such as HLLE and Lax-Friedrichs are free from this phenomenon, but HLLD and Roe's method suffer from it. It seems that numerical viscosity for shearing (tangential) velocity is insufficient and unphysical perturbation is amplified. This problem may be originated from the discretization, especially that we calculate the flux of each direction separately.

It is difficult to cure this problem fundamentally, but practically we can suppress the unphysical oscillations by introducing additional viscosity at the shock. First, we need to locate the shock. We identify the cells which possibly contain a shock using the method proposed in Hanawa et al. (2008). Then we add artificial viscosity for shear motion in the marked cells. We adopt the method proposed by Hanawa et al. (2008) when we solve the MHD system with Roe's solver. In this method, additional shear viscosity is achieved by modifying the characteristic velocities. When we use HLLD solver, we adopt the HLLD$-$ flux by Miyoshi & Kusano (2007). HLLD$-$ is a modified version of the HLLD flux in which tangential velocities $(v_y, v_z)$ in the Riemann fan are replaced by HLL averages while other variables are the same as HLLD. Sufficient (but not too large) additional shear viscosity is introduced by this procedure and it stabilizes the Carbuncle phenomena.

### 2.3.3 Self-Gravity

To solve the Poisson's equation (2.63) on the nested-grid hierarchy, we adopt the multigrid solver developed by Matsumoto & Hanawa (2003a). The solver gives second-order accurate solution in space. We integrate (2.64) and (2.65) using obtained gravitational potential.

### 2.3.4 Resistive MHD

Because of the low ionization degree, non-ideal MHD effects such as the Ohmic dissipation, the ambipolar diffusion and the Hall effect work in star formation problems. The timescale of the non-ideal MHD effects become shorter than the dynamical timescale in the first core phase ($n_H \gtrsim 10^{11}\,\mathrm{cm}^{-3}$) and significant loss of magnetic flux occurs (Nakano et al., 2002). All these effects may be important but in this work we focus on the Ohmic dissipation as the first step.

### Resistivity

We calculate the (Ohmic) resistivity considering both thermal and non-thermal particles. For non-thermal processes, we adopt the table of resistivity based on the reaction network model between grains and chemical species constructed by Umebayashi & Nakano (2009) (see also Okuzumi (2009)). The table of $\eta_{NT}$ is given as a function of the gas density $\rho$, the temperature $T$ and the ionization rate $\xi$. Here we assume the typical interstellar ionization rate due to the cosmic rays: $\xi_{CR} \sim 10^{-17}\,\mathrm{s}^{-1}$, neglecting shielding by the gas. Since the attenuation depth of the cosmic rays is about $100\,\mathrm{g\,cm}^{-2}$, the ionization rate will be lower in the deep interior of the first core. In this sense (and also because we neglect the ambipolar diffusion) our models give lower limit of (but still highly efficient) magnetic flux loss. Note that decay of radionuclides considerably contributes to the ionization rate $\xi_{RA} \sim 7.6 \times 10^{-19}\,\mathrm{s}^{-1}$ (Umebayashi & Nakano, 2009), therefore the effect from neglecting the shielding will be as large as about an order of magnitude at most. We should mention that there is still large uncertainty in the resistivity from the grain properties such as the structure, composition, size distribution and so on.

In order to calculate the resistivity for our simulations, it is sufficient to estimate the contribution to the thermal ionization processes from the species which has low ionization energy. Potassium (K) has very low ionization energy ($kT_{ion} \sim 4.33\,\mathrm{eV}$) and sufficiently abundant, therefore it is the most important electron-supplying species in star formation processes. Here we calculate the resistivity due to the thermal ionization of potassium on the assumption of thermal equilibrium using the following equation:

$$\eta_T = 7.5 \times 10^9 \exp\left(\frac{25188\,\mathrm{K}}{T}\right) T^{-1/4} \rho^{1/2} \quad \mathrm{cm}^2\,\mathrm{s}^{-1}. \tag{2.81}$$

We calculate the total resistivity as follows:

$$\eta^{-1} = \eta_T^{-1} + \eta_{NT}^{-1}, \tag{2.82}$$

because the resistivity is inversely proportional to the ionization degree. We show the resistivity and magnetic Reynolds number $R_m \equiv v_{\mathrm{ff}} \lambda_{\mathrm{J}}/\eta$ as a function of the gas density in Figure 2.3. Here we consider the Jeans length $\lambda_{\mathrm{J}} \equiv 2\pi c_s \sqrt{\frac{3\pi}{32 G\rho}}$ and the free-fall velocity $v_{\mathrm{ff}} \equiv \sqrt{\frac{GM_{\mathrm{J}}}{\lambda_{\mathrm{J}}}}$ (where $M_{\mathrm{J}} = \frac{4\pi}{3}\lambda_{\mathrm{J}}^3\rho$) as typical length and velocity scales to estimate the magnetic Reynolds number. To draw this plot, we adopt the barotropic approximation as a typical thermal evolution to calculate the gas temperature:

$$T = \max\left[10, 10 \times \left(\frac{\rho}{\rho_{crit}}\right)^{\gamma-1}\right] \mathrm{K}, \tag{2.83}$$

where $\rho_{crit} = 2 \times 10^{-13}\,\mathrm{g\,cm^{-3}}$ is the critical density and $\gamma = 7/5$ is the adiabatic index. The resistivity steeply decreases in $n \gtrsim 10^{15}\,\mathrm{cm^{-3}}$ because of the thermal ionization of potassium. The magnetic fields are decoupled from fluid where the magnetic Reynolds number is less than unity. Our resistivity is quite similar to that used in Machida et al. (2006).

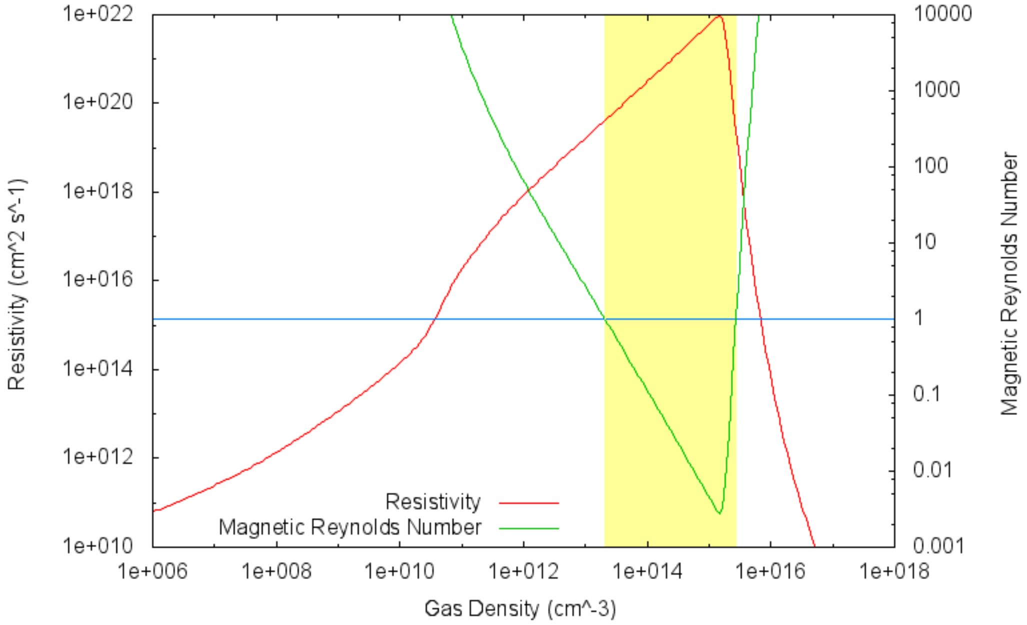

Figure 2.3: The resistivity $\eta$ and the magnetic Reynolds number $R_m$ are plotted as functions of the gas density. Magnetic fields are decoupled from fluid where $R_m < 1$ (yellow).

### Spatial Discretization

We discretize (2.66) and (2.67) as follows. First, we rewrite (2.66) in the conservative form:

$$\frac{\partial \mathbf{B}}{\partial t} + \nabla \cdot \mathbb{F} = 0, \tag{2.84}$$

$$F_{aa} = 0, \tag{2.85}$$

$$F_{ab} = \eta(\partial_a B_b - \partial_b B_a). \tag{2.86}$$

Here $F_{ab}$ represents the flux of $a$-component in $b$-direction. Optionally, we can introduce correction terms proportional to $\nabla \cdot \mathbf{B}$ (Graves et al., 2008):

$$F_{aa} = -\eta(\nabla \cdot \mathbf{B}). \tag{2.87}$$

These correction terms should be zero if the system is physically normal, but since we use cell-centered scheme, this correction improves the nature of the system.

Then we discretize (2.84):

$$\frac{\partial B_a^{i,j,k}}{\partial t}+\frac{(F_{ax}^{i+1/2,j,k}-F_{ax}^{i-1/2,j,k})}{\Delta x}+\frac{(F_{ay}^{i,j+1/2,k}-F_{ay}^{i,j-1/2,k})}{\Delta y} \\ +\frac{(F_{az}^{i,j,k+1/2}-F_{az}^{i,j,k-1/2})}{\Delta z}=0. \tag{2.88}$$

$$\tag{2.89}$$

The flux at the cell surface $(i+1/2,j,k)$ is calculated using the following relations:

$$(\partial_x B_y)_{i+1/2,j,k}=\frac{B_y^{i+1/2,j,k}-B_y^{i-1/2,j,k}}{\Delta x}, \tag{2.90}$$

$$(\partial_y B_x)_{i+1/2,j,k}=\frac{B_x^{i+1,j+1,k}+B_x^{i,j+1,k}-B_x^{i+1,j-1,k}-B_x^{i,j-1,k}}{4\Delta y}, \tag{2.91}$$

$$\eta_{i+1/2,j,k}=\frac{\eta_{i+1,j,k}+\eta_{i,j,k}}{2}. \tag{2.92}$$

The energy flux in (2.67) can be rewritten as:

$$\begin{aligned}[\eta\mathbf{B}\times(\nabla\times\mathbf{B})]_x &= \eta[B_y(\partial_x B_y-\partial_y B_x)-B_z(\partial_z B_x-\partial_x B_z)] \\ &= B_y F_{xy}+B_z F_{xz} \\ &= B_x F_{xx}+B_y F_{xy}+B_z F_{xz} \qquad (F_{xx}=0),\end{aligned} \tag{2.93}$$

and can be discretized in the same way. This discretization gives the second-order accuracy in space.

### Time-integration: Super-Time-Stepping

The timescale of the dissipation of magnetic fields can be far shorter than the dynamical timescale (Machida et al., 2006). To calculate such a fast phenomenon, implicit time-integration methods are often utilized (e.g., Matsumoto (2011) used multigrid method to solve this problem implicitly). However, the Ohmic dissipation requires to solve the complicated system involving multiple variables (magnetic field vector), and it is difficult to apply the implicit method like we do in radiation transfer to such a system because we have to solve a linear system with complicated sparse matrix. Another problem of implicit scheme is its difficulty in extension. If we want to introduce new physical processes like the ambipolar diffusion and Hall effect, we have to reconstruct the matrix. Moreover, we have to adopt more complex technique like Newton-Raphson iterations because they are non-linear processes. Machida et al. (2006), on the other hand, applied simple explicit subcycling scheme to this problem (note that they did not solve (2.66) but $\eta\nabla^2\mathbf{B}$, which is inadequate in reality and does not satisfy the solenoidal constraint (2.51)), but their method requires a number of iterations due to the very short timestep.

In this work, we adopt the Super-Time-Stepping (STS) method proposed by Alexiades et al. (1996) when the timestep for the resistivity part is shorter than the hydrodynamic timestep. In the standard explicit method, we have to take smaller timestep than that given by the Courant-Friedrichs-Lewy (CFL) stability condition in every iteration. STS is constructed based on the simple explicit scheme, but we relax this stability condition; we do not require to satisfy the stability in every step but after a series of integration cycles which consists of $N$ timesteps $\tau_1, \tau_2, ..., \tau_N$. From the optimality properties of the Chebyshev polynomials, it is proved that the maximum time duration $\Delta T = \sum_j \tau_j$ can be stably achieved when we take the following timesteps:

$$\tau_j = \Delta t_{exp}\left[(-1+\nu)\cos\left(\frac{2j-1}{N}\frac{\pi}{2}\right)+1+\nu\right]^{-1}, \tag{2.94}$$

$$\Delta T = \sum_j^N \tau_j = \Delta t_{exp}\frac{N}{2\sqrt{\nu}}\left[\frac{(1+\sqrt{\nu})^{2N}-(1-\sqrt{\nu})^{2N}}{(1+\sqrt{\nu})^{2N}+(1-\sqrt{\nu})^{2N}}\right], \tag{2.95}$$

where $\Delta t_{exp}$ is the explicit timestep smaller than the CFL timestep and $\nu$ is a small positive parameter which controls the stability and efficiency of the scheme. All we need to do is changing the timesteps in the standard explicit scheme and we do not need any modification of the time-integration scheme and discretization. In the limit of $\nu \to 0$, (2.95) yields $\Delta T \to N^2\Delta t_{exp}$ while the standard explicit scheme of $N$ step gives $\Delta T = N\Delta t_{exp}$. This means that STS can be $N$ times faster than the explicit scheme at most. Smaller $\nu$ gives better acceleration but STS may give unphysical results if it is too small. The optimal choice of $\nu$ (and $N$) depends on the problem, but typically $\nu \sim 0.01$ seems to be good for parabolic problems. From (2.95), we can estimate the optimal $N$ for given $\nu$. From Figure 2.4, we can see that the maximum acceleration is $0.5/\sqrt{\nu}$ and the most efficient calculation is realized around $N \sim 0.5/\sqrt{\nu}$. In this work, we adopt $\nu = 0.01$ and $N = 6$. Even in the most time-consuming case (i.e., the magnetic Reynolds number is very low, $n \sim 10^{15}\,\mathrm{cm}^{-3}$), the computational cost is similar to the total of all the other parts (including MHD, self-gravity and radiation transfer). Thus STS achieves sufficient acceleration and is useful in our problems.

In order to estimate the explicit timestep $\Delta t_{exp}$, we rewrite (2.66) as:

$$\begin{aligned}\frac{\partial\mathbf{B}}{\partial t} &= -\eta\nabla\times(\nabla\times\mathbf{B}) - \nabla\eta\times(\nabla\times\mathbf{B})\\ &= \eta\nabla^2\mathbf{B} + (\nabla\eta\cdot\nabla)\mathbf{B}.\end{aligned} \tag{2.96}$$

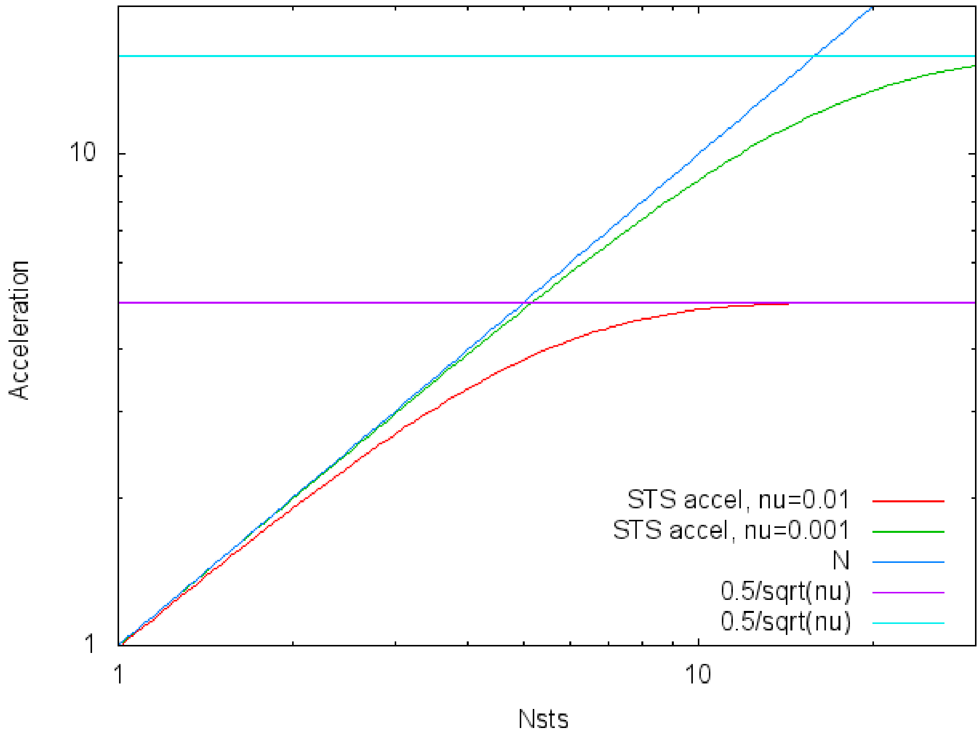

Figure 2.4: The acceleration achieved by STS compared to the explicit scheme for $\nu = 0.01$ and 0.001.

The first term is the normal diffusion term and gives $\Delta t_{exp} < \min(\frac{\Delta x^2}{2\eta})$. The second term can be interpreted as an advection term where $\nabla\eta$ corresponds to the advection velocity. Since the resistivity is a positive value, it yields $\nabla\eta < \max(\frac{\eta}{\Delta x})$. Then the timestep from this term is $\Delta t_{exp} < \min(\frac{\Delta x^2}{\eta})$. Combining these terms, we can estimate the explicit timestep as $\Delta t_{exp} < \min(\frac{\Delta x^2}{3\eta})$, but we conservatively take the timestep $\Delta t_{exp} = 0.15 \min(\frac{\Delta x^2}{\eta})$ including a safety factor.

One of the significant advantages of STS is that it is extremely easy to implement. We do not need the detailed knowledge like the spectral properties of the system. It is very easy to extend and can be also applied for non-linear problems. It can be trivially parallelized with domain decomposition because it is based on the explicit scheme. This scheme is used for ambipolar diffusion (Choi et al., 2009) and Hall effect (O'Sullivan & Downes, 2006) in astrophysical applications (see also Commerçon et al. (2011b)). It is also implemented in a public AMR MHD code PLUTO (Mignone et al., 2007). On the other hand, the best choice of the parameters is not trivial and depends on the problem. Another limitation of STS is the saturation of acceleration; we cannot expect huge acceleration because $\nu$ should not be too small for stability. If we want to solve a problem with extremely short timescale (e.g., radiation), the gain from STS will be insufficient and we should adopt implicit scheme which is unconditionally stable (we should note, however, that the stability of the implicit scheme does not mean that its accuracy (Alexiades et al., 1996; Commerçon et al., 2011b)). It is also worth mentioning that we cannot transcend the (numerical) causality; the information travels only one cell in one step in the explicit scheme. When we want to obtain large acceleration using STS, the propagation speed of the numerical solution tends to be slower than the physical solution.

### 2.3.5 Radiation Transfer

As we mentioned before, the timescale related to radiation can be far shorter than that related to hydrodynamics in star formation simulations (Figure 2.1). The lightspeed $c = 2.99792 \times 10^{10}\,\mathrm{cm\,s^{-1}}$ is far larger than typical fluid velocity in star formation, which is on the order of $1 - 100 \times 10^5\,\mathrm{cm\,s^{-1}}$. Therefore we adopt an implicit time-integration scheme which is stable regardless of the timescale of involved physical processes.

#### Discretization

We adopt the first-order backward Euler method which is simple and stable. We can alternatively use the Cranck-Nicolson scheme which is second-order accurate at almost the same computational costs, but we do not use it because it can suffer from unphysical oscillations. Here we discretize (2.68 – 2.71) in one-dimension (extension to multidimension is straightforward) as follows:

$$\frac{e_{g,i}^{n+1} - e_{g,i}^{n}}{\Delta t} = -c\sigma_P^* \left[ a_r (T_{g,i}^{n+1})^4 - E_{r,i}^{n+1} \right], \tag{2.97}$$

$$\begin{aligned} \frac{E_{r,i}^{n+1} - E_{r,i}^{n}}{\Delta t} - \frac{1}{\Delta x} \left[ \left( \frac{c\lambda}{\sigma_R} \right)^*_{i+\frac{1}{2}} \frac{E_{r,i+1}^{n+1} - E_{r,i}^{n+1}}{\Delta x} - \left( \frac{c\lambda}{\sigma_R} \right)^*_{i-\frac{1}{2}} \frac{E_{r,i}^{n+1} - E_{r,i-1}^{n+1}}{\Delta x} \right] \\ = c\sigma_P^* \left[ a_r (T_{g,i}^{n+1})^4 - E_{r,i}^{n+1} \right] - \mathbb{P}_r^{n+1} : \nabla \mathbf{v}. \end{aligned} \tag{2.98}$$

Superscripts and subscripts denote the indexes of discretized time and space, respectively. To construct a completely implicit scheme, we should in principle use the opacities and the flux limiter at the next time step, i.e., $* = n + 1$. However, it causes computational difficulties because of the strong nonlinearities of the flux limiter and the opacities. Moreover, it requires wider computational stencil in multidimensional cases to estimate the gradient of $E_r$ in the flux limiter, which results in significantly larger computational costs. Therefore we adopt the time-lagged opacities and flux limiter for simplicity and efficiency (Castor, 2004), $* = n$. This may cause loss of time-accuracy of the scheme, but we confirmed that it does not matter in our product runs because the timescale of the evolution of radiation fields is similar to that of hydrodynamic timescale and therefore well resolved. We also use the time-lagged Eddington Tensor $\mathbb{D}_r^n$, which yields the radiation energy tensor $\mathbb{P}_r^{n+1} = \mathbb{D}_r^n E_r^{n+1}$.

There are some ways to evaluate the opacities and flux limiter at the cell interface, $i + \frac{1}{2}$. Here we follow Howell & Greenough (2003) and adopt the surface formula which gives good flux even at the sharp surface of optically thick material like the surface of a first core.

$$\sigma_{R,i+\frac{1}{2}} = \min\left[\frac{\sigma_{R,i} + \sigma_{R,i+1}}{2}, \max\left(\frac{2\sigma_{R,i}\sigma_{R,i+1}}{\sigma_{R,i} + \sigma_{R,i+1}}, \frac{4}{3\Delta x}\right)\right]. \tag{2.99}$$

We evaluate the flux limiter at the cell interface $\lambda(R)_{i+\frac{1}{2}}$ using following equations:

$$R_{i+\frac{1}{2}} = \frac{|(\nabla E_r)_{1+\frac{1}{2}}|}{\sigma_{R,i+\frac{1}{2}} E_{r,i+\frac{1}{2}}}, \tag{2.100}$$

$$E_{r,i+\frac{1}{2}} = \frac{E_{r,i} + E_{r,i+1}}{2}, \tag{2.101}$$

$$(\nabla E_r)_{i+\frac{1}{2}} = \frac{E_{r,i+1} - E_{r,i}}{\Delta x}. \tag{2.102}$$

In three dimension, the radiation energy gradient should be replaced with

$$(\nabla E_r)_{i+\frac{1}{2},j,k} = \begin{pmatrix} \dfrac{E_{r,i+1} - E_{r,i}}{\Delta x} \\ \dfrac{E_{r,i+1,j+1,k} + E_{r,i,j+1,k} - E_{r,i+1,j-1,k} - E_{r,i,j-1,k}}{4\Delta y} \\ \dfrac{E_{r,i+1,j,k+1} + E_{r,i,j,k+1} - E_{r,i+1,j,k-1} - E_{r,i,j,k-1}}{4\Delta z} \end{pmatrix}. \tag{2.103}$$

#### Newton-Raphson Iterations

To solve the non-linear system (2.97) and (2.98), we perform the Newton-Raphson iterations to find the solution (Press et al., 2007). In this method, we search for the zero-point of the residual functions $f_i(\mathbf{X})$. We can find the root iteratively using the following matrix equation based on the Taylor expansion:

$$\sum_{j=1}^{N} \frac{\partial f_i}{\partial x_j} \delta X_j = -f_i(\mathbf{X}) \tag{2.104}$$

In our system, $\mathbf{X}$ is the vector of the gas and radiation energies in all the cells: $\mathbf{X} = (e_{g,1}, ..., e_{g,i}, e_{g,i+1}, ..., E_{r,1}, ..., E_{r,i}, E_{r,i+1}, ...)^T$. The residual functions are given as follows:

$$
\begin{aligned}
f_g^i &= e_{g,i}^{n+1} - e_{g,i}^{n} + \Delta t c \sigma_P^n \left[ a_r \left\{ T_g(\rho_i, e_{g,i}^{n+1}) \right\}^4 - E_{r,i}^{n+1} \right], \qquad (2.105)\\
f_r^i &= E_{r,i}^{n+1} - E_{r,i}^{n} + \Delta t \Bigg[ \frac{1}{\Delta x} \left\{ \left( \frac{c\lambda}{\sigma_R} \right)_{i+\frac{1}{2}}^{n} \frac{E_{r,i+1}^{n+1} - E_{r,i}^{n+1}}{\Delta x} - \left( \frac{c\lambda}{\sigma_R} \right)_{i-\frac{1}{2}}^{n} \frac{E_{r,i}^{n+1} - E_{r,i-1}^{n+1}}{\Delta x} \right\} \\
&\quad - c\sigma_P^n \left[ a_r \left\{ T_g(\rho_i, e_{g,i}^{n+1}) \right\}^4 - E_{r,i}^{n+1} \right] + \left( \mathbb{D}_r^n : \nabla \mathbf{v} \right) E_r^{n+1} \Bigg]. \qquad (2.106)
\end{aligned}
$$

We can rewrite (2.104) explicitly:

$$
\begin{aligned}
&\frac{\partial f_i^g}{\partial e_{g,i}^{n+1}} \delta e_{g,i}^{n+1} + \frac{\partial f_i^g}{\partial E_{r,i}^{n+1}} \delta E_{r,i}^{n+1} = -f_i^g, \qquad (2.107)\\
&\frac{\partial f_i^r}{\partial e_{g,i}^{n+1}} \delta e_{g,i}^{n+1} + \frac{\partial f_i^r}{\partial E_{r,i}^{n+1}} \delta E_{r,i}^{n+1} + \frac{\partial f_i^r}{\partial E_{r,i+1}^{n+1}} \delta E_{r,i+1}^{n+1} + \frac{\partial f_i^r}{\partial E_{r,i-1}^{n+1}} \delta E_{r,i-1}^{n+1} = -f_i^r. \qquad (2.108)
\end{aligned}
$$

By substituting (2.107) into (2.108), we can eliminate the equation related to gas energy (Hayes et al., 2006) (this procedure corresponds to performing partial LU decomposition analytically). Then we obtain the matrix equation:

$$
\begin{aligned}
&\left( \frac{\partial f_i^r}{\partial E_{r,i}^{n+1}} - \frac{\partial f_i^r}{\partial e_{g,i}^{n+1}} \frac{\partial f_i^g}{\partial E_{r,i}^{n+1}} \Bigg/ \frac{\partial f_i^g}{\partial e_{g,i}^{n+1}} \right) \delta E_{r,i}^{n+1} + \frac{\partial f_i^r}{\partial E_{r,i+1}^{n+1}} \delta E_{r,i+1}^{n+1} + \frac{\partial f_i^r}{\partial E_{r,i-1}^{n+1}} \delta E_{r,i-1}^{n+1} \\
&\qquad = \frac{\partial f_i^r}{\partial e_{g,i}^{n+1}} \Bigg/ \frac{\partial f_i^g}{\partial e_{g,i}^{n+1}} f_i^g - f_i^r. \qquad (2.109)
\end{aligned}
$$

The derivatives are given as follows:

$$
\begin{aligned}
\frac{\partial f_i^g}{\partial e_{g,i}^{n+1}} &= 1 + 4\Delta t\, c\sigma_P a_r [T_g(\rho_i, e_{g,i}^{n+1})]^3 \frac{\partial T_g}{\partial e_g}(\rho_i, e_{g,i}^{n+1}), \qquad (2.110)\\
\frac{\partial f_i^g}{\partial E_{r,i}^{n+1}} &= -\Delta t\, c\sigma_P, \qquad (2.111)\\
\frac{\partial f_i^r}{\partial e_{g,i}^{n+1}} &= -4\Delta t\, c\sigma_P a_r [T_g(\rho_i, e_{g,i}^{n+1})]^3 \frac{\partial T_g}{\partial e_g}(\rho_i, e_{g,i}^{n+1}), \qquad (2.112)\\
\frac{\partial f_i^r}{\partial E_{r,i}^{n+1}} &= 1 + \Delta t \left[ c\sigma_P + \mathbb{D}_r^n : \nabla \mathbf{v} - \frac{c}{\Delta x^2} \left\{ \left( \frac{\lambda}{\sigma_R} \right)_{i+\frac{1}{2}}^{n} + \left( \frac{\lambda}{\sigma_R} \right)_{i-\frac{1}{2}}^{n} \right\} \right], \qquad (2.113)\\
\frac{\partial f_i^r}{\partial E_{r,i\pm 1}^{n+1}} &= \frac{c\Delta t}{\Delta x^2} \left( \frac{\lambda}{\sigma_R} \right)_{i\pm\frac{1}{2}}^{n}. \qquad (2.114)
\end{aligned}
$$

$T_g(\rho, e_g)$ and $\frac{\partial T_g}{\partial e_g}(\rho, e_g)$ are given from the tabulated EOS. Note that this Jacobi matrix is symmetric. We can obtain the solution by updating $E_{r,i}$ and $e_{g,i}$ using $\delta E_{r,i}$ and $\delta e_{g,i}$ calculated from (2.109) and (2.107) until $f_i$ and $\delta \mathbf{X}$ become sufficiently small. As the initial guess for $E_{r,i}^{n+1}$ and $e_{g,i}^{n+1}$, we adopt the solution at the timestep $n$. In our simulations, we use the convergence thresholds like $\max\left(\frac{f_i^g}{e_{g,i}}, \frac{f_i^r}{E_{r,i}}\right) < 5 \times 10^{-4}$ and $\max\left(\frac{\delta e_{g,i}}{e_{g,i}}, \frac{\delta E_{r,i}}{E_{r,i}}\right) < 5 \times 10^{-4}$. If these thresholds are not satisfied after many iterations, we take substeps with shorter timesteps and try again until we obtain the converged solution successfully.

### Linear System Solver

In three dimensional Cartesian coordinate, the Jacobi matrix in (2.109) is a very large sparse seven-diagonal matrix. To solve this large (typically $64^3 = 262144$ cells per grid level) linear system, we need an efficient sparse matrix solver. Fortunately, highly optimized program libraries for such a simple configuration are publicly available. We performed a number of experiments using Lis library[1] which provides many solvers and preconditioners with a single programming interface, and found that the combination of the BiCGStab solver and the incomplete LU decomposition preconditioner without fill-in (ILU(0)) works efficiently and robustly. When we perform product runs on NEC SX-9 vector supercomputer, we use ASL library developed by NEC which provides a highly optimized and vectorized version of ILU(0)-BiCGStab solver.[2]

### Radiation Force

We simply integrate the radiation force terms in Step 5 using the obtained solution in Step 4 because these terms are relatively small, at least in the early phase of low-mass star formation processes.

### Mean Opacities

For the gray radiation transfer, we use the compiled tables of the Rosseland and Planck mean opacities of Semenov et al. (2003)[3], Ferguson et al. (2005)[4] and the Opacity Project (OP) (Seaton et al., 1994)[5]. For dust opacities, we adopt the composite aggregate dust model of normal abundance from Semenov's mean opacity tables unless otherwise mentioned. Though Semenov's tables also contain gas opacities, we adopt

---

[1] http://www.ssisc.org/lis/

[2] ILU type preconditioners are very robust and efficient, significantly reducing the number of iterations required in iterative solvers. However, it does not fit parallelization because of the dependencies between the operations (note that CG type solvers can be easily parallelized). Therefore, although it is a good algorithm for supercomputers with high single node performance, its scalability is problematic for massive parallel architectures. Unfortunately, we have no conclusive solution for this problem now. Continuous effort on constructing such efficient and robust parallel solvers is required.

[3] http://www.mpia.de/homes/henning/Dust_opacities/Opacities/opacities.html

[4] http://webs.wichita.edu/physics/opacity/

[5] http://cdsweb.u-strasbg.fr/topbase/TheOP.html

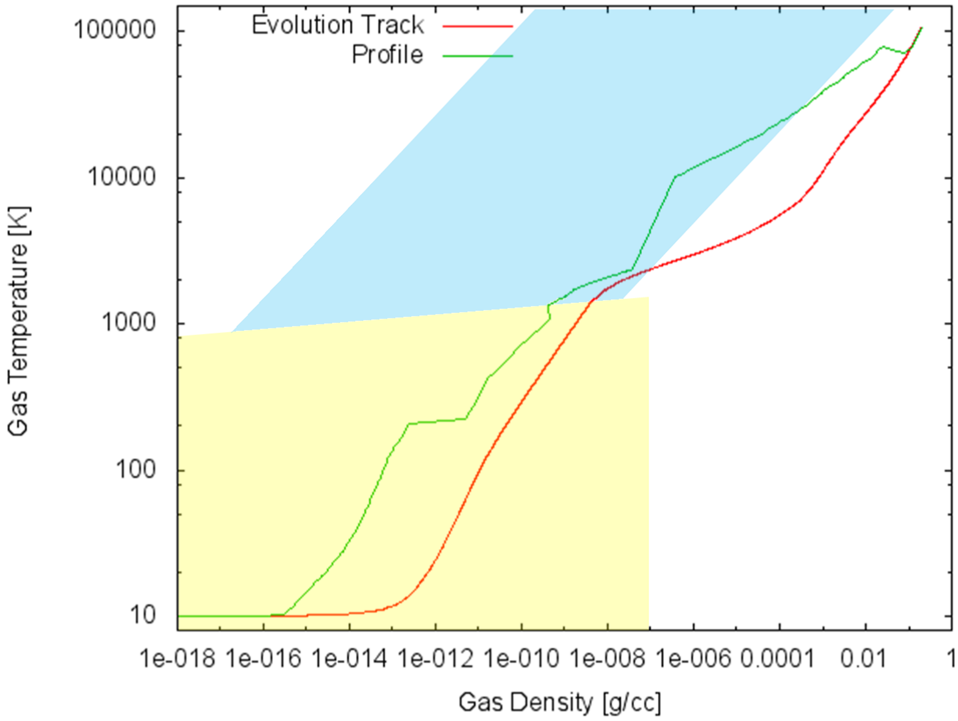

Figure 2.5: The blue shaded region is covered by gas opacity tables (Ferguson et al., 2005; Seaton et al., 1994) and the yellow region is covered by dust opacity tables (Semenov et al., 2003). The border line between blue and yellow corresponds to the dust evaporation temperature. The red line represents the typical evolution track of the central gas element in the spherical protostellar collapse and the green line does the profile at the end of the simulation.

the gas opacities of Ferguson et al. (2005) and Seaton et al. (1994) because Semenov's Planck mean opacity seems to be significantly lower than other opacity tables (Ferguson et al., 2005; Seaton et al., 1994) where atomic and molecular lines dominate the opacity sources. Therefore we combine these tables at the temperature where all the dust components evaporate. The dust evaporation temperature (it weakly depends on the gas density, but in the typical density region, $T \sim 1400 - 1500\,\mathrm{K}$) is given in Semenov's opacity calculation code. We use Ferguson et al. (2005) in low temperature region ($\log T < 4.5$) and OP in high temperature region ($4.5 < \log T < 6$). We tabulate these tables as functions of $(\rho, T)$ and use them with bi-log-linear interpolation.

Unfortunately, the opacity tables do not cover the whole required region. Figure 2.5 shows the coverage of the opacity tables in the $\rho - T$ plane. The typical evolution track of the central gas element and the profile in the spherically symmetric collapse are also plotted. The dust opacities of Semenov et al. (2003) cover $10^{-18} < \rho\,(\mathrm{g\,cm^{-3}}) < 10^{-7}$. OP and Ferguson et al. (2005) cover $-8 < \log R < 1$ where $R = \rho/T_6$ and $T_6 =$

$T\,(\mathrm{K})/10^6$. It is not serious that the very low density region is not covered because that region is extremely optically thin and the details of dust opacities do not matter there. We simply extrapolate the opacities by taking the nearest value at the given temperature. The high density region is far more problematic; we do not have proper opacities for the protostellar core. But actually the thermal evolution in this region is dominated by chemical reactions (dissociation and ionization) and radiation transfer is of less importance there because the gas is highly optically thick. So we dare to extrapolate the tables in the same manner.[6]

We show the combined opacity tables in Figures 2.6 and 2.7 as functions of $\rho$ and $T$. Note that there is quite large uncertainty in opacities, especially due to the dust models such as the structure, composition, size distribution and so on. The thermal evolution and dynamics in star formation remain qualitatively similar even when we change the dust parameters, but the observational properties such as Spectral Energy Distributions (SED) are directly affected by the differences between (monochromatic) opacities.

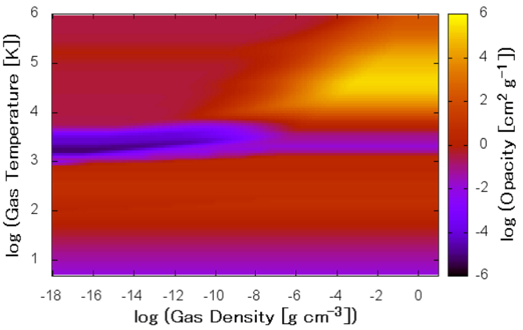

Figure 2.6: The Rosseland mean opacity.

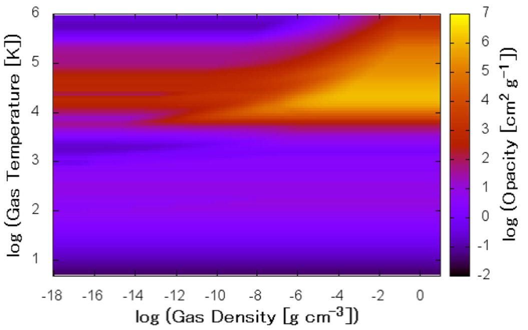

Figure 2.7: The Planck mean opacity.

### 2.3.6 Equation-Of-State

In older version of our code, we used the simple EOS of perfect gas for simplicity, i.e., we assumed the adiabatic index $\gamma$ to be constant throughout simulations, 7/5 which is valid for completely idealized diatomic molecular gas or 5/3 only valid when the gas temperature is very low. However, the adiabatic index is not constant in reality. In star formation, the initial molecular cloud core mainly consists of (literally) hydrogen molecules. In the low temperature region ($T \lesssim 100\,\mathrm{K}$), molecular hydrogen behaves like monoatomic gas, $\gamma \sim 5/3$ because the collisional energy is insufficient to excite

---

[6] We must be careful, however, that this problem becomes more serious when we calculate the evolution of the protostar longer than the Kelvin-Helmholtz timescale before the onset of convection (or deuterium burning). As we can see from Figure 2.5, the earliest phase of the protostar is convectively stable (see also Stahler et al. (1980a,b)) and therefore radiation plays a critical role in heat transfer. More elaborate opacity tables covering wider region are highly demanded.

the rotational degrees of freedom and only translations are excited. When the gas temperature exceeds $T \gtrsim 100\,\mathrm{K}$, the rotations start to be excited and contribute to the heat capacity. Then the adiabatic index decreases, $\gamma \sim 7/5$, close to that of ideal diatomic gas. The adiabatic index is of critical importance in the thermal evolution of the gas, and also in the stability of the gas against the gravitational instability; the stiffer gas (with larger $\gamma$) is more stable gravitationally because it reacts stronger against compression.

The second collapse is driven by the endothermic reaction of hydrogen molecule dissociation. In order to simulate the evolution in the second collapse phase, we need to take the chemical reactions into account. However, it requires quite a large computational cost to solve the network of chemical reactions in every fluid element while solving (radiation) hydrodynamics. Fortunately, because we are mainly interested in dense gas, we can assume that the timescale of chemical reactions is shorter than the dynamical timescale. Therefore we implement the chemical reactions related to major species within the EOS on the assumption of local thermodynamic and chemical equilibrium.

We require some assumptions to calculate the idealized EOS for simplicity:

- The gas is in the local thermodynamic and chemical equilibrium (except for the ortho/para ratio of molecular hydrogen, see below).
- All the atoms and molecules are in the ground state.
- The EOS can be calculated by simple summation of each component and each degree of freedom, i.e., the interactions between components and other non-ideal effects are neglected.
- Only seven major species ($\mathrm{H_2}, \mathrm{H}, \mathrm{H^+}, \mathrm{He}, \mathrm{He^+}, \mathrm{He^{2+}}$ and $\mathrm{e^-}$) are considered and other heavier elements are neglected.

Based on these assumptions, we calculate the EOS using the statistical mechanics theory. Here we also assume that the gas has the solar abundance, $X = 0.7$ and $Y = 0.28$.

### Partition Functions

Here we describe partition functions of each element. The partition function of a species $i$ can be divided into five parts; translation $Z_{\mathrm{tr},i}$, rotation $Z_{\mathrm{rot},i}$, vibration $Z_{\mathrm{vib},i}$, spin $Z_{\mathrm{spin},i}$ and electron excitation $Z_{\mathrm{elec},i}$ (we include contributions from $\mathrm{H_2}$ dissociation and ionization of hydrogen and helium in the electron excitation part):

$$Z_i = V \times Z_{\mathrm{tr},i} \times Z_{\mathrm{rot},i} \times Z_{\mathrm{vib},i} \times Z_{\mathrm{spin},i} \times Z_{\mathrm{elec},i}, \tag{2.115}$$

where V is the volume. We calculate these partition functions by the standard procedure. In the following descriptions, $m_i$ denotes the mass of $i$-species, $h$ the Planck constant and $k$ the Boltzmann constant, respectively. The functions not explicitly described are unity.

Molecular hydrogen:

$$Z_{\mathrm{tr,H_2}} = \frac{(2\pi m_{\mathrm{H_2}} kT)^{3/2}}{h^3}, \tag{2.116}$$

$$Z_{\mathrm{rot,H_2}} = \left(Z^{\mathrm{even}}_{\mathrm{rot,H_2}}\right)^{\frac{1}{4}} \left[3 Z^{\mathrm{odd}}_{\mathrm{rot,H_2}} \exp\left(\frac{\theta_{\mathrm{rot}}}{T}\right)\right]^{\frac{3}{4}}, \tag{2.117}$$

$$Z^{\mathrm{even}}_{\mathrm{rot,H_2}} = \sum_{j=0,2,4,\ldots} (2j+1) \exp\left[-\frac{j(j+1)\theta_{\mathrm{rot}}}{2T}\right], \tag{2.118}$$

$$Z^{\mathrm{odd}}_{\mathrm{rot,H_2}} = \sum_{j=1,3,5,\ldots} (2j+1) \exp\left[-\frac{j(j+1)\theta_{\mathrm{rot}}}{2T}\right], \tag{2.119}$$

$$Z_{\mathrm{vib,H_2}} = \frac{1}{2\sinh\left(\theta_{\mathrm{vib}}/2T\right)}, \tag{2.120}$$

$$Z_{\mathrm{spin,H_2}} = \left(2 \cdot \frac{1}{2} + 1\right)^2 = 4, \tag{2.121}$$

$$Z_{\mathrm{elec,H_2}} = 2, \tag{2.122}$$

where $\theta_{\mathrm{rot}} = 170.64\,\mathrm{K}$ is the excitation temperature of rotation and $\theta_{\mathrm{vib}} = 5984.48\,\mathrm{K}$ is that of vibration. Molecular hydrogen is known to have two forms: orthohydrogen with aligned nuclear spins and odd rotational states, and parahydrogen with antiparallel nuclear spins and even rotational states. Here we assumed the ratio of orthohydrogen to parahydrogen is 3:1. This ratio has significant impact on the dynamics of collapsing molecular cloud cores in the relatively low temperature region because thermodynamic properties related to rotation of molecular hydrogen depend on the nuclear spins and rotational states. When $H_2$ is formed on the dust grains, the ortho:para ratio of molecular hydrogen is supposed to be close to 3:1 which comes from the spin degeneracy because the energy released in $H_2$ formation is sufficiently large ($\sim 1.5\,\mathrm{eV}$). In low temperature gas, orthohydrogen gradually decays into parahydrogen because orthohydrogen is more unstable than parahydrogen, but there will be supply of fresh $H_2$ from the grains. Unfortunately this ratio in star forming regions is quite unclear due to observational difficulties. Some observations of interstellar dark clouds suggest that the ratio is considerably far from the equilibrium value even in the cold environment; Pagani et al. (2011) proposed that the ortho/para ratio is larger than 0.1. On the other hand, Dislaire et al. (2011) claimed that the ratio is quite small, $\sim 10^{-3}$. In this work, we calculate the EOS using the ortho/para ratio of 3:1. This assumption helps us interpret our simulation results because the adiabatic index $\gamma$ decreases monotonically

(Boley et al., 2007) and also compare our results with recent simulations performed by Bate (2010, 2011a) (but Stamatellos & Whitworth (2009) assumed the equilibrium ratio).

Atomic hydrogen:

$$Z_{\mathrm{tr,H}} = \frac{(2\pi m_{\mathrm{H}} kT)^{3/2}}{h^3}, \tag{2.123}$$

$$Z_{\mathrm{spin,H}} = 2 \cdot \frac{1}{2} + 1 = 2, \tag{2.124}$$

$$Z_{\mathrm{elec,H}} = 2 \exp\left(-\frac{\chi_{\mathrm{dis}}}{2kT}\right), \tag{2.125}$$

where $\chi_{\mathrm{dis}} = 7.17 \times 10^{-12}$ erg is the dissociation energy of $H_2$ (Liu et al., 2009).

Ionized hydrogen:

$$Z_{\mathrm{tr,H^+}} = \frac{(2\pi m_{\mathrm{H^+}} kT)^{3/2}}{h^3}, \tag{2.126}$$

$$Z_{\mathrm{spin,H^+}} = 2 \cdot \frac{1}{2} + 1 = 2, \tag{2.127}$$

$$Z_{\mathrm{elec,H^+}} = 2 \exp\left(-\frac{\chi_{\mathrm{dis}} + 2\chi_{\mathrm{ion}}}{2kT}\right), \tag{2.128}$$

where $\chi_{\mathrm{ion}} = 2.18 \times 10^{-11}$ erg is the ionization energy of atomic hydrogen.

Helium:

$$Z_{\mathrm{tr,He}} = \frac{(2\pi m_{\mathrm{He}} kT)^{3/2}}{h^3}, \tag{2.129}$$

$$Z_{\mathrm{tr,He^+}} = \frac{(2\pi m_{\mathrm{He^+}} kT)^{3/2}}{h^3}, \tag{2.130}$$

$$Z_{\mathrm{elec,He^+}} = \exp\left(-\frac{\chi_{\mathrm{He,1}}}{kT}\right), \tag{2.131}$$

$$Z_{\mathrm{tr,He^{2+}}} = \frac{(2\pi m_{\mathrm{He^{2+}}} kT)^{3/2}}{h^3}, \tag{2.132}$$

$$Z_{\mathrm{elec,He^{2+}}} = \exp\left(-\frac{\chi_{\mathrm{He,1}} + \chi_{\mathrm{He,2}}}{kT}\right). \tag{2.133}$$

where $\chi_{\mathrm{He,1}} = 3.94 \times 10^{-11}$ erg and $\chi_{\mathrm{He,2}} = 8.72 \times 10^{-11}$ erg are the first and second ionization energies of helium.

Electron:

$$Z_{\mathrm{tr,e}} = \frac{(2\pi m_{\mathrm{e}} kT)^{3/2}}{h^3}, \tag{2.134}$$

$$Z_{\mathrm{spin,e}} = 2 \cdot \frac{1}{2} + 1 = 2. \tag{2.135}$$

### Chemical Reactions and Number Densities

The grand canonical partition function of each species is defined as:

$$\Theta_i(\mu_i, V, T) = \sum_{N_i} \exp\left(\frac{N_i \mu_i}{kT}\right) \frac{Z_i^{N_i}}{N_i!} = \exp\left[Z_i \exp\left(\frac{\mu_i}{kT}\right)\right], \tag{2.136}$$

where $\mu_i$ is the chemical potential of $i$-species and $N_i$ is the total number of $i$-species. The grand potential can be derived from the grand canonical partition function:

$$\Omega_i(\mu_i, V, T) = -kT \log \Theta_i = -kT Z_i \exp\left(\frac{\mu_i}{kT}\right). \tag{2.137}$$

The total grand potential can be calculated from the summation of each component:

$$\Omega = \sum_i \Omega_i. \tag{2.138}$$

We calculate required thermodynamic variables from these functions. First, we calculate the number density of each species based on chemical equilibrium. The number density of $i$-species is derived from the partial derivative of the grand potential with respect to $\mu_i$:

$$n_i = \frac{1}{V}\left(\frac{\partial \Omega}{\partial \mu_i}\right)_{\mu_j, V, T} = z_i \exp\left(\frac{\mu_i}{kT}\right), \tag{2.139}$$

where $z_i = Z_i/V$. This relation yields:

$$\mu_i = kT \log \frac{n_i}{z_i}. \tag{2.140}$$

We consider (only) four reactions between the seven species dominant in relatively dense (but not too dense) gas for star formation problems:

$$\mathrm{H_2} \longleftrightarrow \mathrm{2H}, \tag{2.141}$$

$$\mathrm{H} \longleftrightarrow \mathrm{H^+} + \mathrm{e^-}, \tag{2.142}$$

$$\mathrm{He} \longleftrightarrow \mathrm{He^+} + \mathrm{e^-}, \tag{2.143}$$

$$\mathrm{He^+} \longleftrightarrow \mathrm{He^{2+}} + \mathrm{e^-}. \tag{2.144}$$

Then the number densities can be calculated from the balance between the chemical potentials in these chemical reactions.

$$\mu_{\mathrm{H}_2} = 2\mu_{\mathrm{H}} \Longrightarrow \frac{n_{\mathrm{H}}^2}{n_{\mathrm{H}_2}} = \frac{z_{\mathrm{H}}^2}{z_{\mathrm{H}_2}} = K_{\mathrm{dis}}, \tag{2.145}$$

$$\mu_{\mathrm{H}} = \mu_{\mathrm{H}^+} + \mu_e \Longrightarrow \frac{n_{\mathrm{H}^+} n_e}{n_{\mathrm{H}}} = \frac{z_{\mathrm{H}^+} z_e}{z_{\mathrm{H}}} = K_{\mathrm{ion}}, \tag{2.146}$$

$$\mu_{\mathrm{He}} = \mu_{\mathrm{He}^+} + \mu_e \Longrightarrow \frac{n_{\mathrm{He}^+} n_e}{n_{\mathrm{He}}} = \frac{z_{\mathrm{He}^+} z_e}{z_{\mathrm{He}}} = K_{\mathrm{He},1}, \tag{2.147}$$

$$\mu_{\mathrm{He}^+} = \mu_{\mathrm{He}^{2+}} + \mu_e \Longrightarrow \frac{n_{\mathrm{He}^{2+}} n_e}{n_{\mathrm{He}^+}} = \frac{z_{\mathrm{He}^{2+}} z_e}{z_{\mathrm{He}^+}} = K_{\mathrm{He},2}. \tag{2.148}$$

The RHS term of each equation, $K_*$, can be calculated from the partition functions. We have three additional relations; conservation of the total number density of hydrogen, conservation of the total number density of helium and the charge neutrality:

$$2n_{\mathrm{H}_2} + n_{\mathrm{H}} + n_{\mathrm{H}^+} = n_{\mathrm{tot}}^{\mathrm{H}} \quad \left( = \frac{\rho X}{m_{\mathrm{H}}} \right), \tag{2.149}$$

$$n_{\mathrm{He}} + n_{\mathrm{He}^+} + n_{\mathrm{He}^{2+}} = n_{\mathrm{tot}}^{\mathrm{He}} \quad \left( = \frac{\rho Y}{m_{\mathrm{He}}} \right), \tag{2.150}$$

$$n_{\mathrm{H}^+} + n_{\mathrm{He}^+} + 2n_{\mathrm{He}^{2+}} = n_e. \tag{2.151}$$

We eliminate $n_{\mathrm{H}_2}, n_{\mathrm{H}^+}, n_{\mathrm{He}^+}$ and $n_{\mathrm{He}^{2+}}$ from (2.149 – 2.151) using (2.145 – 2.148):

$$2\frac{n_{\mathrm{H}}^2}{K_{\mathrm{dis}}} + n_{\mathrm{H}} + \frac{n_{\mathrm{H}}}{n_e} K_{\mathrm{ion}} = n_{\mathrm{tot}}^{\mathrm{H}}, \tag{2.152}$$

$$n_{\mathrm{He}} \left( 1 + \frac{K_{\mathrm{He},1}}{n_e} + \frac{K_{\mathrm{He},1} K_{\mathrm{He},2}}{n_e^2} \right) = n_{\mathrm{tot}}^{\mathrm{He}}, \tag{2.153}$$

$$\frac{n_{\mathrm{H}}}{n_e} K_{\mathrm{ion}} + \frac{n_{\mathrm{He}}}{n_e} K_{\mathrm{He},1} + 2\frac{n_{\mathrm{He}}}{n_e^2} K_{\mathrm{He},1} K_{\mathrm{He},2} = n_e. \tag{2.154}$$

By substituting $n_{\mathrm{H}}$ and $n_{\mathrm{He}}$ (we can determine the solution of (2.152) uniquely since all the physical variables are positive) to (2.154), we obtain one non-linear equation of $n_e$:

$$\begin{aligned} f(n_e) = & \frac{2n_e^2 n_{\mathrm{tot}}^{\mathrm{H}} K_{\mathrm{ion}}}{\sqrt{(n_e + K_{\mathrm{ion}})^2 + \frac{8}{K_{\mathrm{dis}}} n_{\mathrm{tot}}^{\mathrm{H}} n_e^2} + (n_e + K_{\mathrm{ion}})} \\ & + \frac{K_{\mathrm{He},1} n_e + 2K_{\mathrm{He},1} K_{\mathrm{He},2}}{n_e^2 + K_{\mathrm{He},1} n_e + K_{\mathrm{He},1} K_{\mathrm{He},2}} n_{\mathrm{tot}}^{\mathrm{He}} n_e^2 - n_e^3 = 0. \end{aligned} \tag{2.155}$$

Then we solve this equation numerically using the bi-section method. Here $f(n_e)$ is monotonic in the region where the root should exist and the bi-section method works well (the first term of $f(n_e)$ is already modified to avoid the round-off error). Using the obtained $n_e$, it is straightforward to calculate the number density of each species.

In order to derive thermodynamic variables, the temperature and density derivatives of the number densities are required. For this purpose, we take (logarithmic) differentiation of (2.145 – 2.151), then they yield:

$$\begin{pmatrix} 1 & -2 & 0 & 0 & 0 & 0 & 0 \\ 2n_{\mathrm{H}_2} & n_{\mathrm{H}} & n_{\mathrm{H}^+} & 0 & 0 & 0 & 0 \\ 0 & -1 & 1 & 1 & 0 & 0 & 0 \\ 0 & 0 & n_{\mathrm{H}^+} & -n_e & 0 & n_{\mathrm{He}^+} & 2n_{\mathrm{He}^{2+}} \\ 0 & 0 & 0 & 1 & -1 & 1 & 0 \\ 0 & 0 & 0 & 1 & 0 & -1 & 1 \\ 0 & 0 & 0 & 0 & n_{\mathrm{He}} & n_{\mathrm{He}^+} & n_{\mathrm{He}^{2+}} \end{pmatrix} \begin{pmatrix} d\ln n_{\mathrm{H}_2} \\ d\ln n_{\mathrm{H}} \\ d\ln n_{\mathrm{H}^+} \\ d\ln n_{\mathrm{He}} \\ d\ln n_{\mathrm{He}^+} \\ d\ln n_{\mathrm{He}^{2+}} \\ d\ln n_e \end{pmatrix} = \begin{pmatrix} -d\ln K_{\mathrm{dis}} \\ n_{\mathrm{tot}}^{\mathrm{H}} d\ln n_{\mathrm{tot}}^{\mathrm{H}} \\ d\ln K_{\mathrm{ion}} \\ 0 \\ d\ln K_{\mathrm{He},1} \\ d\ln K_{\mathrm{He},2} \\ n_{\mathrm{tot}}^{\mathrm{He}} d\ln n_{\mathrm{tot}}^{\mathrm{He}} \end{pmatrix} . \tag{2.156}$$

From this matrix equation we can numerically derive the required derivatives such as $\left(\frac{\partial \ln n_i}{\partial \ln T}\right)_\rho$ and $\left(\frac{\partial \ln n_i}{\partial \ln \rho}\right)_T$. For $\left(\frac{\partial \ln n_i}{\partial \ln T}\right)_\rho$ the RHS vector becomes

$$\begin{pmatrix} \frac{d\ln z_{\mathrm{H}_2}}{d\ln T} - 2\frac{d\ln z_{\mathrm{H}}}{d\ln T} \\ 0 \\ \frac{d\ln z_{\mathrm{H}^+}}{d\ln T} + \frac{d\ln z_e}{d\ln T} - \frac{d\ln z_{\mathrm{H}}}{d\ln T} \\ 0 \\ \frac{d\ln z_{\mathrm{He}^+}}{d\ln T} + \frac{d\ln z_e}{d\ln T} - \frac{d\ln z_{\mathrm{He}}}{d\ln T} \\ \frac{d\ln z_{\mathrm{He}^{2+}}}{d\ln T} + \frac{d\ln z_e}{d\ln T} - \frac{d\ln z_{\mathrm{He}^+}}{d\ln T} \\ 0 \end{pmatrix} , \tag{2.157}$$

and for $\left(\frac{\partial \ln n_i}{\partial \ln \rho}\right)_T$

$$\begin{pmatrix} 0 \\ n_{\mathrm{tot}}^{\mathrm{H}} \\ 0 \\ 0 \\ 0 \\ 0 \\ n_{\mathrm{tot}}^{\mathrm{He}} \end{pmatrix} . \tag{2.158}$$

The temperature derivatives of the partition functions can be calculated analytically.

The total number density is

$$n = \sum_i n_i, \tag{2.159}$$

and its derivatives are

$$\left(\frac{\partial \ln n}{\partial \ln T}\right)_\rho \equiv n_T = \sum_i \frac{n_i}{n}\left(\frac{\partial \ln n_i}{\partial \ln T}\right)_\rho, \tag{2.160}$$

$$\left(\frac{\partial \ln n}{\partial \ln \rho}\right)_T \equiv n_\rho = \sum_i \frac{n_i}{n}\left(\frac{\partial \ln n_i}{\partial \ln \rho}\right)_T. \tag{2.161}$$

**Thermodynamic Variables**

We use the relation valid in ideal gas:

$$P = nkT \quad \left(= \frac{\rho}{\mu m_\mathrm{H}} kT\right), \tag{2.162}$$

where $\mu = \frac{\rho}{n m_\mathrm{H}}$ is the mean molecular weight. The derivatives of the pressure are:

$$\left(\frac{\partial \ln P}{\partial \ln T}\right)_\rho \equiv P_T = 1 + n_T, \tag{2.163}$$

$$\left(\frac{\partial \ln P}{\partial \ln \rho}\right)_T \equiv P_\rho = n_\rho. \tag{2.164}$$

The specific entropy of each species is derived from the grand potential:

$$S_i = -\frac{1}{\rho V}\left(\frac{\partial \Omega_i}{\partial T}\right)_{V,\mu_i} = \frac{k n_i}{\rho}\left(1 + \frac{d \ln z_i}{d \ln T} - \frac{\mu_i}{kT}\right), \tag{2.165}$$

and its derivatives are:

$$\left(\frac{\partial S_i}{\partial T}\right)_\rho = \frac{k n_i}{\rho T}\left[\frac{d^2 \ln z_i}{d \ln T^2} + \left\{1 + \left(\frac{\partial \ln n_i}{\partial \ln T}\right)_\rho\right\}\frac{d \ln z_i}{d \ln T}\right] - \frac{\partial n_i}{\partial T}\frac{\mu_i}{\rho T}, \tag{2.166}$$

$$\left(\frac{\partial S_i}{\partial \rho}\right)_T = \frac{k n_i}{\rho^2}\left[\left\{\left(\frac{\partial \ln n_i}{\partial \ln \rho}\right)_T - 1\right\}\frac{d \ln z_i}{d \ln T} - 1\right] + \left(\frac{n_i}{\rho} - \frac{\partial n_i}{\partial \rho}\right)\frac{\mu_i}{\rho T}. \tag{2.167}$$

The last terms in these derivatives are canceled out by taking summation of species when the chemical reactions are in equilibrium, so we can omit these terms. Then the total entropy and its derivatives are defined as:

$$S = \sum_i S_i, \tag{2.168}$$

$$\left(\frac{\partial S}{\partial T}\right)_\rho \equiv S_T = \sum_i \left(\frac{\partial S_i}{\partial T}\right)_\rho, \tag{2.169}$$

$$\left(\frac{\partial S}{\partial \rho}\right)_T \equiv S_\rho = \sum_i \left(\frac{\partial S_i}{\partial \rho}\right)_T. \tag{2.170}$$

Now we can derive thermodynamic properties we require in radiation hydrodynamic simulations.

The isothermal and adiabatic sound speeds:

$$c_T \equiv \sqrt{\left(\frac{\partial P}{\partial \rho}\right)_T} = \sqrt{\frac{P}{\rho} P_\rho}, \tag{2.171}$$

$$c_S \equiv \sqrt{\left(\frac{\partial P}{\partial \rho}\right)_S} = \sqrt{\frac{P}{\rho} P_\rho - \frac{P}{T}\frac{P_T S_\rho}{S_T}}. \tag{2.172}$$

The adiabatic index:

$$\Gamma = \left(\frac{d \ln P}{d \ln \rho}\right)_S = \frac{\rho}{P} c_S^2. \tag{2.173}$$

The internal energy per volume and its derivative:

$$e_g = \sum_i n_i k T \frac{d \ln z_i}{d \ln T}, \tag{2.174}$$

$$\left(\frac{\partial e_g}{\partial T}\right)_\rho = \rho C_V = \rho T S_T. \tag{2.175}$$

Note that we do not use the relation $e = \rho C_V T$ which is valid only in the completely idealized cases, as Boley et al. (2007) suggested (see also Black & Bodenheimer (1975)).

We tabularize these thermodynamic variables as functions of $(\rho, e_g)$ and $(\rho, T)$ with sufficiently high resolution ($\Delta \log \rho = 0.05$, $\Delta \log e_g = 0.025$ and $\Delta \log T = 0.02$) in $\rho = 10^{-22} - 10\,\mathrm{g\,cm^{-3}}$ and $T = 3 - 10^6\,\mathrm{K}$. We use this EOS table with bi-log-linear interpolation. In Figure 2.8, we show the adiabatic index $\Gamma$.

### Comments on EOS

Our treatment of EOS for hydrogen and helium is valid in relatively low-density regions ranging from interstellar gas to the second collapse phase. However, in very dense region like a deep interior of the protostellar core, non-ideal effects are not negligible: interactions between particles, weak quantum effects in low-temperature but high-density region, pressure ionization of hydrogen, and contributions from other chemical species. Such non-ideal effects will affect the thermodynamics and the dynamics (e.g., the quasi-equilibrium state of the second core may vary). Actually, our EOS results in a serious unphysical behavior in the very high density region ($\rho > 0.1\,\mathrm{g\,cm^{-3}}$) that almost all the hydrogen particles are turned into the molecular form even when the gas temperature is high enough to destruct the hydrogen molecule. This is because of the assumption of the ideal chemical equilibrium, but in reality this assumption is broke

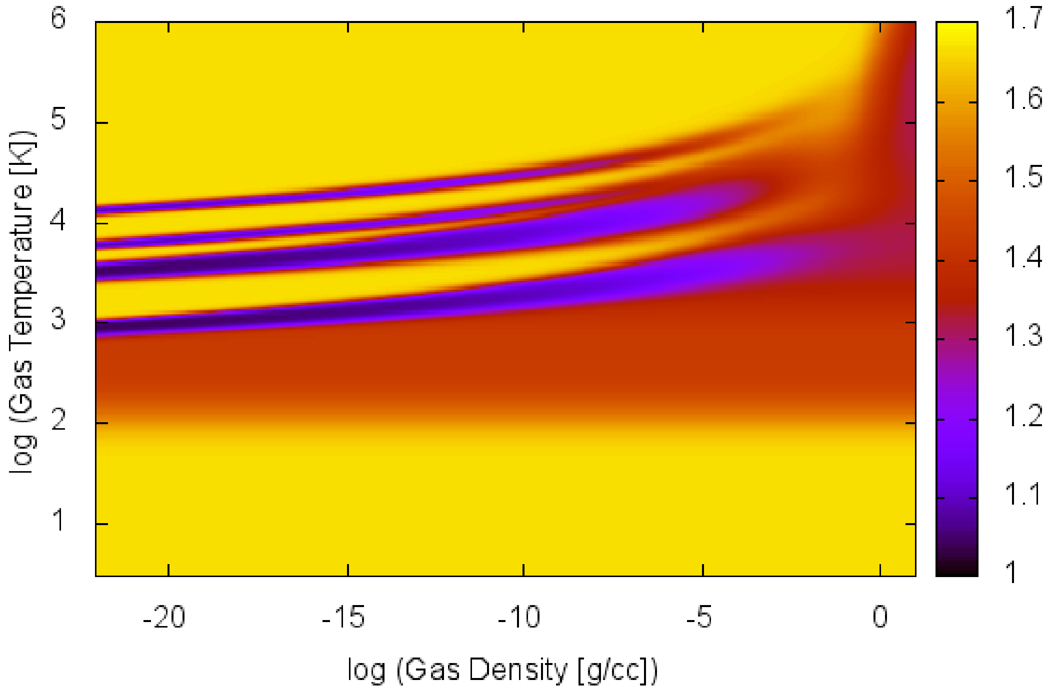

Figure 2.8: The adiabatic index $\Gamma$ in the $\rho - T$ plane. $\Gamma$ decreases around $\log T \sim 2$ due to the excitation of rotation. Four low-$\gamma$ (blue) bands correspond to the endothermic reactions of the dissociation of molecular hydrogen, the ionization of hydrogen, the first and second ionization of helium, from bottom to top.

down there due to the neglected interaction between particles (Saumon et al., 1995). Then our EOS gives the considerably soft adiabatic index $\gamma$ (Figure 2.8) because of the contribution from the vibration transitions of molecular hydrogen. Since this behavior is completely unphysical, our EOS is invalid in such high density regions. Of course we can use (and we tried) the realistic EOS such as SCVH EOS, but the problem is the coverage of the EOS table; it is difficult to connect different tables smoothly. Anyway, we are willing to adopt more realistic EOS when new one is available.

### 2.3.7 Nested-Grid

In order to achieve very large dynamic range required in protostellar collapse simulations, we adopt the three dimensional nested-grid technique (Yorke et al., 1993; Yorke & Kaisig, 1995; Ziegler & Yorke, 1997; Matsumoto & Hanawa, 2003b; Machida et al., 2004). This is a simplified version of adaptive mesh refinement (AMR) technique. Each grid level consists of $N_x \times N_y \times N_z$ cubic cells. The number of the cells in one direction $N_*$ must be a power of 2. The finer grid is placed around the center of the coarser grid self-similarly. The size of a finer cell is half of that of a coarser cell. We number the levels from coarsest to finest: $l = 1(\text{coarsest}), 2, ..., L(\text{finest})$.

### Refinement

In our simulations, we adopt so-called Jeans condition proposed by Truelove et al. (1997) (see also Commerçon et al. (2008)); we generate a finer grid to resolve the minimum Jeans length typically with 16 cells. Physical quantities such as $\rho, \mathbf{v}, e$, and so on in the finer grid are given using linear interpolation of quantities in the coarser grid. We confirmed the convergence of the code for spatial resolution in spherically symmetric collapse and we found that the Jeans condition and our typical resolution ($64^3$ cells per level) are satisfactory. But we should note that this condition cannot be always satisfied since our nested-grid technique can refine only the center of the computational domain. When the Jeans condition is violated, artificial fragmentation may occur. Therefore we must carefully investigate whether the fragmentation is physical or not when it happens in coarse levels.

We do not impose any other refinement condition in current works. Probably we require another independent condition related to magnetic fields or radiation transfer. For example, Krumholz et al. (2009) adopted another criterion based on the radiation energy gradient in their simulations of massive star formation. Federrath et al. (2011) suggested more strict condition that the Jeans length should be resolved with 32 cells in isothermal magnetized turbulence simulations (see also Turk et al. (2011)). It may work well practically, but we should find another criterion related to the magnetic fields. Although the detailed resolution studies are out of scope of this thesis, we will study this point in the near future.

### Time-Stepping

We determine the timestep by the Courant-Friedrich-Levy (CFL) criterion derived for the MHD part. All the grids have this common timestep and are advanced synchronously, although individual (asynchronous) timesteps are generally used in nested-grid and AMR simulations. In usual MHD simulations using individual timesteps, boundary values in the finer level are constructed by time- and spatial-interpolation of the values in the coarser level. This procedure causes no problem in the explicit time integration scheme. However, if we use an implicit time-integrator and a far larger timestep than that determined by the CFL condition for radiation transfer (i.e., $\Delta t \gg \Delta t_{RT} = \Delta x/c$), this time-interpolation is not adequate, at least in principle.

Since we require the boundary conditions at the next timestep in the implicit update, we calculate the coarsest grid $l = 1$ at first and then proceed to finer grid levels. We update all the grid levels in each step described in Section 2.3.1.

### Grid Interaction

For the MHD and resistivity parts, we apply standard procedures to the boundaries between the levels of different resolution. That is, when we update a level $l$, we construct the boundaries from the coarse level $l - 1$ using time and spatial interpolation. For the spatial interpolation, we adopt linear interpolation with a slope limiter to assure the monotonicity. Then we recalculate the flux in the coarser level $l - 1$ using the obtained flux in the finer level $l$, conserving the total flux at the cell surface. After updating all the levels, we transfer the results in the overlapped region from the finer grid to the coarser grid using conserved variables.

For the radiation transfer part, basically we do in a similar way but the radiation transfer part is a bit more tricky. While we solve the coarse grid levels, we need to estimate the temperature and energy of gas and radiation properly in the region overlapped by the finer grids because the information propagates more than one cell even in a single step in the implicit scheme. To relieve the contributions from the artificial thermalization of the internal motion and magnetic fields which occurs in the grid interaction using the conserved variables, we take the temperature average of nearest eight cells in the overlapped finest levels[7] and calculate the gas energy using the gas density and the averaged temperature. To satisfy the consistency between the gas and radiation, we also take the average temperature of nearest eight cells in the finest level for radiation. This procedure violates the conservation of the energy (only) in the overlapped region in the coarse level, but its effects are kept small because we overwrite the overlapped region with the results in the finer levels at the end of every timestep, which satisfy the local conservation laws.

In our implicit scheme, we only consider the interaction between different levels at the level boundaries. In principle, we should solve all the levels consistently treating as a single non-uniform grid because all the cells interact with each other and the information propagates the whole computational domain in the implicit scheme. However, it makes the grid geometry more complicated and requires solving the larger and more complicated matrix than the seven-diagonal matrix. Therefore we adopt our scheme integrating the system in each level for simplicity and efficiency, although it may cause the loss of consistency and accuracy. In our product runs, we confirmed that this treatment only causes minor discrepancies between grid levels in the highly optically-thin

---

[7] The cell center of $l - 1$ grid level is located in the middle of eight cell center points of $l$ (or higher) level grid cells covering the coarse cell.

region. Because we are mainly interested in the evolution of the condensed objects, we can tolerate these errors. We are going to work on improving our radiation transfer solver to hold the consistency in all the grid levels (like the multigrid methods) in the near future.

### 2.3.8 Initial and Boundary Conditions

We use unstable Bonnor-Ebert spheres as the initial conditions of our simulations. We construct a critical Bonnor-Ebert sphere (Bonnor, 1956; Ebert, 1955) and make it unstable by increasing the gas density by a factor of $A_0$. Then we introduce uniform rotation, magnetic fields and $m = 2$ density perturbation, where $m$ is the number of the longitudinal modes. The initial density profile is given as follows:

$$\rho(r) = \rho_0(r)(1 + A_0)\left[1 + A_2 \frac{r^2}{R^2} \cos(2\phi)\right], \tag{2.176}$$

where $\rho_0(r)$ is the density profile of the critical BE sphere, $R$ the radius of the critical BE sphere, $A_2$ the amplitude of $m = 2$ perturbation, respectively. In order to minimize the effect of the initial resolution, we adopt this "regularized" $m = 2$ perturbation which is smooth at the center of the cloud in contrast to Boss & Bodenheimer (1979).

As the outer boundary conditions for magnetohydrodynamics and radiation parts, we set all the cells outside the initial BE sphere to maintain their initial values, mimicking an isolated molecular cloud core confined in a static environment. For the Poisson's equation of self-gravity, we compute the gravitational potential of the isolated system at the boundaries by the multi-pole expansion (Matsumoto & Hanawa, 2003a). Our boundary conditions allow the gas to inflow into the computational domain through the boundaries, but the amount of mass inflow during the simulation is sufficiently smaller than that of the total mass of the initial cloud.

### 2.3.9 Computational Artifices

Basically our scheme described above works well, but we adopt some artifices for more robust calculations. First, we set a floor for temperature; when the gas temperature in a certain cell becomes lower than a threshold ($T_{min} = 7\,\mathrm{K}$), we set the temperature to be $T_{min}$. This situation may happen in the non-magnetized or very weakly magnetized calculations where the gravitational torque dominates the angular momentum transport. In such a case, dense (optically thick) gas with a low entropy in the first core disk sometimes experiences strong adiabatic expansion and the temperature can decrease below the threshold. The very low temperature can cause crash of the simulation. This temperature floor injects additional energy into the cell and violates local energy conservation, but the amount is small and it does not affect the dynamics.

Another artifice we introduce is a symmetrizer to keep spatial symmetry of the system. In our nested-grid simulations, higher resolution grids are placed only around the center of the computational domain. Since we are mainly interested in investigating physics in star formation process in idealized systems, we neglect the turbulence and the perturbations of odd modes, which make the concentrated objects move around the center of the domain. However, the symmetry of the system can spontaneously break due to the inevitable numerical noises and physical instabilities, even when we solve symmetric systems with symmetric initial and boundary conditions. When the non-symmetric modes grow, the concentrated object can move around and get out of the box of the finest resolution. The growth of odd modes in the simulations implies that the symmetry breaking can physically happen in reality, but here we suppress the growth of the non-symmetric perturbations in order to keep the simulations stable. For this purpose, we perform the following operations for all the physical variables and all the cells in every step:

$$f(\mathbf{r}) \Longrightarrow \frac{1}{2}\left[f(\mathbf{r}) + \mathrm{parity}(f) f(-\mathbf{r})\right] \tag{2.177}$$

where $f = (\rho, \mathbf{v}, \mathbf{B}, e_g, \Psi, E_r)$. parity($f$) is the parity function which gives $+1$ or $-1$ depending on the symmetry of the each physical quantity. parity($f$) $= +1$ for $f = \rho, \mathbf{B}, e_g, E_r$ and parity($f$) $= -1$ for $f = \mathbf{v}, \Psi$. Note that this symmetrization is different from assuming mirror symmetry. It allows non-mirror symmetric motions such as precession and convection. It suppresses all the non-point-symmetric modes and allows only point-symmetric perturbations to grow. This can affect the angular momentum transport especially when the gravitational instabilities are dominant where low-$m$ perturbations tend to grow. Therefore, this symmetrizer is optional, but is useful to keep our nested-grid simulations stable while maintaining essential physical processes. We do not use this symmetrization when we study the first core phase, but use it when we simulate the protostellar core because the size of the protostellar core is extremely small compared to that of the initial molecular cloud core.

# Chapter 3

# Protostellar Collapse I: First Cores

## 3.1 Backgrounds

Radiation transfer plays a critical role in star formation and affects the structure of accretion flow and resulting adiabatic cores even in a low-mass regime. However multi-dimensional radiation hydrodynamics (RHD) simulations have been rarely performed due to their high computational costs and difficulties. Therefore, the barotropic approximation, which ignores the radiation transfer and simplifies the thermal evolution of the gas, is widely used in multi-dimensional simulations. Recent advancement of the computers and development of numerical techniques enable us to incorporate radiation transfer into a multi-dimensional magnetohydrodynamics (MHD) simulation within reasonable computational time.

RHD and RMHD simulation codes have been actively developed and some of them are used to study star formation. For example, Yorke & Kaisig (1995) solved radiation hydrodynamics by using the FLD approximation on 2D nested-grids. Whitehouse & Bate (2006) performed SPH simulations with FLD radiation transfer and showed different thermal evolution between models with and without radiation transfer. Orion AMR RHD code developed by Krumholz et al. (2007) is used to study main accretion phase of low-mass star formation (Offner et al., 2009) and high-mass star formation (Krumholz et al., 2009). Price & Bate (2009) examined the role of magnetic fields and radiative transfer on a large (cluster-forming) scale using SPH RMHD simulations. Recently AMR RMHD simulations based on RAMSES were reported by Commerçon et al. (2010), who studied the influence of radiation on fragmentation.

Magnetic fields and self-gravity are also the key physical processes in star formation because they play leading roles in the transport of angular momentum which dominates the global evolution of a cloud. Magnetic braking and outflows driven by magnetic fields efficiently carry the initial angular momentum away from the cloud (Tomisaka, 2000, 2002; Machida et al., 2006). If the cloud rotates very fast, it will fragment through self-gravitational instability (Machida et al., 2008b; Saigo et al., 2008). Since the structure and fate of the core strongly depend on its rotation and the efficiency of angular momentum transport, 3D RMHD simulations with self-gravity are required to understand star formation processes.

Here we present FLD RMHD simulation of protostellar collapse. We show that the overall scenario of the early evolution of low mass stars does not qualitatively change by introducing radiation transfer. The dynamical properties like outflow velocity also remain similar. However, radiation transfer affects the thermal properties of the gas and first core properties such as size, mass and lifetime become quantitatively larger. It is crucial to determine the temperature distribution and luminosity properly for comparison with observations because the emissivity sensitively depends on temperature.

This work is one of the first direct radiation magnetohydrodynamic simulations of protostellar collapse (see also Commerçon et al. (2010)), and already published in The Astrophysical Journal Letters, Volume 714, L58-L63 (Tomida et al., 2010b).

## 3.2 Method and Model

We solve 3D self-gravitational RMHD equations on nested-grids. The details of the code are given in Chapter 2. We assume ideal MHD with no resistivity and adopt Roe's Riemann solver. The EOS of the gas is also assumed to be ideal for simplicity, where the gas mainly consists of hydrogen molecules and the adiabatic index $\gamma$ is set to 7/5 throughout the simulation, following the precedent studies (e.g., Machida et al., 2008a). We assume that the gas and the dust have the common temperature locally.

We take a Bonnor-Ebert sphere of 10K with the central gas density $\rho_c = 1.0 \times 10^{-19}\mathrm{g\,cm^{-3}}$ for the initial condition. The mass and radius of the cloud are $M_c \sim 6.1\ M_\odot$ and $R_c \sim 0.178$ pc, respectively. Initial rotation and magnetic fields are given uniformly along $z$-axis, $\omega = 0.1/t_{ff} \simeq 1.5 \times 10^{-14}\ \mathrm{sec}^{-1}$ and $B_z = 1.1\ \mu$G. The outermost boundary values are fixed to keep their initial values and no geometric symmetry is assumed. The number of grid points in each level of nested-grids is $64^3$. The size of the finer grid is half of the coarser grid, and the finer grid is placed around the center of the simulation box self-similarly. The simulation starts with 5 levels of nested-grids, and finer grids are generated adaptively to resolve the local Jeans length with 32 meshes not to induce artificial fragmentation (Truelove et al., 1997). This is also because insufficient resolution causes the gas entropy to be overestimated near the center of the core. At the end of the simulation 18 levels of nested-grids are generated and finest resolution is $\Delta x \sim 0.009$AU. We stop the simulation when the gas temperature of the central region reaches 2000K at which temperature hydrogen molecule starts to dissociate and the second collapse begins.

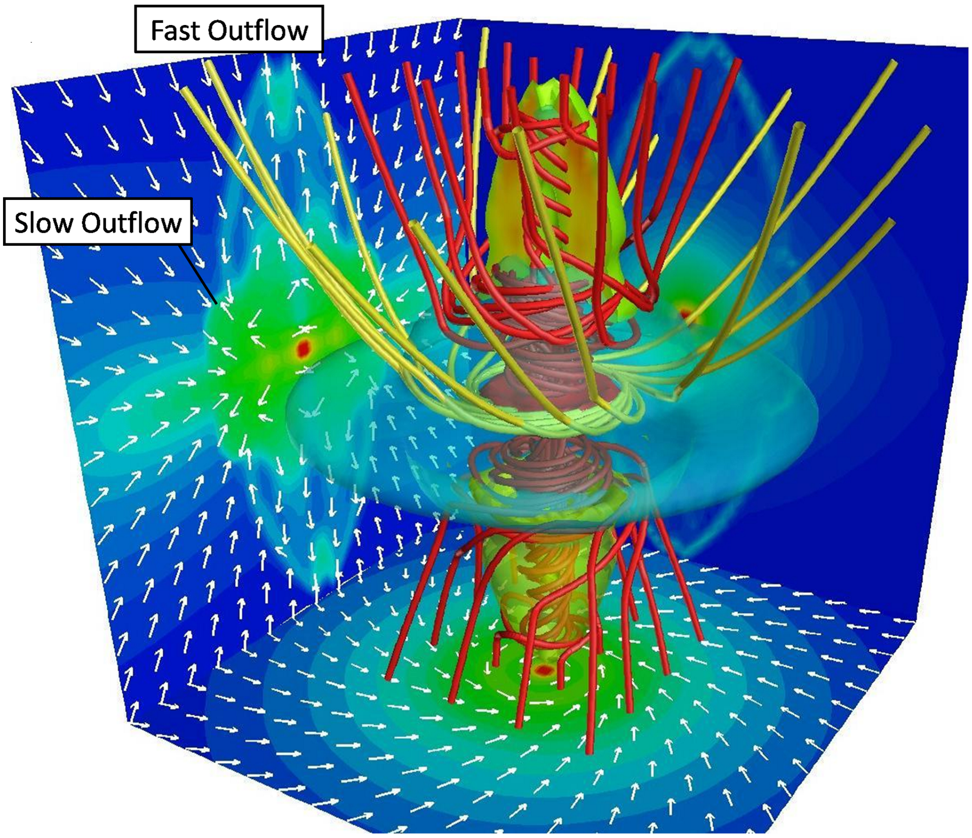

Figure 3.1: 3D structure of the first core and outflow in level $L = 10$. The left and bottom panels are density profiles and the right panel shows the temperature distribution. The cyan surface is a density isosurface. The fast outflowing region ($v_z > 0.3$ km s$^{-1}$) is also visualized with volume rendering. Red and yellow lines are the magnetic field lines.

## 3.3 Results

### 3.3.1 Overview

Figure 3.1 is a typical bird's-eye view of the first adiabatic core and the outflow $\sim$ 500 yrs after the first core formation. There coexist two components of outflow: well collimated fast outflow (associated with red magnetic field lines) and slow outflow with a large opening angle (associated with yellow magnetic field lines). The former is driven by magnetic pressure and the latter by magneto-centrifugal force (Blandford & Payne, 1982). Tomisaka (2002) showed that the magnetic pressure mode typically appears in case of weak magnetic fields, while the magneto-centrifugal mechanism appears in case of relatively strong magnetic fields.

Vertical slices of the outflow scale and core scale are shown in Figure 3.2. Hereafter we discuss only vertical slices since the process occurs nearly axisymmetric. Although

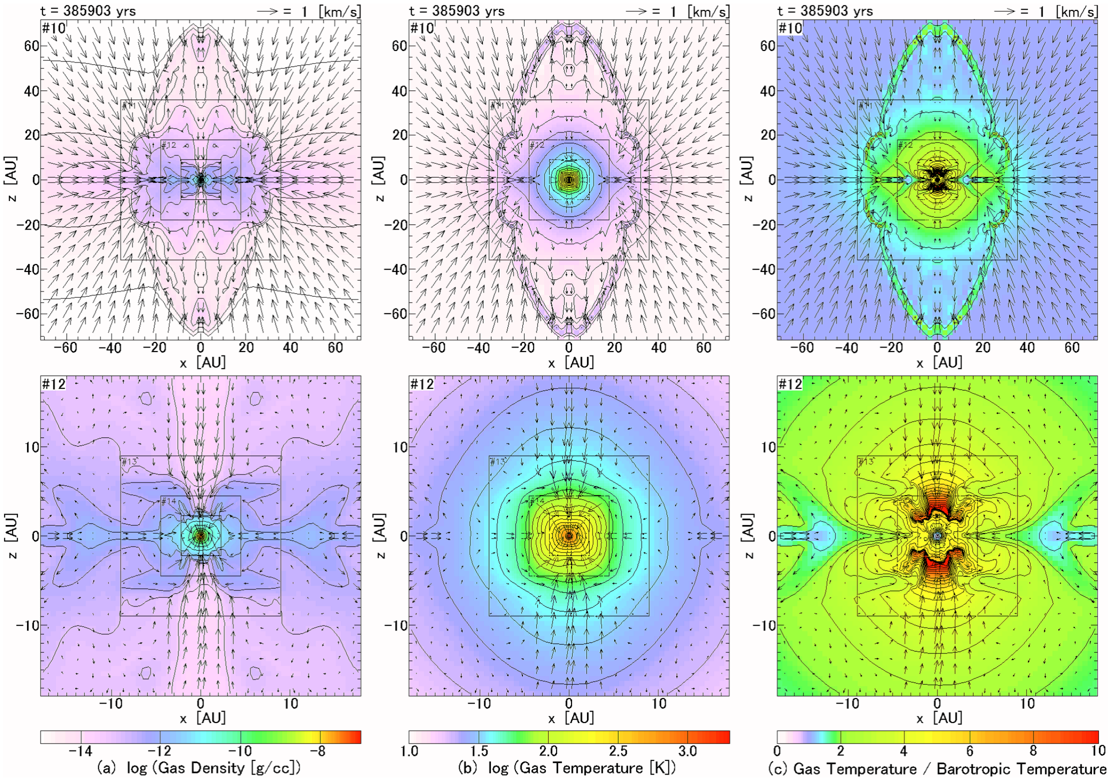

Figure 3.2: Vertical slices of (a) gas density, (b) gas temperature, and (c) gas temperature to the barotropic temperature ratio. The upper row is level $L = 10$ corresponding to a scale of $\sim$ 150AU and the lower is level $L = 12$ corresponding to a scale of $\sim$ 40AU. Projected velocities are overplotted with arrows.

the density distribution shows the complicated structure as a result of MHD processes, the temperature distribution is almost spherically symmetric in the center of the cloud. The gas is heated up by the radiation before it enters the first core. This means that the temperature distribution in the outer region is dominated by the radiation from the central hot region. This picture is considerably different from that of the barotropic approximation used in previous studies, in which the temperature is determined only by the local gas density.

The difference between the RMHD simulation and the barotropic approximation is clearly seen in the right column (c) in Figure 3.2 where the ratio of the gas temperature obtained in RMHD to the barotropic temperature given by the local gas density is plotted. In the RMHD simulation, the gas tends to attain the temperature typically 2-3 times higher than that in barotropic approximation around $\sim$ 10AU from the center, although the two models are very close in the innermost region of the core ( $\lesssim$ 0.1AU). This is consistent with the results of Whitehouse & Bate (2006) and Stamatellos et al. (2007). The difference is most striking just above the shock at the surface of the first core because of pre-shock heating by radiation from the core. The luminosity of this object is higher compared to the result based on the barotropic approximation because the temperature around the photosphere is higher. Here we use the following polytropic relation to evaluate the barotropic temperature:

$$T = 10 \left[ \frac{\max(\rho, \rho_c)}{\rho_c} \right]^{\gamma - 1} \quad \mathrm{K}, \tag{3.1}$$

where $\rho_c = 2.0 \times 10^{-13}\mathrm{g\,cm^{-3}}$ is the critical density and $\gamma = 7/5$ is the adiabatic index of diatomic molecular gas. The parameters used here are chosen to trace the thermal evolution track of the central region in a spherical RHD simulation by Masunaga & Inutsuka (2000).

## 3.3.2 Two-Component Outflow

We visualize the outgoing mass flux and angular momentum flux defined as $|\rho \mathbf{v_p}|$ and $|\rho \mathbf{v_p}|\mathbf{r} \times \mathbf{v_t}||$ where $v_r > 0$ respectively where $\mathbf{v_p}(\mathbf{v_t})$ is poloidal (toroidal) velocity at the early driving phase ($\sim$ 350 yrs after the first core formation) of the outflow in Figure 3.3. In the figure we can recognize two components of outflow driven by different mechanisms: the outer magneto-centrifugal mode and the inner magnetic pressure mode.

The inner magnetic pressure mode has a relatively high velocity $\sim$ 2 km s$^{-1}$ and is well collimated. The front of this outflow becomes hot by shock heating due to its high Mach number. However, the outer, slow outflow has the mass and angular momentum flux, one order of magnitude larger, since the gas in the inner region has a relatively small angular momentum. This trend is enhanced as the outflow evolves. Accordingly we can say that the outer magneto-centrifugal mode is more important for the kinematic structure of the accretion flow as a carrier of angular momentum; however, the fast, inner outflow will stand out more for observation because it travels a long distance and achieves a high temperature.

In Figure 3.2, we can observe warm gas heated up to $T \sim 30$ K by the shock in front of the outflow. This region is clearly seen in the right column (c) since the gas density around the shock is not so high that the gas temperature remains $T \sim 10$ K in the barotropic approximation. On the other hand, the velocities of the outflow in the two models are almost the same, since the location of the outflow driving region is not significantly different. This is because the kinematic structure of the outflow depends mainly on the angular momentum and its interaction with magnetic fields but weakly on the thermal properties of the gas. As we mention in the next subsection, the lifetime of the first core becomes longer in RMHD than in the barotropic approximation. Therefore the outflow travels further in the RMHD simulation during the lifetime.

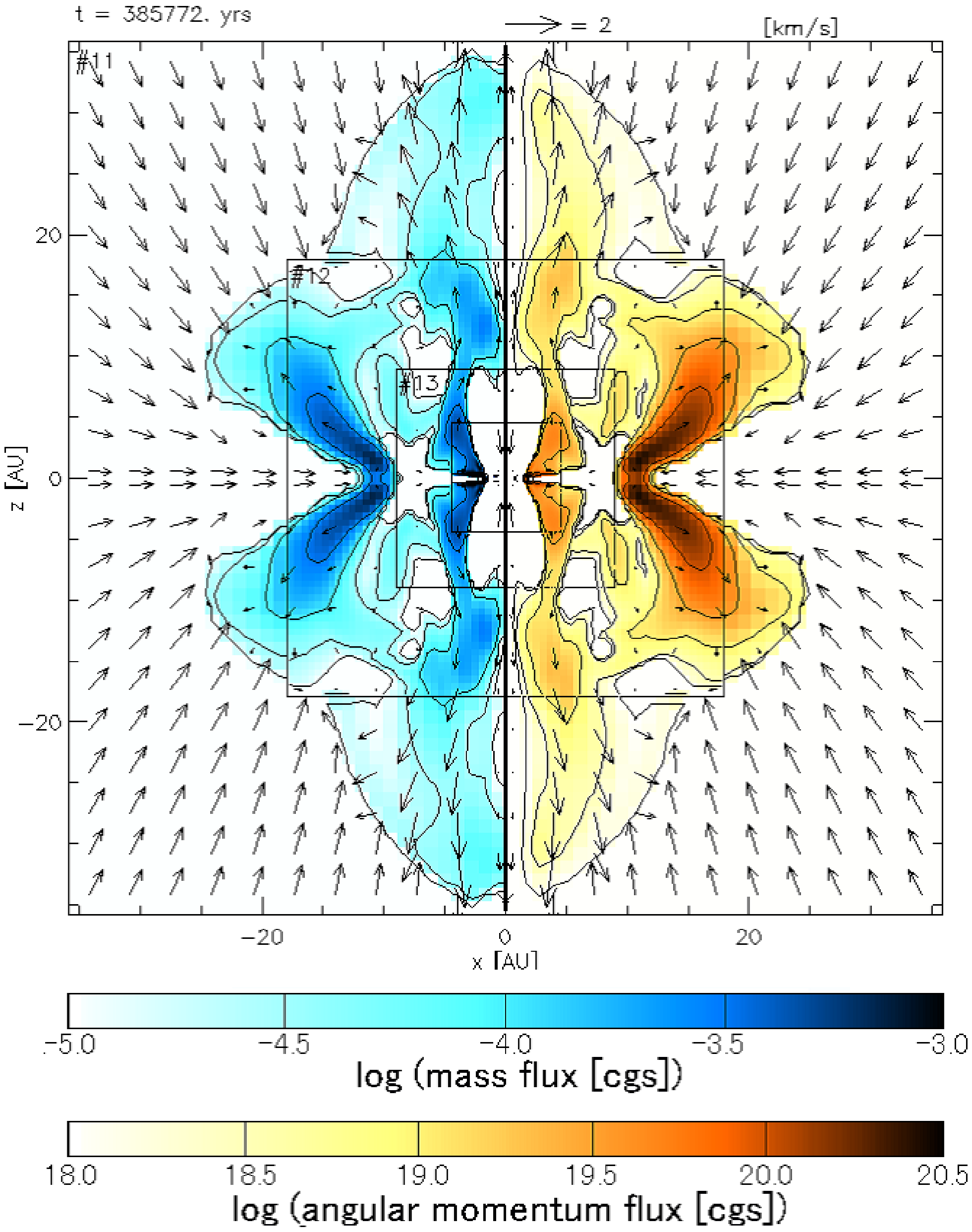

Figure 3.3: Outward mass flux (left) and outward angular momentum flux (right) in level $L = 11$ at the early driving phase of the outflow. Two components of the outflow are clearly observable.

### 3.3.3 Structure of the First Core

We can see a more detailed structure of the collapsing cloud from Figure 3.4 where we plot the distribution of physical quantities at the end of the simulation, just before the second collapse starts ($\sim$ 650 yrs after the first core formation). Panels (a)-(c) show the distribution of physical quantities in the disk midplane and along the rotational axis. At this time the fast outflow reaches $z \sim$ 85 AU. The surface of the core is located at $r \sim$ 35AU in the disk midplane and $z \sim$ 4AU along the rotational axis. This height of the first core is larger than that with the barotropic approximation, which is typically $\sim$ 1AU (Saigo et al., 2008). Along the $z$-axis there is a high entropy radiative precursor outside the core ($z \gtrsim$ 5AU) seen in (b) and (c). The central region within $\sim$ 2AU from the center seems nearly spherically symmetric due to the slow rotation because of efficient magnetic braking.

In order to clarify the impact of radiation transfer on the first core structure and the dynamics, we performed MHD simulation with the barotropic approximation using the Eq.3.1 from the same initial conditions. We compare the results when the central densities are the same. The density cross sections are shown in Figure 3.5. Obviously we have larger outflow and larger first core in the RMHD case. This is because the outer region of the first core attains a higher entropy in the RMHD simulation than in the barotropic approximation. The radius of the first core in the RMHD case is consistent with previous 1D spherically-symmetric RHD simulations (Masunaga et al., 1998; Masunaga & Inutsuka, 2000) . The barotropic approximation only consider compressional heating and radiation cooling for the central gas element, but in reality additional heating and cooling by shock and radiation transfer must be taken into account. The core with a higher entropy can support more mass even with the same central densities; therefore, the first core lives longer in RMHD under the same accretion rate, which is mostly determined by the initial condition. In other words, the first core evolves more slowly in the RMHD case even under the same accretion rate and the same equation-of-state (see also Bate (2011a)). On the other hand, the kinematic properties of the outflow such as velocity and driving region are not so affected because these are mainly determined by interaction between rotation and magnetic fields. We have larger outflow in the RMHD simulation simply because of the extended lifetime of the first core.

The structure of the disk and the behavior of angular momentum transport are visible in panel (d) of Figure 3.4 and Figure 3.2. The profiles of infalling velocity $-v_r$ and rotational velocity $v_\phi$ are plotted in panel (d) of Figure 3.4. The infalling gas initially decelerates at the weak shock near $\sim$ 35AU associated with the first core. There exist two centrifugal barriers, and the outer one near $\sim$ 20AU corresponds to the driving region of the slow and wide outflow driven via the magneto-centrifugal force.

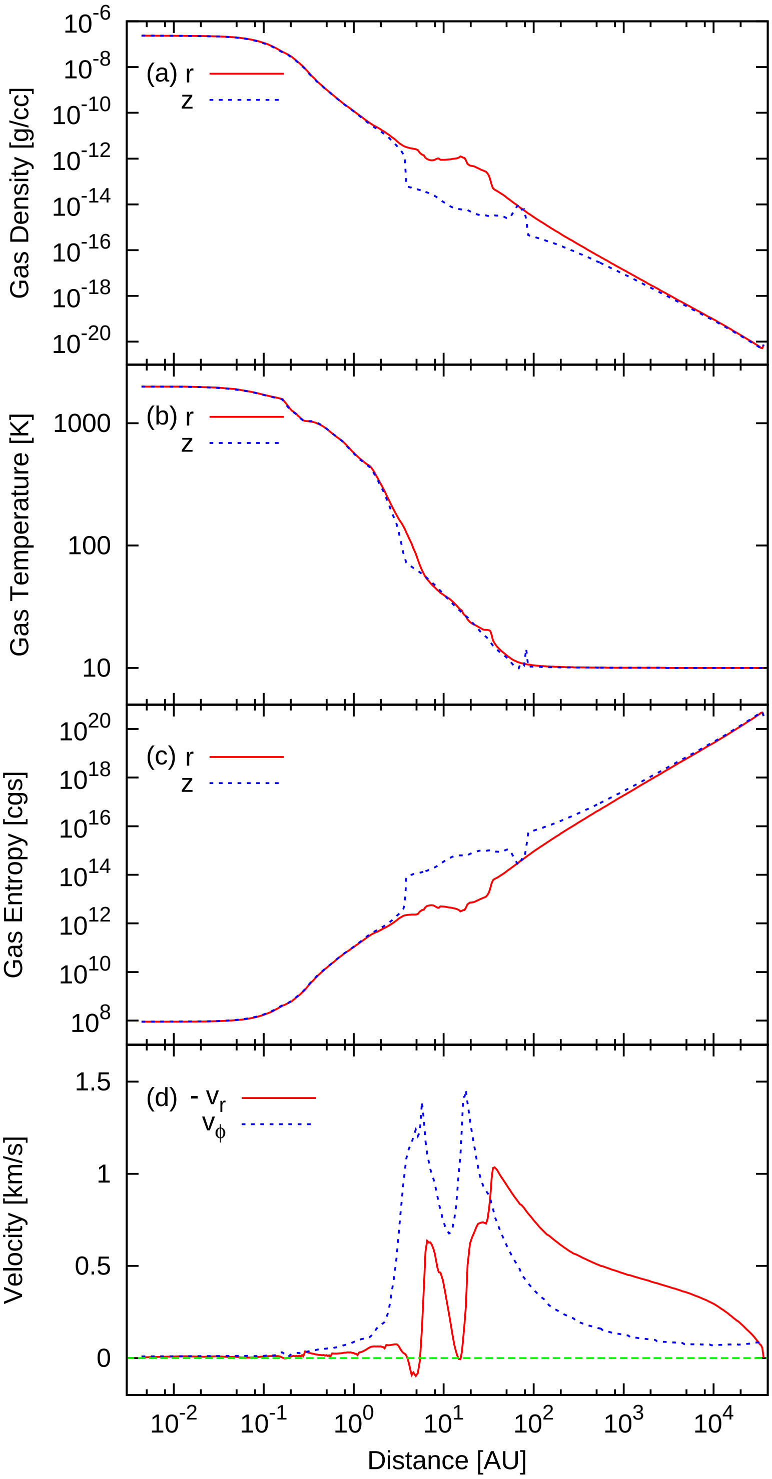

Figure 3.4: Plots of (a) gas density, (b) gas temperature, and (c) gas entropy ($K = P/\rho^{\gamma}$) in the disk midplane ($r$; red solid line) and along the rotational axis ($z$; blue dashed line), and (d) infalling/rotational ($-v_r$; red solid line / $v_\phi$; blue dashed line) velocities in the disk midplane at the end of the simulation.

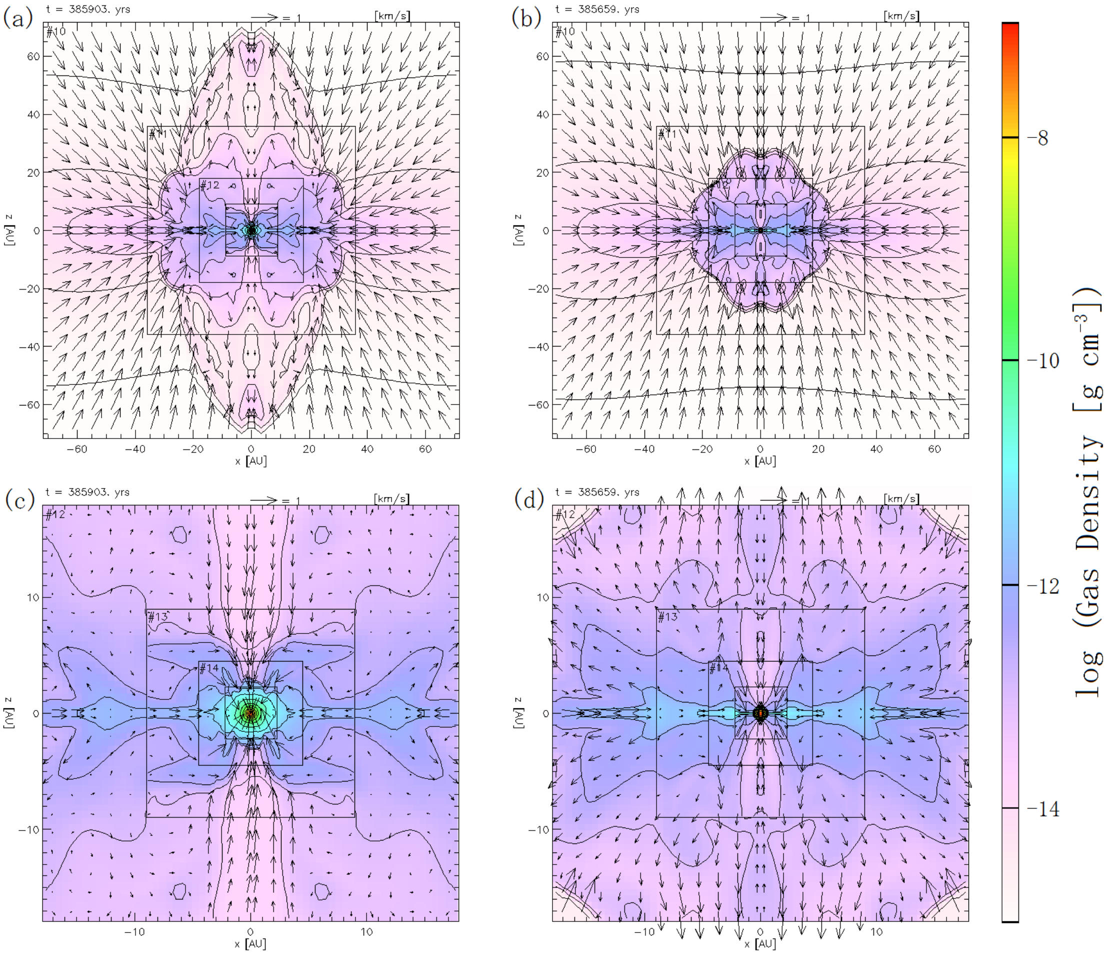

Figure 3.5: Comparison between the RMHD simulation and MHD simulation with the barotropic approximation at the epoch of the same central density. Left column: RMHD (same as Figure 3.2 (a)), Right: barotropic MHD. The upper row is level $L = 10$ corresponding to a scale of $\sim$ 150AU and the lower is level $L = 12$ corresponding to a scale of $\sim$ 40AU.

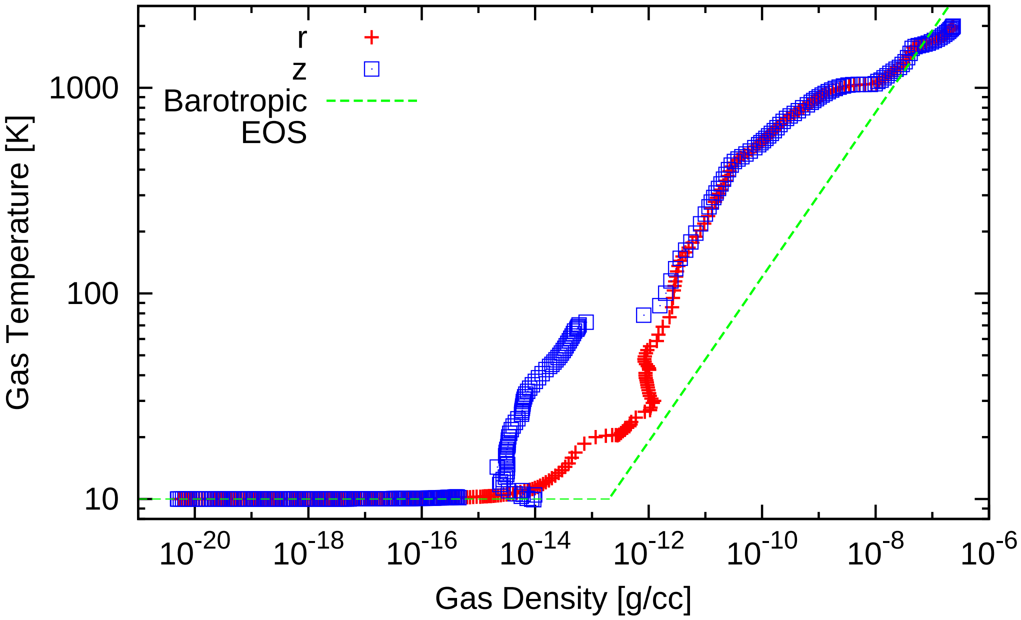

Figure 3.6: Distribution of thermal properties of the gas at just before the second collapse starts ($\sim 650$ yrs after the first core formation) in the $\rho - T$ plane in the disk midplane ($r$; red crosses) and along the rotational axis ($z$; blue squares). The green dashed line is the barotropic EOS used in previous simulations.

This outflow carries off the angular momentum efficiently and the gas falls radially. Since the initial magnetic fields are not so strong, the gas spins up again as it falls and hits the inner centrifugal barrier near $\sim$ 5AU. Then, the magnetic field lines are wound up tightly and magnetic pressure launches the fast, well collimated outflow.

The variety of the gas's thermal behavior is shown in the $\rho - T$ plane in Figure 3.6. The distribution in this plane indicates a strong dependence on the geometry. We can see again that the gas tend to be hotter in the RMHD simulation than in the barotropic approximation. Although this was already pointed out by Whitehouse & Bate (2006), our simulation can resolve more detailed features. The jump around $\rho \sim 10^{-13} \mathrm{g\,cm^{-3}}$ is caused by the shock at the surface of the first core. This density is very close to the critical density in the barotropic approximation. This shock is nearly isothermal since radiation can transfer thermal energy produced at the shock to the upstream efficiently. Radiation transfer is not so efficient beyond this critical density. When the temperature reaches $\sim$ 1500K the evolution track in the $\rho - T$ plane gets shallow. This is because all the dust components evaporate and the opacity drops sharply at this temperature, and then radiation transfer becomes effective again. The structure of the first core is slightly modified by this effect but not drastically since the gas soon becomes optically thick and adiabatic again. We emphasize that radiation transfer is required to treat the realistic thermal evolution described here.

## 3.4 Conclusions and Discussions

We performed numerical simulations of the early phase of the low-mass star formation process. Our simulation used a newly developed three-dimensional nested-grid self-gravitational FLD RMHD simulation code. In our case, radiation transfer does not seem to change the qualitative scenario of low-mass star formation drastically. However, the temperature distribution is significantly changed by introducing radiation transfer. Realistic treatment of gas thermodynamics alters some properties and structure of the core quantitatively. The mass and size of the first core at a certain central density become larger because of the higher entropy, and the lifetime becomes slightly longer. The outflow travels further during this extended lifetime. Furthermore, the temperature and luminosity of the first core and the outflow become higher in the RMHD simulation. This suggests that the observational probability of such very young star forming sites is larger when compared to previous predictions based on the simulations with the barotropic approximation.

We showed that the barotropic approximation adopted in previous simulations is just crude approximation and fail to reproduce realistic thermal evolution. In the barotropic approximation all the gas elements trace the thermal evolution track of the gas at the center of the cloud which experiences no shock and, therefore, has minimum entropy in the spherically symmetric simulation. In this sense barotropic approximation tends to underestimate the gas entropy and temperature. In 3D, the RMHD simulation shows more striking and complex differences from the barotropic simulation (see also Bate (2010); Commerçon et al. (2010)). On the other hand if there exists fast initial rotation and angular momentum transport is ineffective, then the entropy of the resulting thin disk-like first core may be lower than in the barotropic EOS due to the efficient radiation cooling. Thus radiation transfer will affect the mechanical properties such as stability or fragmentation through the thermal property of the gas (Gammie, 2001). Determining a realistic temperature distribution is essential for predicting or interpreting the properties acquired in both the molecular emission lines and thermal continuum observations, for strong temperature dependences of the emissivity. Chemical reactions are also sensitive to temperature, so our results can be applied to a study of chemistry in molecular clouds and star forming regions.

Though on-going star formation like this simulation has never been observed directly, new telescopes are expected to reveal them, and ALMA is the most promising in the near future. Compact ($\sim 100$ AU scale) and warm ($\sim 30$ K) molecular outflow can be a good indicator of the first core. Our results can be compared with future observations.

# Chapter 4

# Prediction for First Core Observations

## 4.1 Backgrounds

A first core is the first object formed in the course of the protostellar collapse. Since significant amount of the angular momentum must be transported during the first core phase, it is regarded as a key object to understand the early phase of star formation and therefore it has been well studied theoretically (Saigo & Tomisaka, 2006; Omukai, 2007; Saigo et al., 2008; Yamada et al., 2009; Commerçon et al., 2010, 2011a,b; Tomida et al., 2010b,a; Saigo & Tomisaka, 2011). In spite of the continuous effort, however, it has never been confirmed observationally. There are two major reasons why first cores are difficult to be observed: (1) they are very faint ($< 0.1 L_\odot$) and compact ($\lesssim 100\,\mathrm{AU}$) (2) they are rare because of their short lifetime (typically on the order of thousand years; but see the next Chapter) compared to the timescale of star formation; roughly speaking we can expect only one first core in $100 \sim 1000$ dense molecular cloud cores.

In spite of such difficulties, some first core candidates were recently discovered. Chen et al. (2010) found a very faint and compact core and claimed that it was a good first core candidate. Their object must be very young, but it seems to be more evolved than a first core because it is associated with a well-collimated and high-velocity outflow, which is thought to be driven from a protostar after the second collapse. Chen & Arce (2010) reported another candidates in the R Corona Australis cloud. Enoch et al. (2010) found a good candidate for a first core whose spectral energy distribution (SED) is consistent with a theoretical model. Very recently well-collimated jet-like outflow associated with this object was detected (Dunham et al., 2011), which implies this object may be more evolved than the first core phase. Another promising first core candidate ever reported is L1451-mm in the Perseus Molecular Cloud Complex (Pineda et al., 2011). This object has a very faint SED consistent with theoretical prediction and very compact structure. Moreover, it is associated with slow ( $\lesssim 1.5\,\mathrm{km\,s^{-1}}$ in the line of sight), loosely collimated outflow, which is very similar to the outflow predicted in MHD simulations of protostellar collapse (Tomisaka, 1998, 2002; Banerjee & Pudritz, 2006; Machida et al., 2008a; Tomida et al., 2010b). Kawabe et al. (in preparation) also discovered two first core candidates; "Core B" in the Lupus-I star forming region and "Source A" in the $\rho$-Ophiuchus star forming region. These candidates must be confirmed by future observations, but these candidates indicate that first cores are now receiving much attention in the star formation research.

In 2011, ALMA started the Cycle-0 Early Science operations. We can expect that first cores will be directly observed with ALMA in the near future because the unprecedented potential of ALMA is sufficient to detect and resolve the first core directly. In such a situation, sophisticated theoretical models which can directly compared with observations are highly demanded.

In this Chapter, we present the observational properties such as SEDs, interferometric images, visibility amplitude distributions and position-velocity diagrams directly calculated from the results of our radiation (magneto)hydrodynamic simulations. Based on the results, we predict future observations of first cores and propose the observational strategy to identify first cores.

## 4.2 Methods

### 4.2.1 Thermal Continuum

To derive various observational properties, we first draw an intensity distribution map. We solve the following radiation-transfer equation in one direction for various viewing angles and wavelengths using the results of our nested-grid radiation (magneto)hydrodynamic simulations:

$$\frac{dI_\nu}{ds} = \rho\kappa_\nu(T)\left[B_\nu(T) - I_\nu\right], \tag{4.1}$$

where $I_\nu$ is the (monochromatic) intensity, $ds$ the path length along the line of sight, $B_\nu(T)$ the Planck function of temperature $T$, and $\kappa_\nu$ the monochromatic (absorption) opacity, respectively. Here, we assume that the temperature $T$ obtained in the RHD simulations is correct, and we ignore scattering, which is a valid assumption in mid-infrared or longer wavelengths. We adopt the monochromatic dust opacities provided by Semenov et al. (2003)[1], considering the evaporation temperature of each dust component. We neglect the contribution from the region hotter than the dust evapo-

---

[1] http://www.mpia.de/homes/henning/Dust_opacities/Opacities/opacities.html

ration temperature ($T \gtrsim 1500\,\mathrm{K}$). Such a hot region is deeply embedded in the highly optically-thick first core and does not contribute to the observational properties. Note that the dust properties such as size distribution, structure and composition are quite uncertain and have significant impact on the monochromatic opacities (more than one order of magnitude in radio wavelengths longer than 1 mm) and therefore on resulting predictions.

Using the intensity map, we can derive various observational information. We can draw SED by integrating the intensity within a given aperture. We can simulate interferometric observations for ALMA, eVLA and SMA with the Common Astronomy Software Applications (CASA) provided by NRAO[2], which is a software package of standard data analysis and simulation tools. Another important observational information is visibility amplitude distribution (VAD) which is the spatial Fourier transform of the intensity distribution, and is the direct observable of radio interferometers. We typically measure VADs as functions of the UV distance, or the baseline length of interferometric observations. The visibility amplitude can be interpreted as the intensity from the scale corresponding to the UV distance. VAD is useful because we can measure VADs even the data quality (such as sensitivity, UV coverage and resolution) is poor. VADs can be calculated using CASA, too.

### 4.2.2 Molecular Lines

To predict molecular line observations, we perform molecular line transfer calculations without assuming local thermodynamical equilibrium (LTE). The details of the non-LTE radiation transfer simulations are beyond the scope of this thesis, so we refer readers to Tomisaka & Tomida (2011). Here we briefly describe our non-LTE calculations. We treat a single chemical species (such as CO and CS) and consider the transitions between the levels. The current version of our code can handle the rotational transitions of simple molecules. We calculate the level populations in each cell by consistently solving the balance equations and radiation transfer with Monte-Carlo methods in the results of our nested-grid RMHD simulations. Here we use the gas temperature obtained in the RMHD simulations as the kinetic temperature controlling the collisional excitations/deexcitations in the non-LTE simulations. Once we obtain the level populations, we can calculate the frequency dependent intensity distribution (or channel map) using the radiation transfer equation. Then we perform imaging simulations with CASA.

---

[2] http://casa.nrao.edu/

## 4.3 Results

### 4.3.1 Thermal Continuum

We show the results in comparison with the observations of a first core candidate “Source A”. This object was first identified by Kamazaki et al. (2001). Since the mass of “Source A” is estimated to be about $1 M_\odot$ or less, here we adopt a radiation hydrodynamic model of a rotating first core whose mass is $1 M_\odot$. Here we neglect the effect of magnetic fields for simplicity. The observations are best-fitted by the first core model in relatively young phase, whose central temperature is $T_c \sim 600\,\mathrm{K}$ and radius is $R_{\mathrm{FC}} \sim 40\,\mathrm{AU}$. Our theoretical SEDs are in good agreement with observations in mid/far-infrared and radio wavelengths (Figure 4.1). Dependence on the inclination angles is not so prominent, but edge-on ($i = 90^\circ$) is faintest because of the central hot region is shrouded in the first core disk. It is quite puzzling that near-infrared emissions ($4.5\mu$m and $5.6\mu$m) are detected by Spitzer Space Telescope. These near-infrared emissions are detected at $\sim 1$ arcsec away from the peak of dust continuum. Interestingly enough, an one-sided outflow is also detected toward “Source A” in CO(3-2) with SMA and its position coincides with the near-infrared emissions. We speculate that these emissions may be explained by scattering of hot photons from the central core, leaking through the outflow cavity. Another possibility to explain these emissions are emission lines excited in the outflow shock. We require further observations and more precise modeling including outflows to solve this puzzle. For more information about “Source A”, we refer readers to Kawabe et al.

First cores emit most strong radiation in far-infrared wavelengths ($\lambda \sim 100\,\mu$m). Unfortunately, the sensitivities of Spitzer are not sufficient to detect those far-infrared emissions. Therefore we have large uncertainties on the properties of our targets. Observations with *Herschel* Space Observatory (and SPICA in the next generation) will help this situation.

We show the VAD of “Source A” measured at $870\,\mu$m with SMA (the beam size is about 0.9 arcsec × 2.8 arcsec) and our theoretical prediction in Figure 4.2. The observed VAD shows excellent agreement with the theoretical VAD both in the slope and amplitude. But actually, this observed VAD means that “Source A” is not well resolved and we only can say that there present some unresolved finer structures. We require further observations to confirm whether it is a first core or not. In the Cycle-0 Early Science operations of ALMA, the resolution will be improved by a factor of three in Band 7. But if we use Band 9 ($\lambda \sim 435\,\mu$m) and the extended configuration, higher resolution will be achieved and we may possibly resolve the first core disk itself (Figure 4.3) even in Cycle-0. If we see the steep drop in the VAD at a certain UV distance, it corresponds to the scale of the structure.

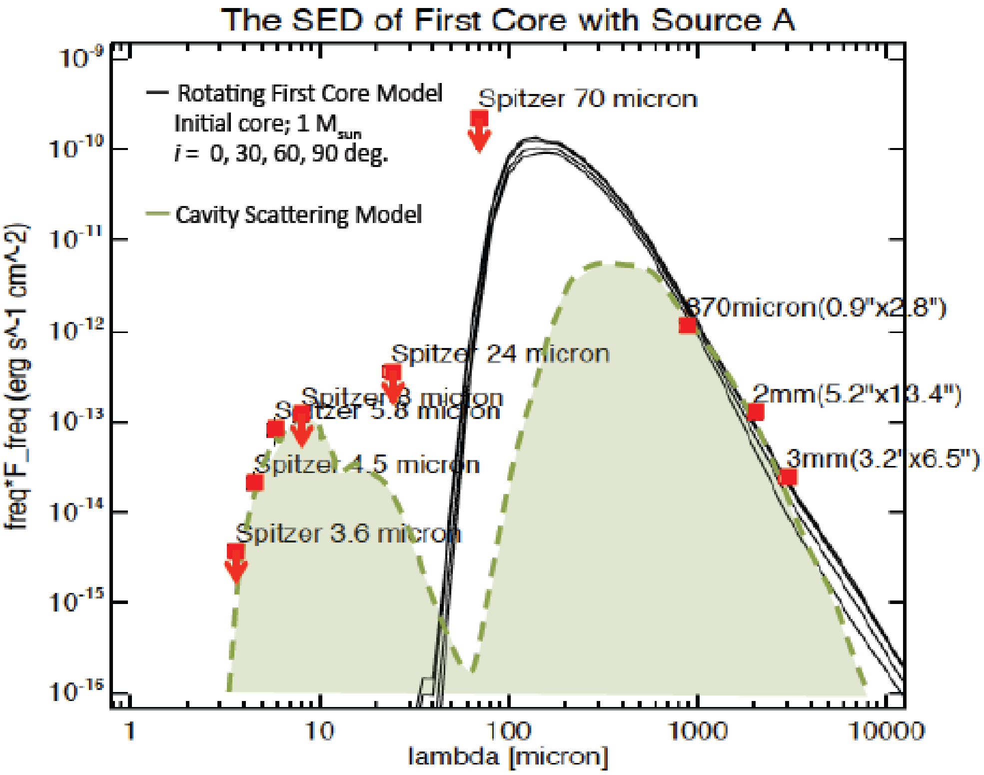

Figure 4.1: The SED of "Source A" (red) and the best fit RHD model (black lines). The SED is calculated with the aperture of 2 arcsec × 2 arcsec, or 300AU × 300AU covering the whole first core and surrounding warm envelope. The excess detected at 4.5 and 5.6 $\mu$m may be explained by scattered light from a cavity (green dashed line, see the text). Adapted from Kawabe et al. (in prep.)

We show another examples of SED and VAD in the next Chapter (Figures 5.4 and 5.5).

Finally, we demonstrate imaging simulations for future observations with ALMA. For the imaging simulations using CASA, we set the position of the object to be (RA = $16^{\mathrm{h}}\,25^{\mathrm{m}}\,00^{\mathrm{s}}$, Dec = $-23^\circ\,23'\,00''$) and the distance $D = 150\,\mathrm{pc}$, supposing a nearby star forming region. Here we use 50 antennae and maximum baseline is about 12 km (we adopt "alma.out24.cfg" antennae list file distributed in the CASA package), corresponding angular resolution is about 0.02 arcsec, high enough to resolve the spiral arms in the first core disk formed via gravitational instability whose typical thickness is about 10 AU (see Chapter 5). We "observe" the intensity map obtained from the radiation transfer calculation at 345GHz (Band 7), which we used for VAD calculations. The continuum sensitivity of ALMA in the full operation phase is very high and nearby first cores can be easily detected, but here we take 4-hour integration time to obtain good UV coverage. Here we neglect thermal noise, but we estimate the sensitivity below. We show the raw image before being processed by the CASA simulator in

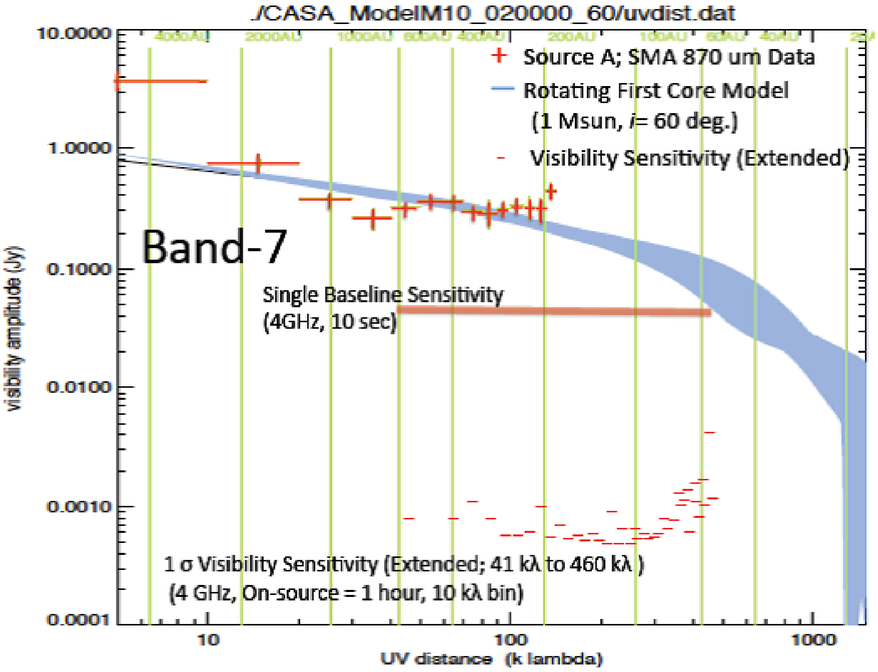

Figure 4.2: The VAD of "Source A" at 870 $\mu m$ measured with SMA (red crosses) and the theoretical prediction (blue). The inclination angle is assumed to be 60° from the rotation axis. The visibility sensitivities of ALMA Cycle-0 are also plotted (red lines). Adapted from the observation proposal for ALMA (Kawabe et al.).

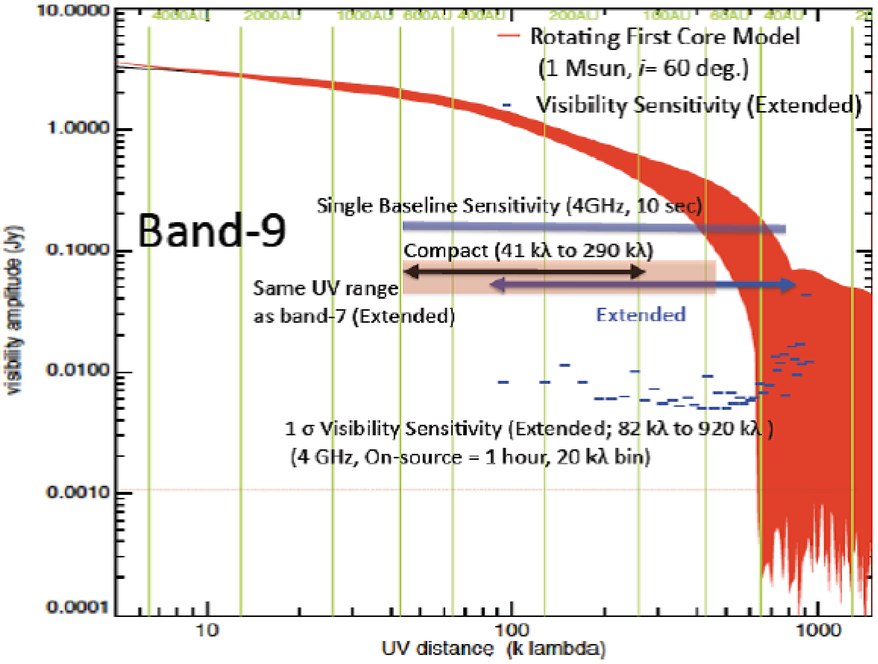

Figure 4.3: Theoretical prediction of VAD in Band 9 of ALMA ($\lambda \sim 350\,\mu$m) using the same model as Figure 4.2 (red). The visibility sensitivities of ALMA are also plotted (blue lines). Adapted from the observation proposal for ALMA (Kawabe et al.).

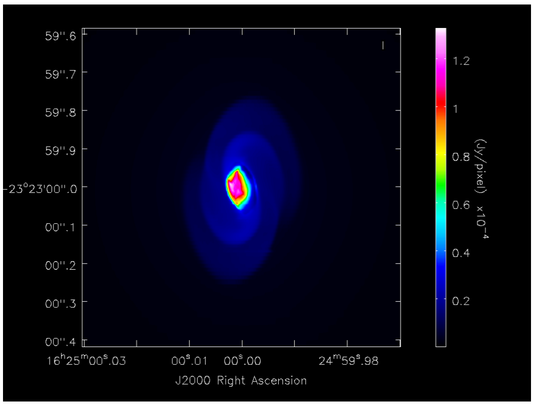

Figure 4.4: The raw image at 345GHz before processing by CASA. The image size is 125 AU × 125 AU, corresponding to 0.83 arcsec × 0.83 arcsec.

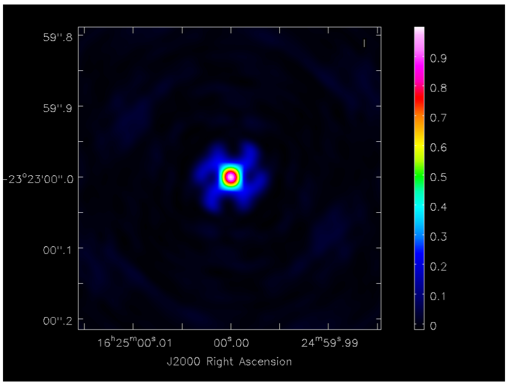

Figure 4.5: The point spread function (beam pattern) obtained with 50 antennae and 4-hour integration. The maximum baseline is about 12 km and corresponding angular resolution is about 0.03 arcsec or 5 AU at $D = 150$ pc. The side lobe is well suppressed.

Figure 4.4, the point spreading function (PSF) in Figure 4.5 and the simulated image in Figure 4.6.

The spiral arms in the first core disk are clearly visible. According to the ALMA sensitivity calculator, $1\sigma$ sensitivity with 4-hour integration with 2 GHz bandwidth per polarization is estimated to be 0.023 mJy in typical observational conditions (1.262mm water vapour column density, $\tau = 0.211$, $T_{\mathrm{sky}} = 55.8$ K and $T_{\mathrm{sys}} = 173.8$ K). The spiral arms are detected above 1 mJy, therefore these structures can be easily observed (we may observe them with even higher angular or spectral resolution). If we observe such a large first core disk with spiral arms, it tells us that the first core disk is quite massive and gravitational instability takes place there, suggesting early formation of the circumstellar disk. Here we simulated the first core in relatively early phase for comparison with our first core candidate. More evolved first cores can be observed more easily.

Note that we simulate the collapse of the whole molecular cloud core, therefore not only the first core but also the contribution from the envelope are consistently included in the simulated observations described above. Our results prove that we can observe first cores directly even through the thick envelope.

### 4.3.2 Molecular Lines

Here we show the results of non-LTE molecular line transfer simulations of CS and $C^{34}S$ lines. We use the results of RMHD simulations we described in the previous chapter. We assume that the abundances of CS and $C^{34}S$ relative to $H_2$ are uniform,

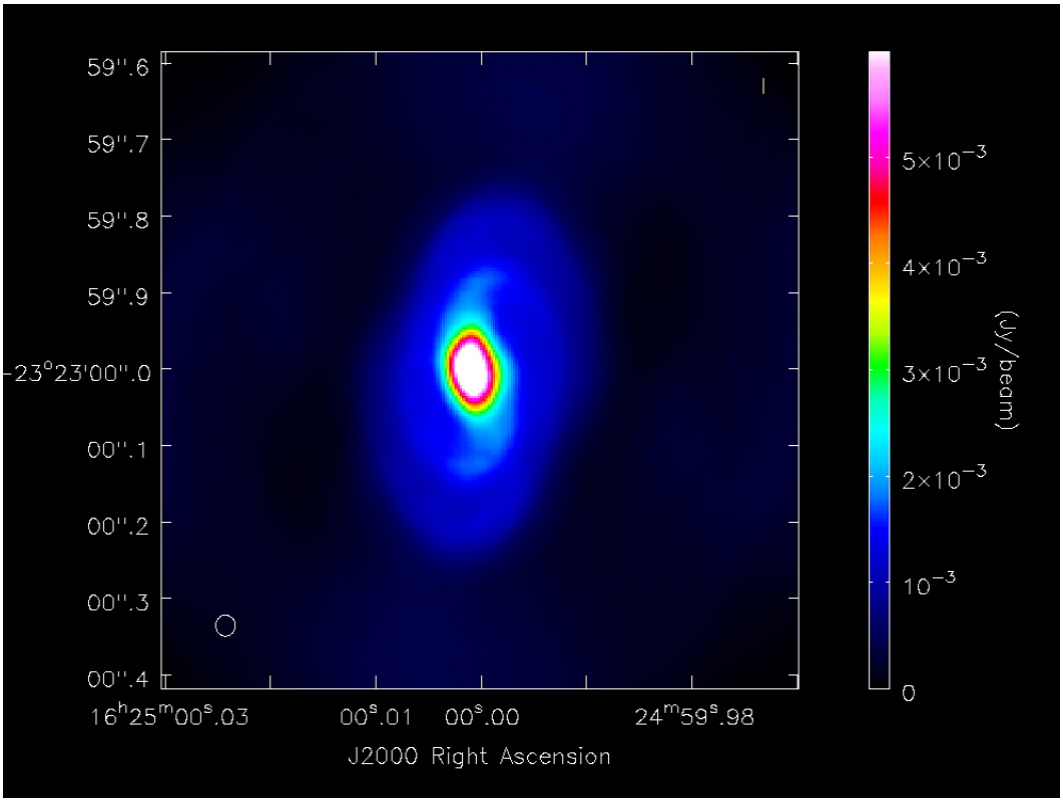

Figure 4.6: The simulated 345GHz imaging observation for ALMA in the full operation phase. The beam size is showed in the bottom-left corner. The spiral arms formed in the first core disk are clearly visible.

$X_{\rm CS} = 4 \times 10^{-19}$ and $X_{\rm C^{34}S} = 0.04 X_{\rm CS}$. We show the results of the high transitions ($J = 5-4$ and $7-6$) because we are interested in identifying the first core warmer and denser than the envelope. These lines are suitable to trace the dense and warm region because of their high upper-state energies and critical densities and because they fit the observation bands of ALMA (Bands 6 and 7).

We “observe” the results of non-LTE line transfer simulations for four hours using the extended configuration of ALMA Cycle-0 with 16 antennae. The maximum baseline is about 400 m and corresponding resolutions are $\sim$ 0.7 arcsec in Band 6 and $\sim$ 0.5 arcsec in Band 7. The velocity resolution is set to be $0.1\,{\rm km\,s^{-1}}$. Thermal noise is included in the simulated observations. Other parameters are the same as the imaging simulations of thermal continuum. We show the dirty maps of our simulated observations without performing CLEAN procedures, but we can obtain sufficiently crisp images because the beam pattern of ALMA is quite sharp even in Cycle-0. The viewing angle is set to be 45° from the rotational axis.

Figure 4.7 is the “raw” image of the integrated intensity of the CS(7-6) line emission obtained from the non-LTE simulations. The resolution of this image is determined

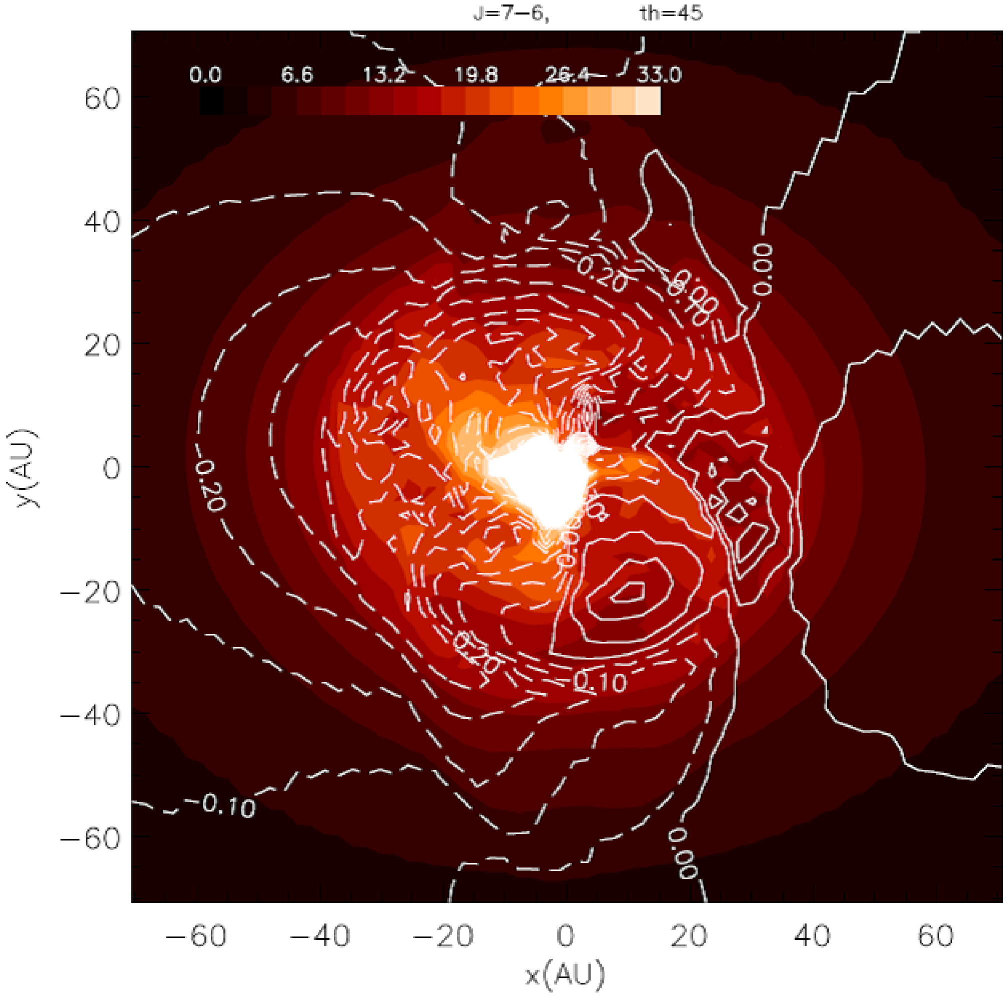

Figure 4.7: The integrated intensity distribution (color) and the first moment (the intensity-weighted velocity along the line of sight; contour) of the CS(7-6) line. For details and other images, see Tomisaka & Tomida (2011)

.

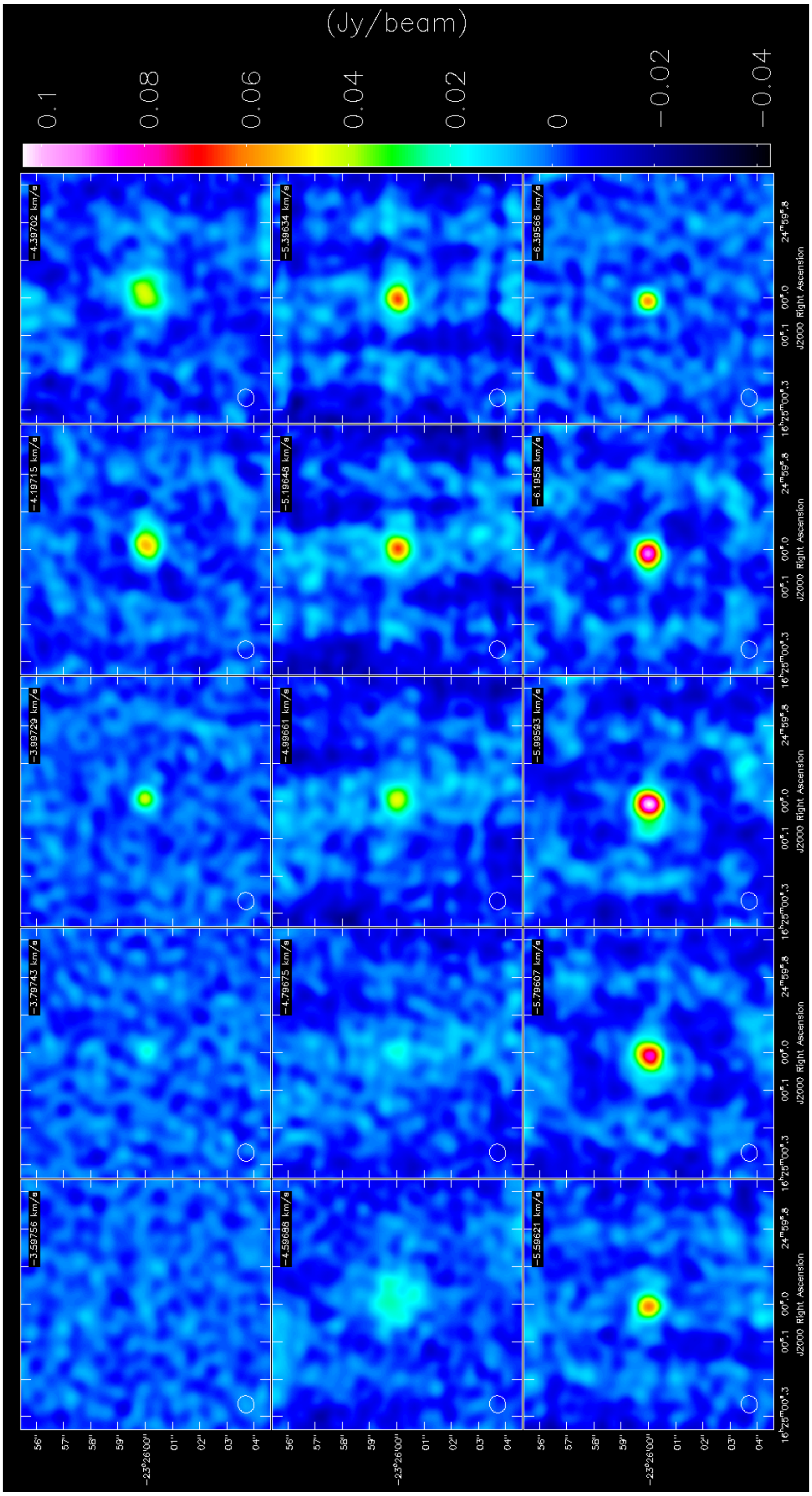

Figure 4.8: Simulated CS(5 − 4) channel maps from $-3.6\,\mathrm{km\,s^{-1}}$ (top left) to $-6.4\,\mathrm{km\,s^{-1}}$. The central panel is the map of the systemic velocity ($-5.0\,\mathrm{km\,s^{-1}}$). The beam size is indicated at the right-bottom corner of each panel. The image size is 10 arcsec × 10 arcsec, corresponding to 1500 AU × 1500 AU.

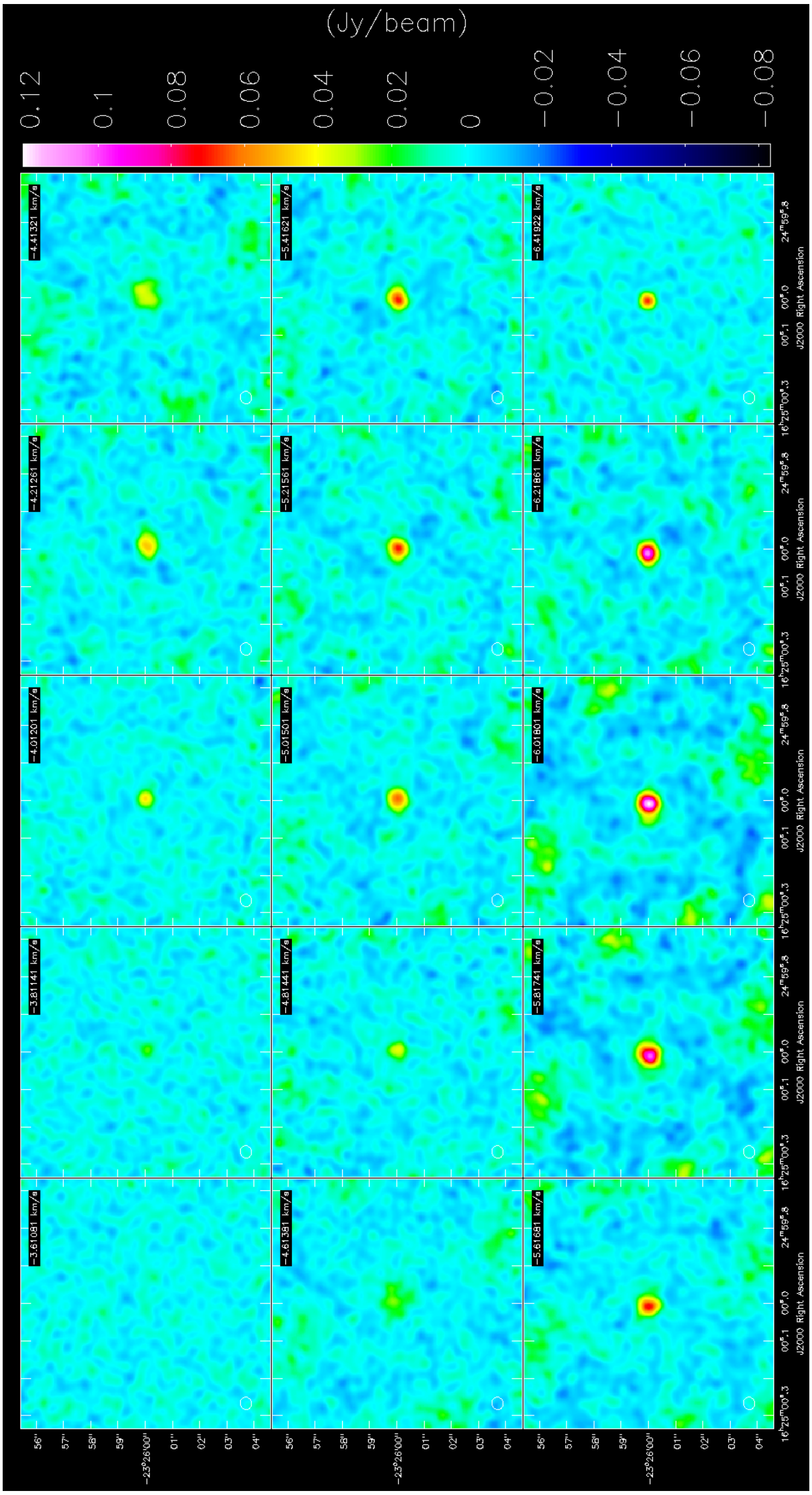

Figure 4.9: Simulated CS$(7-6)$ channel maps.

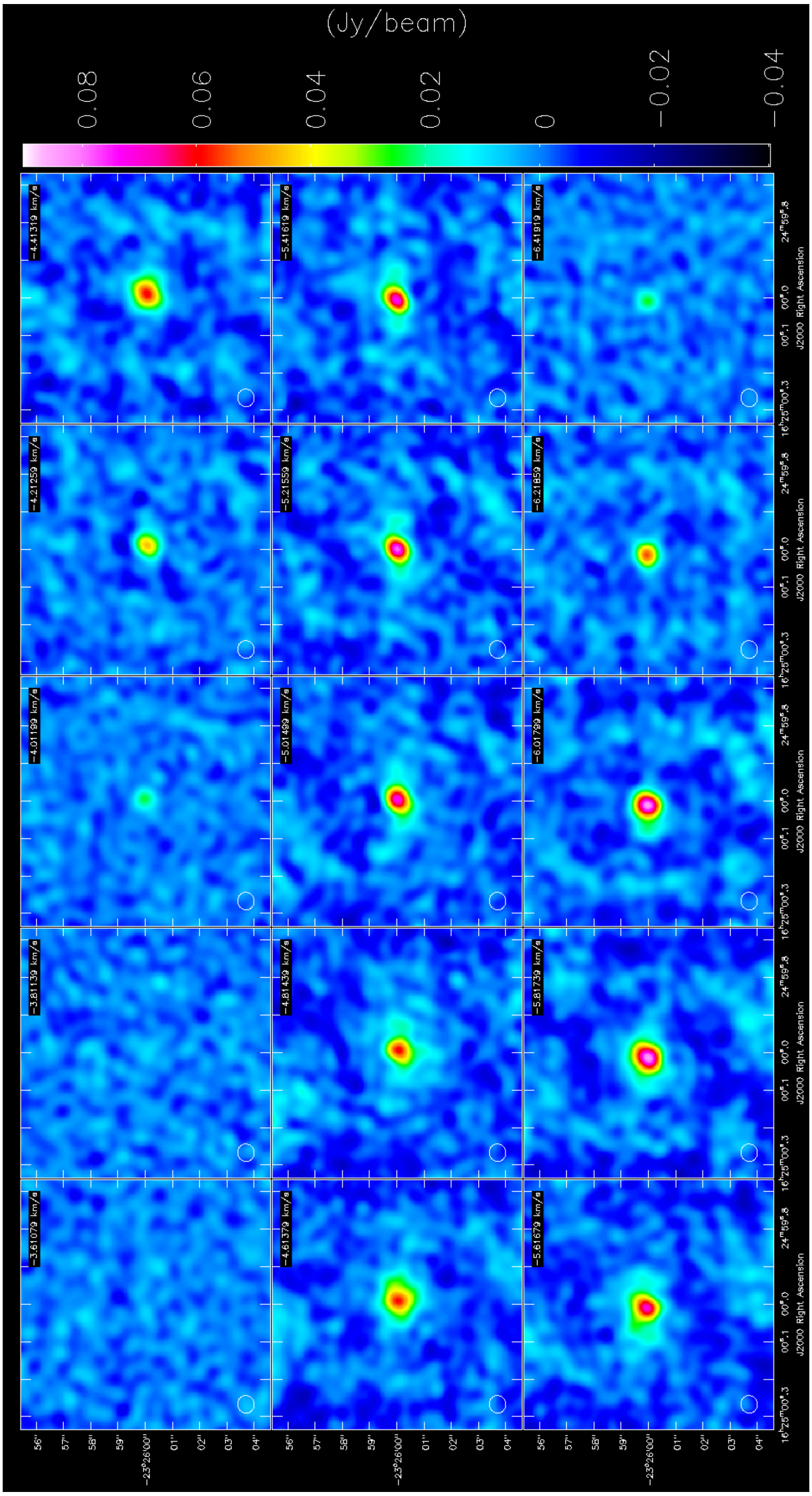

Figure 4.10: Simulated $C^{34}S(5-4)$ channel maps.

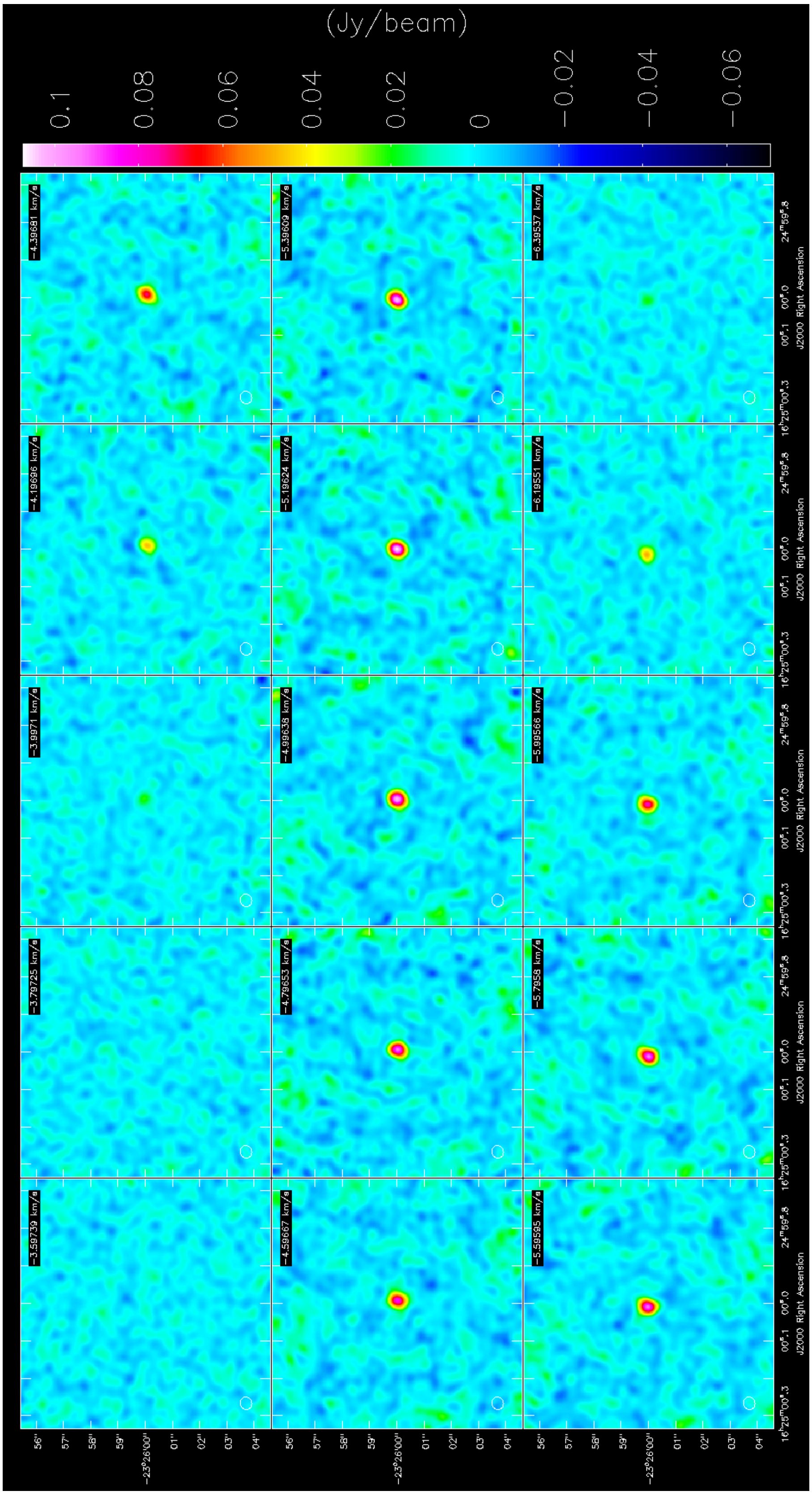

Figure 4.11: Simulated $C^{34}S(7-6)$ channel maps.

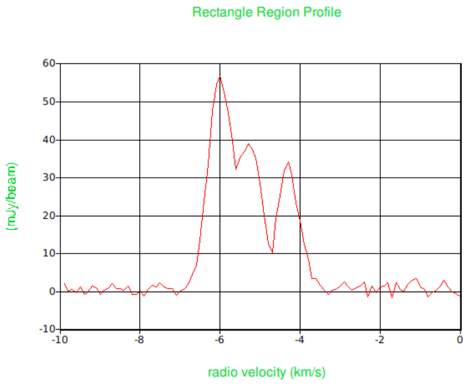

Figure 4.12: Simulated CS$(5-4)$ line spectrum integrated in the central $1\,\mathrm{arcsec} \times 1\,\mathrm{arcsec}$ area.

.

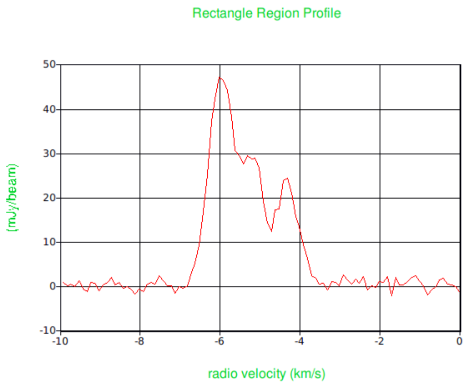

Figure 4.13: Simulated CS$(7-6)$ line spectrum.

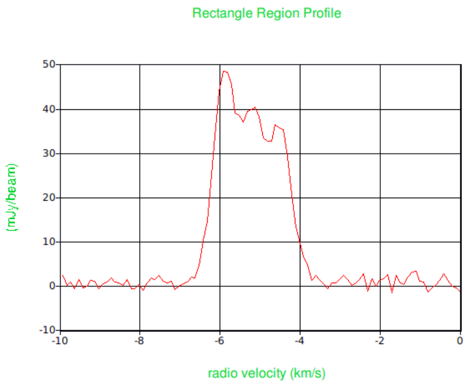

Figure 4.14: Simulated C$^{34}$S$(5-4)$ line spectrum.

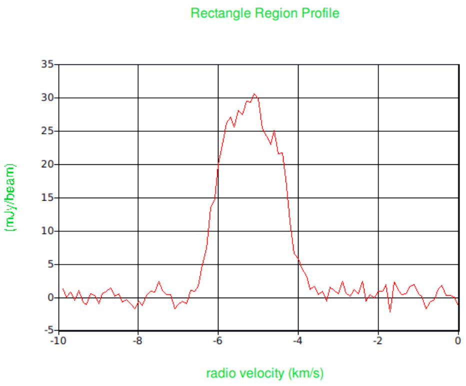

Figure 4.15: Simulated C$^{34}$S$(7-6)$ line spectrum.

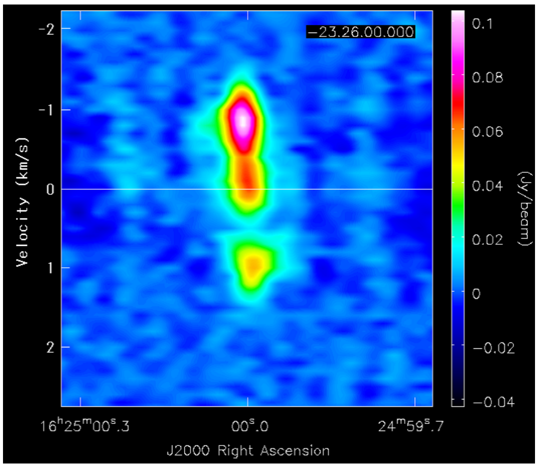

Figure 4.16: Simulated CS(5 − 4) line position-velocity diagram along the horizontal line of Dec = −23° 26′ 00”. The horizontal coverage is 5 arcsec, corresponding to ∼ 750 AU

.

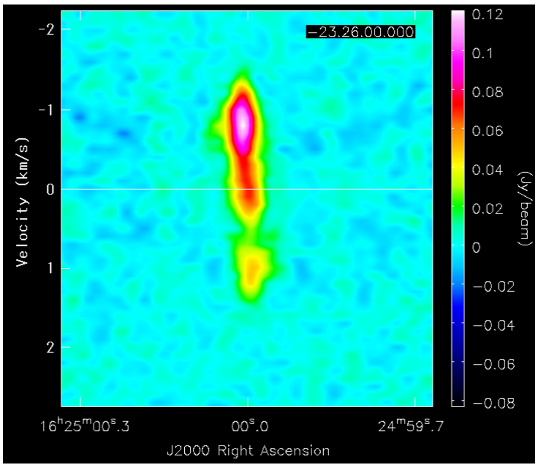

Figure 4.17: Simulated CS(7 − 6) line position-velocity diagram.

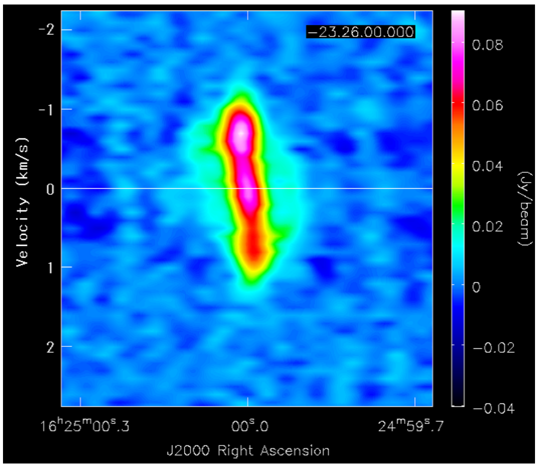

Figure 4.18: Simulated $C^{34}S(5-4)$ line position-velocity diagram.

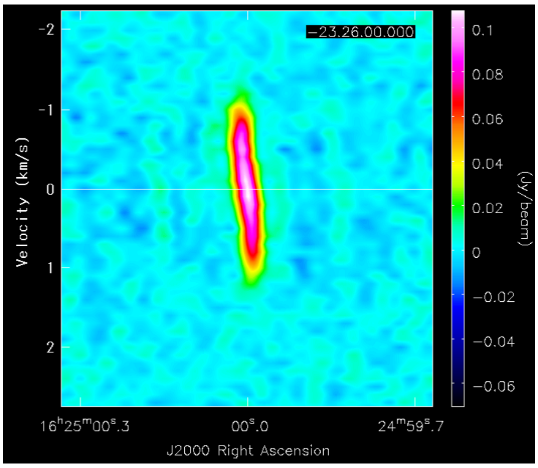

Figure 4.19: Simulated $C^{34}S(7-6)$ line position-velocity diagram.

by the RMHD simulation and far better than present-day observations. After the imaging simulations, we can obtain the channel maps (Figures 4.8 – 4.11), the line spectra integrated in a given aperture (Figures 4.12 – 4.15) and the position-velocity diagrams (Figures 4.16 – 4.19). First cores are barely resolved with these resolutions, but we can see the signature of the simultaneous rotation and infall in these figures. For example, the approaching side of rotation is brighter than the receding side if the cloud is simultaneously rotating and contracting. The emission from the outflow is insignificant because CS lines trace high density gas. Lines which trace lower densities such as CO and its isotopes will be better for outflow observations.

The line spectra show so-called blue skewed profiles due to the infall motion in the envelope in front of the first core. Interestingly, the peak intensities of CS and $C^{34}S$ lines are similar despite the large difference in their abundances. CS(5-4) and (7-6) lines are significantly weak around the systemic velocity ($-5\,\mathrm{km\,s^{-1}}$). This is because these lines suffer from the absorption in the infalling envelop in front of the first core, and because interferometric observations miss the extended emission (so-called missing flux). The latter effect will be relieved in future observations with more antennae including ACA (Atacama Compact Array), but the absorption in the envelope is inevitable. $C^{34}S$ lines, on the other hand, still suffer from these effects but they are less significant. Therefore, we can say that the less abundant $C^{34}S$ lines will be good tracers of dense objects deeply embedded in the thick envelope like first cores.

## 4.4 Conclusions and Discussions

We have constructed the procedures to derive observational quantities, both thermal continuum and molecular lines, directly from R(M)HD simulations. First cores are observable and distinguishable with current and future instruments like ALMA and *Herschel*. With the full capabilities of ALMA, we will be able to study the dynamics within first cores directly in the near future.

Although we have strange near infrared emissions at 4.5 and 5.6 $\mu$m, our first core candidate “Source A” agrees well with our theoretical predictions. Therefore, we assume this is one of the best first core candidates and will carry out further observations with ALMA and other telescopes.

Common features of first cores predicted from theoretical simulations can be summarized as follows:

- Its SED is faint and looks like low-temperature black body emission.
- It looks like a compact dust core with shallow visibility amplitude distributions, which can be barely resolved with current interferometric observations.

- Associated with no/weak near-infrared emission, which is supposed to come from a hot source like a protostar.
- Slow, small and weak (or undetectable) outflow without high-velocity jet

Based on these features, we can find first cores by searching for compact dust cores with shallow VADs but without stellar signatures. However, as first cores are rare objects, we require very large survey to identify first cores.

The SEDs of our first core models are qualitatively similar to those of Masunaga & Inutsuka (2000). However, our models give qualitatively more luminous SEDs because first cores can be more massive owing to its rotation. Our models are also similar to Boss & Yorke (1995), although we do not have their hump in the mid-infrared region ($\lambda \sim 30\,\mu$m). This is because the model plotted in Figure 4.1 is still in the intermediate stage of the first core phase. When the first core evolves more and it gets hotter, we sometimes have a hump like theirs in the face-on configuration, but it is still very weak. This is probably because it depends on the structure and mass of the envelope (i.e., the optical depth of the envelope) since such infrared photons are easily reprocessed to colder photons by dust grains.

In this thesis, we omitted magnetic fields in SED and VAD calculations. However, it is well known that magnetic fields have significant impact on the collapse of molecular cloud cores. The first core will be more compact and fainter if magnetic fields present because the mass of the first core will be smaller due to the efficient angular momentum transport. In order to construct reliable and useful theoretical models, we are going to perform wide parameter survey including magnetic fields.

For molecular line simulations, we assumed spatially and temporally constant abundances. Chemical evolution is beyond the scope of this thesis, but chemistry is of great importance on the observational consequences. For example, depletion of gaseous species onto dust grains will significantly reduce the abundance in the gas phase. For this purpose, we have already started collaboration for studying chemistry in collapsing molecular cloud cores (Furuya et al. submitted).

## 4.5 Appendix: Analytic Formula of Starless Core VADs

For future surveys of starless cores and first cores, an analytic formula of VAD will be useful as templates for discussing their evolutionary states. Here we derive the analytic formula of VAD of a critical BE sphere as a model of the isothermal starless core. Here we assume that the cloud is optically thin, i.e., $I_\nu = \kappa_\nu \Sigma B_\nu(T)$, where $I_\nu$ denotes the intensity, $\kappa_\nu$ the monochromatic (absorption) opacity, $\Sigma$ the column density and $B_\nu(T)$

the Planck function of the temperature $T$.

First, we approximate the density profile of a critical BE sphere with a simple function. Here we use the normalized scales given by the following relations:

$$l_0 = c_s t_{\rm grav} = c_s \sqrt{\frac{1}{4\pi G \rho_0}} \tag{4.2}$$

$$M_0 = \rho_0 l_0^3 \tag{4.3}$$

where $c_s \sim 190\,{\rm m\,s^{-1}} \left(\frac{T}{10\,{\rm K}}\right)^{1/2}$ is the soundspeed of molecular gas and $\rho_0$ is the gas density at the center. In these normalized units, the radius and mass of a critical BE sphere are $R_{\rm BE} \sim 6.45$ and $M \sim 197$. The central density is related to the gas temperature and the total mass in the physical units thorough the following relation:

$$M \sim 0.88 M_\odot \left(\frac{\rho_0}{10^{-18}\,{\rm g\,cm^{-3}}}\right)^{-1/2} \left(\frac{T}{10{\rm K}}\right)^{3/2} \tag{4.4}$$

$$\left(\frac{\rho_0}{10^{-18}\,{\rm g\,cm^{-3}}}\right) \sim 0.78 \left(\frac{M}{1M_\odot}\right)^{-2} \left(\frac{T}{10{\rm K}}\right)^{3} \tag{4.5}$$

The normalized profile of a critical BE sphere can be fitted by the following formula with $r_c^2 = 26/3$ (Figure 4.20):

$$\rho(r) = \left(1 + \frac{r^2}{r_c^2}\right)^{-\frac{3}{2}} \tag{4.6}$$

Since the mass calculated from this function diverges logarithmically, we should regard that this formula is valid only within a finite radius.

The column density from this formula is:

$$\Sigma(R) = \int_{-\infty}^{\infty} \rho(r) dz = 2\int_0^{\infty} \left(1 + \frac{x^2}{r_c^2} + \frac{y^2}{r_c^2} + \frac{z^2}{r_c^2}\right)^{-3/2} dz = \frac{2r_c}{1 + R^2/r_c^2} \tag{4.7}$$

where $R^2 = x^2 + y^2$. Then we perform the Fourier transform:

$$V(k) = \frac{1}{2\pi} \int_{-\infty}^{\infty} \int_{-\infty}^{\infty} \Sigma(R) dx dy = \frac{1}{2\pi} \int_{-\infty}^{\infty} \int_{-\infty}^{\infty} \frac{2r_c}{1 + R^2/r_c^2} e^{-i\mathbf{k}\cdot\mathbf{x}} dx dy \tag{4.8}$$

It can be rewritten as the Hankel transform:

$$V(k) = 2r_c \int_0^{\infty} \frac{R}{1 + R^2/r_c^2} J_0(kR) dR \tag{4.9}$$

$$= 2r_c^3 \int_0^{\infty} \frac{\xi}{1 + \xi^2} J_0(k r_c \xi) d\xi \tag{4.10}$$

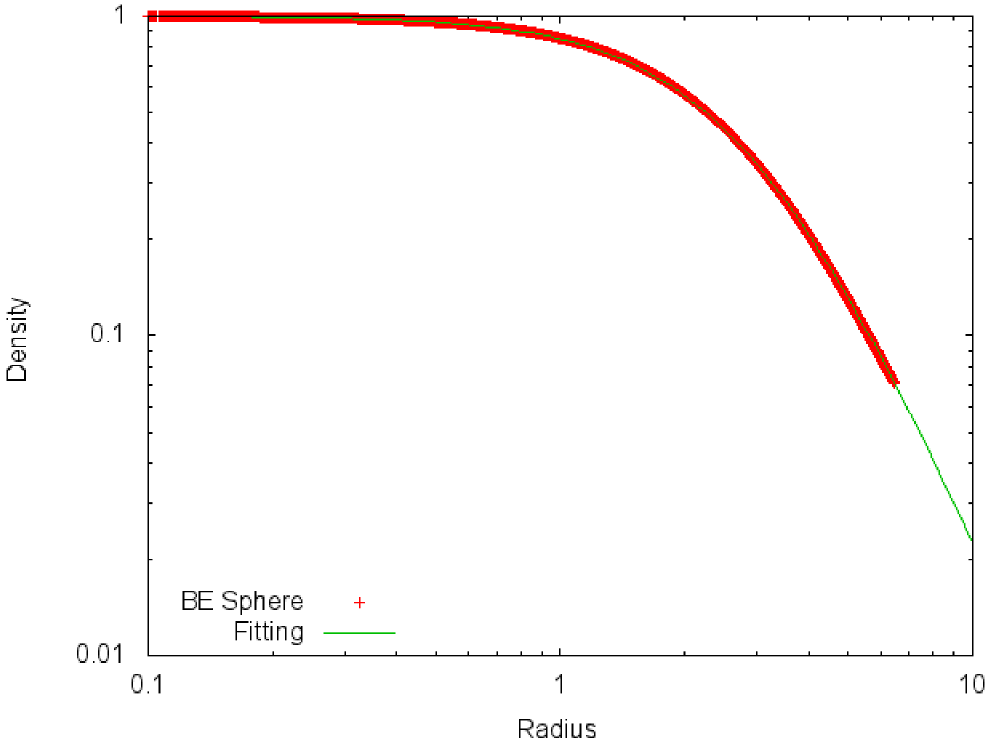

Figure 4.20: Comparison between the normalized profile of a critical BE sphere and our simple fitting formula.

Finally, it yields very simple formula involving the modified Bessel function of the second kind $K_0$:

$$V(k) = 2r_c^3 K_0(kr_c) \tag{4.11}$$

To convert it into observational quantities, we recover the physical units:

$$\begin{align} V(k) &= 2r_c^3 \rho_0 \kappa_\nu B_\nu(T) K_0(kr_c) \tag{4.12} \\ r_c &= \sqrt{\frac{26}{3}} l_0 \sim 4080\mathrm{AU} \left(\frac{\rho_0}{10^{-18}\,\mathrm{g\,cm^{-3}}}\right)^{-1/2} \left(\frac{T}{10\mathrm{K}}\right)^{1/2} \nonumber \\ &= 4640\mathrm{AU} \left(\frac{M}{1M_\odot}\right) \left(\frac{T}{10\mathrm{K}}\right)^{-1} \tag{4.13} \end{align}$$

Practically, the amplitude and the core radius $r_c$ should be determined to meet the observation at a given radius (aperture or baseline).

# Chapter 5

# First Cores in Very Low Mass Cloud Cores

## 5.1 Backgrounds

In the context of low-mass star formation, formation of $1M_\odot$ stars has been well studied so far. However, there are far larger number of low mass objects in both IMF and CMF. It is well known that there is very good resemblance between CMF and IMF in wide range of masses. The shapes of the mass functions are similar while dense cloud cores tend to be more massive, about factor of several. This fact implies that the origin of IMF is already implemented in CMF, and one molecular cloud core directly corresponds to one star (or several). However, the low mass ends of both IMF and CMF are quite uncertain because of observational difficulties. The formation processes of brown dwarfs and very low mass stars, or connection between CMF and IMF, are quite unknown and there are two major hypotheses to explain their formation. First one is rather simple; a brown dwarf forms as the consequence of the collapse of a low mass molecular cloud core. This is just a scaled-down version of ordinary protostellar collapse models. The other is the disk fragmentation model, that is, a brown dwarf forms as a result of fragmentation of gravitationally unstable disk and ejected from the system by some reason. Observations of brown dwarfs about such as binary fraction, disk fraction, suggest that the properties of brown dwarfs are continuous from low mass stars, which means brown dwarfs are similar to ordinary stars, but there is a still on-going debate. One of our motivations is to contribute to this argument with our simulations.

Another interesting point is recent observations of first core candidates (Chen et al. (2010); Chen & Arce (2010); Enoch et al. (2010); Pineda et al. (2011); for detailed review, see the previous Chapter). In spite of the incomplete survey, we already have more than seven candidates. Considering the lifetime of first cores obtained from numerical simulations on the order of thousand years (typically about 2,000 - 3,000 years in rotating non-magnetized cases, and even shorter when magnetic fields present), first cores should be rare objects. That is, comparing the timescale of first cores and natal molecular cloud cores, the existence probability of first cores will be like one first core per thousand molecular cloud cores. Therefore the number of first core candidates seems to be too large. Of course, those first core candidates must be confirmed by further precise observations, but we should also reconsider our theoretical models. Interestingly, some first core candidates (and their natal cloud cores) are estimated to have fairly small gas masses of the order of $0.1M_\odot$ with radio observations. Although such observations of masses have large uncertainty, the facts again cast a question on the formation of very low mass stars.

Motivated by these facts, here we study the collapse of very low mass molecular cloud cores. The main question is, is star formation in very low mass cloud cores similar to that in $1M_\odot$ cores? Here we consider the properties of first cores as the first step. We know that first cores in $1M_\odot$ cores evolve under short dynamical time scale by accretion (typical values of the first core mass $\sim 0.03M_\odot$ and the accretion rate $\sim$ (several) $\times\, 10^{-5} M_\odot\,\mathrm{yr}^{-1}$ give a timescale of $\sim 10^3\,\mathrm{yrs}$). However, if the molecular cloud cores are small enough, first cores cannot reach the second collapse by accretion, and then first cores in very low mass cloud cores may survive much longer. If this consideration is true, it is not inconsistent that the number of first cores is larger than expected and the observed number of candidates can be reasonable. In order to examine this idea, we perform RHD simulations of the collapse of a low mass cloud core and compare with the evolution of typical molecular cloud cores. Since the timescale of radiation diffusion in first cores is estimated about thousand years, so need to to take account of the radiation transfer and cooling effects properly.

This work was already published in The Astrophysical Journal Letters, Volume 725, L239-L244 (2010) (Tomida et al., 2010a).

## 5.2 Method and Models

We perform 3D nested-grid self-gravitational RHD simulations. The details of the simulation code are described in Chapter 2, but we neglect magnetic fields in this work because initially we just intend to prove the concept. We use Roe's Riemann solver and an idealized equation-of-state (EOS) with adiabatic index $\gamma = 5/3$, which is different from that used in our previous work (Chapter 3), $\gamma = 7/5$, to make the calculations easier. This affects the results quantitatively, for example the lifetime of a first core can be longer about a factor of two at most, but the qualitative scenario is still valid. We use the compiled tables of Rosseland and Planck mean opacities of

Semenov et al. (2003) and Ferguson et al. (2005). The number of grid points in each level of the nested-grids is $64^3$, and the finer grid is generated around the center of the computational domain to resolve the local Jeans length with at least 16 grid cells to prevent artificial fragmentations (Truelove et al., 1997).

We calculated three models for comparison: *S1* is a non-rotating $1M_\odot$ model, *R1* is a rotating $1M_\odot$ model, and *R01* is a rotating very low-mass model whose mass is $0.1M_\odot$. As the initial conditions, we take critical Bonnor-Ebert-like spheres with uniform rotation, and increase the density by a factor of 1.6 to make them unstable. The initial gas densities at the center and the radii of the clouds are $(\rho_c, R_c) = (3.2 \times 10^{-18}\ \mathrm{g\,cm^{-3}},\ 6300\ \mathrm{AU})$ in *S1* and *R1*, and $(\rho_c, R_c) = (3.2 \times 10^{-16}\ \mathrm{g\,cm^{-3}},\ 630\ \mathrm{AU})$ in *R01*. It is not trivial how we should scale the angular velocity between models with different masses, but here, we assume that both *R1* and *R01* initially have the same amount of rotational energy, $T \equiv \alpha M R^2 \Omega^2$ ($\alpha$ is a constant of order unity). The initial angular velocities are $4.3 \times 10^{-14}\ \mathrm{s^{-1}}$ and $1.4 \times 10^{-12}\ \mathrm{s^{-1}}$ in *R1* and *R01*, respectively. We adopt the boundary conditions that all the cells outside the sphere of the cloud radius maintain their initial values. The initial gas temperature and boundary conditions for radiation transfer are set to 10K. Our boundary conditions allow the gas to inflow into the computational domain through the boundaries, and at the end of the simulations about 30% of the initial mass increased in the low-mass case and less than 10% increased in the $1M_\odot$ cases.

## 5.3 Results

We show the cross sections of the gas density and temperature of Model *R1* and Model *R01* at the epoch when they have the same first core masses, $1.06 \times 10^{-1} M_\odot$, in Figure 5.1. Here, the first core mass $M_{\mathrm{FC}}$ is defined as

$$M_{\mathrm{FC}} = \sum_{\rho > \rho_{\mathrm{FC}}} \rho \Delta V_c, \tag{5.1}$$

where $\Delta V_c$ is the volume of the cell and $\rho_{\mathrm{FC}}$ is the critical density defined as the minimum density in the gas that experienced the shock, which we identified as the region where the radial velocity is smaller than the local sonic speed, $|v_r| < c_s$. The age of the first core at this epoch, $t_{\mathrm{FC}}$, is 3,100 yrs in *R1* and 10,600 yrs in *R01* from the core-formation. Model *R01* has a significantly larger ($\sim$ 100 AU) first core disk because it is more evolved and the gas with a larger specific angular momentum from the outer region has accreted onto the core. But note that the detailed differences between models depend on the initial parameters. Since we cannot construct “the same” initial conditions for different masses, we should focus on clear tendencies which

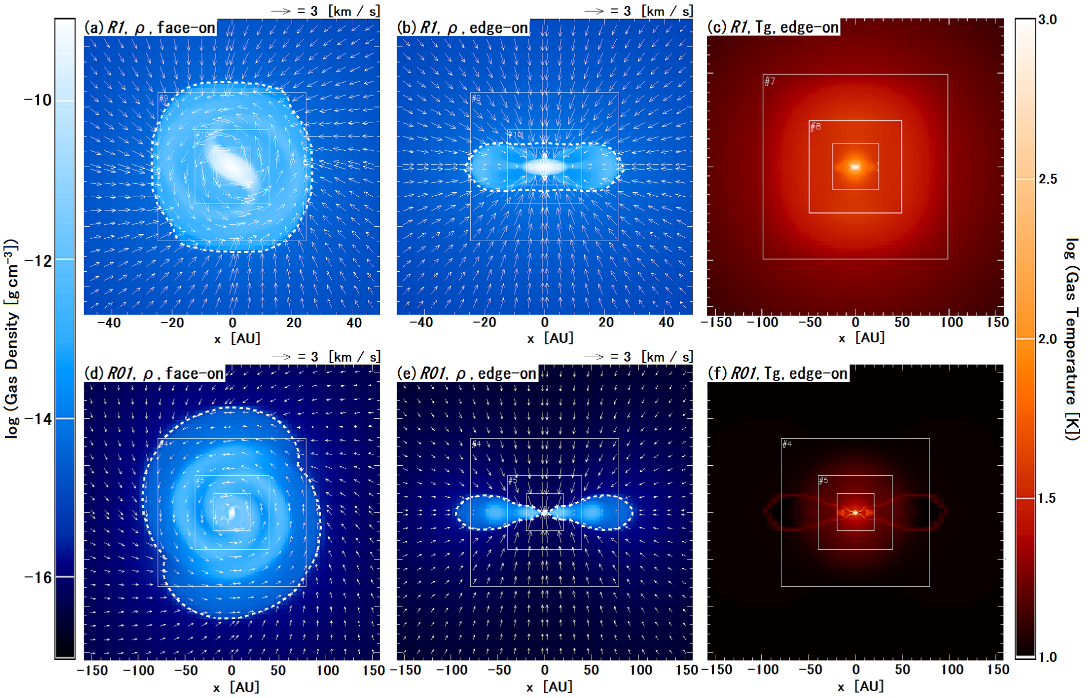

Figure 5.1: Horizontal (a, d) and vertical (b, c, e, f) cross sections of gas density (a, b, d, e) and temperature (c, f) at the epoch of the same first-core masses. (a)-(c): *R1* at $t_{\rm FC} = 3,100$ yrs, (d)-(f): *R01* at $t_{\rm FC} = 10,600$ yrs. The first cores are indicated by white dashed lines. $\rho_{\rm FC} = 1.0 \times 10^{-14}$ g cm$^{-3}$ and $7.6 \times 10^{-16}$ g cm$^{-3}$ in *R1* and *R01*, respectively. Despite the same first core masses, the envelope in *R01* is clearly depleted and colder. Note that the spatial scales in (a) and (b) are different from others.

we can give physical explanations. Another outstanding difference between the models can be seen in the gas density and temperature in their envelopes. For the low mass core model, almost all the materials in the natal core have already accreted onto the first core, and therefore, the gas density in the envelope is reduced drastically. Two factors cause the lower temperature in the envelope of *R01*: the smaller accretion rate in the very low-mass core results in the weaker shock at the surface of the first core, and thus, less entropy is produced at the shock (in other words, the first core is intrinsically colder and fainter), and the smaller optical depth of the envelope contributes to the efficient radiation transport and cooling. These characteristics result in the differences in the observational appearances of the two models.

In Figure 5.2, we show the time-evolution of physical quantities in each model such as central gas density (a), temperature (b), first core mass (c) and accretion rate onto the first core (d). It is obvious that *R01* has a smaller accretion rate and its mass increases more slowly than in other models. As a result, the gas density and temperature at the center of the first core evolve significantly slower. The lifetime of the first core, from its formation to the second collapse, reaches more than $10^4$ yrs in

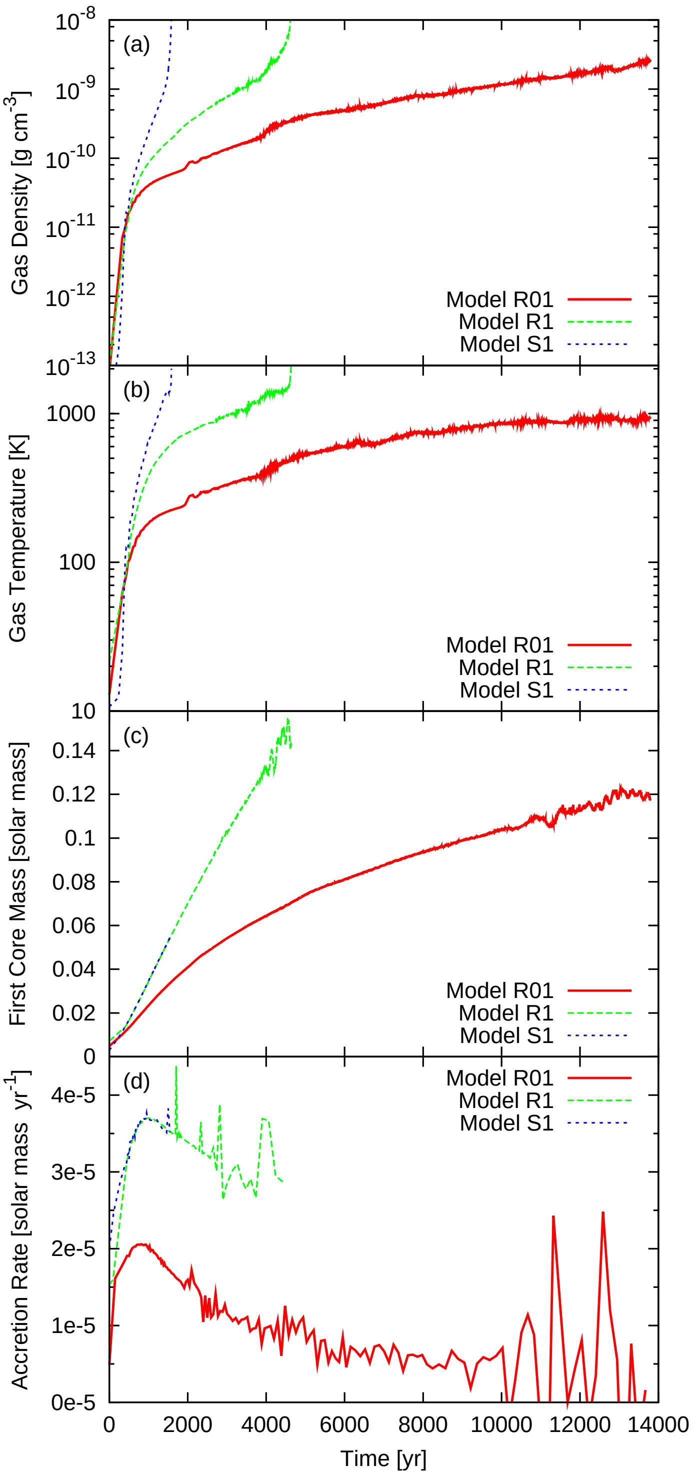

Figure 5.2: Time-evolution of the physical quantities, central gas density (a), temperature (b), first core mass (c), and smoothed accretion rate (d). Model *R01* shows prominently longer lifetime than $1M_\odot$ models, *S1* and *R1*.

*R01*. Both $1M_\odot$ models achieved similar accretion rates because the initial structure of the cloud core determines the accretion rate (Saigo et al., 2008), although the non-rotating model evolves faster than the rotating model. These results clearly indicate that centrifugal force supports a considerable mass and prevents the first core from collapsing. We note that the lifetime of the non-rotating model is longer than previous predictions (Masunaga & Inutsuka, 2000), by about a factor of two, because we assume a simple stiff EOS of $\gamma = 5/3$, and our model has a smaller accretion rate due to stable initial conditions. But in the rotating models, the difference of EOS affects the results less significantly because the centrifugal force dominates the structure of the first core disk.

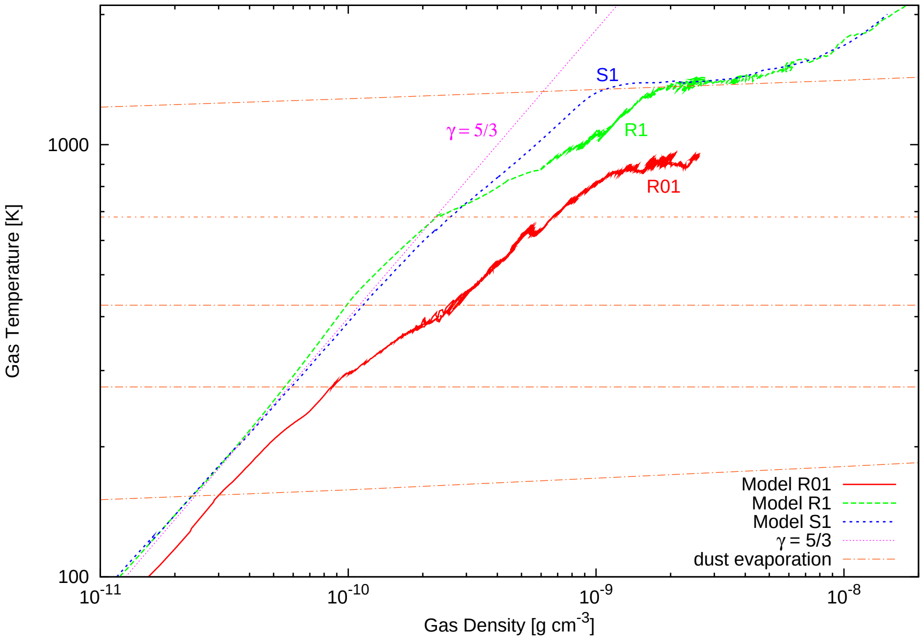

Figure 5.3: The evolution tracks of the thermal properties of the central gas elements in the $\rho - T$ plane. The dust evaporation temperatures are over-plotted with orange dash-dotted lines. All the models show the influence of radiation cooling but it is most significant in the low mass model.

We show the thermal evolution tracks of the gas elements at the center of the clouds in the $\rho - T$ plane in Figure 5.3. All the models show the effects of radiation cooling, but it appears most significantly in the low mass model. We also plot the evaporation temperatures of each dust component, which affect the thermal evolution of the gas. When the gas temperature reaches the evaporation temperature of iron and silicates, $T \sim 1400$ K, the opacity drops substantially and the core collapses violently, similar to the second collapse due to the endothermic reaction of hydrogen molecule dissociation. However, if we adopt a soft EOS with $\gamma = 7/5$, the impact of dust evaporation becomes less important because the gas density (and therefore the optical depth) at the same temperature is higher. Thus the effect of radiation cooling is important in the low mass core where dynamical accretion does not dominate the evolution. RHD simulations are required for these systems because the barotropic approximation fails to reproduce the realistic thermal evolution.

Our results show that the low-mass model has a longer lifetime compared to the dynamical time-scale of its natal core. This suggests that a large fraction of low-mass cores can harbor a first core when we carry out an unbiased survey of collapsing starless cores. Although only a small fraction of the low-mass cloud cores may be gravitationally bound and will collapse into stars, there are a lot of low mass cores in star-forming regions, and we can, therefore, expect that a considerable number of ELFs can form.

## 5.4 Observational Properties of First Cores

We calculated the SEDs of first cores in the RHD simulations by performing post-processing radiation transfer. For the details of calculations, see the previous Chapter. We adopt the monochromatic dust opacities provided by Semenov et al. (2003), using the homogeneous aggregates model of normal abundances. We should be careful when we simulate observations because the dust opacities have large uncertainties and there are significant model dependencies.

In Figure 5.4, we show the SEDs of our RHD models in the face-on configurations. For comparison, we also plot the SED of $0.1 M_{\odot}$ Bonnor-Ebert sphere, a model of a low mass starless core, and observed SED of L1521F-IRS (Bourke et al., 2006), which is a very low-luminosity object (VeLLO) in the Taurus molecular cloud. The distance toward the targets is set to 150 pc and the SEDs are measured with a $(1000\ \mathrm{AU})^2$ aperture. The flux in the far-infrared wavelengths increases when the first core forms. We can expect that we can observe the emissions from first cores with *Herschel*. Compared to L1521F-IRS, Model *R1* has similar brightness in submillimeter region but it disagrees in the mid-infrared region. In contrast, Model *R01* is fainter than L1521F-IRS in all the wavelengths. In radio wavelengths, in spite of the larger mass of one order of magnitude, *R1* is only about twice as bright as *R01*. However, the peak flux around the far-infrared wavelengths is significantly larger in *R1*. This is because it has a warmer first-core disk and envelope, as we mentioned before (Fig. 5.1). In contrast, *R01* is more luminous in the mid-infrared wavelengths because it has a thinner envelope. If we follow the more long-term evolution of the low mass cloud model, this tendency is enhanced. Our models may explain the weak emission in mid-infrared wavelengths in some observed first core candidates (Enoch et al., 2010). We will discuss the time-evolution of observational properties of first cores in a subsequent paper.

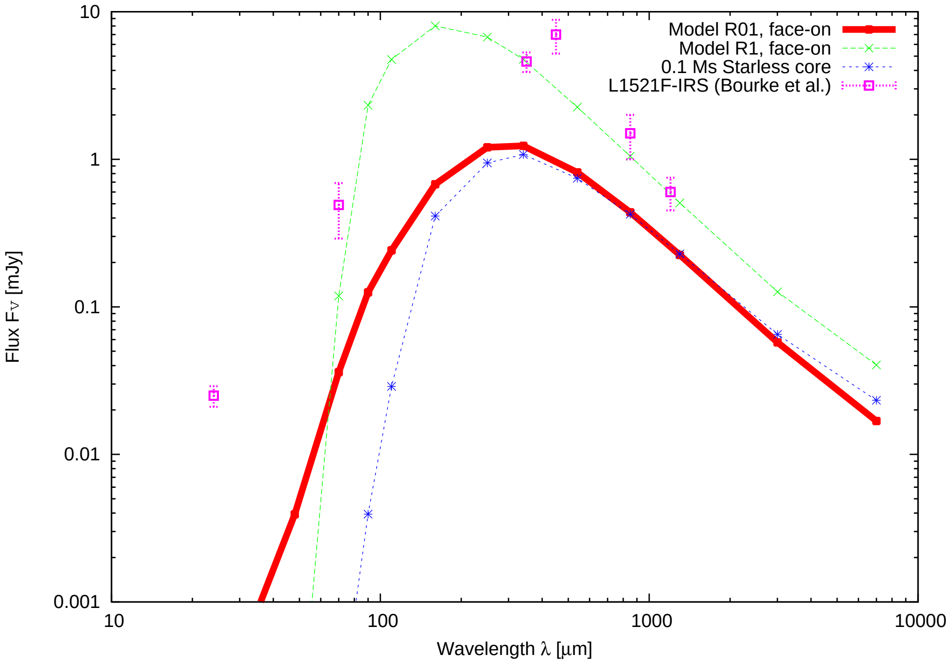

Figure 5.4: SEDs of the first core models at the same epoch as in Figure 5.1 in face-on configuration and a $0.1M_\odot$ star-less core. The observed SED of L1521F-IRS (Bourke et al., 2006) is also plotted. The distance toward the targets is 150 pc and the aperture is $(1000\ \mathrm{AU})^2$. First cores are more luminous than starless cores, especially in the far-infrared wavelengths. Model *R1* is brighter than Model *R01* in radio wavelengths. On the other hand, Model *R01* exceeds Model *R1* in the mid-infrared region.

First cores emit larger flux in the infrared region than starless cores, but it is still difficult to identify the existence of a first core only from the SED, because it is so faint in the infrared wavelengths and the differences in radio wavelengths between the first cores and the starless cores are not so prominent. Another good method to distinguish first cores from starless cores is high resolution observation measuring visibility amplitude (Fourier components of the intensity map) distributions with (sub)millimeter interferometers. We show simulated visibility amplitude profiles of Model *R01* measured in 850 $\mu$m, obtained with the Common Astronomy Software Applications (CASA) in Figure 5.5. The visibility amplitude of the starless core decreases steeply in the small scale because it contains no fine structure. In contrast, the first core clearly shows a shallow distribution. This feature is not solely seen in the ELF but common in first cores. This is firm evidence of the existence of the first cores. Current observations with SMA is not sufficient to resolve the first core directly, but sufficient to identify the first core. ALMA in full operation will reveal the detailed structure of first cores.

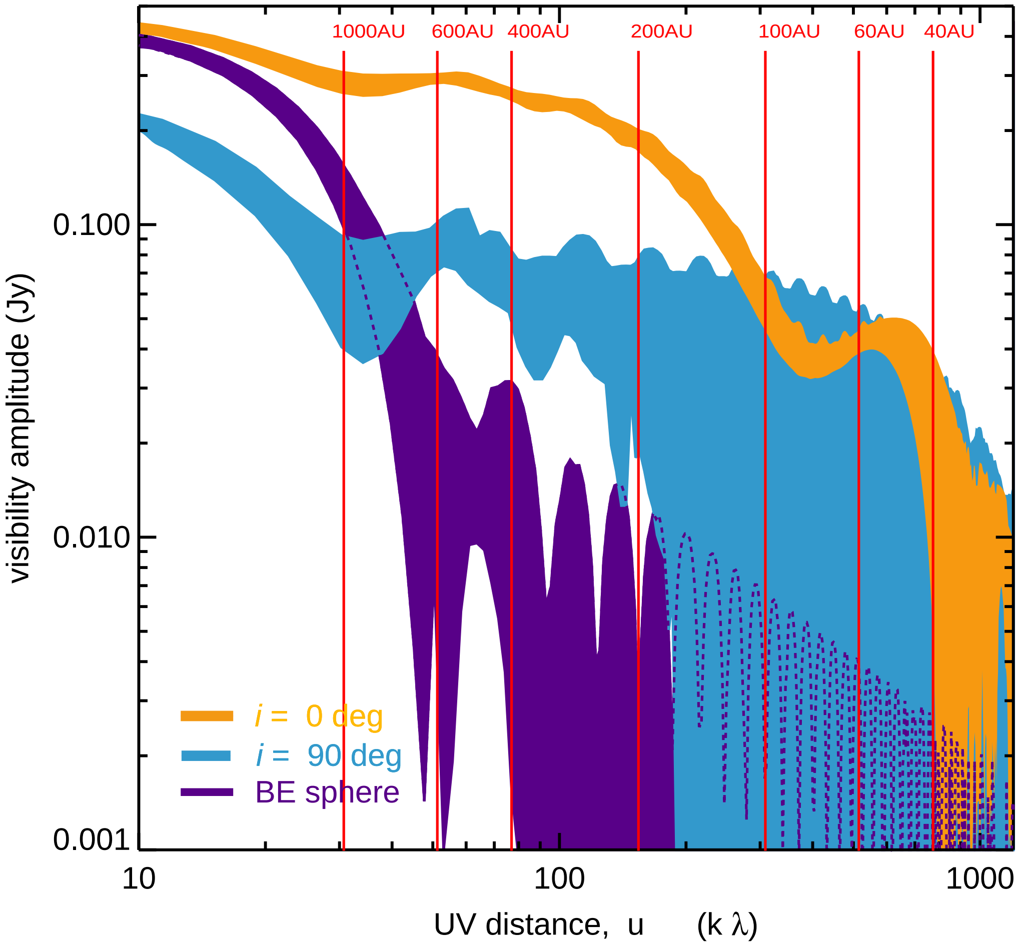

Figure 5.5: Visibility amplitude distributions of the 0.1 $M_\odot$ first core model and a 0.1 $M_\odot$ Bonnor-Ebert sphere as a model of a starless core. The first core model shows clearly shallower distribution compared to the starless core. The edge-on configuration shows more widely scattered visibility amplitude corresponding to its oblate morphology. Note that the small amplitude oscillations in the large UV disntace are originated from the finite volume effect.

## 5.5 Conclusions and Discussions

We performed 3D RHD simulations of low-mass cloud cores and showed that first cores formed in very low mass ($0.1M_\odot$) cloud cores live more than $10^4$ yrs. Those first cores have thin envelopes, therefore we name this first core an "Exposed Long-lifetime First core (ELF)." ELFs experience different evolution from ordinary first cores whose evolution is dominated by accretion from the natal core. ELFs use up the gas in the envelope in the early stages of their evolution, and then the mass and angular momentum redistribution in the disk control the evolution of ELFs. Radiation cooling plays a critical role there similar to the Kelvin-Helmholtz contraction, dominating the disk stability and angular momentum transport with the time-scale longer than the dynamical time-scale of accretion. Thus, the evolution of ELFs is qualitatively different from that of the first cores formed in ordinary mass cloud cores, which have been well studied so far. The gas in ELFs does not behave adiabatically anymore and the barotropic approximation breaks down.

We also calculated the observational properties of ELFs. We found that in radio and far infrared wavelengths they have slightly fainter but quite similar SEDs to ordinary mass first cores. This fact suggests that ELFs are detectable as well as ordinary first cores and they can be detected even with current instruments like SMA. On the other hand, ELFs are more luminous in the mid-infrared region because they have less massive envelopes than those of typical first cores.

In this work we omitted the effects of magnetic fields. Magnetic fields accelerate the evolution of first cores by very efficient angular momentum transport and shorten the lifetime. On the other hand, the outflow driven by magnetic fields carries gas away from the first core. This effect will be more significant in very low mass cores. We will study this problem including magnetic fields in future, but leastwise, the mechanism proposed here must work even under the presence of magnetic fields and the first core lifetime must be longer in such low mass cores because the accretion rate itself is smaller.

Very low-mass cores will not collapse so often by self-gravity and the formation probability of ELFs may be low. However, ELFs are still worth considering because there are a number of low-mass cores both in observations (Motte et al., 1998; Enoch et al., 2007; Rathborne et al., 2009; André et al., 2010) and in theoretical predictions (Padoan & Nordlund, 2002; Hennebelle & Chabrier, 2008). ELFs are long-lived compared to the dynamical time-scale of their natal cloud cores, so observation possibilities are higher than for usual first cores. Therefore, we can expect a considerable number of ELFs exist in the star-forming regions. Other mechanisms such as external pressure, cloud-cloud collision, radiation driven implosion (Motoyama et al., 2007), and dynamical ejection (Bate, 2009a) may help the formation of ELFs.

# Chapter 6

# Protostellar Collapse II: Second Collapse

## 6.1 Backgrounds

In previous studies, the second collapse phase and formation of protostellar (or second) cores have been rarely studied because such simulations require extremely high spatial resolution and therefore cost a lot of computational resources. To avoid such expensive calculations and perform long-term simulations, the sink particle technique is often adopted (Bate et al., 1995; Krumholz et al., 2004; Federrath et al., 2010), in which gas entering a sink zone is removed from the hydrodynamic calculation and treated as a collisionless accreting particle. However, the environment in the vicinity of the protostar should have significant impact on the feedback from the protostar, and therefore affect the global evolution of collapsing cloud cores (like the flash light effect, Yorke & Bodenheimer (1999)). Moreover, the early evolution of protostars must be influenced by the accretion flow properties (Baraffe et al., 2009; Hosokawa et al., 2011a). Therefore, it is of crucial importance to investigate the detailed physics resolving the protostellar core itself.

In spherically symmetric configurations, the second collapse and subsequent evolution of the protostellar core were well studied using radiation hydrodynamic simulations (Larson, 1969; Winkler & Newman, 1980a,b; Stahler et al., 1980a,b, 1981; Masunaga & Inutsuka, 2000). Bate (1998) first showed the whole evolution from molecular cloud cores to protostellar cores with 3D SPH simulations, and Machida et al. (2006) performed nested-grid MHD simulations of protostellar collapse until the second core formation. In those simulations, they adopted the barotropic approximation for gas thermodynamics in which the thermal evolution is approximated with simple polytropic relations mimicking the results of 1D RHD simulations (e.g., Masunaga & Inutsuka (2000), Figure 1.4), instead of solving radiation transfer.

Recently, Bate (2010, 2011a) (see also (Whitehouse & Bate, 2006)) reported 3D SPH FLD RHD simulations of formation of protostellar cores. Schönke & Tscharnuter (2011) also performed similar calculations of protostellar collapse using 2D axisymmetric FLD RHD simulations. They commonly found interesting phenomena happen when the protostellar cores form; a bipolar outflow is temporarily launched from the first core disk via radiation heating (not radiation force) from the protostellar core. Considering the energy released in the second collapse and subsequent accretion onto the protostellar core, the irradiation is sufficient to heat up the gas in the first core disk and launch the outflow (Bate, 2011a). The precedent studies with the barotropic approximation did not reproduce such outflows driven by radiation heating. The structure of the first core disk which is affected by the angular momentum distribution seems to be important in this phenomenon, and in an extreme case, the first core disk is almost blown up (Schönke & Tscharnuter, 2011). Such violent phenomena may affect the story of protostellar collapse, circumstellar disk formation, and evolution of protostars.

It is well known that magnetic fields play significant roles in the angular momentum transport in protostellar collapse. Therefore, it will be crucial to treat both radiation transfer and magnetic fields in simulations to understand the formation of the protostellar core. In this Chapter, we report the first 3D RMHD simulations of protostellar core formation using our newly-developed 3D nested-grid resistive RMHD simulation code. The goal of this study is to reveal the realistic evolution in the early phase of protostellar collapse (i.e., until the formation of the protostellar core) involving both radiation transfer and magnetic fields.

## 6.2 Methods and Models

We perform 3D RMHD simulations of protostellar collapse entirely from molecular cloud cores to protostellar cores using our code described in Chapter 2. We setup the initial conditions according to the procedure described in Section 2.3.8; first we prepare a critical BE sphere of 10K with the central gas density $\rho_c = 10^{-18}\,\mathrm{g\,cm^{-3}}$, and increase the gas density by 20 % to make it gravitationally unstable. Then we have the unstable BE like sphere whose mass and radius are $M \sim 1 M_\odot$ and $R \sim 4.25{\times}10^{-2}\,\mathrm{pc} \sim 8800\,\mathrm{AU}$, respectively. The initial free fall time at the center of the cloud is $t_{\mathrm{ff}} \sim 6.08 \times 10^4\,\mathrm{yrs}$. We calculated a spherically symmetric model and four magnetized rotating models with and without resistivity; the parameters of models are summarized in Table 6.1. The first letter of the model name denotes the treatment of magnetic fields: $I$ denotes an ideal MHD model and $R$ a resistive MHD model. The second letter represents the initial rotation speed: $F$ is fast and $S$ is slow. Note that we choose these parameters so that the first core disks do not fragment because of the limitation of our nested-grids.

| Model | $\Omega t_{\rm ff}$ | $\Omega\,(\times 10^{-14}\,{\rm s}^{-1})$ | $B_0\,(\mu{\rm G})$ | $\mu_0$ | $\lambda_0$ | $A_2$ | Resistive? |
|---|---|---|---|---|---|---|---|
| *SP* | 0 | 0 | 0 | $\infty$ | $\infty$ | 0 | – |
| *IS* | 0.023 | 1.2 | 20 | 3.8 | 7.2 | 0.1 | N |
| *IF* | 0.046 | 2.4 | 20 | 3.8 | 7.2 | 0.1 | N |
| *RS* | 0.023 | 1.2 | 20 | 3.8 | 7.2 | 0.1 | Y |
| *RF* | 0.046 | 2.4 | 20 | 3.8 | 7.2 | 0.1 | Y |

Table 6.1: Summary of the initial model parameters. From left to right: the normalized angular velocity, the angular velocity, the magnetic field strength, the averaged mass-to-flux ratio, the local mass-to-flux ratio at the cloud center, the amplitude of $m = 2$ perturbation and whether the resistivity is introduced or not. Other parameters are common: $M = 1\,M_\odot$, $R \sim 8800\,{\rm AU}$, $\rho_c = 1.2 \times 10^{-18}\,{\rm g\,cm^{-3}}$, and $T_0 = 10\,{\rm K}$.

Model *SP* is the spherical model without rotation and magnetic fields. For magnetized models, we impose the uniform magnetic fields of $20\,\mu$G parallel to the rotation axis. The corresponding mass-to-flux ratio normalized by the critical value of stability is $\mu_0 \equiv \frac{M/\Phi}{(M/\Phi)_{\rm crit}} \sim 3.8$ where $\Phi = \pi R^2 B_0$ and $(M/\Phi)_{\rm crit} = \frac{0.53}{3\pi}\left(\frac{5}{G}\right)^{1/2}$. Here we adopt the critical mass-to-flux ratio of Mouschovias & Spitzer (1976) but we should regard this value as just a guide because our initial conditions are not uniform. There is another similar threshold for stability between gravity and magnetization derived for disks (Nakano & Nakamura, 1978); we have $\lambda_0 \equiv \frac{\Sigma_0/B_0}{(\Sigma/B)_{\rm crit}} = 7.2$ at the center of the cloud, where $(\Sigma/B)_{\rm crit} = (4\pi^2 G)^{-1/2}$. These mass-to-flux ratios indicate that our magnetized models are in the magnetically super-critical regime but considerably magnetized.

In this Chapter, we redefine the origin of time as the epoch of formation of the protostellar core, i.e., when the central gas density exceeds $\rho_c = 10^{-3}\,{\rm g\,cm^{-3}}$ for the first time, for descriptive purpose.

## 6.3 Results

### 6.3.1 Spherical Model

First, we show the results of the spherical model *SP* to understand the whole evolution from a molecular cloud core to a protostellar core, and to demonstrate validity of our code. We show the profiles of the gas density and temperature in Figure 6.2 and 6.3 and the thermodynamic properties in the $\rho - T$ plane in Figure 6.4.

#### Thermal Evolution and EOS

Before discussing the global structure and evolution, we discuss the thermal evolution of the central gas element. To see the effects of EOS on the thermal evolution, we show the evolution track of the central gas element in the $\rho - T$ plane and the adiabatic index $\Gamma$ in Figure 6.1.

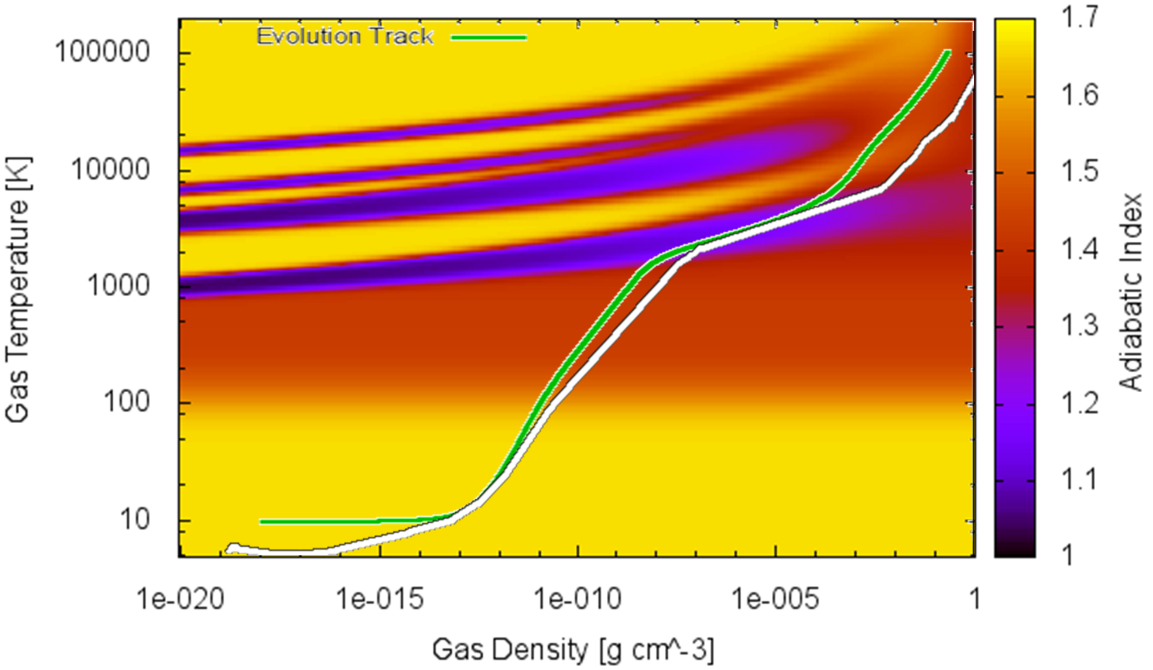

Figure 6.1: The evolution track of the central gas element (green) in *SP* overplotted on the distribution of the adiabatic index $\Gamma$ in the $\rho - T$ plane. The same track adapted from Masunaga & Inutsuka (2000) is also overplotted (white).

While the gas density is low ($\rho_c \lesssim 10^{-13}\,\mathrm{g\,cm^{-3}}$), the gas collapses isothermally because the radiation cooling is very efficient, and EOS does not matter in this regime. When the gas density gets sufficiently high and radiation cooling becomes inefficient, the gas starts to evolve quasi-adiabatically and the temperature starts to rise. Beyond this point, the EOS plays almost dominant roles in the thermal evolution of the gas (at the center of the cloud; note that the gas in outer region can be affected by radiation transfer). While the gas is still cold ($T_c \lesssim 100\,\mathrm{K}$), the adiabatic index $\Gamma$ is about $5/3$ because the rotational transitions cannot be excited and molecular hydrogen behaves like monoatomic molecules. $\Gamma$ becomes $\sim 7/5$ when the gas becomes warm enough to excite rotation (actually $\Gamma$ is slightly larger than $7/5$ because of the contribution from helium). When the temperature exceeds $T_c \sim 2000\,\mathrm{K}$, molecular hydrogen starts to dissociate and it triggers the second collapse. The endothermic reaction of hydrogen molecule dissociation significantly decreases the effective adiabatic index to $\gamma \sim 1.1$, below the critical value of stability of a self-gravitational sphere, $\gamma_{\mathrm{crit}} = 4/3$. After the completion of the dissociation, the gas evolves quasi-adiabatically again, although the ionization of hydrogen and helium slightly affect the evolution making the adiabatic index softer. From the figure, we can see that the ionization of hydrogen and helium does not cause the "third collapse"; those endothermic reactions proceed gradually because the reverse reactions (recombinations) occur rapidly in the high density regions and the adiabatic index remains larger than the critical value[1].

Actually, just before the onset of the second collapse, the gas experiences radiation cooling when the opacities drop suddenly at $T_c \sim 1500\,\mathrm{K}$ due to the dust evaporation. However, its effect does not seem prominent in spherically symmetric cases.

Compared to the evolution track of Masunaga & Inutsuka (2000), the gas in our simulation goes along a track with higher entropies. Those differences must be caused mainly by the differences in EOS because the radiation transfer does not significantly affect the thermal evolution after the first core formation and both simulations have similar thermal properties when the first cores are formed. A part of this difference possibly comes from the different treatment of EOS; we calculate the internal energy directly from the partition functions, but Masunaga & Inutsuka (2000) derive the heat capacity $C_V$ from the partition functions and use the relation $e = C_V T$, which is valid only in the completely ideal case. This treatment results in the softer effective adiabatic index $\gamma$ (Boley et al., 2007), which may explain the difference in Figure 6.1. In the protostellar core phase, the non-ideal effects can cause the difference; we simply neglected the non-ideal effects for which Masunaga & Inutsuka (2000) adopted the EOS of Saumon et al. (1995). For the details of EOS, see Section 2.3.6. On the other hand, Bate (2011a) showed very similar evolution tracks to our results because we and they consider virtually the same thermodynamic processes in EOS.

Note that in this work we adopt the ortho:para ratio of 3:1, but if we assume the equilibrium ratio, additional energy is consumed to convert the parahydrogen to the orthohydrogen ($\Delta E \sim 170\,\mathrm{K}$), resulting in the softer effective adiabatic index (Boley et al., 2007; Stamatellos & Whitworth, 2009). The gas does not forget the thermal history in this phase because its evolution is almost completely adiabatic, therefore the ortho-para ratio has non-negligible impact on the whole star formation processes. We have to keep it in mind that the differences in EOS quantitatively affect the evolution and properties of the first and second cores, such as the radius of the protostellar core.

### First Core

The first core is formed at $t \sim -650\,\mathrm{yr}$. Its radius is initially about $\sim 5.4\,\mathrm{AU}$, and contracts gradually to $\sim 3\,\mathrm{AU}$ as it evolves. The evolution and structure of the first core are in good agreement with the results of 1D spherically symmetric RHD simulations using the full non-gray radiation transfer (Masunaga et al., 1998; Masunaga & Inutsuka, 2000) and 3D SPH RHD simulations using the gray FLD approximation (Whitehouse & Bate, 2006). The outer region attains a higher entropy than the central gas element

---

[1] We thank Prof. Inutsuka for his thoughtful suggestion on this point.

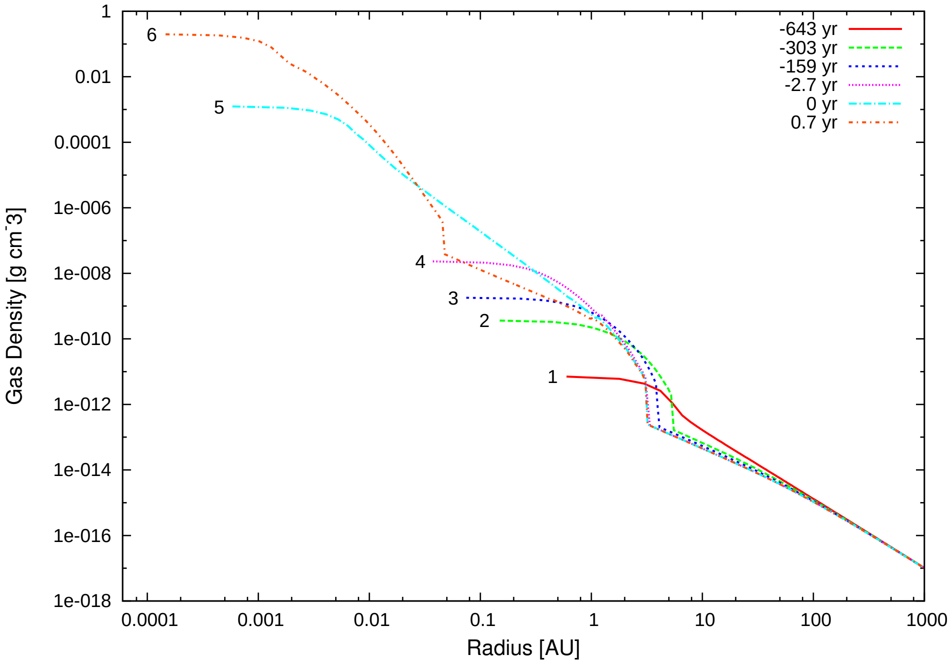

Figure 6.2: The evolution of the gas density profile in Model *SP*.

because of heating at the shock and radiation from the central hot region (see Chapter 3). The shock at the surface of the first core is isothermal, i.e., it is a supercritical shock as discussed in Commerçon et al. (2011a). The lifetime of the spherical first core is a bit longer than that in Bate (2011a), this is probably due to the choice of the initial density profile; Bate (2011a) adopted uniform spheres with higher central density, which are more unstable and give higher accretion rate than our BE spheres.

When the temperature exceeds the evaporation temperature of all the dust components ($T \sim 1500\,\mathrm{K}$), the opacities around the central region drop significantly. The temperature within this dust free region becomes almost flat. As Figure 6.3 indicates, the dust evaporation front is located at $R \sim 1.2\,\mathrm{AU}$ at the end of the (pure) first core phase ($t \sim -2.7\,\mathrm{yr}$). Schönke & Tscharnuter (2011) pointed out the importance of the dust evaporation on the dynamics of first cores, but it does not seem to be prominent in spherically symmetric cases, and probably therefore it is not discussed in previous studies.

### Protostellar Core

The second collapse begins when the central temperature exceeds $T_c \sim 2000\,\mathrm{K}$. Soon after the onset of the second collapse, the protostellar core forms in the short dynamical timescale of several years (the free fall time corresponding to the central density when the second collapse starts ($\rho_c \sim 10^{-8}\,\mathrm{g\,cm^{-3}}$) is only about 0.67 yr). Within 0.7 years

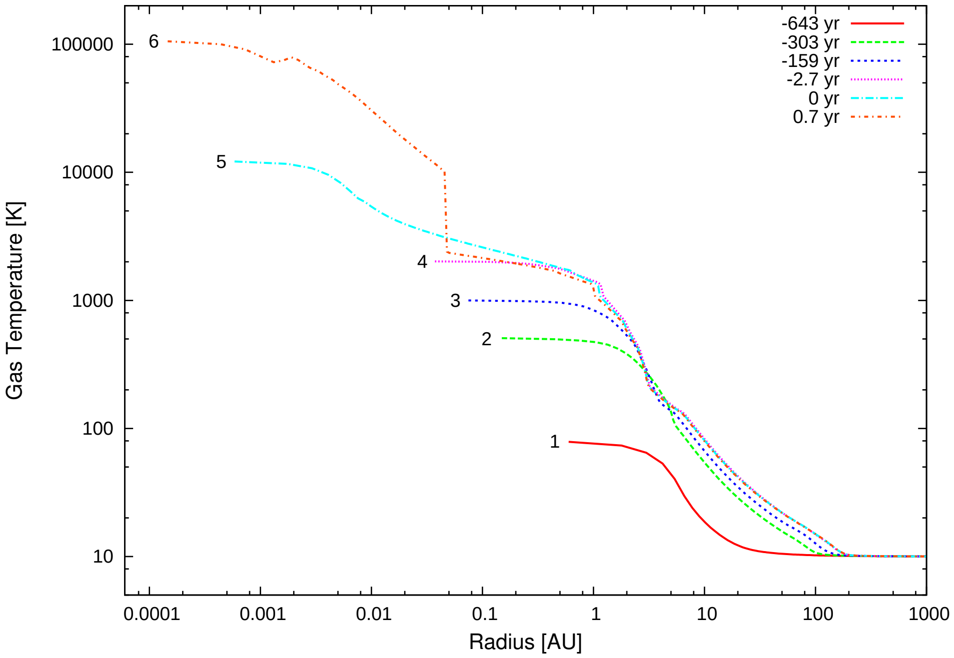

Figure 6.3: The evolution of the gas temperature profile in Model *SP*.

after the formation of the protostellar core, it acquires $M_{\rm PC} \sim 2\times10^{-2}\,M_\odot$ and averaged accretion rate is very high, $2.7\times10^{-2} M_\odot\,{\rm yr}^{-1}$. The protostellar core expands due to the addition of newly accreted gas and the accretion shock at the surface of the protostellar core quickly propagates outward. The jump condition at this shock is almost adiabatic, which means that the flow is radiatively inefficient ("hot accretion") in this early phase. The outer region of the protostellar core is heated up by the shock and attain a high entropy, leading the protostellar core to be initially convectively stable (Stahler et al., 1980a,b). At the end of the simulation, the radius of the protostellar core is about $R_{\rm PC} \sim 0.047\,{\rm AU} \sim 10R_\odot$. From the virial theorem, the energy released in this phase can be estimated to be $\frac{GM_{\rm PC}^2}{2R_{PC}} \sim 6.8\times10^{43}\,{\rm erg}$, which is consistent with the total dissociation energy of molecular hydrogen, $\frac{XM_{PC}}{2m_{\rm H}}\chi_{\rm dis} \sim 5.7\times10^{43}\,{\rm erg}$.

This radius at the end of our simulation is about 2.5 times larger than the radius of the protostellar core obtained in Masunaga & Inutsuka (2000) ($\sim 4R_\odot$), and still increasing. The expansion in the adiabatic accretion phase had been already reported in Larson (1969) and also discussed in Stahler et al. (1986) (see also Winkler & Newman (1980b)), and our radius is qualitatively consistent with their estimate, $R \gtrsim 10R_\odot$. It will expand until almost all the gas in the first core has accreted onto the protostellar core when the accretion rate gets significantly low and the optical depth of the envelope becomes low enough for radiation cooling. It will take about the average free-fall time of the whole first core, $t_{\rm ff,FC} = \sqrt{\frac{3\pi}{32G\rho_{\rm FC}}} \sim 5.5\,{\rm yrs}$ where $\rho_{\rm FC} = \frac{3M_{\rm FC}}{4\pi R_{\rm FC}^2} = 1.5\times10^{-10}\,{\rm g\,cm^{-3}}$, $M_{\rm FC} \sim 3\times10^{-2}M_\odot$ and $R_{\rm FC} \sim 3\,{\rm AU}$. Therefore this expansion is a very transient

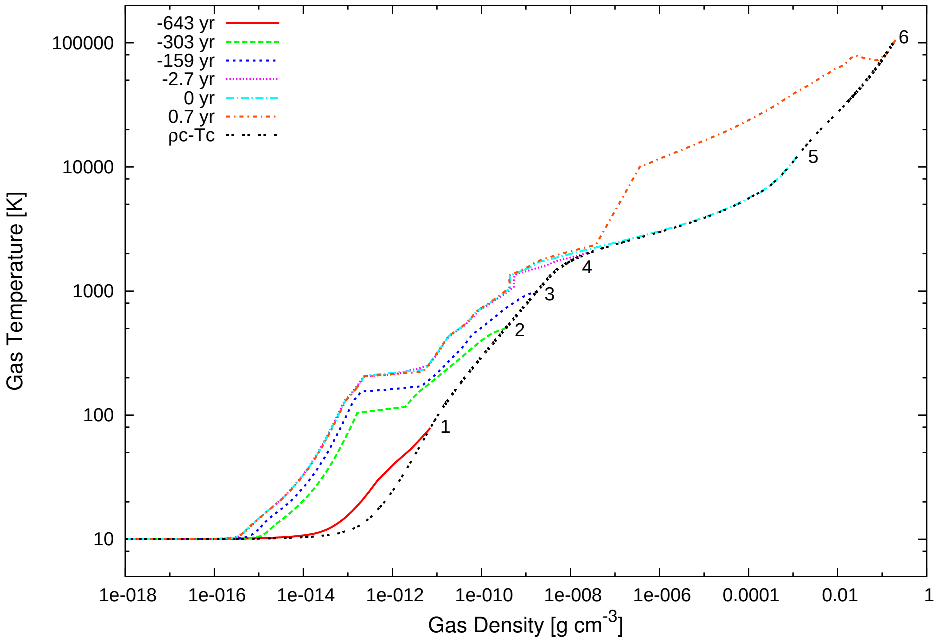

Figure 6.4: The evolution of thermodynamic properties in the $\rho - T$ plane. The evolution track of the central gas element is also plotted.

phenomenon. In other words, our protostellar core has not settled yet. Masunaga & Inutsuka (2000) showed the snapshots at just after the protostellar core formation (labeled "9") and 19 years after that ("10"), so this transient expansion could happen in their simulations but was not described (or not resolved as their simulations are fully implicit in time). This behavior is also consistent with those in SPH FLD RHD simulations of spherically symmetric cases (Bate, in private communication)[2]. Note that the gas does not flow outward in this expansion phase, but the newly accreted gas is loaded on top of the core. So it is different from the "hiccup" of the protostellar core discussed years ago (e.g., Boss, 1989). Although the EOS can cause the difference of the protostellar core properties, this transient expansion itself seems to depend weakly on the EOS.

In this work, we mainly discuss the dynamical properties of the protostellar cores such as rotation and magnetic fields which are relatively less affected by the transient phenomena (and by the differences in the EOS). When we discuss the properties sensitive to these problems, we will explicitly indicate them. Note that the effects of EOS in the first core phase are not so large but other effects such as rotation and uncertainties

---

[2] Bate (2011a) reported that the protostellar core does not expand and its radius is small, $\sim 2R_\odot$, in rotating models. It can be interpreted that in the rotating cases the heat generated at the shock is smaller because the accretion along the rotational axis is weak, and also the gas behind the shock can cool via radiation because the envelope is significantly thin in the vertical direction.

of dust properties are more significant.

The simulation timestep at the end of the simulation is about only 1 minute (!), which is extremely shorter than the timescale of star formation. So it is almost hopeless to follow the further evolution of the protostellar core with direct simulations like ours. This timescale is corresponding to the sound crossing timescale of the protostellar core, but actually we are not interested in such short-timescale oscillations; what we need in our simulations is resolving the timescale of the evolution of the protostellar core. Therefore we require to replace the region of short-timescale with a subgrid model of stellar evolution with the sink cell/particle technique. We discuss this point later (Section 6.4 and Future Prospects in Chapter 7).

## 6.3.2 Rotating Models

### Overview

First, we show the evolution tracks of the central gas density and temperature as functions of time in Figures 6.5 and 6.6. The first cores are formed when the central density exceeds $\rho_c \gtrsim 10^{-13}\,\mathrm{g\,cm^{-3}}$ and the second collapse begins when $\rho_c \gtrsim 10^{-8}\,\mathrm{g\,cm^{-3}}$. The lifetimes of the first cores are about 650, 720, 800, 850 and 950 years in Model *SP, IS, IF, RS* and *RF*, respectively. The presence of rotation extends the first core lifetime but its effect is not significant compared to non-magnetized cases (Saigo et al. (2008); Bate (2011a), see also Chapter 5). Resistive cases have slightly longer lifetimes because magnetic fields are weakened by the Ohmic dissipation and the efficiency of the angular momentum transport is reduced, but they are still not so long.

Figure 6.7 shows the evolution of the gas and magnetic fields at the center of the cloud as a function of the central gas density. We can see that the evolution track of the central gas elements are not distinguishable between models. This is because the central region of the first cores contracts almost spherically due to the efficient angular momentum transport via magnetic fields.

From the evolution of the plasma beta $\beta = \frac{P_{\mathrm{gas}}}{P_{\mathrm{mag}}}$ and the magnetic field strength at the center (normalized by the square root of the gas density), the effects of the resistivity are clearly visible. The latter quantity (panel (c) in Figure 6.7) is a good indicator of the geometry of the collapse in the central region (Machida et al., 2008a). In the ideal MHD limit, if $\frac{B_c}{\sqrt{\rho_c}}$ remains constant, it means that the Lorentz force and the centrifugal force balance with the thermal pressure gradient force and the gravity (disk-like collapse). On the other hand, if gravity dominates the collapse and thus the gas collapses almost spherically, then the magnetic field strength increases as $B_c \propto \rho_c^{2/3}$ (spherical collapse).

The ideal MHD models *IF* and *IS* show very similar evolution tracks each other.

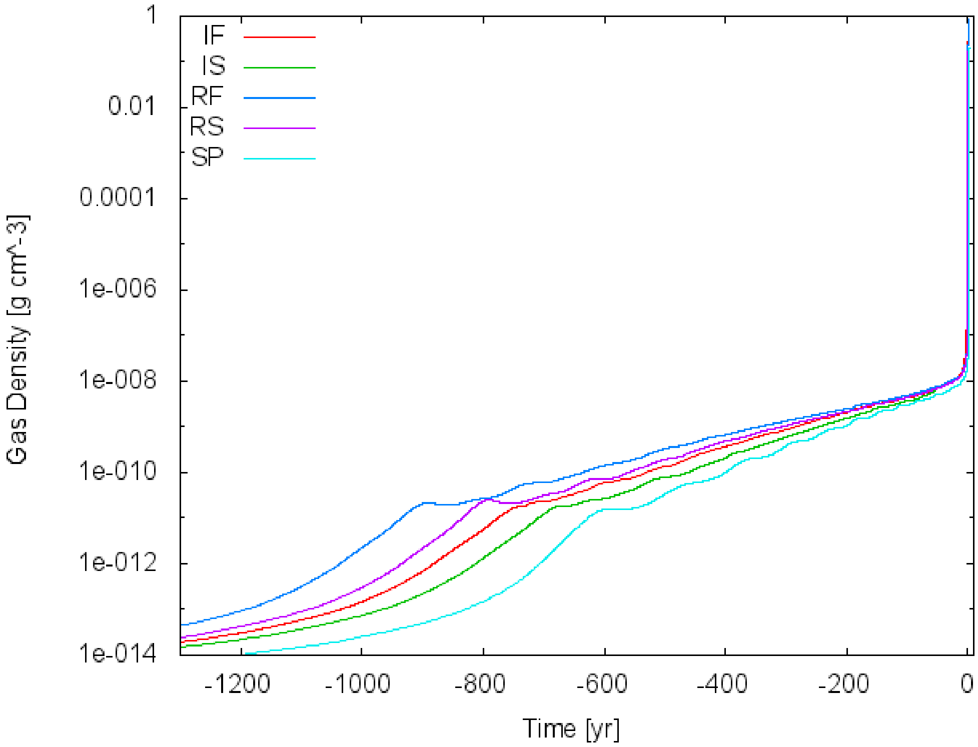

Figure 6.5: The evolution of the central gas density as a function of time.

Initially, in the isothermal phase, they collapse spherically and then disk-like. They evolve in the disk-like geometry during the first core phase. Obviously, the second collapse occurs in a spherical manner because the rotation of the first core is very slow. In the resistive models *RF* and *RS*, on the other hand, we can see the effects of Ohmic dissipation clearly. The early evolution is similar to the ideal MHD models, but the magnetic fields decrease significantly in the first core phase by an order of magnitude. Then the magnetic braking is suppressed and considerable amount of angular momentum remains in the central region of the first core. As a result, the second collapse goes spherically at first, but then turned into the disk-like collapse because of the remaining rotation. This rotation has a strong impact on the evolution in the protostellar core phase.

We should mention that the sudden drop of the magnetic flux (and the increase of the plasma beta) in the ideal MHD models around $\rho_c \sim 10^{-8}\,\mathrm{g\,cm^{-3}}$ may be originated from numerical errors. In this phase, the first cores and the surrounding (pseudo) disks warp by some reasons (see below) in the ideal MHD models. Since the magnetic fields are strongly pinched onto the disk mid-plane, the directions of the magnetic fields above and below the mid-plane are anti-parallel. In such situations, perturbation in the vertical direction easily cause numerical reconnections of the magnetic fields

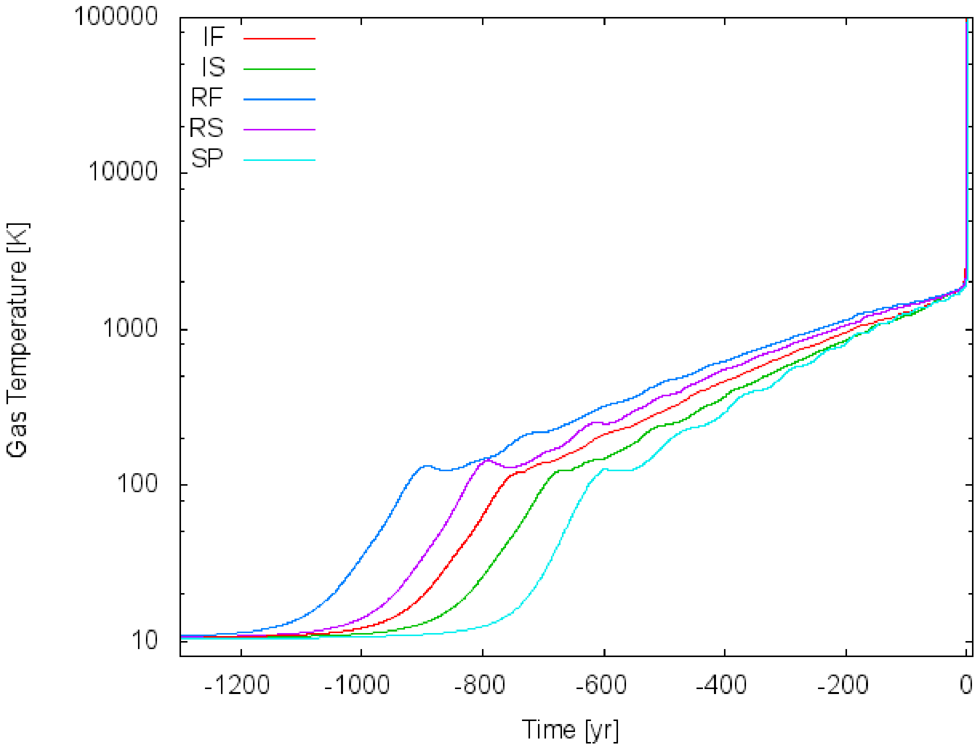

Figure 6.6: The evolution of the central gas temperature as a function of time.

(this numerical diffusion reduces the strength of the toroidal magnetic fields, although the vertical component is preserved). The first cores in the resistive models do not warp and therefore do not suffer from this problem in this phase. Similarly, all the models indicate the sudden decrease of the magnetic flux in the protostellar core phase ($\rho_c \gtrsim 10^{-2}\,\mathrm{g\,cm^{-3}}$). These are also possibly caused by numerical reconnections caused by similar mechanisms. In the resistive models, physical kink instabilities trigger these numerical reconnections in the mid-plane. Thus the magnetic fields at the very center of the cloud are numerically underestimated. However, these numerical errors are not too serious in the dynamical evolution because the total flux threading the first core vertically is not affected by these errors. If we assume the $z$-mirror symmetry like Machida et al. (2008a), we can avoid these errors but some physical phenomena like the kink instability will be also modified.

### Outflows and First Cores

We show the density and temperature distribution in the cross sections of the outflow scale (corresponding to the grid level $l = 8$ or $\sim 140\,\mathrm{AU}$) and the first core scale ($l = 11$ or $\sim 18\,\mathrm{AU}$) in Figures 6.8 – 6.15 at the end of the (pure) first core phase. We also show the profiles along $x$- and $z$-axes in Figures 6.16 – 6.19.

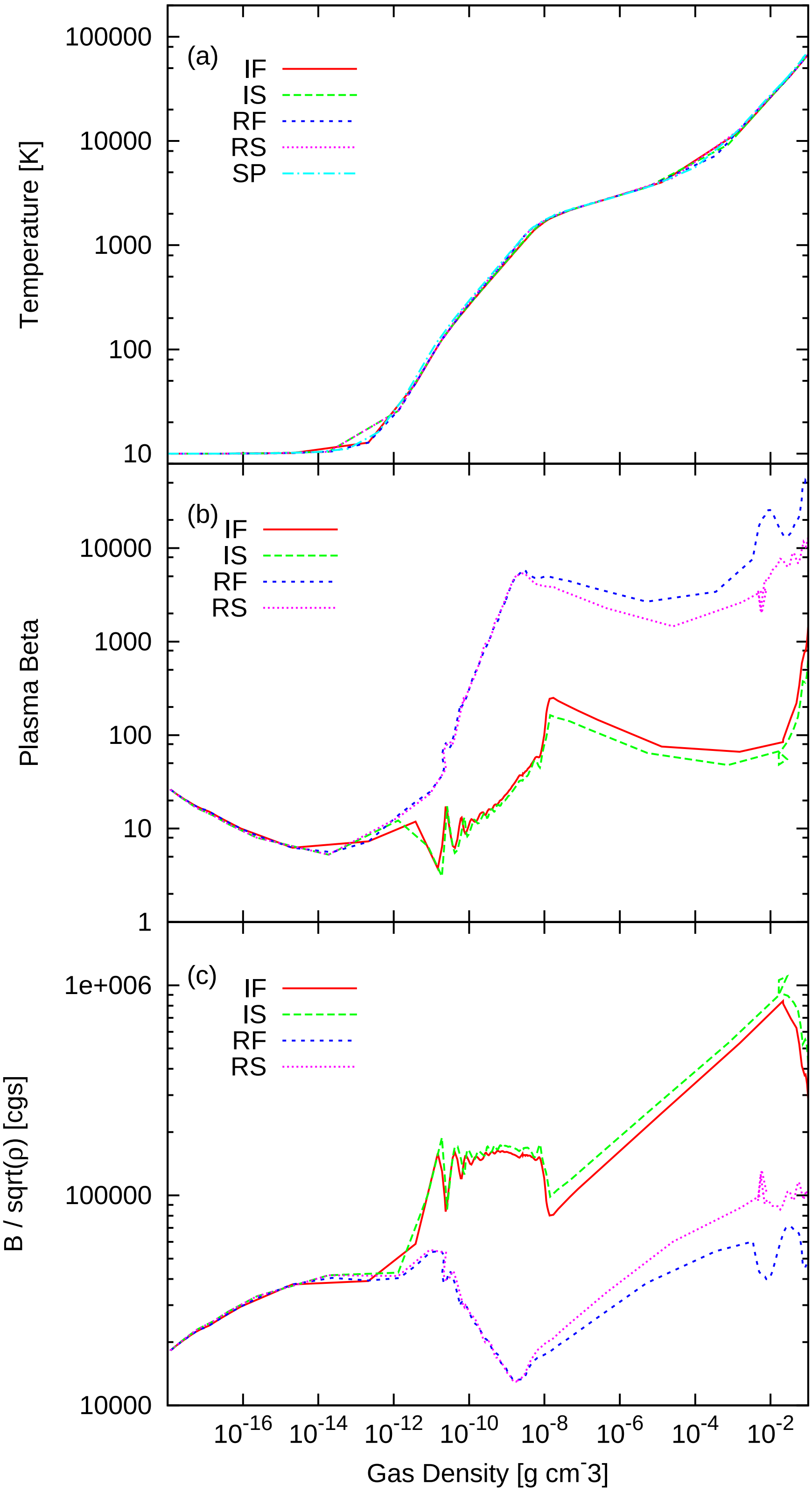

Figure 6.7: The evolution of the central gas temperature (panel a), the plasma beta (b) and the magnetic flux density normalized by the square root of the central gas density (c) as functions of the central gas density.

Since the first core and outflow properties are similar to those in previous studies (including ours, see Chapter 3), we describe them only briefly here.

The properties of the outflows such as velocities and traveling distances are similar in all the models. This is because the driving radii are similar in all the models, $\sim 10\,\mathrm{AU}$, where the gas density is not high enough for resistivity to work. The outflow velocities are comparable to the rotational velocities at this radius, $\sim 1\,\mathrm{km\,s^{-1}}$. Therefore the traveling distances are almost proportional to the first core lifetimes. It seems difficult to find the effect of the resistivity from the outflow properties, because there is no essential difference in the outflows between the resistive and ideal MHD models.

Although the outflows are similar, the first cores look quite different between the resistive and ideal MHD models. In the ideal models, the first cores are virtually non-rotating because of the efficient magnetic braking. However, the magnetic braking is not efficient in the resistive models and there remain considerable amount of the angular momentum. To show the effects of the resistivity clearly, we plot the total angular momentum within the first cores in Figure 6.20. Since it is difficult to identify the first core, here we simply measure the angular momentum where the gas density is above a critical value, $\rho_{\rm crit} = 10^{-13}\,\mathrm{g\,cm^{-3}}$. The resistivity is efficient where $\rho \gtrsim 5 \times 10^{-11}\,\mathrm{g\,cm^{-3}}$. Both in the models with fast and slow rotation, the resistive models attain about twice larger angular momenta compared with the corresponding ideal MHD models. Even these differences do not have significant impact on the evolution of the first cores, they become important later in the protostellar core phase.

The outstanding difference between the resistive and ideal models is that the first cores and the surrounding (pseudo) disks warp (a warped disk extends out of the $z = 0$ plane) in the ideal MHD models. Since it is difficult to analyze the stability of such a complex system with rotation, accretion and magnetic fields, we cannot determine the origin of the warp. Actually, there are many possible mechanisms triggering this warp, for example, the Kelvin-Helmholtz instability (there presents velocity shear in the disks), the Parker instability, the convective instability, and so on. It is likely to be the magnetically driven warping instability discussed by Lai (2003). The gas above the disk is strongly magnetized, therefore it can be unstable against a sort of MHD instabilities. The warp seems to have a typical azimuthal wavenumber of $m \sim 4 - 6$, and therefore the structure is numerically well resolved. Whatever the case may be, even small perturbation induces the artificial reconnection of the magnetic fields at the mid-plane, then things go chaotic. Anyway, this warp will not affect the evolution of the protostellar core (at least in our short simulations) because only the gas in the very central region collapses into the protostellar core. Therefore, we do not discuss this warp further in this work.

We can see that the gas within the dust evaporation front slowly infalls due to

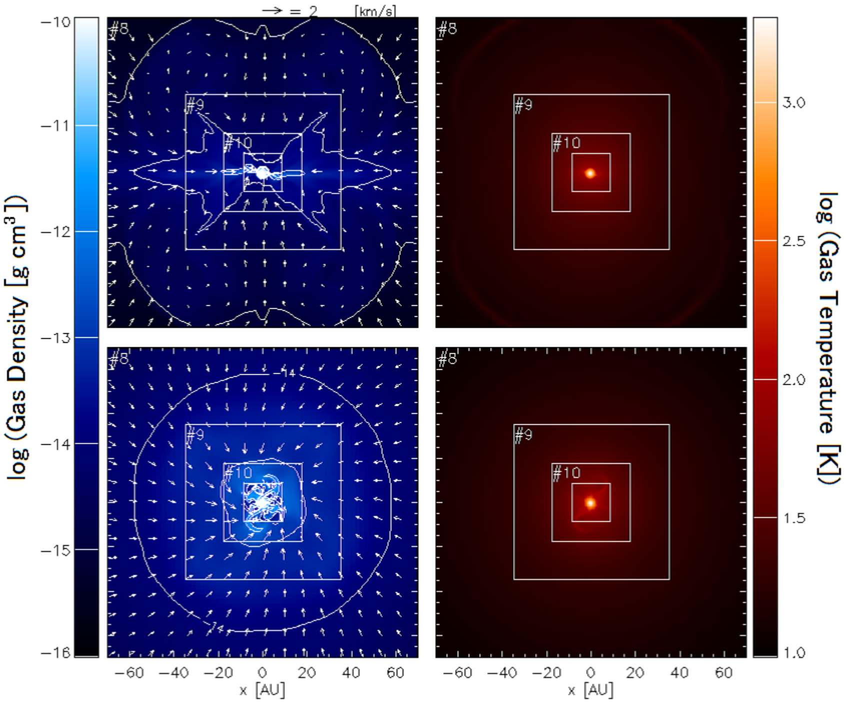

Figure 6.8: The vertical (top) and horizontal (bottom) cross sections of the gas density (left) and temperature (right) in the outflow scale ($l = 8$ or $\sim 140\,\mathrm{AU}$) of Model *IF*. Projected velocity vectors are overplotted.

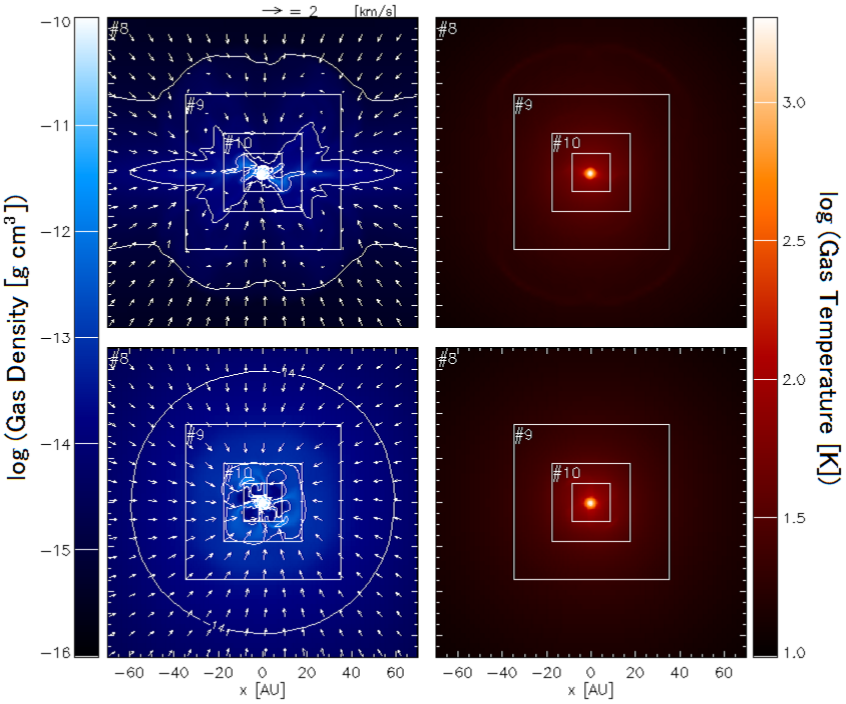

Figure 6.9: The same as Figure 6.8 but of *IS*.

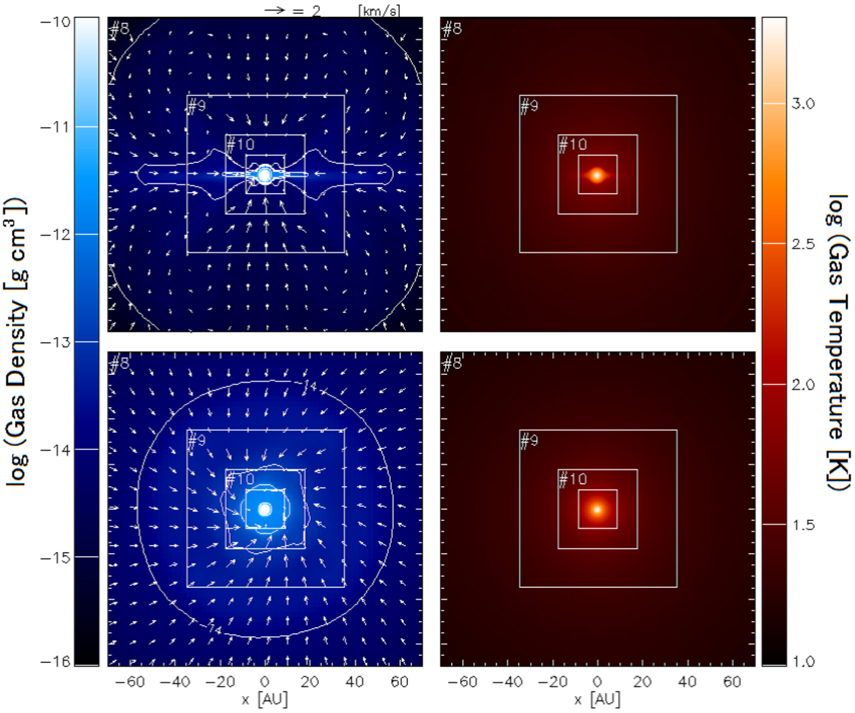

Figure 6.10: The same as Figure 6.8 but of *RF*.

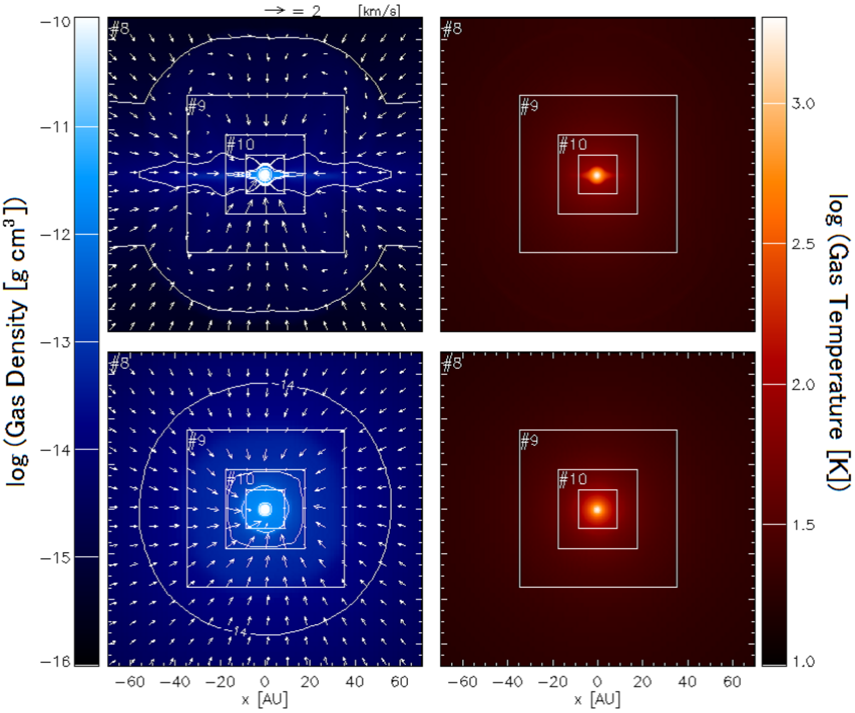

Figure 6.11: The same as Figure 6.10 but of *RS*.

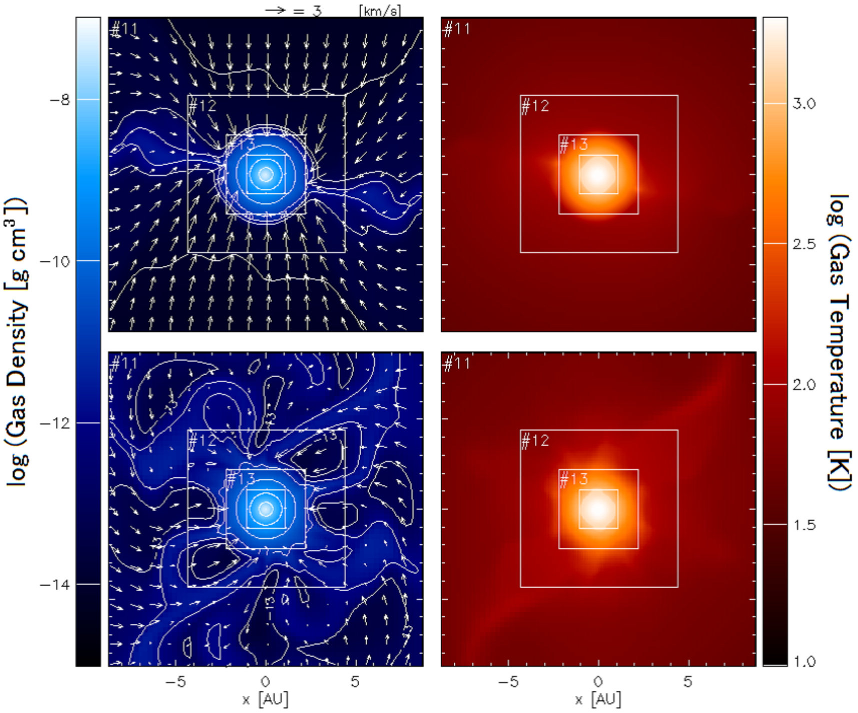

Figure 6.12: The vertical (top) and horizontal (bottom) cross sections of the gas density (left) and temperature (right) in the first core scale ($l = 11$ or $\sim 18\,\mathrm{AU}$) of Model *IF*.

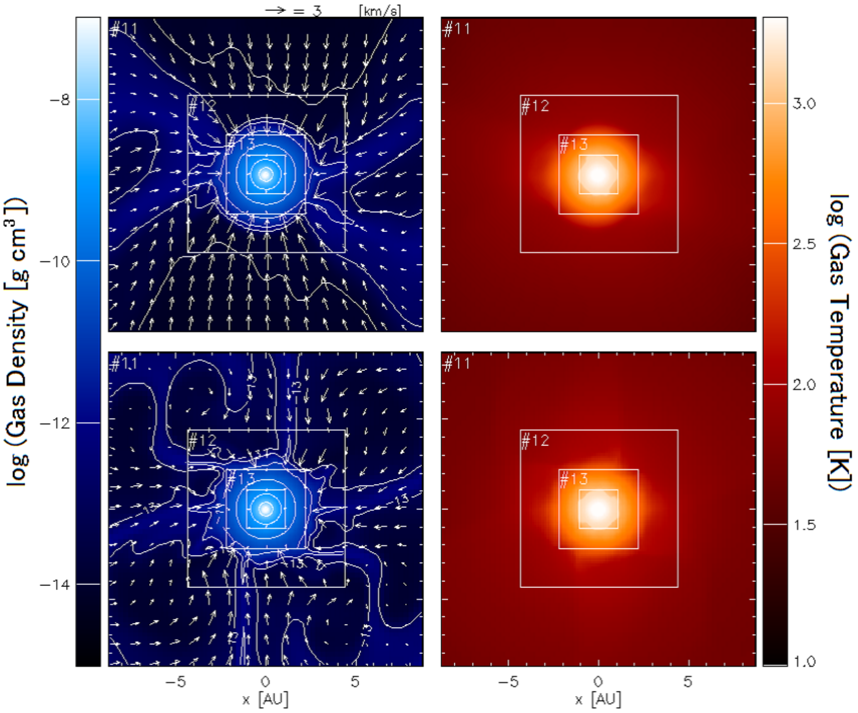

Figure 6.13: The same as Figure 6.12 but of *IS*.

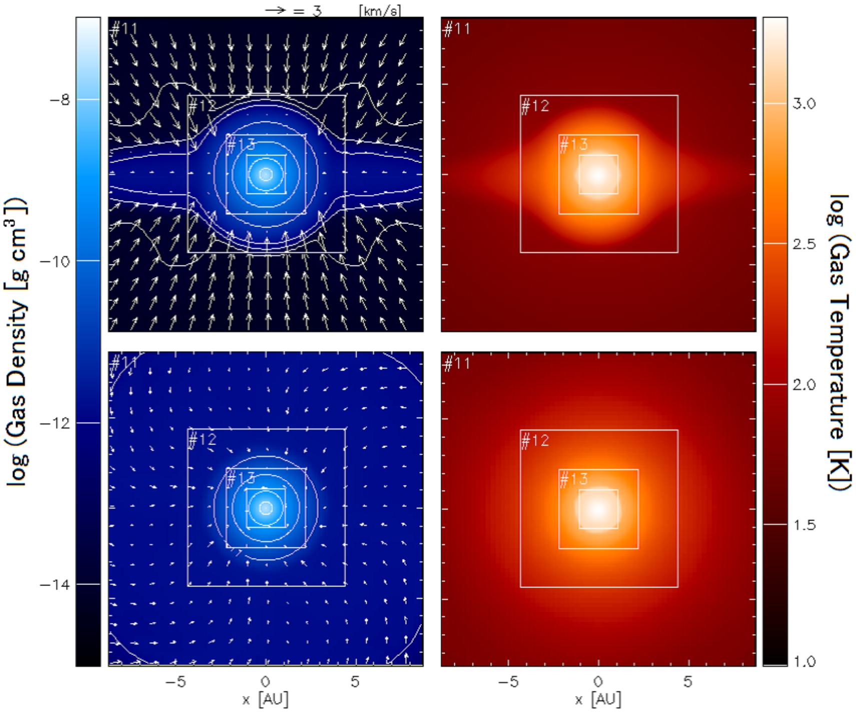

Figure 6.14: The same as Figure 6.12 but of *RF*.

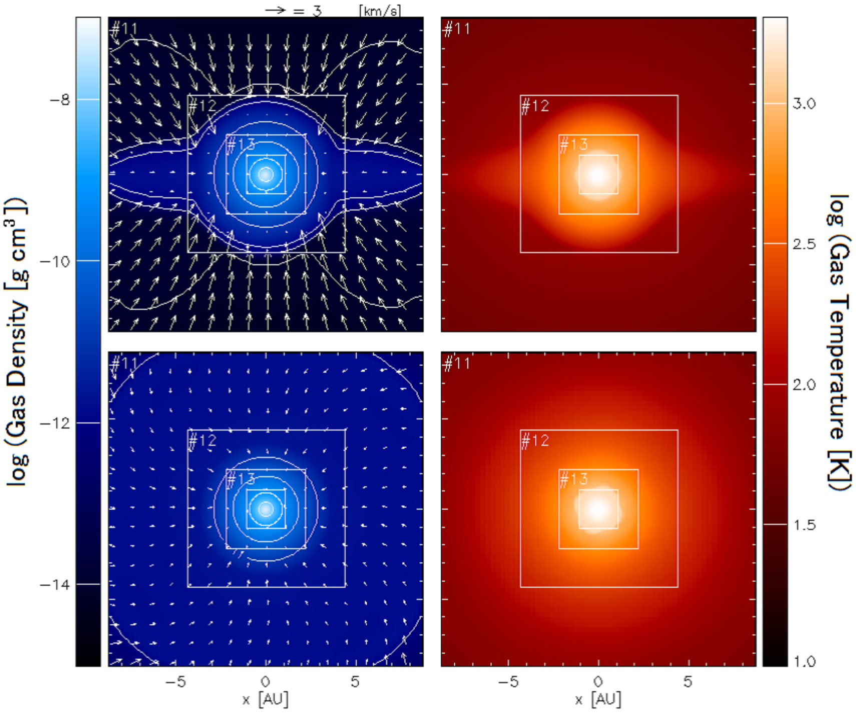

Figure 6.15: The same as Figure 6.14 but of *RS*.

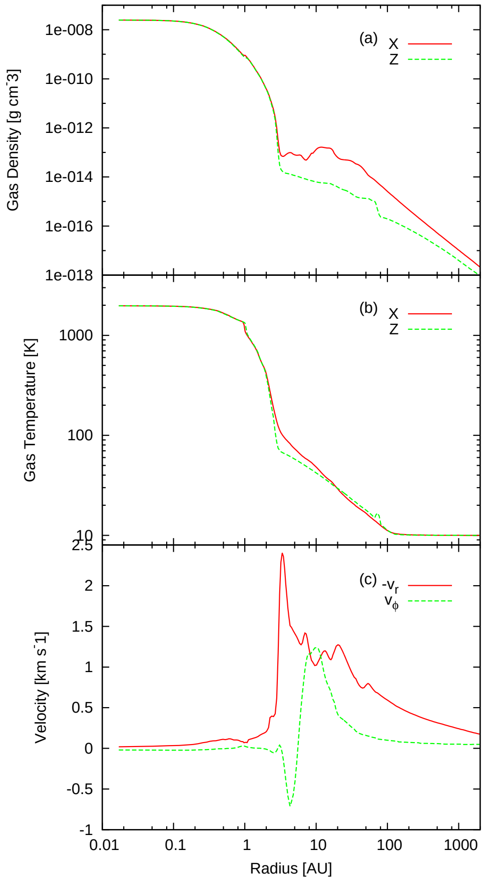

Figure 6.16: The radial profiles of (a) the gas density, (b) temperature along the $x$- (in the disk mid-plane, red) and $z$-axes (along the rotational axis, green), and (c) the infall (red) and rotation (green) velocities along the $x$-axis at the end of the first core phase of Model *IF*.

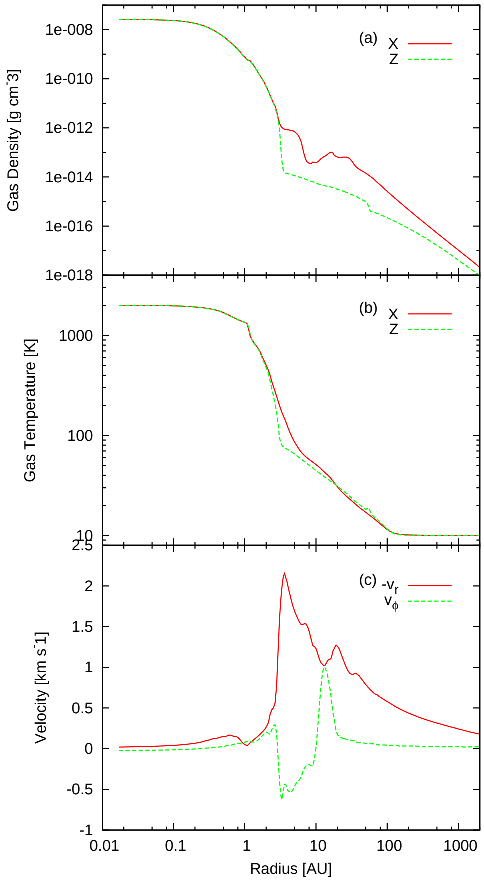

Figure 6.17: The same as Figure 6.16 but of *IS*.

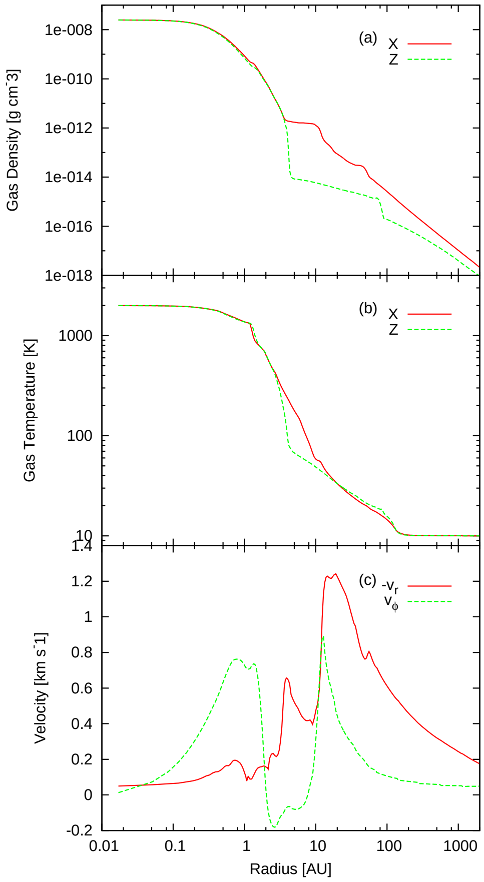

Figure 6.18: The same as Figure 6.16 but of *RF*.

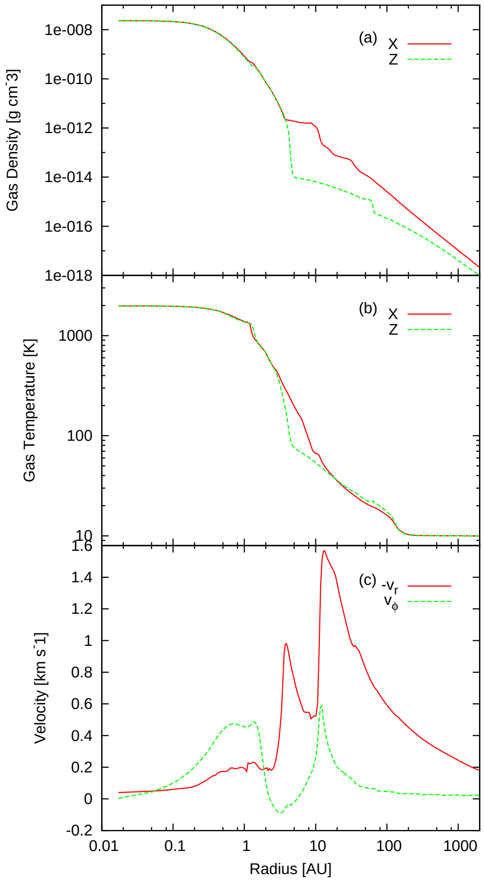

Figure 6.19: The same as Figure 6.16 but of *RS*.

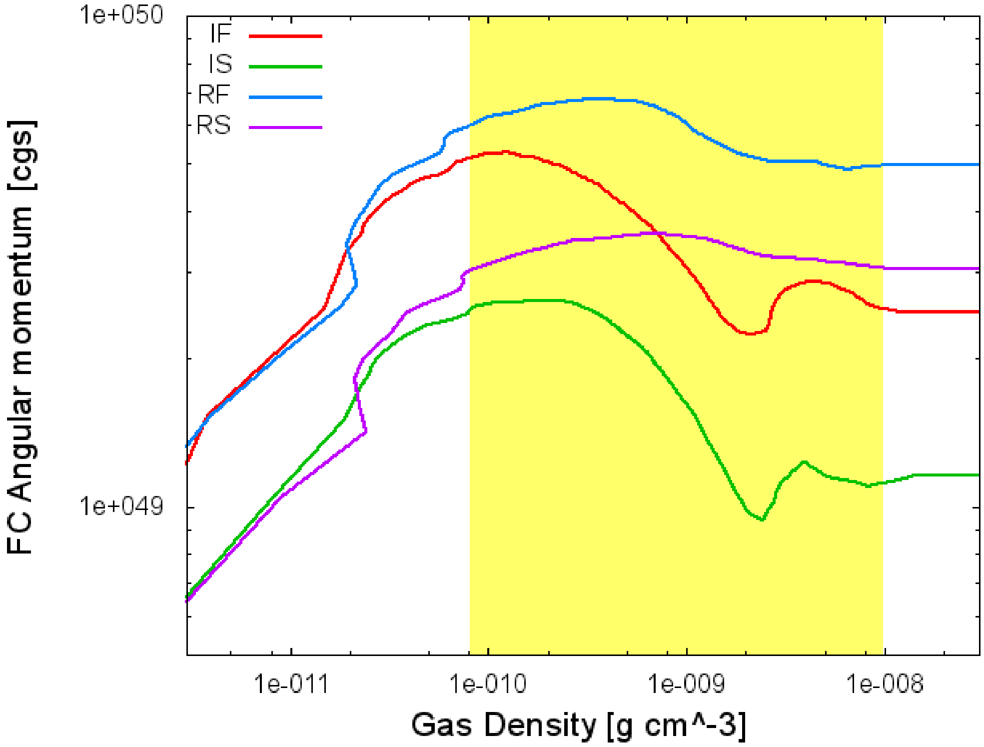

Figure 6.20: The evolution of the total angular momenta in the first cores as a function of the central gas density. Magnetic fields are decoupled from fluid where the magnetic Reynolds number is smaller than unity, $R_m < 1$ (yellow shaded region).

loss of the pressure gradient in all the models. However, the dust evaporation front is still confined in the first core and therefore its effects do not seem significant. This is different from the non-magnetized RHD simulations where the front expands beyond the first core surface (Schönke & Tscharnuter, 2011). In our simulations, the angular momentum transport is very efficient and the first cores properties are quite similar to the spherically symmetric cases, even in the resistive models.

Interestingly, the size (or height) of the first core is slightly larger in the resistive models. It is about 3 AU in the ideal MHD models, which is similar to the spherical model, but 5 AU in the resistive models. This is interpreted as the consequence of energy transport and additional heating by the Ohmic dissipation. The magnetic fields are transported outward, then heat up and inflate the outer region (note that the resistivity is most effective around $\rho \sim 10^{-9}\,\mathrm{g\,cm^{-3}}$).

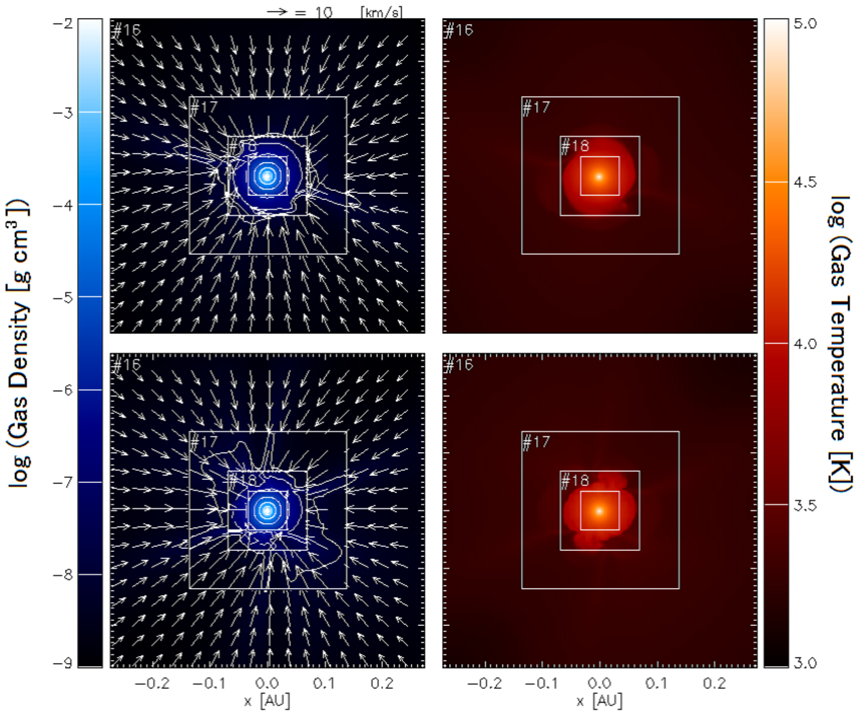

Figure 6.21: The vertical (top) and horizontal (bottom) cross sections of the gas density (left) and temperature (right) in the protostellar core scale ($l = 16$ or $\sim 0.54\,\mathrm{AU}$) of Model *IF*.

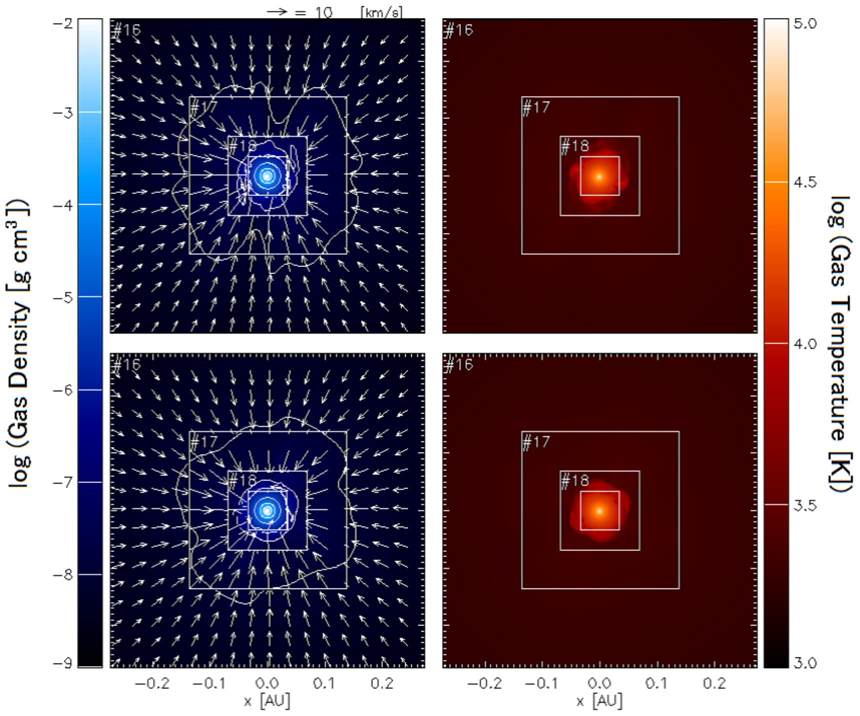

Figure 6.22: The same as Figure 6.21 but of *IS*.

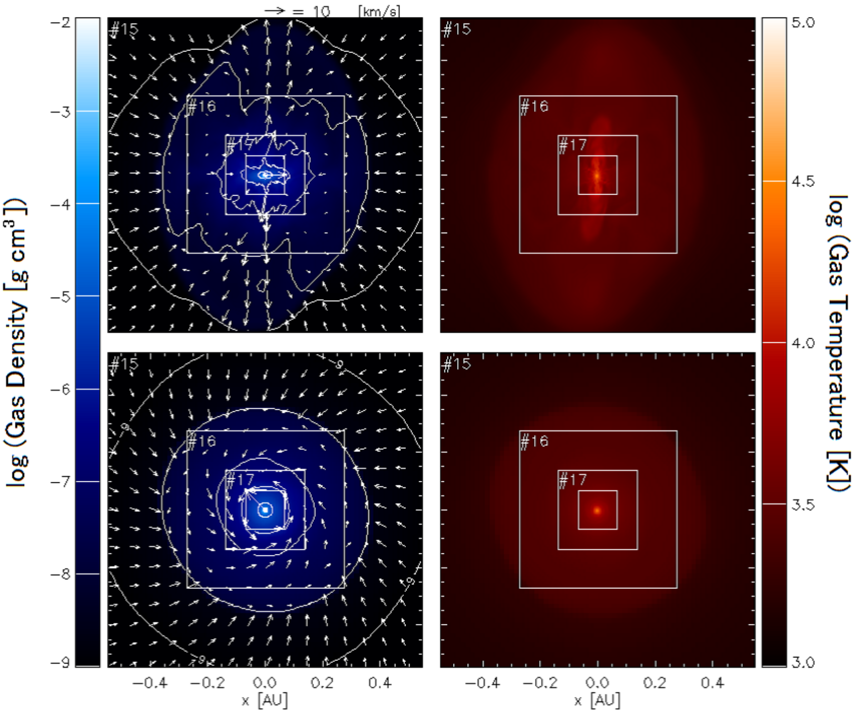

Figure 6.23: The same as Figure 6.21 but of *RF* ($l = 15$ or $\sim 1.1\,\mathrm{AU}$). Note that the scale is twice larger than that in Figure 6.21.

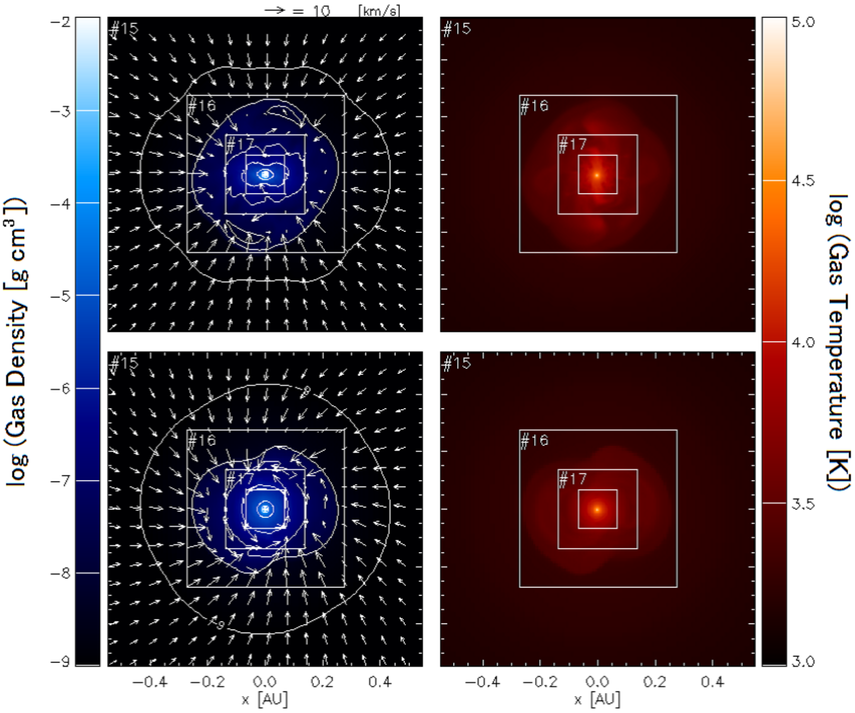

Figure 6.24: The same as Figure 6.23 but of *RS*.

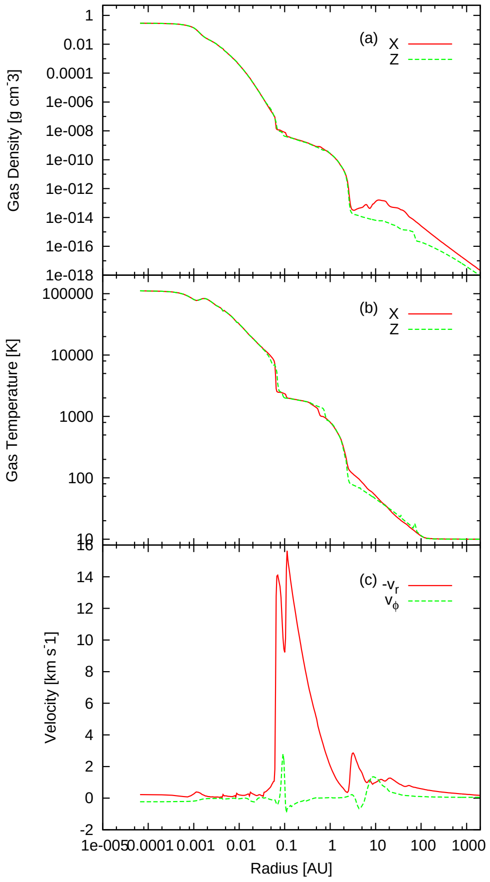

Figure 6.25: The same as Figure 6.16 but in the protostellar core phase.

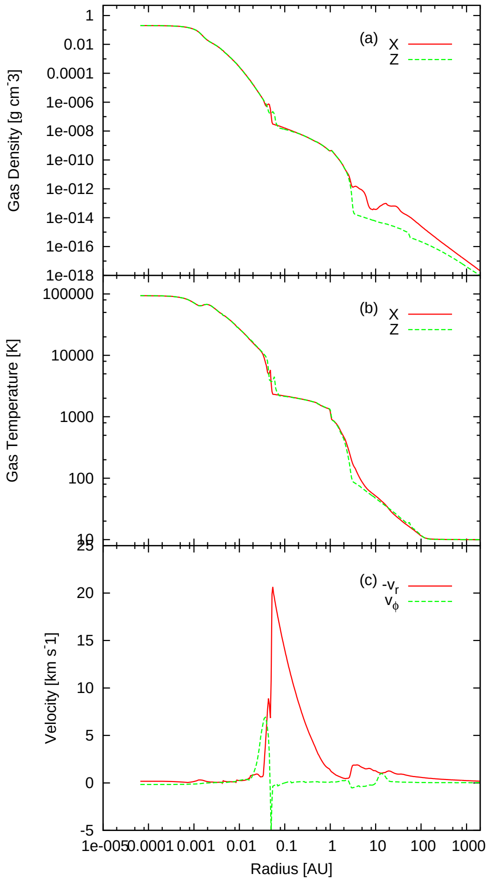

Figure 6.26: The same as Figure 6.25 but of *IS*.

### Protostellar Cores (and Jets)

We show the density and temperature cross sections of the the protostellar core scale ($l = 15$ or 16, corresponding to $\sim 1.1\,\mathrm{AU}$ or $\sim 0.54\,\mathrm{AU}$) at the end of the simulations in Figures 6.21 – 6.24. We also show the profiles along $x$- and $z$-axes in Figures 6.25 – 6.28. We stop our simulations when the central temperature reaches $T_c \sim 10^5\,\mathrm{K}$, corresponding to $1.05, 0.44, 0.90$ and 1.25 years after the formation of the protostellar cores in *IF, IS, RF* and *RS*, respectively. Our simulations correspond to the earliest phase of the protostars.

In the ideal MHD models, the protostellar cores have the properties very similar to the spherical model. This is because the magnetic fields take almost all the angular momentum away from the gas in the central region. Contrarily, the resistive models have relatively large angular momenta and the protostellar cores are strongly supported by rotation. To clarify the differences of the evolution between models, we show the evolution of the radii, masses and angular momenta of the protostellar cores in Figure 6.29. Here we define the radius of the protostellar core as the radius

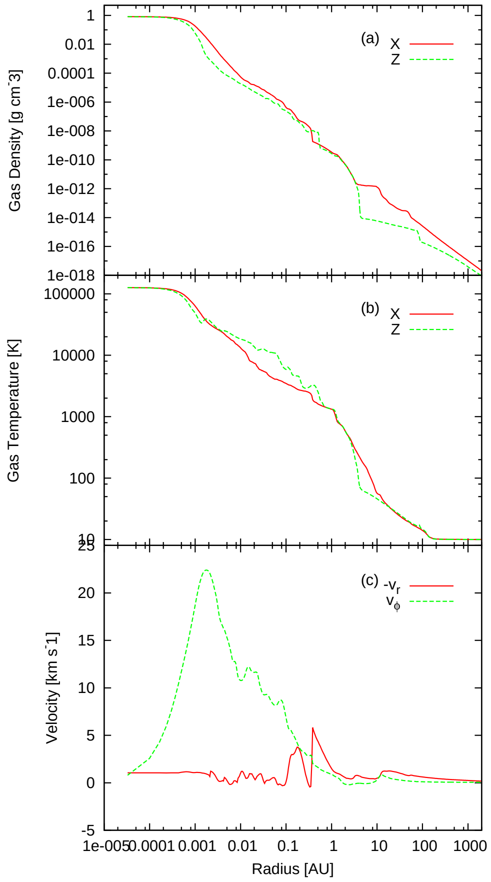

Figure 6.27: The same as Figure 6.25 but of *RF*.

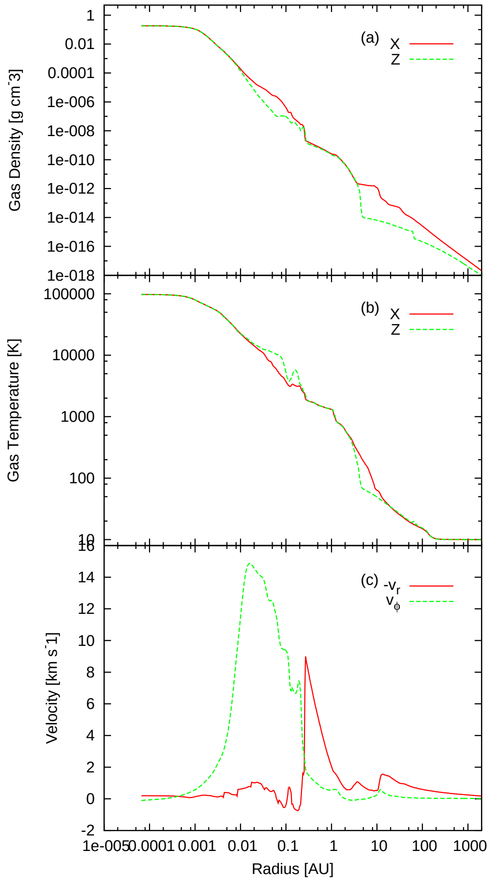

Figure 6.28: The same as Figure 6.25 but of *RS*.

where the infall velocity is largest (corresponding to the shock at the surface of the protostellar core) in the mid-plane, and measure the mass and angular momentum within this radius. The angular momentum in the protostellar cores in the resistive models are larger than those in the ideal MHD models by more than two orders of magnitudes. The rotationally-supported protostellar cores (or "circumstellar disks") are quickly built up within $\sim 1$ year after the formation of the protostellar cores. At the end of the simulations, the radii of the disks are about 0.35 AU in *RF* and 0.2 AU in *RS*, and they are still growing as the gas with larger angular momentum accretes. (Because these protostellar cores in the resistive models are supported dominantly by rotation, we can expect that the EOS and the transient expansion does not affect the results significantly in the resistive models.)

The protostellar cores in the resistive models also look like nearly spherical, but this is actually just a coincidence. They are supported by rotation in the horizontal direction, but they are vertically inflated due to the outflows. The toroidal magnetic fields are rapidly amplified in these rotating cores and the magnetic pressure gradient force drives the well-collimated outflows (or "jets") (Figures 6.30 – 6.32). The outflows

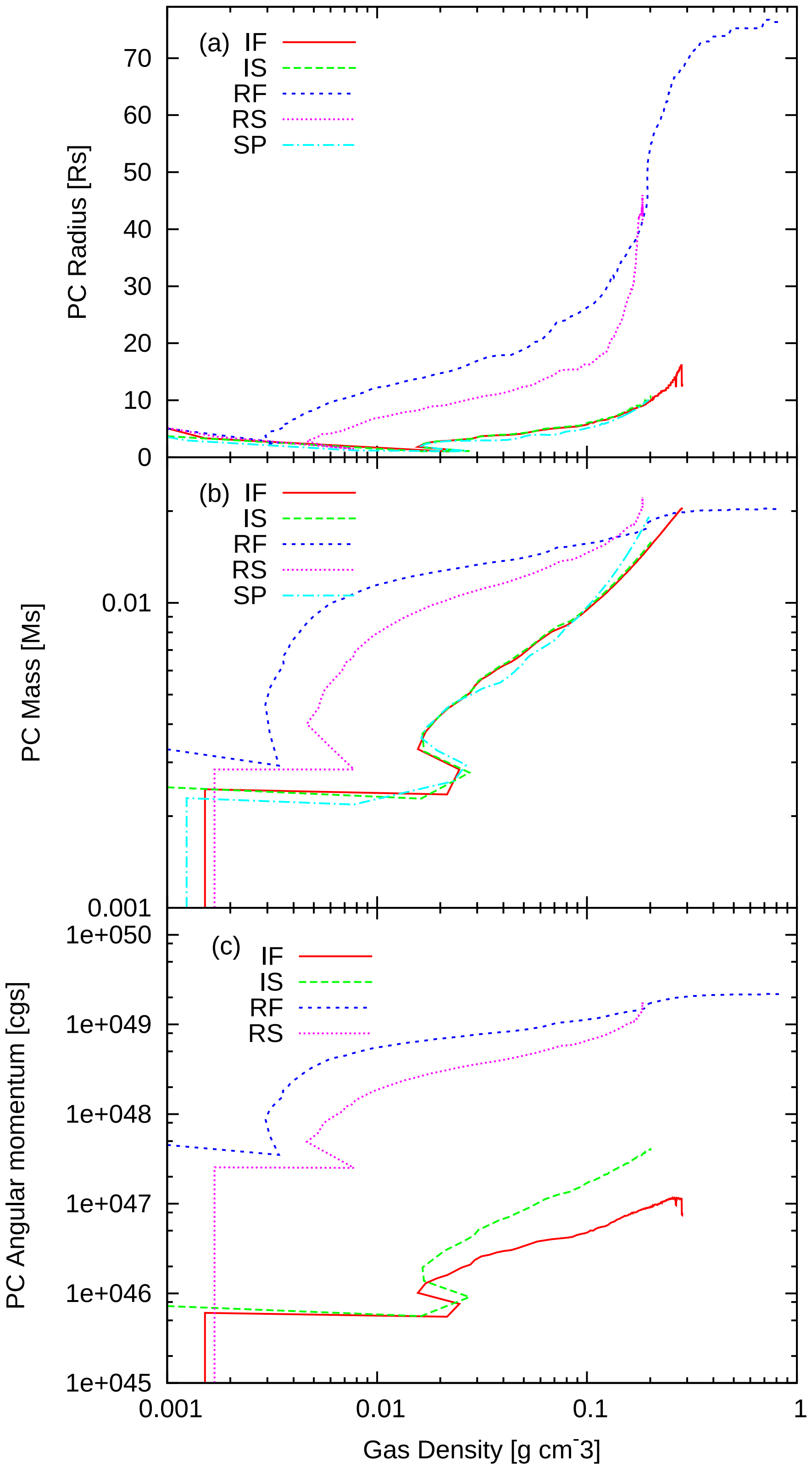

Figure 6.29: The evolution of the radii, masses and angular momenta of the protostellar cores as functions of the central gas density.

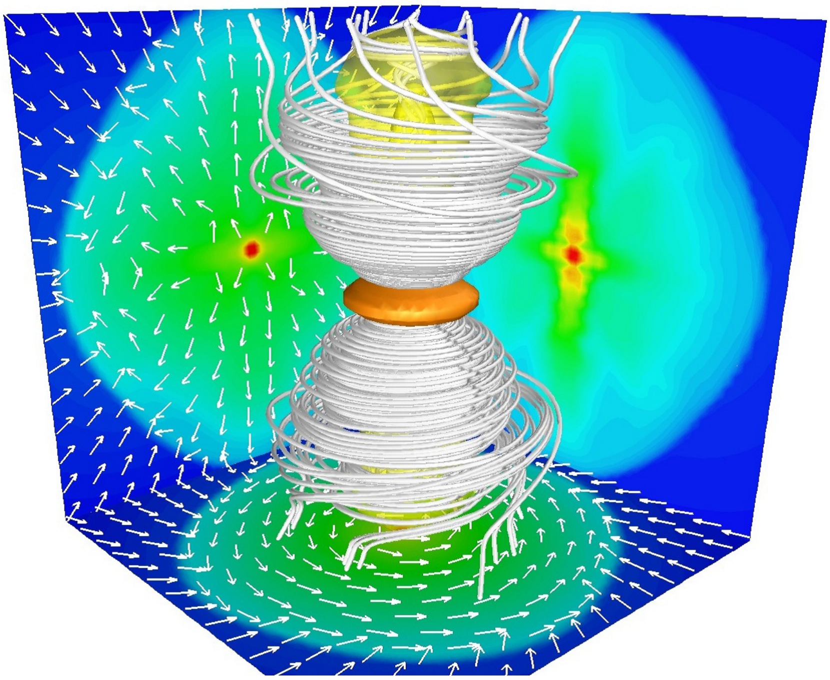

Figure 6.30: 3D view of the protostellar core ($l = 17$) in Model *RF*, before the growth of the kink instability. The edge of the figure corresponds to $\sim 0.27\,\mathrm{AU}$. The left and bottom panels are cross sections of the density and the right panel shows the temperature cross section. The high density region ($\rho > 10^{-5}\,\mathrm{g\,cm^{-3}}$) is visualized with the orange surface. White arrows denote the direction of the fluid motion and white lines the magnetic field lines. Fast outflowing gas ($v_z > 3\,\mathrm{km\,s^{-1}}$) is volume-rendered with pale yellow.

are visible in the cross sections of the temperature as hot towers. In the fast rotating model *RF*, the maximum outflow velocity reaches $v_z \sim 15\,\mathrm{km\,s^{-1}}$, while it is $\sim 6\,\mathrm{km\,s^{-1}}$ in Model *RS*. These velocities are comparable to the rotational velocities seen in the protostellar cores, and therefore far faster than the outflows driven from the first cores.

The magnetic fields in the rotating protostellar core are quickly wound up and form the so-called magnetic tower. The tightly-wound magnetic fields are susceptible to the kink instability in long wavelengths. In our resistive models, the kink instabilities grow rapidly and the outflows start precession (Figures 6.30 – 6.32). Although this instability disturbs the coherent toroidal magnetic fields, the outflow velocity is still getting accelerated because the bulk angular momentum in the protostellar core is increasing (Figure 6.29), since the matter with higher angular momentum continuously accretes from the envelope, or the remnant of the first core. Therefore we expect that the outflow will be faster as the disk acquires the larger angular momentum and the gravitational potential becomes deeper.

In all the models, the feedback on the first core and outer envelope from the pro-

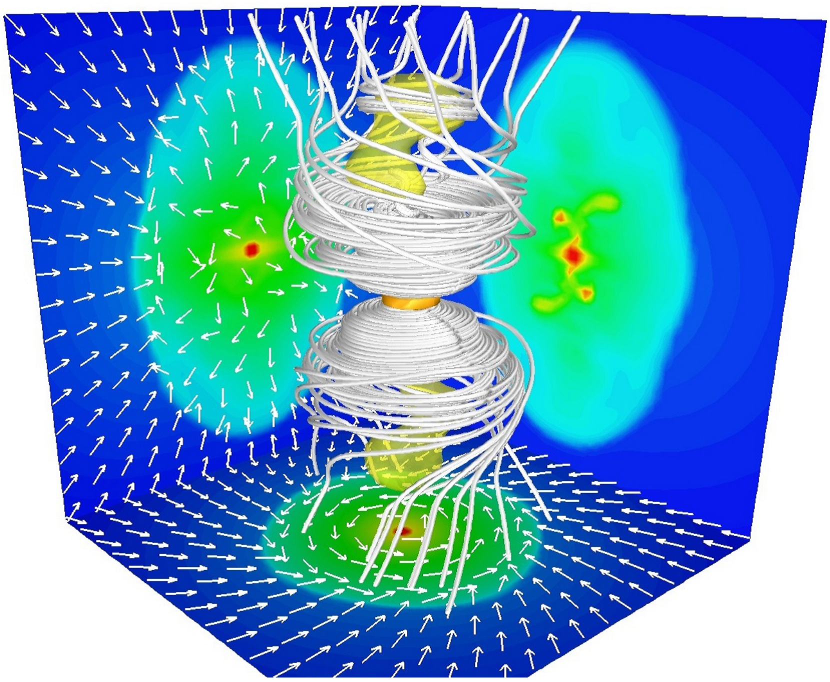

Figure 6.31: 3D view of the protostellar core ($l = 16$) in Model *RF*, in the growing phase of the kink instability. The edge of the figure is $\sim 0.54\,\mathrm{AU}$. The gas with $v_z > 4\,\mathrm{km\,s^{-1}}$ is rendered with pale yellow.

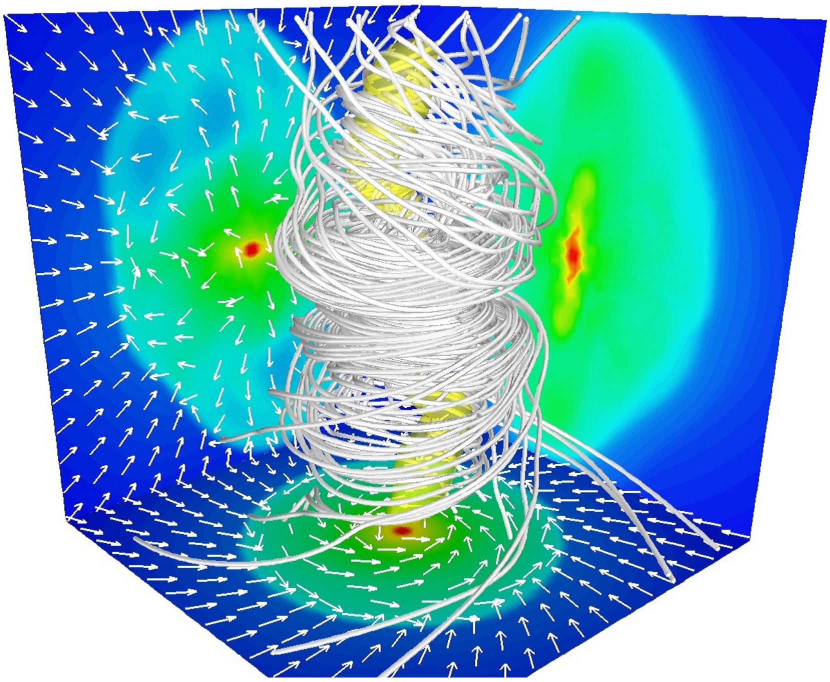

Figure 6.32: 3D view of the protostellar core ($l = 15$) in Model *RF*, the kink instability is already grown up significantly. The edge of the figure is $\sim 1.1\,\mathrm{AU}$. The gas with $v_z > 7\,\mathrm{km\,s^{-1}}$ is rendered with pale yellow.

tostellar core formation is not significant. The first cores seem to remain almost unaffected after the formation of the protostellar cores. However, this is because we only calculate the earliest ($t \lesssim 1\,\mathrm{yr}$) evolution of the protostellar cores; Bate (2011a) and Schönke & Tscharnuter (2011) followed the long term evolution of the protostellar cores more than 15 years, longer than the free-fall time of the first cores.

## 6.4 Conclusions and Discussions

We performed 3D nested-grid RMHD simulations of the formation of the protostellar cores from the molecular cloud cores with and without the Ohmic dissipation, and revealed the earliest (only 1 year) evolution of the protostellar cores. These simulations are, to our knowledge, the first 3D RMHD simulations in the world with realistic physics following the whole evolution from molecular cloud cores to protostellar cores. We successfully revealed the realistic evolution in the early phase of protostellar collapse.

We summarize the properties of the first cores and protostellar cores at the end of the simulations in Table 6.2. The properties of the first cores and associated outflows in the rotating models are similar to those in the previous studies. The properties of the protostellar cores are largely different from previous studies, but probably they are the consequences of the transient expansion which happens in the earliest evolution of the protostellar core. The protostellar core acquires its mass very quickly in this phase ($\sim 0.02\,M_\odot$ in a year). Because this phenomenon has very short time scale (estimated to be $\sim 5$ years), our models are not inconsistent with previous works by Masunaga & Inutsuka (2000). Our results are also consistent with the present-day case of Omukai et al. (2010). This expansion will affect the properties of the protostellar core even when the core settles after this expansion, but its consequence is fairly unknown. However, it may be critically important in the further evolution of the protostellar core as the initial condition. To confidently discuss this phenomenon and the properties of the protostellar cores, we have to calculate the evolution far longer.

We showed that the barotropic approximation fails to reproduce the realistic thermal properties in the first core phase in Chapter 3, but here we also revealed that the discrepancy is even more prominent in the protostellar core phase, because the barotropic approximation does not take account of the shock heating and therefore tend to underestimate the temperature, which results in the smaller radius of the protostellar core.

In the resistive models, the protostellar cores attain considerably large angular momenta and the rotationally-supported disks emerge there even in their earliest phases. It seems to continuously evolve into the circumstellar disks. Although it is difficult to distinguish the disk and the central protostar in our simulations at this phase, they

| Model | $\tau_{\rm FC}$(yrs) | $R_{\rm FC}$(AU) | $D_{\rm OF}$(AU) | $R_{\rm PC}$($\rm R_\odot$) | $M_{\rm PC}$($\rm M_\odot$) | $V_{\rm Jet}$ ($\rm km\,s^{-1}$) |
|---|---|---|---|---|---|---|
| *SP* | 650 | 3 | 0 | $10^*$ | 0.02 | 0 |
| *IS* | 720 | 3 | 55 | $10^*$ | 0.02 | 0 |
| *IF* | 800 | 3 | 70 | $17^*$ | 0.02 | 0 |
| *RS* | 850 | 5 | 60 | 45 | 0.02 | 5 |
| *RF* | 950 | 5 | 80 | 75 | 0.02 | 15 |
| *MI* | 650 | 3 | 0 | 4 | 0.016 | 0 |
| *MR* | – | 0.5 | – | 8.2 | 0.008 | 15 |

Table 6.2: Summary of the properties of the first cores and the protostellar cores. From left to right: the lifetime of the first core, the radius of the first core, the distance the outflow traveled during the first core lifetime, the radius of the protostellar core, the mass of the protostellar core and the maximum velocity of the jet driven from the protostellar core. The quantities marked with * can be seriously affected by the transient expansion (and possibly by EOS). For comparison, we also show the results of Masunaga & Inutsuka (2000) (*MI*), the snapshot labeled "10" which corresponds to 19 years after the second collapse, and the model *MR* of Machida et al. (2008a) (we adopt their disk radius as the protostellar core radius and we show the total mass of the protostar, disk and outflow because we do not distinguish them in our simulations; the size of the thermally supported protostellar core is small, $\sim 1R_\odot$, because of the barotropic approximation).

will differentiate into a thermally-supported protostar and a rotationally-supported disk when radiation cooling takes place and reduces the thermal support. Thus it is concluded that the resistivity drastically remedies the magnetic braking catastrophe. The disk is quite hot but considerably massive, so the disk may suffer from the gravito-rotational instability and subsequent fragmentation (Machida et al., 2008b). Indeed, we can see the spiral-like structures in Figure 6.24, which is a signature of such an instability.

Despite the significant difference of the thermal evolution in the protostellar cores, the properties of the outflows and circumstellar disks associated with the protostellar cores in the resistive models are consistent with previous MHD studies (Machida et al., 2006, 2007, 2008a). The slow loosely-collimated outflow is driven from the first core and the fast well-collimated jet is driven from the protostellar core. Although the maximum velocity of the outflow is still not so fast ($v_z \sim 15\,\rm km\,s^{-1}$), we can expect that it will get faster as the protostellar core grows. If it is the case, our simulations can naturally explain the observed high-velocity jets, especially the multicomponent outflows (e.g., Lee et al., 2000; Santiago-García et al., 2009). In the ideal MHD cases, on the other hand, the protostellar cores are almost the same with the spherically symmetric case and the outflows are not launched there. We speculate, however, that the circumstellar disks and outflows may be formed later when the gas with large angular momentum accretes sufficiently because the magnetic braking is not a process which reduce the total angular momentum but transport the angular momentum from the disk to the thin envelope within the molecular cloud via Alfvén waves, although we cannot simulate such long-term evolution.

In our simulations, the protostellar cores do not affect the first cores and outer envelope because of the short duration of the simulations. Considering the large energy released in the second collapse and subsequent accretion with the high accretion rate, we expect that the feedback like Bate (2011a) and Schönke & Tscharnuter (2011) reported can happen. So how long does it take that the feedback becomes prominent? As we discussed above, the answer is the free fall timescale of the first core, which is about 5 years. Another interesting factor is the interaction between the first core and the outflow from the protostellar core. When the outflow from the protostellar core penetrate the first core, it will have some influence on the first core. Assuming the constant traveling velocity of $15\,\mathrm{km\,s^{-1}}$, it will reach the surface of the first core in about 1.5 years. In order to simulate the long-term evolution, we have to modify our simulations drastically, for example, introducing the sink particle technique to replace the protostellar core with a subgrid stellar evolution model (see Chapter 7).

Since only the earliest evolution (about 1 year) of the protostellar cores and surrounding circumstellar disks are revealed in the simulations presented here, we need to continue our simulations to discuss the evolution of the protostars, jets and circumstellar disks more clearly.

# Chapter 7

# Summary

## Summary of This Thesis

We developed a new nested-grid RMHD simulation code to study protostellar collapse from molecular cloud cores to protostellar cores. This work is one of the most sophisticated simulations of star formation processes involving many physical processes required in star formation studies.

In Chapter 2, we described the methods adopted in our simulations. Main features of our code are: the 3D nested-grid technique to follow the very large dynamic range with reasonable computational resources, the HLLD MHD solver (with the HLLD− cure for Carbuncle phenomena), self-gravity with the multigrid method, radiation transfer with gray FLD approximation using the implicit time-integrator, the Ohmic dissipation accelerated with the STS technique, and the realistic EOS including chemical reactions of hydrogen and helium. Our code covers as many physical processes work in protostellar collapse as possible.

Using the code, we performed RMHD simulations of the early phase of protostellar collapse, focusing on the first core and the outflow driven from it, and we reported the results in Chapter 3. We discussed the effects of the radiation transfer on the thermodynamics compared with previous simulations using the barotropic approximation instead of solving radiation transfer. We showed that the first core properties such as mass, radius and lifetime are quantitatively changed by a factor of two. On the other hand, the dynamical properties of the outflow such as the velocity and driving scale remain similar because they are mainly determined by the interaction between rotation and magnetic fields and therefore insensitive to the thermodynamics. Although the results are qualitatively similar to the previous simulations, the realistic thermal evolution obtained in RMHD simulations is of crucial importance for precise modeling, especially when we discuss the observational properties from our simulations.

Chapter 4 is devoted to predictions for observations. Based on our R(M)HD simulations, we derived observational properties of the first cores. We predicted the SED, VAD and images of thermal continuum and the channel maps, spectra and position-velocity diagrams of CS molecular lines for future observations with ALMA and other instruments. We showed that the first cores can be directly observed and studied with ALMA both in thermal continuum and molecular lines. We also compared our predictions with the observations of a first core candidate “Source A” in the $\rho$ Ophiuchus molecular cloud, and we found good agreement between them.

In Chapter 5, we proposed a new model of first cores based on RHD simulations. We found that first cores formed in very low mass ($\sim 0.1 M_\odot$) molecular cloud cores have considerably longer lifetimes than those formed in ordinary mass ($\sim 1 M_\odot$) cloud cores. In a very low mass cloud core, the first core cannot reach the second collapse even after almost all the gas in the cloud core has accreted onto the first core. The first core evolves very slowly under the effects of radiation cooling, and as a consequence, this type of a first core has long lifetime, more than (at least) fourteen thousand years. We also calculated the observational properties of such first cores, and showed that they can be observed and distinguished from other evolutionary stages in star formation processes.

Finally, we reported the results of the (resistive) RMHD simulations of the protostellar core formation in Chapter 6. We succeeded to simulate the realistic evolution in the early phase of protostellar collapse. These are the first direct 3D RMHD simulations resolving the protostellar cores in the world. Unfortunately, we could not follow the long-term evolution after the formation of the protostellar cores due to the limitation of computational resources, but we confirmed that two different types of outflows are naturally launched from the first cores and the protostellar cores in the resistive RMHD simulations, as proposed in Machida et al. (2008a). We found that the circumstellar disks are rapidly (or simultaneously) formed in the resistive models. We also showed that the structures around the protostellar cores are significantly different from the previous simulations assuming the barotropic approximation, because they severely underestimate the shock heating and the thermal support in the protostellar cores. Compared with the RHD simulations previously reported (Bate, 2010, 2011a; Schönke & Tscharnuter, 2011), we found that the feedback from the protostellar core formation is not significant, but this is probably because the duration we followed after the second collapse is too short. We require further calculations to study the effects of the protostellar core formation on the large scale, although such calculations must be computationally expensive.

Though we have achieved very tough simulations of protostellar collapse and demonstrated the performance of our code, these are only the beginning. We have to study the star formation processes extensively, especially the formation and evolution of protostellar cores which have been poorly studied so far with multidimensional simulations involving realistic physics. We require further constant effort in this field.

# Future Prospects

Here we give some directions for future studies in this field. We are still halfway to the ultimate goal of the star formation studies, i.e., determining the final mass of a protostar and the initial mass function. We have incorporated many required physical processes in our works so far, but there are still more and more physics and techniques to be considered.

## Radiation Transfer and Numerical Algorithms

In the radiation transfer part of our current simulations, we adopted two major approximations; FLD and gray approximation. In the earliest phase of the protostellar core, the accretion flow is still optically thick and therefore these approximations are adequate. However, more sophisticated treatment of radiation transfer will be required when the protostellar core evolves more. The radiative feedback from the formed protostar can be anisotropic ("flash light effect") due to the small-scale optically-thick disk around the protostar (Yorke & Bodenheimer, 1999; Vaidya et al., 2009; Tanaka & Nakamoto, 2011). Moreover, there will be complicated structures such as the outflows and the cavities opened up by radiative and magnetic activities. Therefore, more elaborate treatment of radiation transfer which can handle complex geometry and strong anisotropy will be important. We should adopt a method solving higher-order moment equations like the variable tensor Eddington factor (VTEF) method with ray-tracing (Stone et al., 1992; Hayes & Norman, 2003; Davis et al., 2012; Jiang et al., 2012).

Another large limitation in our scheme is the gray approximation. The radiation from the formed protostar can be far hotter than the gas temperature in the envelope and the gray approximation breaks down there. There are some studies demonstrating the importance of the frequency-dependent radiation transfer in the main accretion phase (after the formation of the protostellar core) of star formation (Yorke & Sonnhalter, 2002; Kuiper et al., 2010, 2011b,a). It seems that we should consider at least two components of radiation; hot stellar (direct) radiation and reprocessed diffuse radiation. Additionally, the ionizing radiation feedback is also of great importance, particularly in the massive star formation as a mechanism to cease the accretion (Hosokawa et al., 2011b; McKee & Tan, 2008). So we need to properly treat these frequency-dependent radiation transfer as long as the chemical reactions related to the photoionization.

Practically, the largest technical problem in radiation hydrodynamic simulations is the efficiency and scalability of the algorithm. Because the radiation timescale can be much shorter than the dynamical one, an implicit time-integrator is an indispensable technique in star formation studies. However, an implicit algorithm in principle requires global information to update the system (typically it requires inversion of a huge sparse matrix), and the global communication between computational nodes is rather expensive and results in poor scalability. A robust, efficient and scalable algorithm (a miracle!) is highly demanded. It is a highly mathematical problem, and such a technique is required not only in astrophysics but also in other fields, therefore, we believe, we should make efforts in wide collaboration with other fields.

## Long Term Simulations with Subgrid Models

When a protostellar core is formed, the simulation timestep becomes extremely short, which is on the order of minutes or even less. Our simulations are still faster than the real star formation by (only) an order of magnitude, but trivially the long-term direct simulations of the main accretion phase are impossible. Therefore we need to replace the central hot and dense protostellar core with a subgrid model consistently including the protostellar evolution (Baraffe et al., 2002; McKee & Tan, 2003; Yorke & Bodenheimer, 2008; Hosokawa & Omukai, 2009) to achieve the long-term simulation following the main accretion phase and investigate the mechanism which determines the final mass of a protostar.

Such a stellar evolution model can be introduced using the sink cell/particle technique (Bate et al., 1995; Krumholz et al., 2004; Federrath et al., 2010). Although the sink particles have already been utilized in many works, we should be careful about the consistency of simulations; i.e., the evolution of the flow should be reproduced even when we introduce the sink particles, at least in the scale of interest. In many current studies, the sink particles are treated as collisionless accreting particles interacting via gravity (and radiation) with surrounding gas. If we introduce a sink particle in a thermally-supported region, it will result in loss of pressure support and modify the flow considerably. If we insert a sink particle in a supersonically collapsing region, on the other hand, it means that it introduce unphysical scale in the flow, the radius of the sink particle. The situations become even worse when magnetic fields present; we have to model the magnetic fields at the surface of the sink particle consistently. In many works using sink particles in MHD simulations, they do nothing about magnetic fields; magnetic fields do not accrete but just pile up around the sink particle. However, it causes artificial decoupling between the magnetic fields and the gas even in ideal MHD simulations and is obviously unrealistic. So we need to model the interaction between the sink particle and the accretion flow more carefully. Also, the internal structures within the particle are crudely simplified assuming spherical symmetry, but the radiation feedback, for example, must be anisotropic when non-zero angular momentum exists. The outflows driven from protostars also should be taken into account. Such modeling must be a tough work, but we believe we need to develop more sophisticated sink particle techniques for accurate numerical simulations.

## Microphysics

Though the details of the microphysics are beyond the scope of our works, the microphysics involved in the simulations should be surely improved. For example, the difference of EOS directly affect the properties of the protostellar cores and the stability of the disks. Particularly, the ratio between ortho- and parahydrogen seems to have significant impact on star formation processes, but it is quite uncertain. Opacities and resistivity also have large uncertainty originated from the properties of the dust grains. In order to improve our simulations and make them quantitatively reliable, these microphysical properties should be updated and extended.

In our non-ideal MHD simulations, we only take the Ohmic dissipation into account as the first step. However, the ambipolar diffusion is known to be important especially in the early phase of star formation, and the Hall effect also may take place. So we should incorporate these processes in our simulations.

Now we are steadily and certainly approaching the heart of star formation processes both theoretically and observationally. We can now simulate star formation processes including realistic physics in three dimension with highly advanced supercomputers and sophisticated numerical techniques. The new observational instruments such as ALMA, *Herschel*, coming JWST and SPICA will surely open new frontiers in this field. Therefore, we believe, we are now in the most exciting era for star formation studies!

# References

Alexiades, V., Amiez, G., & Gremaud, P. 1996, Communications in numerical methods in engineering, 12, 31

André, P. et al. 2010, A&A, 518, L102

Arce, H. G., Borkin, M. A., Goodman, A. A., Pineda, J. E., & Halle, M. W. 2010, ApJ, 715, 1170

Arce, H. G., Shepherd, D., Gueth, F., Lee, C., Bachiller, R., Rosen, A., & Beuther, H. 2007, Protostars and Planets V, 245

Ballesteros-Paredes, J., Hartmann, L., & Vázquez-Semadeni, E. 1999, ApJ, 527, 285

Banerjee, R., & Pudritz, R. E. 2006, ApJ, 641, 949

Baraffe, I., Chabrier, G., Allard, F., & Hauschildt, P. H. 2002, A&A, 382, 563

Baraffe, I., Chabrier, G., & Gallardo, J. 2009, ApJ, 702, L27

Bate, M. R. 1998, ApJ, 508, L95

——. 2009a, MNRAS, 392, 590

——. 2009b, MNRAS, 392, 1363

——. 2010, MNRAS, 404, L79

——. 2011a, MNRAS, 417, 2036

——. 2011b, MNRAS, 2080

Bate, M. R., Bonnell, I. A., & Bromm, V. 2003, MNRAS, 339, 577

Bate, M. R., Bonnell, I. A., & Price, N. M. 1995, MNRAS, 277, 362

Black, D. C., & Bodenheimer, P. 1975, ApJ, 199, 619

——. 1976, ApJ, 206, 138

Blandford, R. D., & Payne, D. G. 1982, MNRAS, 199, 883

Boley, A. C. 2009, ApJ, 695, L53

Boley, A. C., & Durisen, R. H. 2008, ApJ, 685, 1193

Boley, A. C., Hartquist, T. W., Durisen, R. H., & Michael, S. 2007, ApJ, 656, L89

Boley, A. C., Helled, R., & Payne, M. J. 2011, ApJ, 735, 30

Bonnor, W. B. 1956, MNRAS, 116, 351

Bontemps, S., Andre, P., Terebey, S., & Cabrit, S. 1996, A&A, 311, 858

Boss, A. P. 1989, ApJ, 346, 336

——. 1997, Science, 276, 1836

——. 2008, ApJ, 677, 607

——. 2011, MNRAS, 1737

Boss, A. P., & Bodenheimer, P. 1979, ApJ, 234, 289

Boss, A. P., & Yorke, H. W. 1995, ApJ, 439, L55

Bourke, T. L. et al. 2006, ApJ, 649, L37

Burrows, C. J. et al. 1996, ApJ, 473, 437

Bürzle, F., Clark, P. C., Stasyszyn, F., Dolag, K., & Klessen, R. S. 2011, MNRAS, 417, L61

Castor, J. I. 2004, Radiation Hydrodynamics (Radiation Hydrodynamics, by John I. Castor, pp. 368. ISBN 0521833094. Cambridge, UK: Cambridge University Press)

Chabrier, G. 2003, PASP, 115, 763

Chabrier, G. 2005, in Astrophysics and Space Science Library, Vol. 327, The Initial Mass Function 50 Years Later, ed. E. Corbelli, F. Palla, & H. Zinnecker, 41

Chan, C.-k. 2011, ApJ, 727, 67

Chen, X., & Arce, H. G. 2010, ApJ, 720, L169

Chen, X., Arce, H. G., Zhang, Q., Bourke, T. L., Launhardt, R., Schmalzl, M., & Henning, T. 2010, ApJ, 715, 1344

Choi, E., Kim, J., & Wiita, P. J. 2009, ApJS, 181, 413

Commerçon, B., Audit, E., Chabrier, G., & Chièze, J.-P. 2011a, A&A, 530, A13

Commerçon, B., Hennebelle, P., Audit, E., Chabrier, G., & Teyssier, R. 2008, A&A, 482, 371

——. 2010, A&A, 510, L3+

Commerçon, B., Teyssier, R., Audit, E., Hennebelle, P., & Chabrier, G. 2011b, A&A, 529, A35+

Crutcher, R. M., Hakobian, N., & Troland, T. H. 2009, ApJ, 692, 844

Dapp, W. B., & Basu, S. 2010, A&A, 521, L56

Davis, S. W., Stone, J. M., & Jiang, Y.-F. 2012, ArXiv e-prints, 1201.2222

Dedner, A., Kemm, F., Kröner, D., Munz, C.-D., Schnitzer, T., & Wesenberg, M. 2002, Journal of Computational Physics, 175, 645

Dislaire, V., Hily-Blant, P., Faure, A., Maret, S., Bacmann, A., & Pineau Des Forêts, G. 2011, ArXiv e-prints, 1111.1572

Dubroca, B., & Feugeas, J. 1999, Academie des Sciences Paris Comptes Rendus Serie Sciences Mathematiques, 329, 915

Duffin, D. F., & Pudritz, R. E. 2009, ApJ, 706, L46

Dunham, M. M., Chen, X., Arce, H. G., Bourke, T. L., Schnee, S., & Enoch, M. L. 2011, ApJ, 742, 1

Dunham, M. M., Crapsi, A., Evans, II, N. J., Bourke, T. L., Huard, T. L., Myers, P. C., & Kauffmann, J. 2008, ApJS, 179, 249

Ebert, R. 1955, Zeitschrift fur Astrophysik, 36, 222

Elmegreen, B. G. 2000, ApJ, 530, 277

Enoch, M. L., Glenn, J., Evans, II, N. J., Sargent, A. I., Young, K. E., & Huard, T. L. 2007, ApJ, 666, 982

Enoch, M. L., Lee, J., Harvey, P., Dunham, M. M., & Schnee, S. 2010, ApJ, 722, L33

Evans, II, N. J. et al. 2003, PASP, 115, 965

——. 2009, ApJS, 181, 321

Falgarone, E., Troland, T. H., Crutcher, R. M., & Paubert, G. 2008, A&A, 487, 247

Federrath, C., Banerjee, R., Clark, P. C., & Klessen, R. S. 2010, ApJ, 713, 269

Federrath, C., Sur, S., Schleicher, D. R. G., Banerjee, R., & Klessen, R. S. 2011, ApJ, 731, 62

Ferguson, J. W., Alexander, D. R., Allard, F., Barman, T., Bodnarik, J. G., Hauschildt, P. H., Heffner-Wong, A., & Tamanai, A. 2005, ApJ, 623, 585

Field, G. B. 1965, ApJ, 142, 531

Fukuda, N., & Hanawa, T. 1999, ApJ, 517, 226

Gammie, C. F. 2001, ApJ, 553, 174

Girart, J. M., Beltrán, M. T., Zhang, Q., Rao, R., & Estalella, R. 2009, Science, 324, 1408

Girart, J. M., Rao, R., & Marrone, D. P. 2006, Science, 313, 812

González, M., Audit, E., & Huynh, P. 2007, A&A, 464, 429

Graves, D. T., Trebotich, D., Miller, G. H., & Colella, P. 2008, Journal of Computational Physics, 227, 4797

Hanawa, T., Mikami, H., & Matsumoto, T. 2008, Journal of Computational Physics, 227, 7952

Harten, A., & Hyman, J. M. 1983, Journal of Computational Physics, 50, 235

Hartmann, L. 2001, AJ, 121, 1030

Hartmann, L., Ballesteros-Paredes, J., & Heitsch, F. 2011, MNRAS, 2068

Hayashi, C. 1981, Progress of Theoretical Physics Supplement, 70, 35

Hayes, J. C., & Norman, M. L. 2003, ApJS, 147, 197

Hayes, J. C., Norman, M. L., Fiedler, R. A., Bordner, J. O., Li, P. S., Clark, S. E., ud-Doula, A., & Mac Low, M.-M. 2006, ApJS, 165, 188

Heiles, C., & Crutcher, R. 2005, in Lecture Notes in Physics, Berlin Springer Verlag, Vol. 664, Cosmic Magnetic Fields, ed. R. Wielebinski & R. Beck, 137

Hennebelle, P., & Audit, E. 2007, A&A, 465, 431

Hennebelle, P., Audit, E., & Miville-Deschênes, M.-A. 2007, A&A, 465, 445

Hennebelle, P., & Chabrier, G. 2008, ApJ, 684, 395

——. 2009, ApJ, 702, 1428

Hennebelle, P., & Ciardi, A. 2009, A&A, 506, L29

Hennebelle, P., & Fromang, S. 2008, A&A, 477, 9

Hennebelle, P., & Pérault, M. 1999, A&A, 351, 309

——. 2000, A&A, 359, 1124

Hennebelle, P., & Teyssier, R. 2008, A&A, 477, 25

Heyer, M. H., & Brunt, C. M. 2004, ApJ, 615, L45

Hirano, N., Ho, P. P. T., Liu, S.-Y., Shang, H., Lee, C.-F., & Bourke, T. L. 2010, ApJ, 717, 58

Hirsch, C. 1990, Numerical computation of internal and external flows. Volume 2: Computational methods for inviscid and viscous flows (Wiley Series in Numerical Methods in Engineering)

Hosking, J. G., & Whitworth, A. P. 2004, MNRAS, 347, 1001

Hosokawa, T., Offner, S. S. R., & Krumholz, M. R. 2011a, ApJ, 738, 140

Hosokawa, T., & Omukai, K. 2009, ApJ, 691, 823

Hosokawa, T., Omukai, K., Yoshida, N., & Yorke, H. W. 2011b, Science, 334, 1250

Howell, L. H., & Greenough, J. A. 2003, Journal of Computational Physics, 184, 53

Hunter, C. 1977, ApJ, 218, 834

Ikeda, N., & Kitamura, Y. 2009, ApJ, 705, L95

——. 2011, ApJ, 732, 101

Inoue, T., & Inutsuka, S.-i. 2008, ApJ, 687, 303

——. 2009, ApJ, 704, 161

Inutsuka, S.-i., Machida, M. N., & Matsumoto, T. 2010, ApJ, 718, L58

Jiang, Y.-F., Stone, J. M., & Davis, S. W. 2012, ArXiv e-prints, 1201.2223

Jørgensen, J. K., van Dishoeck, E. F., Visser, R., Bourke, T. L., Wilner, D. J., Lommen, D., Hogerheijde, M. R., & Myers, P. C. 2009, A&A, 507, 861

Kamazaki, T., Saito, M., Hirano, N., & Kawabe, R. 2001, ApJ, 548, 278

Kenyon, S. J., Hartmann, L. W., Strom, K. M., & Strom, S. E. 1990, AJ, 99, 869

Koyama, H., & Inutsuka, S.-I. 2000, ApJ, 532, 980

Koyama, H., & Inutsuka, S.-i. 2002, ApJ, 564, L97

Kroupa, P. 2001, MNRAS, 322, 231

Krumholz, M. R., Klein, R. I., & McKee, C. F. 2011, ApJ, 740, 74

Krumholz, M. R., Klein, R. I., McKee, C. F., & Bolstad, J. 2007, ApJ, 667, 626

Krumholz, M. R., Klein, R. I., McKee, C. F., Offner, S. S. R., & Cunningham, A. J. 2009, Science, 323, 754

Krumholz, M. R., McKee, C. F., & Klein, R. I. 2004, ApJ, 611, 399

Krumholz, M. R., & Tan, J. C. 2007, ApJ, 654, 304

Kudoh, T., Matsumoto, R., & Shibata, K. 1998, ApJ, 508, 186

Kuiper, R., Klahr, H., Beuther, H., & Henning, T. 2010, ApJ, 722, 1556

——. 2011a, ArXiv e-prints, 1111.5625

——. 2011b, ApJ, 732, 20

Lai, D. 2003, ApJ, 591, L119

Larson, R. B. 1969, MNRAS, 145, 271

——. 1972, MNRAS, 156, 437

——. 1981, MNRAS, 194, 809

Launhardt, R. et al. 2009, A&A, 494, 147

Lee, C.-F., Mundy, L. G., Reipurth, B., Ostriker, E. C., & Stone, J. M. 2000, ApJ, 542, 925

Leung, C. M. 1975, ApJ, 199, 340

Levermore, C. D. 1984, Journal of Quantitative Spectroscopy and Radiative Transfer, 31, 149

Levermore, C. D., & Pomraning, G. C. 1981, ApJ, 248, 321

Li, Z.-Y., Krasnopolsky, R., & Shang, H. 2011, ApJ, 738, 180

Li, Z.-Y., & Nakamura, F. 2006, ApJ, 640, L187

Liu, J., Salumbides, E., Hollenstein, U., Koelemeij, J., Eikema, K., Ubachs, W., & Merkt, F. 2009, The Journal of chemical physics, 130, 174306

Lowrie, R. B., Mihalas, D., & Morel, J. E. 2001, J. Quant. Spec. Radiat. Transf., 69, 291

Luhman, K. L. 2004, ApJ, 617, 1216

Luhman, K. L., Rieke, G. H., Young, E. T., Cotera, A. S., Chen, H., Rieke, M. J., Schneider, G., & Thompson, R. I. 2000, ApJ, 540, 1016

Mac Low, M.-M., Klessen, R. S., Burkert, A., & Smith, M. D. 1998, Physical Review Letters, 80, 2754

Machida, M. N., Inutsuka, S.-i., & Matsumoto, T. 2006, ApJ, 647, L151

——. 2007, ApJ, 670, 1198

——. 2008a, ApJ, 676, 1088

——. 2009a, ApJ, 699, L157

Machida, M. N., Inutsuka, S.-I., & Matsumoto, T. 2011a, PASJ, 63, 555

Machida, M. N., Inutsuka, S.-i., & Matsumoto, T. 2011b, ApJ, 729, 42

Machida, M. N., Kokubo, E., Inutsuka, S.-I., & Matsumoto, T. 2010, MNRAS, 405, 1227

Machida, M. N., & Matsumoto, T. 2011, MNRAS, 413, 2767

Machida, M. N., Matsumoto, T., Hanawa, T., & Tomisaka, K. 2005a, MNRAS, 362, 382

Machida, M. N., Matsumoto, T., Tomisaka, K., & Hanawa, T. 2005b, MNRAS, 362, 369

Machida, M. N., Omukai, K., Matsumoto, T., & Inutsuka, S.-I. 2009b, MNRAS, 399, 1255

Machida, M. N., Tomisaka, K., & Matsumoto, T. 2004, MNRAS, 348, L1

Machida, M. N., Tomisaka, K., Matsumoto, T., & Inutsuka, S.-i. 2008b, ApJ, 677, 327

Masunaga, H., & Inutsuka, S.-I. 1999, ApJ, 510, 822

Masunaga, H., & Inutsuka, S.-i. 2000, ApJ, 531, 350

Masunaga, H., Miyama, S. M., & Inutsuka, S.-I. 1998, ApJ, 495, 346

Matsumoto, T. 2011, PASJ, 63, 317

Matsumoto, T., & Hanawa, T. 2003a, ApJ, 583, 296

——. 2003b, ApJ, 595, 913

——. 2011, ApJ, 728, 47

Matsumoto, T., Nakazato, T., & Tomisaka, K. 2006, ApJ, 637, L105

Matsumoto, T., & Tomisaka, K. 2004, ApJ, 616, 266

Mayer, L., Lufkin, G., Quinn, T., & Wadsley, J. 2007, ApJ, 661, L77

McKee, C. F., Li, P. S., & Klein, R. I. 2010, ApJ, 720, 1612

McKee, C. F., & Ostriker, E. C. 2007, ARA&A, 45, 565

McKee, C. F., & Tan, J. C. 2003, ApJ, 585, 850

——. 2008, ApJ, 681, 771

Mellon, R. R., & Li, Z.-Y. 2008, ApJ, 681, 1356

——. 2009, ApJ, 698, 922

Meru, F., & Bate, M. R. 2010, MNRAS, 406, 2279

Mignone, A., Bodo, G., Massaglia, S., Matsakos, T., Tesileanu, O., Zanni, C., & Ferrari, A. 2007, ApJS, 170, 228

Mihalas, D., & Auer, L. 2001, Journal of Quantitative Spectroscopy and Radiative Transfer, 71, 61

Mihalas, D., & Weibel Mihalas, B. 1984, Foundations of radiation hydrodynamics (New York: Oxford University Press)

Mikami, H., Sato, Y., Matsumoto, T., & Hanawa, T. 2008, ApJ, 683, 357

Minerbo, G. N. 1978, J. Quant. Spec. Radiat. Transf., 20, 541

Miyoshi, T., & Kusano, K. 2005, Journal of Computational Physics, 208, 315

——. 2007, AGU Fall Meeting Abstracts, A311+

Mizuno, A., Onishi, T., Yonekura, Y., Nagahama, T., Ogawa, H., & Fukui, Y. 1995, ApJ, 445, L161

Motoyama, K., Umemoto, T., & Shang, H. 2007, A&A, 467, 657

Motte, F., Andre, P., & Neri, R. 1998, A&A, 336, 150

Mouschovias, T. C., & Paleologou, E. V. 1979, ApJ, 230, 204

——. 1980, ApJ, 237, 877

Mouschovias, T. C., & Spitzer, Jr., L. 1976, ApJ, 210, 326

Nakamura, F. et al. 2011a, ApJ, 726, 46

Nakamura, F., & Li, Z.-Y. 2007, ApJ, 662, 395

Nakamura, F. et al. 2011b, ApJ, 737, 56

Nakano, T., Hasegawa, T., & Norman, C. 1995, ApJ, 450, 183

Nakano, T., & Nakamura, T. 1978, PASJ, 30, 671

Nakano, T., Nishi, R., & Umebayashi, T. 2002, ApJ, 573, 199

Narayanan, G., Heyer, M. H., Brunt, C., Goldsmith, P. F., Snell, R., & Li, D. 2008, ApJS, 177, 341

Offner, S. S. R., Klein, R. I., McKee, C. F., & Krumholz, M. R. 2009, ApJ, 703, 131

Ohashi, N., Hayashi, M., Ho, P. T. P., Momose, M., Tamura, M., Hirano, N., & Sargent, A. I. 1997, ApJ, 488, 317

Okuzumi, S. 2009, ApJ, 698, 1122

Omukai, K. 2007, PASJ, 59, 589

Omukai, K., Hosokawa, T., & Yoshida, N. 2010, ApJ, 722, 1793

Onishi, T., Mizuno, A., Kawamura, A., Ogawa, H., & Fukui, Y. 1996, ApJ, 465, 815

——. 1998, ApJ, 502, 296

Onishi, T., Mizuno, A., Kawamura, A., Tachihara, K., & Fukui, Y. 2002, ApJ, 575, 950

O'Sullivan, S., & Downes, T. P. 2006, MNRAS, 366, 1329

Padoan, P., & Nordlund, Å. 2002, ApJ, 576, 870

Pagani, L., Roueff, E., & Lesaffre, P. 2011, ApJ, 739, L35

Penston, M. V. 1969, MNRAS, 144, 425

Peters, T., Banerjee, R., Klessen, R. S., Mac Low, M.-M., Galván-Madrid, R., & Keto, E. R. 2010, ApJ, 711, 1017

Phan-Bao, N. et al. 2008, ApJ, 689, L141

Pineda, J. E. et al. 2011, ArXiv e-prints, 1109.1207

Press, W., Teukolsky, S., Vetterling, W., & Flannery, B. 2007, Numerical recipes: the art of scientific computing (Cambridge University Press)

Price, D. J., & Bate, M. R. 2007, MNRAS, 377, 77

——. 2009, MNRAS, 398, 33

Pyo, T.-S., Hayashi, M., Kobayashi, N., Terada, H., Goto, M., Yamashita, T., Tokunaga, A. T., & Itoh, Y. 2002, ApJ, 570, 724

Raga, A., & Cabrit, S. 1993, A&A, 278, 267

Raga, A. C., Canto, J., Calvet, N., Rodriguez, L. F., & Torrelles, J. M. 1993, A&A, 276, 539

Rathborne, J. M., Lada, C. J., Muench, A. A., Alves, J. F., Kainulainen, J., & Lombardi, M. 2009, ApJ, 699, 742

Reipurth, B., Yu, K. C., Rodríguez, L. F., Heathcote, S., & Bally, J. 1999, A&A, 352, L83

Ridge, N. A. et al. 2006, AJ, 131, 2921

Rybicki, G. B., & Lightman, A. P. 1986, Radiative Processes in Astrophysics (Radiative Processes in Astrophysics, by George B. Rybicki, Alan P. Lightman, pp. 400. ISBN 0-471-82759-2. Wiley-VCH)

Saigo, K., & Tomisaka, K. 2006, ApJ, 645, 381

——. 2011, ApJ, 728, 78

Saigo, K., Tomisaka, K., & Matsumoto, T. 2008, ApJ, 674, 997

Salpeter, E. E. 1955, ApJ, 121, 161

Santiago-García, J., Tafalla, M., Johnstone, D., & Bachiller, R. 2009, A&A, 495, 169

Saumon, D., Chabrier, G., & van Horn, H. M. 1995, ApJS, 99, 713

Scalo, J. M. 1986, Fund. Cosmic Phys., 11, 1

Schönke, J., & Tscharnuter, W. M. 2011, A&A, 526, A139

Seaton, M. J., Yan, Y., Mihalas, D., & Pradhan, A. K. 1994, MNRAS, 266, 805

Seifried, D., Banerjee, R., Klessen, R. S., Duffin, D., & Pudritz, R. E. 2011a, MNRAS, 417, 1054

Seifried, D., Pudritz, R. E., Banerjee, R., Duffin, D., & Klessen, R. S. 2011b, ArXiv e-prints, 1109.4379

Semenov, D., Henning, T., Helling, C., Ilgner, M., & Sedlmayr, E. 2003, A&A, 410, 611

Shu, F. H. 1977, ApJ, 214, 488

Shu, F. H., Adams, F. C., & Lizano, S. 1987, ARA&A, 25, 23

Stahler, S. W., Palla, F., & Salpeter, E. E. 1986, ApJ, 302, 590

Stahler, S. W., Shu, F. H., & Taam, R. E. 1980a, ApJ, 241, 637

——. 1980b, ApJ, 242, 226

——. 1981, ApJ, 248, 727

Stamatellos, D., & Whitworth, A. P. 2008, A&A, 480, 879

——. 2009, MNRAS, 400, 1563

Stamatellos, D., Whitworth, A. P., Bisbas, T., & Goodwin, S. 2007, A&A, 475, 37

Stone, J. M., Gardiner, T. A., Teuben, P., Hawley, J. F., & Simon, J. B. 2008, ApJS, 178, 137

Stone, J. M., Mihalas, D., & Norman, M. L. 1992, ApJS, 80, 819

Stone, J. M., Ostriker, E. C., & Gammie, C. F. 1998, ApJ, 508, L99

Sugitani, K. et al. 2011, ApJ, 734, 63

Tafalla, M., Santiago-García, J., Hacar, A., & Bachiller, R. 2010, A&A, 522, A91

Takami, M., Takakuwa, S., Momose, M., Hayashi, M., Davis, C. J., Pyo, T.-S., Nishikawa, T., & Kohno, K. 2006, PASJ, 58, 563

Tanaka, K. E. I., & Nakamoto, T. 2011, ApJ, 739, L50

Tassis, K., & Mouschovias, T. C. 2004, ApJ, 616, 283

Tomida, K., Machida, M. N., Saigo, K., Tomisaka, K., & Matsumoto, T. 2010a, ApJ, 725, L239

Tomida, K., Tomisaka, K., Matsumoto, T., Ohsuga, K., Machida, M. N., & Saigo, K. 2010b, ApJ, 714, L58

Tomisaka, K. 1998, ApJ, 502, L163+

——. 2000, ApJ, 528, L41

——. 2002, ApJ, 575, 306

Tomisaka, K., & Tomida, K. 2011, PASJ, 63, 1151

Toro, E. 2009, Riemann solvers and numerical methods for fluid dynamics: a practical introduction (Springer Verlag)

Troland, T. H., & Crutcher, R. M. 2008, ApJ, 680, 457

Truelove, J. K., Klein, R. I., McKee, C. F., Holliman, II, J. H., Howell, L. H., & Greenough, J. A. 1997, ApJ, 489, L179

Tscharnuter, W. 1975, A&A, 39, 207

Tsukamoto, Y., & Machida, M. N. 2011, MNRAS, 416, 591

Turk, M. J., Oishi, J. S., Abel, T., & Bryan, G. 2011, ArXiv e-prints, 1112.4479

Turner, N. J., & Stone, J. M. 2001, ApJS, 135, 95

Umebayashi, T., & Nakano, T. 2009, ApJ, 690, 69

Vaidya, B., Fendt, C., & Beuther, H. 2009, ApJ, 702, 567

Vázquez-Semadeni, E., Banerjee, R., Gómez, G. C., Hennebelle, P., Duffin, D., & Klessen, R. S. 2011, MNRAS, 414, 2511

Velusamy, T., Langer, W. D., & Marsh, K. A. 2007, ApJ, 668, L159

Vorobyov, E. I. 2009, ApJ, 704, 715

Vorobyov, E. I., & Basu, S. 2010, ApJ, 719, 1896

Wang, P., Li, Z.-Y., Abel, T., & Nakamura, F. 2010, ApJ, 709, 27

Whitehouse, S. C., & Bate, M. R. 2004, MNRAS, 353, 1078

——. 2006, MNRAS, 367, 32

Whitehouse, S. C., Bate, M. R., & Monaghan, J. J. 2005, MNRAS, 364, 1367

Whitworth, A., & Summers, D. 1985, MNRAS, 214, 1

Winkler, K.-H. A., & Newman, M. J. 1980a, ApJ, 236, 201

——. 1980b, ApJ, 238, 311

Wolfire, M. G., & Cassinelli, J. P. 1987, ApJ, 319, 850

Yamada, M., Machida, M. N., Inutsuka, S.-i., & Tomisaka, K. 2009, ApJ, 703, 1141

Yorke, H. W., & Bodenheimer, P. 1999, ApJ, 525, 330

Yorke, H. W., & Bodenheimer, P. 2008, in Astronomical Society of the Pacific Conference Series, Vol. 387, Massive Star Formation: Observations Confront Theory, ed. H. Beuther, H. Linz, & T. Henning, 189

Yorke, H. W., Bodenheimer, P., & Laughlin, G. 1993, ApJ, 411, 274

Yorke, H. W., & Kaisig, M. 1995, Computer Physics Communications, 89, 29

Yorke, H. W., & Sonnhalter, C. 2002, ApJ, 569, 846

Zapata, L. A., Schmid-Burgk, J., Muders, D., Schilke, P., Menten, K., & Guesten, R. 2010, A&A, 510, A2

Zhu, Z., Hartmann, L., Gammie, C., & McKinney, J. C. 2009, ApJ, 701, 620

Ziegler, U., & Yorke, H. W. 1997, Computer Physics Communications, 101, 54

Zuckerman, B., & Evans, II, N. J. 1974, ApJ, 192, L149

# References

Alexiades, V., Amiez, G., & Gremaud, P. 1996, Communications in numerical methods in engineering, 12, 31

André, P. et al. 2010, A&A, 518, L102

Arce, H. G., Borkin, M. A., Goodman, A. A., Pineda, J. E., & Halle, M. W. 2010, ApJ, 715, 1170

Arce, H. G., Shepherd, D., Gueth, F., Lee, C., Bachiller, R., Rosen, A., & Beuther, H. 2007, Protostars and Planets V, 245

Ballesteros-Paredes, J., Hartmann, L., & Vázquez-Semadeni, E. 1999, ApJ, 527, 285

Banerjee, R., & Pudritz, R. E. 2006, ApJ, 641, 949

Baraffe, I., Chabrier, G., Allard, F., & Hauschildt, P. H. 2002, A&A, 382, 563

Baraffe, I., Chabrier, G., & Gallardo, J. 2009, ApJ, 702, L27

Bate, M. R. 1998, ApJ, 508, L95

——. 2009a, MNRAS, 392, 590

——. 2009b, MNRAS, 392, 1363

——. 2010, MNRAS, 404, L79

——. 2011a, MNRAS, 417, 2036

——. 2011b, MNRAS, 2080

Bate, M. R., Bonnell, I. A., & Bromm, V. 2003, MNRAS, 339, 577

Bate, M. R., Bonnell, I. A., & Price, N. M. 1995, MNRAS, 277, 362

Black, D. C., & Bodenheimer, P. 1975, ApJ, 199, 619

——. 1976, ApJ, 206, 138

Blandford, R. D., & Payne, D. G. 1982, MNRAS, 199, 883

Boley, A. C. 2009, ApJ, 695, L53

Boley, A. C., & Durisen, R. H. 2008, ApJ, 685, 1193

Boley, A. C., Hartquist, T. W., Durisen, R. H., & Michael, S. 2007, ApJ, 656, L89

Boley, A. C., Helled, R., & Payne, M. J. 2011, ApJ, 735, 30

Bonnor, W. B. 1956, MNRAS, 116, 351

Bontemps, S., Andre, P., Terebey, S., & Cabrit, S. 1996, A&A, 311, 858

Boss, A. P. 1989, ApJ, 346, 336

——. 1997, Science, 276, 1836

——. 2008, ApJ, 677, 607

——. 2011, MNRAS, 1737

Boss, A. P., & Bodenheimer, P. 1979, ApJ, 234, 289

Boss, A. P., & Yorke, H. W. 1995, ApJ, 439, L55

Bourke, T. L. et al. 2006, ApJ, 649, L37

Burrows, C. J. et al. 1996, ApJ, 473, 437

Bürzle, F., Clark, P. C., Stasyszyn, F., Dolag, K., & Klessen, R. S. 2011, MNRAS, 417, L61

Castor, J. I. 2004, Radiation Hydrodynamics (Radiation Hydrodynamics, by John I. Castor, pp. 368. ISBN 0521833094. Cambridge, UK: Cambridge University Press)

Chabrier, G. 2003, PASP, 115, 763

Chabrier, G. 2005, in Astrophysics and Space Science Library, Vol. 327, The Initial Mass Function 50 Years Later, ed. E. Corbelli, F. Palla, & H. Zinnecker, 41

Chan, C.-k. 2011, ApJ, 727, 67

Chen, X., & Arce, H. G. 2010, ApJ, 720, L169

Chen, X., Arce, H. G., Zhang, Q., Bourke, T. L., Launhardt, R., Schmalzl, M., & Henning, T. 2010, ApJ, 715, 1344

Choi, E., Kim, J., & Wiita, P. J. 2009, ApJS, 181, 413

Commerçon, B., Audit, E., Chabrier, G., & Chièze, J.-P. 2011a, A&A, 530, A13

Commerçon, B., Hennebelle, P., Audit, E., Chabrier, G., & Teyssier, R. 2008, A&A, 482, 371

——. 2010, A&A, 510, L3+

Commerçon, B., Teyssier, R., Audit, E., Hennebelle, P., & Chabrier, G. 2011b, A&A, 529, A35+

Crutcher, R. M., Hakobian, N., & Troland, T. H. 2009, ApJ, 692, 844

Dapp, W. B., & Basu, S. 2010, A&A, 521, L56

Davis, S. W., Stone, J. M., & Jiang, Y.-F. 2012, ArXiv e-prints, 1201.2222

Dedner, A., Kemm, F., Kröner, D., Munz, C.-D., Schnitzer, T., & Wesenberg, M. 2002, Journal of Computational Physics, 175, 645

Dislaire, V., Hily-Blant, P., Faure, A., Maret, S., Bacmann, A., & Pineau Des Forêts, G. 2011, ArXiv e-prints, 1111.1572

Dubroca, B., & Feugeas, J. 1999, Academie des Sciences Paris Comptes Rendus Serie Sciences Mathematiques, 329, 915

Duffin, D. F., & Pudritz, R. E. 2009, ApJ, 706, L46

Dunham, M. M., Chen, X., Arce, H. G., Bourke, T. L., Schnee, S., & Enoch, M. L. 2011, ApJ, 742, 1

Dunham, M. M., Crapsi, A., Evans, II, N. J., Bourke, T. L., Huard, T. L., Myers, P. C., & Kauffmann, J. 2008, ApJS, 179, 249

Ebert, R. 1955, Zeitschrift fur Astrophysik, 36, 222

Elmegreen, B. G. 2000, ApJ, 530, 277

Enoch, M. L., Glenn, J., Evans, II, N. J., Sargent, A. I., Young, K. E., & Huard, T. L. 2007, ApJ, 666, 982

Enoch, M. L., Lee, J., Harvey, P., Dunham, M. M., & Schnee, S. 2010, ApJ, 722, L33

Evans, II, N. J. et al. 2003, PASP, 115, 965

——. 2009, ApJS, 181, 321

Falgarone, E., Troland, T. H., Crutcher, R. M., & Paubert, G. 2008, A&A, 487, 247

Federrath, C., Banerjee, R., Clark, P. C., & Klessen, R. S. 2010, ApJ, 713, 269

Federrath, C., Sur, S., Schleicher, D. R. G., Banerjee, R., & Klessen, R. S. 2011, ApJ, 731, 62

Ferguson, J. W., Alexander, D. R., Allard, F., Barman, T., Bodnarik, J. G., Hauschildt, P. H., Heffner-Wong, A., & Tamanai, A. 2005, ApJ, 623, 585

Field, G. B. 1965, ApJ, 142, 531

Fukuda, N., & Hanawa, T. 1999, ApJ, 517, 226

Gammie, C. F. 2001, ApJ, 553, 174

Girart, J. M., Beltrán, M. T., Zhang, Q., Rao, R., & Estalella, R. 2009, Science, 324, 1408

Girart, J. M., Rao, R., & Marrone, D. P. 2006, Science, 313, 812

González, M., Audit, E., & Huynh, P. 2007, A&A, 464, 429

Graves, D. T., Trebotich, D., Miller, G. H., & Colella, P. 2008, Journal of Computational Physics, 227, 4797

Hanawa, T., Mikami, H., & Matsumoto, T. 2008, Journal of Computational Physics, 227, 7952

Harten, A., & Hyman, J. M. 1983, Journal of Computational Physics, 50, 235

Hartmann, L. 2001, AJ, 121, 1030

Hartmann, L., Ballesteros-Paredes, J., & Heitsch, F. 2011, MNRAS, 2068

Hayashi, C. 1981, Progress of Theoretical Physics Supplement, 70, 35

Hayes, J. C., & Norman, M. L. 2003, ApJS, 147, 197

Hayes, J. C., Norman, M. L., Fiedler, R. A., Bordner, J. O., Li, P. S., Clark, S. E., ud-Doula, A., & Mac Low, M.-M. 2006, ApJS, 165, 188

Heiles, C., & Crutcher, R. 2005, in Lecture Notes in Physics, Berlin Springer Verlag, Vol. 664, Cosmic Magnetic Fields, ed. R. Wielebinski & R. Beck, 137

Hennebelle, P., & Audit, E. 2007, A&A, 465, 431

Hennebelle, P., Audit, E., & Miville-Deschênes, M.-A. 2007, A&A, 465, 445

Hennebelle, P., & Chabrier, G. 2008, ApJ, 684, 395

——. 2009, ApJ, 702, 1428

Hennebelle, P., & Ciardi, A. 2009, A&A, 506, L29

Hennebelle, P., & Fromang, S. 2008, A&A, 477, 9

Hennebelle, P., & Pérault, M. 1999, A&A, 351, 309

——. 2000, A&A, 359, 1124

Hennebelle, P., & Teyssier, R. 2008, A&A, 477, 25

Heyer, M. H., & Brunt, C. M. 2004, ApJ, 615, L45

Hirano, N., Ho, P. P. T., Liu, S.-Y., Shang, H., Lee, C.-F., & Bourke, T. L. 2010, ApJ, 717, 58

Hirsch, C. 1990, Numerical computation of internal and external flows. Volume 2: Computational methods for inviscid and viscous flows (Wiley Series in Numerical Methods in Engineering)

Hosking, J. G., & Whitworth, A. P. 2004, MNRAS, 347, 1001

Hosokawa, T., Offner, S. S. R., & Krumholz, M. R. 2011a, ApJ, 738, 140

Hosokawa, T., & Omukai, K. 2009, ApJ, 691, 823

Hosokawa, T., Omukai, K., Yoshida, N., & Yorke, H. W. 2011b, Science, 334, 1250

Howell, L. H., & Greenough, J. A. 2003, Journal of Computational Physics, 184, 53

Hunter, C. 1977, ApJ, 218, 834

Ikeda, N., & Kitamura, Y. 2009, ApJ, 705, L95

——. 2011, ApJ, 732, 101

Inoue, T., & Inutsuka, S.-i. 2008, ApJ, 687, 303

——. 2009, ApJ, 704, 161

Inutsuka, S.-i., Machida, M. N., & Matsumoto, T. 2010, ApJ, 718, L58

Jiang, Y.-F., Stone, J. M., & Davis, S. W. 2012, ArXiv e-prints, 1201.2223

Jørgensen, J. K., van Dishoeck, E. F., Visser, R., Bourke, T. L., Wilner, D. J., Lommen, D., Hogerheijde, M. R., & Myers, P. C. 2009, A&A, 507, 861

Kamazaki, T., Saito, M., Hirano, N., & Kawabe, R. 2001, ApJ, 548, 278

Kenyon, S. J., Hartmann, L. W., Strom, K. M., & Strom, S. E. 1990, AJ, 99, 869

Koyama, H., & Inutsuka, S.-I. 2000, ApJ, 532, 980

Koyama, H., & Inutsuka, S.-i. 2002, ApJ, 564, L97

Kroupa, P. 2001, MNRAS, 322, 231

Krumholz, M. R., Klein, R. I., & McKee, C. F. 2011, ApJ, 740, 74

Krumholz, M. R., Klein, R. I., McKee, C. F., & Bolstad, J. 2007, ApJ, 667, 626

Krumholz, M. R., Klein, R. I., McKee, C. F., Offner, S. S. R., & Cunningham, A. J. 2009, Science, 323, 754

Krumholz, M. R., McKee, C. F., & Klein, R. I. 2004, ApJ, 611, 399

Krumholz, M. R., & Tan, J. C. 2007, ApJ, 654, 304

Kudoh, T., Matsumoto, R., & Shibata, K. 1998, ApJ, 508, 186

Kuiper, R., Klahr, H., Beuther, H., & Henning, T. 2010, ApJ, 722, 1556

——. 2011a, ArXiv e-prints, 1111.5625

——. 2011b, ApJ, 732, 20

Lai, D. 2003, ApJ, 591, L119

Larson, R. B. 1969, MNRAS, 145, 271

——. 1972, MNRAS, 156, 437

——. 1981, MNRAS, 194, 809

Launhardt, R. et al. 2009, A&A, 494, 147

Lee, C.-F., Mundy, L. G., Reipurth, B., Ostriker, E. C., & Stone, J. M. 2000, ApJ, 542, 925

Leung, C. M. 1975, ApJ, 199, 340

Levermore, C. D. 1984, Journal of Quantitative Spectroscopy and Radiative Transfer, 31, 149

Levermore, C. D., & Pomraning, G. C. 1981, ApJ, 248, 321

Li, Z.-Y., Krasnopolsky, R., & Shang, H. 2011, ApJ, 738, 180

Li, Z.-Y., & Nakamura, F. 2006, ApJ, 640, L187

Liu, J., Salumbides, E., Hollenstein, U., Koelemeij, J., Eikema, K., Ubachs, W., & Merkt, F. 2009, The Journal of chemical physics, 130, 174306

Lowrie, R. B., Mihalas, D., & Morel, J. E. 2001, J. Quant. Spec. Radiat. Transf., 69, 291

Luhman, K. L. 2004, ApJ, 617, 1216

Luhman, K. L., Rieke, G. H., Young, E. T., Cotera, A. S., Chen, H., Rieke, M. J., Schneider, G., & Thompson, R. I. 2000, ApJ, 540, 1016

Mac Low, M.-M., Klessen, R. S., Burkert, A., & Smith, M. D. 1998, Physical Review Letters, 80, 2754

Machida, M. N., Inutsuka, S.-i., & Matsumoto, T. 2006, ApJ, 647, L151

——. 2007, ApJ, 670, 1198

——. 2008a, ApJ, 676, 1088

——. 2009a, ApJ, 699, L157

Machida, M. N., Inutsuka, S.-I., & Matsumoto, T. 2011a, PASJ, 63, 555

Machida, M. N., Inutsuka, S.-i., & Matsumoto, T. 2011b, ApJ, 729, 42

Machida, M. N., Kokubo, E., Inutsuka, S.-I., & Matsumoto, T. 2010, MNRAS, 405, 1227

Machida, M. N., & Matsumoto, T. 2011, MNRAS, 413, 2767

Machida, M. N., Matsumoto, T., Hanawa, T., & Tomisaka, K. 2005a, MNRAS, 362, 382

Machida, M. N., Matsumoto, T., Tomisaka, K., & Hanawa, T. 2005b, MNRAS, 362, 369

Machida, M. N., Omukai, K., Matsumoto, T., & Inutsuka, S.-I. 2009b, MNRAS, 399, 1255

Machida, M. N., Tomisaka, K., & Matsumoto, T. 2004, MNRAS, 348, L1

Machida, M. N., Tomisaka, K., Matsumoto, T., & Inutsuka, S.-i. 2008b, ApJ, 677, 327

Masunaga, H., & Inutsuka, S.-I. 1999, ApJ, 510, 822

Masunaga, H., & Inutsuka, S.-i. 2000, ApJ, 531, 350

Masunaga, H., Miyama, S. M., & Inutsuka, S.-I. 1998, ApJ, 495, 346

Matsumoto, T. 2011, PASJ, 63, 317

Matsumoto, T., & Hanawa, T. 2003a, ApJ, 583, 296

——. 2003b, ApJ, 595, 913

——. 2011, ApJ, 728, 47

Matsumoto, T., Nakazato, T., & Tomisaka, K. 2006, ApJ, 637, L105

Matsumoto, T., & Tomisaka, K. 2004, ApJ, 616, 266

Mayer, L., Lufkin, G., Quinn, T., & Wadsley, J. 2007, ApJ, 661, L77

McKee, C. F., Li, P. S., & Klein, R. I. 2010, ApJ, 720, 1612

McKee, C. F., & Ostriker, E. C. 2007, ARA&A, 45, 565

McKee, C. F., & Tan, J. C. 2003, ApJ, 585, 850

——. 2008, ApJ, 681, 771

Mellon, R. R., & Li, Z.-Y. 2008, ApJ, 681, 1356

——. 2009, ApJ, 698, 922

Meru, F., & Bate, M. R. 2010, MNRAS, 406, 2279

Mignone, A., Bodo, G., Massaglia, S., Matsakos, T., Tesileanu, O., Zanni, C., & Ferrari, A. 2007, ApJS, 170, 228

Mihalas, D., & Auer, L. 2001, Journal of Quantitative Spectroscopy and Radiative Transfer, 71, 61

Mihalas, D., & Weibel Mihalas, B. 1984, Foundations of radiation hydrodynamics (New York: Oxford University Press)

Mikami, H., Sato, Y., Matsumoto, T., & Hanawa, T. 2008, ApJ, 683, 357

Minerbo, G. N. 1978, J. Quant. Spec. Radiat. Transf., 20, 541

Miyoshi, T., & Kusano, K. 2005, Journal of Computational Physics, 208, 315

——. 2007, AGU Fall Meeting Abstracts, A311+

Mizuno, A., Onishi, T., Yonekura, Y., Nagahama, T., Ogawa, H., & Fukui, Y. 1995, ApJ, 445, L161

Motoyama, K., Umemoto, T., & Shang, H. 2007, A&A, 467, 657

Motte, F., Andre, P., & Neri, R. 1998, A&A, 336, 150

Mouschovias, T. C., & Paleologou, E. V. 1979, ApJ, 230, 204

——. 1980, ApJ, 237, 877

Mouschovias, T. C., & Spitzer, Jr., L. 1976, ApJ, 210, 326

Nakamura, F. et al. 2011a, ApJ, 726, 46

Nakamura, F., & Li, Z.-Y. 2007, ApJ, 662, 395

Nakamura, F. et al. 2011b, ApJ, 737, 56

Nakano, T., Hasegawa, T., & Norman, C. 1995, ApJ, 450, 183

Nakano, T., & Nakamura, T. 1978, PASJ, 30, 671

Nakano, T., Nishi, R., & Umebayashi, T. 2002, ApJ, 573, 199

Narayanan, G., Heyer, M. H., Brunt, C., Goldsmith, P. F., Snell, R., & Li, D. 2008, ApJS, 177, 341

Offner, S. S. R., Klein, R. I., McKee, C. F., & Krumholz, M. R. 2009, ApJ, 703, 131

Ohashi, N., Hayashi, M., Ho, P. T. P., Momose, M., Tamura, M., Hirano, N., & Sargent, A. I. 1997, ApJ, 488, 317

Okuzumi, S. 2009, ApJ, 698, 1122

Omukai, K. 2007, PASJ, 59, 589

Omukai, K., Hosokawa, T., & Yoshida, N. 2010, ApJ, 722, 1793

Onishi, T., Mizuno, A., Kawamura, A., Ogawa, H., & Fukui, Y. 1996, ApJ, 465, 815

——. 1998, ApJ, 502, 296

Onishi, T., Mizuno, A., Kawamura, A., Tachihara, K., & Fukui, Y. 2002, ApJ, 575, 950

O'Sullivan, S., & Downes, T. P. 2006, MNRAS, 366, 1329

Padoan, P., & Nordlund, Å. 2002, ApJ, 576, 870

Pagani, L., Roueff, E., & Lesaffre, P. 2011, ApJ, 739, L35

Penston, M. V. 1969, MNRAS, 144, 425

Peters, T., Banerjee, R., Klessen, R. S., Mac Low, M.-M., Galván-Madrid, R., & Keto, E. R. 2010, ApJ, 711, 1017

Phan-Bao, N. et al. 2008, ApJ, 689, L141

Pineda, J. E. et al. 2011, ArXiv e-prints, 1109.1207

Press, W., Teukolsky, S., Vetterling, W., & Flannery, B. 2007, Numerical recipes: the art of scientific computing (Cambridge University Press)

Price, D. J., & Bate, M. R. 2007, MNRAS, 377, 77

——. 2009, MNRAS, 398, 33

Pyo, T.-S., Hayashi, M., Kobayashi, N., Terada, H., Goto, M., Yamashita, T., Tokunaga, A. T., & Itoh, Y. 2002, ApJ, 570, 724

Raga, A., & Cabrit, S. 1993, A&A, 278, 267

Raga, A. C., Canto, J., Calvet, N., Rodriguez, L. F., & Torrelles, J. M. 1993, A&A, 276, 539

Rathborne, J. M., Lada, C. J., Muench, A. A., Alves, J. F., Kainulainen, J., & Lombardi, M. 2009, ApJ, 699, 742

Reipurth, B., Yu, K. C., Rodríguez, L. F., Heathcote, S., & Bally, J. 1999, A&A, 352, L83

Ridge, N. A. et al. 2006, AJ, 131, 2921

Rybicki, G. B., & Lightman, A. P. 1986, Radiative Processes in Astrophysics (Radiative Processes in Astrophysics, by George B. Rybicki, Alan P. Lightman, pp. 400. ISBN 0-471-82759-2. Wiley-VCH)

Saigo, K., & Tomisaka, K. 2006, ApJ, 645, 381

——. 2011, ApJ, 728, 78

Saigo, K., Tomisaka, K., & Matsumoto, T. 2008, ApJ, 674, 997

Salpeter, E. E. 1955, ApJ, 121, 161

Santiago-García, J., Tafalla, M., Johnstone, D., & Bachiller, R. 2009, A&A, 495, 169

Saumon, D., Chabrier, G., & van Horn, H. M. 1995, ApJS, 99, 713

Scalo, J. M. 1986, Fund. Cosmic Phys., 11, 1

Schönke, J., & Tscharnuter, W. M. 2011, A&A, 526, A139

Seaton, M. J., Yan, Y., Mihalas, D., & Pradhan, A. K. 1994, MNRAS, 266, 805

Seifried, D., Banerjee, R., Klessen, R. S., Duffin, D., & Pudritz, R. E. 2011a, MNRAS, 417, 1054

Seifried, D., Pudritz, R. E., Banerjee, R., Duffin, D., & Klessen, R. S. 2011b, ArXiv e-prints, 1109.4379

Semenov, D., Henning, T., Helling, C., Ilgner, M., & Sedlmayr, E. 2003, A&A, 410, 611

Shu, F. H. 1977, ApJ, 214, 488

Shu, F. H., Adams, F. C., & Lizano, S. 1987, ARA&A, 25, 23

Stahler, S. W., Palla, F., & Salpeter, E. E. 1986, ApJ, 302, 590

Stahler, S. W., Shu, F. H., & Taam, R. E. 1980a, ApJ, 241, 637

——. 1980b, ApJ, 242, 226

——. 1981, ApJ, 248, 727

Stamatellos, D., & Whitworth, A. P. 2008, A&A, 480, 879

——. 2009, MNRAS, 400, 1563

Stamatellos, D., Whitworth, A. P., Bisbas, T., & Goodwin, S. 2007, A&A, 475, 37

Stone, J. M., Gardiner, T. A., Teuben, P., Hawley, J. F., & Simon, J. B. 2008, ApJS, 178, 137

Stone, J. M., Mihalas, D., & Norman, M. L. 1992, ApJS, 80, 819

Stone, J. M., Ostriker, E. C., & Gammie, C. F. 1998, ApJ, 508, L99

Sugitani, K. et al. 2011, ApJ, 734, 63

Tafalla, M., Santiago-García, J., Hacar, A., & Bachiller, R. 2010, A&A, 522, A91

Takami, M., Takakuwa, S., Momose, M., Hayashi, M., Davis, C. J., Pyo, T.-S., Nishikawa, T., & Kohno, K. 2006, PASJ, 58, 563

Tanaka, K. E. I., & Nakamoto, T. 2011, ApJ, 739, L50

Tassis, K., & Mouschovias, T. C. 2004, ApJ, 616, 283

Tomida, K., Machida, M. N., Saigo, K., Tomisaka, K., & Matsumoto, T. 2010a, ApJ, 725, L239

Tomida, K., Tomisaka, K., Matsumoto, T., Ohsuga, K., Machida, M. N., & Saigo, K. 2010b, ApJ, 714, L58

Tomisaka, K. 1998, ApJ, 502, L163+

——. 2000, ApJ, 528, L41

——. 2002, ApJ, 575, 306

Tomisaka, K., & Tomida, K. 2011, PASJ, 63, 1151

Toro, E. 2009, Riemann solvers and numerical methods for fluid dynamics: a practical introduction (Springer Verlag)

Troland, T. H., & Crutcher, R. M. 2008, ApJ, 680, 457

Truelove, J. K., Klein, R. I., McKee, C. F., Holliman, II, J. H., Howell, L. H., & Greenough, J. A. 1997, ApJ, 489, L179

Tscharnuter, W. 1975, A&A, 39, 207

Tsukamoto, Y., & Machida, M. N. 2011, MNRAS, 416, 591

Turk, M. J., Oishi, J. S., Abel, T., & Bryan, G. 2011, ArXiv e-prints, 1112.4479

Turner, N. J., & Stone, J. M. 2001, ApJS, 135, 95

Umebayashi, T., & Nakano, T. 2009, ApJ, 690, 69

Vaidya, B., Fendt, C., & Beuther, H. 2009, ApJ, 702, 567

Vázquez-Semadeni, E., Banerjee, R., Gómez, G. C., Hennebelle, P., Duffin, D., & Klessen, R. S. 2011, MNRAS, 414, 2511

Velusamy, T., Langer, W. D., & Marsh, K. A. 2007, ApJ, 668, L159

Vorobyov, E. I. 2009, ApJ, 704, 715

Vorobyov, E. I., & Basu, S. 2010, ApJ, 719, 1896

Wang, P., Li, Z.-Y., Abel, T., & Nakamura, F. 2010, ApJ, 709, 27

Whitehouse, S. C., & Bate, M. R. 2004, MNRAS, 353, 1078

——. 2006, MNRAS, 367, 32

Whitehouse, S. C., Bate, M. R., & Monaghan, J. J. 2005, MNRAS, 364, 1367

Whitworth, A., & Summers, D. 1985, MNRAS, 214, 1

Winkler, K.-H. A., & Newman, M. J. 1980a, ApJ, 236, 201

——. 1980b, ApJ, 238, 311

Wolfire, M. G., & Cassinelli, J. P. 1987, ApJ, 319, 850

Yamada, M., Machida, M. N., Inutsuka, S.-i., & Tomisaka, K. 2009, ApJ, 703, 1141

Yorke, H. W., & Bodenheimer, P. 1999, ApJ, 525, 330

Yorke, H. W., & Bodenheimer, P. 2008, in Astronomical Society of the Pacific Conference Series, Vol. 387, Massive Star Formation: Observations Confront Theory, ed. H. Beuther, H. Linz, & T. Henning, 189

Yorke, H. W., Bodenheimer, P., & Laughlin, G. 1993, ApJ, 411, 274

Yorke, H. W., & Kaisig, M. 1995, Computer Physics Communications, 89, 29

Yorke, H. W., & Sonnhalter, C. 2002, ApJ, 569, 846

Zapata, L. A., Schmid-Burgk, J., Muders, D., Schilke, P., Menten, K., & Guesten, R. 2010, A&A, 510, A2

Zhu, Z., Hartmann, L., Gammie, C., & McKinney, J. C. 2009, ApJ, 701, 620

Ziegler, U., & Yorke, H. W. 1997, Computer Physics Communications, 101, 54

Zuckerman, B., & Evans, II, N. J. 1974, ApJ, 192, L149